
Neuroscience Bulletin
The Official Journal of The Chinese Neuroscience Society
神经科学通报
Volume 36
Number 8
August 2020
Impaired PHG–OFC Circuit Associated with Visuospatial Memory Deficit
SIBS
Springer

www.neurosci.cn

CONTENTS

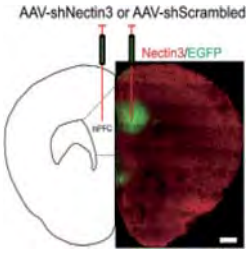

p 871

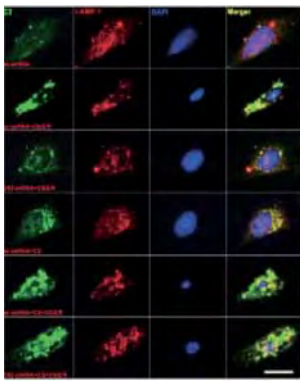

p 888

Letters to the Editor

CONTENTS

Neuroscience Bulletin

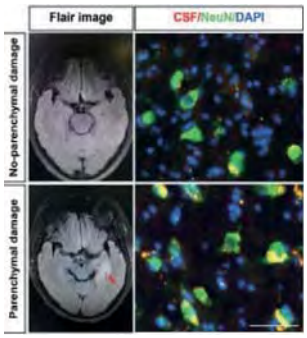

p 944

Research Highlights

Neurosci. Bull. August, 2020, 36(8):829–830
https://doi.org/10.1007/s12264-020-00560-0

www.neurosci.cn
www.springer.com/12264

EDITORIAL

Visuospatial Memory Alteration in Alzheimer's Disease

Sen Lin[1]

Received: 11 June 2020 / Accepted: 19 July 2020 / Published online: 2 August 2020

Although the treatment and drug discovery for Alzheimer's disease (AD) are limited and some have failed recently, the search for potential biomarkers and early predictors continue. AD is not only characterized by the decline of episodic memory, but also by amnestic mild cognitive impairment (aMCI) that deserves more attention. MCI is a positive prodrome of subsequent AD, and the rate of conversion to AD can rise to 50% at 2–3 years from the initial stage. It has been reported that, after 6 years, 61 out of 76 MCI patients (mean age = 81 years) converted to AD [1, 2]. The assessment of visuospatial abilities, which are necessary pre-requisites of independent mobility in the environment, is crucial to monitor elderly people's well-being. Navigational impairment in AD patients has been linked to a disorder of extrastriate visual cortical motion processing that is reflected in specific perceptual and memory measures of spatial abilities [3].

Cortical visual processing is divided into distinct dorsal and ventral streams that originate in the striate cortex. The dorsal stream processes spatial or "where/how" information for object localization, while the ventral stream processes visual or "what" features for object recognition [4, 5]. The dorsal stream actually gives rise to three distinct, major pathways: parieto–prefrontal, parieto–premotor, and parieto–medial temporal lobe (MTL) pathways. A new neural framework for primates proposed by Mishkin and collaborators indicates that the MTL pathway (including the hippocampus, parahippocampal gyrus (PHG), and entorhinal cortex) and the frontal lobes are critical regions for visuospatial memory (Fig. 1); they are key structures supporting both visuospatial and mnemonic processes, responding strongly to visual scenes such as landscapes, cityscapes, and buildings [5–7]. Neuropathology and structural MRI studies have demonstrated that the MTL is the earliest affected brain region in AD [8]. Although clinical evidence from patients with lesions and research on non-human primates have enriched the anatomy of visuospatial pathways, the detailed neural circuits are still under investigation. The postrhinal cortex (POR), which is homologous to the PHG in humans, has been shown by Zhang's group to include a POR-ventrolateral orbitofrontal cortex (vlOFC) glutamatergic pathway that specifically regulates spatial memory retrieval [9]. The anterior temporal lobe-OFC pathway (including the PHG) is connected by the uncinate fasciculus (UF), which originates within the OFC and then forms a single bundle that projects dorsally and arches down to reach the anterior temporal lobe. Compared with the traditional fMRI and perception research, their refined serial studies dissected the basic neural circuit of the POR-vlOFC pathway, and provided a deeper understanding of UF function and dysfunction related to disorders of memory, as in MCI and AD [9, 10].

In the current issue of *Neuroscience Bulletin*, Lin Zhu and collaborators report the relationship between and impairment of the POR-vlOFC circuit and visuospatial memory deficits through retrograde tracing and *in vivo* local field potential recording in 5XFAD mice as well as the investigation of alterations of the PHG-OFC circuit in AD patients by MRI [10]. They first found impaired integrity of the glutamatergic POR-vlOFC circuit along with the visuospatial memory deficit. In mice, they also used opto-stimulation to successfully improve the impaired visuospatial memory. In addition, by MRI measurement of

✉ Sen Lin
sam.lin@tmmu.edu.cn

[1] Department of Ophthalmology, Daping Hospital, Army Medical Center of the People's Liberation Army, Army Medical University, Chongqing 400042, China

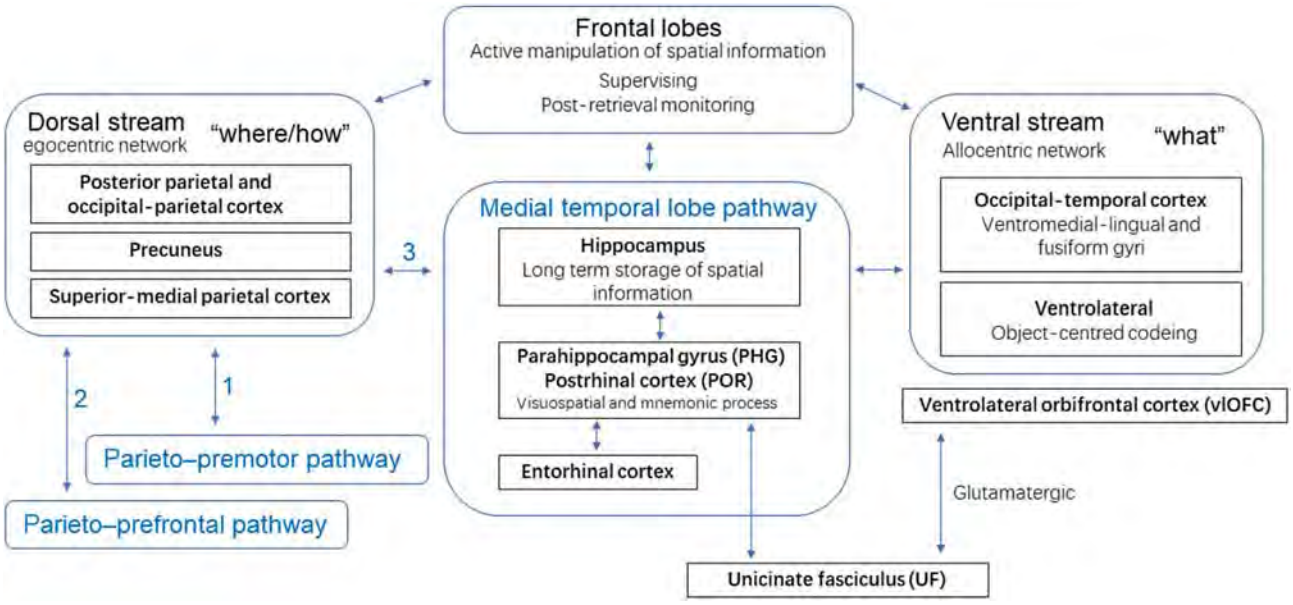

Fig. 1 Graphic illustration of the relationships of neocortical regions and the dorsal and ventral streams. (1) The parieto-premotor pathway: the occipito-parietal circuit is linked to a pre-arcuate region and the caudal portions of the banks of the principal sulcus in the prefrontal cortex. (2) The parieto-prefrontal pathway has major sources in areas of V6A and the medial intraparietal area targeting the dorsal premotor cortex, and the ventral intraprietal area projecting to the ventral premotor cortex, mediating eye movements. (3) The MTL pathway includes portions of the entorhinal cortex, parahippocampal cortex, and perirhinal cortex, receiving spatial information from the posterior cingulate cortex (PCC) and retrosplenial cortex.

progressive damage in the PHG-OFC in aMCI converters and non-converters and healthy controls, they found that the annual change of diffuse tensor imaging (DTI) is a clinical estimator to indicate the conversion of aMCI to AD, and may aid the development of methods to treat AD. In addition, their findings also expand the MTL pathway by revealing a glutamatergic POR-vlOFC circuit associated with visuospatial memory, containing the mainly allocentric spatial representation of scenes. Furthermore, the findings illustrate the neuroanatomical basis of visuospatial memory and provide an opportunity to explore new clinical predictors of AD conversion and novel methods for the early diagnosis of AD.

Comparisons of rodents, non-human primates, and humans need to be distinguished in these initial findings, by experimental and clinical fMRI studies. The neural circuits in human and non-human primates are more complex than in rodents. The diversity of neurons, the specific metabolism in specific brain regions, and the novel neural activity associated with visuospatial memory enrich the understanding of the POR-vlOFC visuospatial pathway.

Acknowledgements This editorial article was supported by the Basic Research and Scientific Frontier Foundation of Chongqing Municipality, China (cstc2019jcyj-msxmX0010).

References

1. Petersen RC, Doody R, Kurz A, Mohs RC, Morris JC, Rabins PV, *et al*. Current concepts in mild cognitive impairment. Arch Neurol 2001, 58: 1985–1992.
2. Morris JC, Storandt M, Miller JP, McKeel DW, Price JL, Rubin EH, *et al*. Mild cognitive impairment represents early-stage Alzheimer disease. Arch Neurol 2001, 58: 397–405.
3. Iachini I, Iavarone A, Senese VP, Ruotolo F, Ruggiero G. Visuospatial memory in healthy elderly, AD and MCI: a review. Curr Aging Sci 2009, 2: 43–59.
4. Weller RE. Two cortical visual systems in Old World and New World primates. Prog Brain Res 1988, 75: 293–306.
5. Kravitz DJ, Saleem KS, Baker CI, Mishkin M. A new neural framework for visuospatial processing. Nat Rev Neurosci 2011, 12: 217–230.
6. Epstein R and Kanwisher N. A cortical representation of the local visual environment. Nature 1998, 392: 598–601.
7. Epstein RA and Ward EJ. How reliable are visual context effects in the parahippocampal place area? Cereb Cortex 2010, 20: 294–303.
8. Mosconi L. Brain glucose metabolism in the early and specific diagnosis of Alzheimer's disease. FDG-PET studies in MCI and AD. Eur J Nucl Med Mol Imaging 2005, 32: 486–510.
9. Qi X, Du ZJ, Zhu L, Liu X, Xu H, Zhou Z, *et al*. The glutamatergic postrhinal cortex-ventrolateral orbitofrontal cortex pathway regulates spatial memory retrieval. Neurosci Bull 2019, 35: 447–460.
10. Zhu L, Wang Z, Du Z, Qi X, Shu H, Liu D, *et al*. Impaired parahippocampal gyrus-orbitofrontal cortex circuit associated with visuospatial memory deficit as a potential biomarker and interventional approach for Alzheimer disease. Neurosci Bull 2020. https://doi.org/10.1007/s12264-020-00498-3.

Neurosci. Bull. August, 2020, 36(8):831–844
https://doi.org/10.1007/s12264-020-00498-3

www.neurosci.cn
www.springer.com/12264

ORIGINAL ARTICLE

Impaired Parahippocampal Gyrus–Orbitofrontal Cortex Circuit Associated with Visuospatial Memory Deficit as a Potential Biomarker and Interventional Approach for Alzheimer Disease

Lin Zhu[1] · Zan Wang[1] · Zhanhong Du[2] · Xinyang Qi[1] · Hao Shu[1] · Duan Liu[1] · Fan Su[1] · Qing Ye[1] · Xuemei Liu[2] · Zheng Zhou[2] · Yongqiang Tang[2] · Ru Song[2] · Xiaobin Wang[3] · Li Lin[4] · Shijiang Li[5] · Ying Han[4,7,8,9] · Liping Wang[2,6] · Zhijun Zhang[1]

Received: 5 October 2019 / Accepted: 10 December 2019 / Published online: 29 April 2020

Abstract The parahippocampal gyrus–orbitofrontal cortex (PHG–OFC) circuit in humans is homologous to the postrhinal cortex (POR)–ventral lateral orbitofrontal cortex (vlOFC) circuit in rodents. Both are associated with visuospatial malfunctions in Alzheimer's disease (AD). However, the underlying mechanisms remain to be elucidated. In this study, we explored the relationship between an impaired POR–vlOFC circuit and visuospatial memory deficits through retrograde tracing and *in vivo* local field potential recordings in 5XFAD mice, and investigated alterations of the PHG–OFC circuit by multi-domain magnetic resonance imaging (MRI) in patients on the AD spectrum. We demonstrated that an impaired glutamatergic POR–vlOFC circuit resulted in deficient visuospatial memory in 5XFAD mice. Moreover, MRI measurements of the PHG–OFC circuit had an accuracy of 77.33% for the classification of amnestic mild cognitive impairment converters *versus* non-converters. Thus, the PHG–OFC circuit explains the neuroanatomical basis of visuospatial memory deficits in AD, thereby providing a potential predictor for AD progression and a promising interventional approach for AD.

Electronic supplementary material The online version of this article (https://doi.org/10.1007/s12264-020-00498-3) contains supplementary material, which is available to authorized users.

Lin Zhu, Zan Wang and Zhanhong Du contributed equally to this work.

✉ Ying Han
hanying@xwh.ccmu.edu.cn

✉ Liping Wang
lp.wang@siat.ac.cn

✉ Zhijun Zhang
janemengzhang@vip.163.com

[1] Department of Neurology, Affiliated ZhongDa Hospital, School of Medicine, Southeast University, Nanjing 210009, China

[2] Shenzhen Key Laboratory of Neuropsychiatric Modulation, Guangdong Provincial Key Laboratory of Brain Connectome and Behavior, Chinese Academy of Science (CAS) Key Laboratory of Brain Connectome and Manipulation, the Brain Cognition and Brain Disease Institute (BCBDI), Shenzhen Institutes of Advanced Technology, Chinese Academy of Sciences, Shenzhen-Hong Kong Institute of Brain Science-Shenzhen Fundamental Research Institutions, Shenzhen 518055, China

[3] Laboratory Animal Center, Southeast University, Nanjing 210009, China

[4] Department of Neurology, Xuan Wu Hospital of Capital Medical University, Beijing 100053, China

[5] Department of Biophysics, Medical College of Wisconsin, Milwaukee, WI 53226, USA

[6] University of the Chinese Academy of Sciences, Beijing 100049, China

[7] Beijing Institute of Geriatrics, Beijing, China

[8] National Clinical Research Center for Geriatric Disorders, Beijing, China

[9] Center of Alzheimer's Disease, Beijing Institute for Brain Disorders, Beijing, China

Keywords Alzheimer's disease · Amnestic mild cognitive impairment · Postrhinal cortex · Visuospatial memory · Ventral lateral orbitofrontal cortex · Uncinate fasciculus

Background

Alzheimer's disease (AD) is a highly prevalent neurodegenerative disease that is characterized by a progressive decline in memory and other cognitive functions [1]. Amnestic mild cognitive impairment (aMCI) is a well-characterized high-risk factor for AD, and is defined as an early stage in the AD spectrum [2]. A core clinical feature of AD is episodic memory deficits, which can predict disease progression [3]. Recently, a deficit in visuospatial function has also been considered as a potential early predictive indicator for AD [4–6]. In 2018, the A/T/N (amyloid, tau, and neurodegeneration) biomarker classification scheme was proposed; this is based on the nature of the pathology, thereby emphasizing the importance of cerebrospinal fluid (CSF) and molecular positron emission tomography (PET) in the diagnosis of AD [7–9]. However, in China, obtaining CSF is challenging, and molecular PET is rarely implemented, particularly during the screening of patients with MCI. Thus, identifying novel methods for the early diagnosis of AD is of utmost importance.

The postrhinal cortex (POR) in rodents is homologous to the parahippocampal gyrus (PHG) in humans [10]. In previous studies, advances in visuospatial processing have shown that an array of networks contributes to visuospatial memory [11–13]. Recently, a new neural framework for primates proposed by Mishkin and coworkers indicated that the mesial temporal lobe (including the hippocampus, PHG, and entorhinal cortex) and the frontal lobes are critical regions for visuospatial memory [14]. Lesions in the PHG in humans [15, 16] or in the POR in rats [17] cause severe visuospatial learning and memory deficits, with profound effects on memory retrieval, but only mild effects on memory encoding [17]. We previously demonstrated that inhibition of the glutamatergic input from the POR to the ventral lateral orbitofrontal cortex (vlOFC) specifically impairs visuospatial memory retrieval in wild-type mice [18], suggesting that impairment of the POR–vlOFC circuit contributes to visuospatial memory deficits. However, changes in the anatomy and function of this circuit in a mouse model of AD have not yet been reported.

In humans, the uncinate fasciculus (UF) is a hook-shaped long-range association pathway that connects the anterior temporal lobes (including the anterior PHG) to the orbitofrontal cortex (OFC) [19]. Disruption of the UF as measured by magnetic resonance imaging (MRI) has been reported in patients with autism spectrum disorder [20], MCI [21], temporal lobe epilepsy [22], Parkinson disease [23], and schizophrenia [19]. In addition, impaired diffuse tensor imaging (DTI) indexes of the UF have been reported in patients with subjective cognitive decline [24], aMCI [25] and AD [26], and have been correlated with general cognitive impairment [27, 28], visuospatial malfunction [29], and episodic memory deficits [25, 30, 31]. Moreover, improvement in visuospatial working memory during childhood is significantly associated with changes in DTI indexes in the right UF [32], suggesting that the UF contributes to visuospatial functions. During visuospatial tasks, PHG activation is enhanced in participants with normal cognition [21, 33, 34] and in prodromal AD patients [35], but the activation declines in the PHG [36] and OFC [37] of AD patients. However, it remains unclear how the anatomy and function of the PHG–OFC circuit are changed in the AD spectrum.

In the present study, we investigated the role of the POR–vlOFC circuit during visuospatial memory through exploring neuron-specific alterations in 5XFAD mice. Furthermore, we assessed the changes in structural and functional connectivity (FC) of the PHG–OFC circuit in the AD spectrum. Together, our findings further illustrate the neuroanatomical basis of visuospatial memory and identify novel predictors of AD conversion.

Materials and Methods

Mice

Adult (4–6 months) male 5XFAD mice and their wild-type (WT) littermates were purchased from the Jackson Laboratory (Bar Harbor, ME, USA) and were housed at the Animal Center of the Medical School of Southeast University and Shenzhen Institutes of Advanced Technology, Chinese Academy of Sciences. Mice were maintained at 22 °C–24 °C under a 12-h light/dark cycle with food and water provided *ad libitum*.

Behavioral Tests

To assess visuospatial memory, we used the novel object place recognition (NOPRT) and Y-maze tests. Moreover, the open field test (OFT) and elevated plus maze (EPM) tests were used to assess anxiety-like behaviors. All behavioral tests were carried out as previously described [32, 38–40] with minor modifications (Supplementary Material). Behavior was monitored and analyzed using ANY-maze software (Stoelting, Co., Wood Dale, IL, USA) by two experienced investigators who were blinded to the grouping of the experimental mice.

Immunofluorescence

To determine and compare differences in activation of the POR and vlOFC regions during the NOPRT in WT and 5XFAD mice, the expression profiles of c-Fos, CamKIIα, and GAD67 proteins in the two regions were quantified by immunofluorescence analysis as previously described [39, 41] (Supplementary Material).

Retrograde Tracing

To analyze structural integrity, 200 nL of cholera toxin B (CTB)-Alexa Fluor 488 was injected unilaterally into the vlOFC (AP, 2.30 mm; ML, −1.20 mm; DV, 2.60 mm). Four weeks later, the mice were deeply anaesthetized and perfused transcardially, and the expression of CTB and CamKIIα was assessed in the POR and vlOFC regions using immunofluorescence analysis (Fig. 2A). Brain sections (40 μm) were imaged on an Olympus VS120 digital slice scanner (Tokyo, Japan).

In vivo Optogenetic Manipulation and Microelectrode Array Implantation

For *in vivo* optogenetic manipulations, 250 nL of virus was injected into the POR. Three weeks later, an optical fiber was implanted into the ipsilateral vlOFC for the stimulation of terminals. All mice received the same intensity of blue laser stimulation.

For *in vivo* electrophysiological recordings, a 16-channel microelectrode array containing 2 hand-crafted tetrodes was implanted into WT and 5XFAD mice, separately in the POR and vlOFC. To quantify the FC between the POR and vlOFC during visuospatial memory, the coherence of local field potentials (LFPs) between the two regions during exploration in the NOPRT was assessed (Fig. 3A). Detailed procedures are provided in Supplementary Materials.

Recruitment of Participants and Neuroimaging Data Analysis

Patients with aMCI and healthy controls (HCs) were recruited to establish a registry at the Affiliated Zhongda Hospital of Southeast University and Xuanwu Hospital Affiliated to Capital Medical University. Written informed consent was given by all participants prior to the start of the study. Based on the outcome of an average of 3 years of follow-up (i.e., whether patients with aMCI converted to AD), 37 aMCI converters (aMCI-Cs), 38 aMCI non-converters (aMCI-NCs) were identified. Also, 45 HCs, who were all right-handed Han Chinese, were recruited through routine community health screening and advertisements. All participants underwent a standardized clinical interview and a neuropsychological assessment battery. The inclusion and exclusion criteria are described in Supplementary Materials.

All participants [29/37 aMCI-Cs, 31/38 aMCI-NCs, and 45/45 HCs (the number in the follow-up/that at baseline)] underwent baseline and follow-up multi-modal MRI examination (high-resolution T1-weighted and resting-state functional imaging). Notably, none of the selected aMCI patients showed excessive motion artifacts (≥3 mm translational or ≥3° rotational movements) during MRI scans or incomplete image coverage. Details of imaging acquisition and preprocessing are presented in Supplementary Materials.

To investigate changes in the volume of grey matter (GM) and brain neuronal activity [indicated by the amplitude of low-frequency fluctuations (ALFFs)] in the bilateral PHG and OFC, regions of interest (ROIs) were defined based on the Brainnetome atlas (Fig. 5A), a fine-gained, cross-validated atlas that correlates brain anatomy with psychological and cognitive functions [42]. Accordingly, for all patients, the mean GM volume and ALFF values for each OFC and PHG subregion were extracted. Furthermore, to measure inter-regional resting-state functional connectivity (RSFC), Pearson correlation coefficients between pairs of ROIs were calculated, generating a 24 × 24 correlation matrix for each patient. These coefficients were subjected to Fisher's z-transformation to yield variants from the normal distribution. The RSFC was investigated between all OFC and PHG sub-regions, and the pattern of connectivity between 144 (12 × 12) pairs of ROIs was explored.

Statistical Analysis

Data are presented as the mean ± standard error of the mean (SEM). For animal behavioral tests and immunofluorescence analysis, the Shapiro-Wilkes test was used to assess the normality of the distributions. Normally distributed data were compared using paired and unpaired independent *t*-tests (two groups), and one-way or two-way analysis of covariance (ANCOVA) (multiple groups). In addition, non-normally distributed data were analyzed using the Mann-Whitney *U* test. ANCOVA was used to investigate aMCI-C-related changes of the mean GM volume and ALFF values in the OFC and PHG ROIs, and to determine the pattern of connectivity between the 144 pairs of ROIs at baseline, with age, gender, and years of education as covariate variables. Comparisons were adjusted using the false discovery rate (FDR) at a significance threshold of $P < 0.05$. The support vector machine (SVM) [43] was used to classify GM volume, ALFF, and connectivity, which were combined to

distinguish aMCI-Cs, aMCI-NCs, and HCs. The merged classifier was evaluated through 10-fold cross-validations.

For each patient, annual change (AC) estimates were calculated using the mean GM and ALFF values from the OFC and PHG ROIs, as well as the connectivity between the pairs of ROIs from baseline and follow-up scans. The following equation was used:

$$AC = \frac{MRI\ measure(t1) - MRI\ measure(t0)}{t1 - t0}$$

, where *MRI measure* ($t0$) and *MRI measure* ($t1$) represent MRI measurements (GM volume, ALFF, and RSFC) at the time of entry and at an average of 3 years of follow-up, and $t1 - t0$ represents the individual delay between evaluations. ANOVA assessments were further used to evaluate group differences in AC estimates with an FDR-corrected $P < 0.05$ considered as a significant difference. Furthermore, using relevance vector regression as a multivariate analytical approach, we further examined the relationship between aMCI-C-related changes in AC estimates (GM and RSFC) and the AC of mini-mental state examination (MMSE) scores.

Results

Retrieval Deficit of Visuospatial Memory in 5XFAD Mice is Associated with Anatomical and Functional Disruption of the POR–vlOFC Circuit

The visuospatial memory of mice was initially assessed by NOPRT (Fig. 1A). Both 5XFAD and WT mice at 6 months of age showed no preference for either object in the study phase (Fig. 1B), however, 5XFAD mice showed a prominent reduction in the discrimination index (D2) (Fig. 1C) (for the measurement in 4-month-old mice see Fig. S1). In addition, 6-month-old 5XFAD mice showed decreased spontaneous alternations in the Y-maze test as compared to WT mice (Fig. S2A). Again, no changes were found in the time and distance spent in the center of the OFT, or the time and number of entries into the closed arms in the EPM between 5XFAD and WT mice (Fig. S2B–C).

After NOPRT, the differences in activation of the POR and vlOFC regions were quantified by c-Fos, CamKIIα, GAD67, c-Fos/CamKIIα, and c-Fos/GAD67 protein staining in both WT and 5XFAD mice. When compared to WT mice, 5XFAD mice showed a significant decrease in the numbers of both c-Fos- and c-Fos/CamKIIα-positive neurons in the vlOFC region (Fig. 1H, J, K,), but not in the POR region (Fig. 1D, F, G). However, no significant differences between the two groups were shown in the numbers of CamKIIα-positive neurons in the POR and vlOFC regions (Fig. 1E, I). Notably, no significant differences between the two groups in the numbers of both GAD67- and c-Fos/GAD67-positive neurons were found in either region (Fig. S3).

Glutamatergic neurons in the vlOFC were deactivated in visuospatial memory-impaired 5XFAD mice as measured by the integrity of the anatomical connection in the glutamatergic POR–vlOFC circuit through retrograde anatomical tracing using CTB labeling (Fig. 2A). Compared to WT mice, 5XFAD mice had significantly fewer CTB neurons (Fig. 2C, D), as well as a lower ratio of CamKIIα-positive CTB neurons to total CTB neurons in the POR (Fig. 2C, E). Furthermore, compared to WT mice, 5XFAD mice had a slightly lower ratio of CamKIIα-positive CTB neurons in the POR to that in the vlOFC (Fig. 2B, C, F).

Subsequently, we determined the integrity of the functional connection between the two regions in both WT and 5XFAD mice by LFP recording during NOPRT. Our data showed that, compared to WT mice, 5XFAD mice showed reduced power of LFP signals in the beta band of the vlOFC region during exploration of the displaced object (Fig. 3B, D, E). In contrast, no significant differences were found between groups in the power of the beta, theta, and delta bands of the POR region (Fig. 3B–D). Importantly, coherence spectral analysis showed a significant increase in FC between the two regions at 15 Hz in 5XFAD mice during exploration of the displaced object as compared to WT mice (Fig. 3F, G).

Opto-stimulation of CamKIIα:: POR-vlOFC Terminals in 5XFAD Mice Rescues the Visuospatial Memory Deficit

After determining that the impaired POR-vlOFC glutamatergic pathway in 5XFAD mice is involved in the visuospatial memory deficit, we further explored whether optical activation of the CamKIIα:: POR-vlOFC circuit could rescue this deficit in 5XFAD mice. After surgery (Fig. 4A), similar times and distances in the center of the OFT were recorded among the four experimental groups (Fig. S4), and no significant difference was found for locomotor activity between groups with and without optogenetic manipulation among the four groups (Fig. S5). Furthermore, mice did not show a preference for either object during the NOPRT study phase (Fig. 4D). However, during the recognition phase, significant effects on D2 were found for "group" [F (1, 34) = 6.242, $P = 0.018$] or for the interaction of "group" and "optical stimulation" [F (1, 34) = 17.50, $P < 0.001$]. Moreover, *post-hoc* analysis showed that during the recognition phase, the D2 decreased in the 5XFAD-CamKIIα-mCherry group that was exposed to opto-stimulation compared to the WT-CamKIIα-mCherry, WT-CamKIIα-ChR2-mCherry and

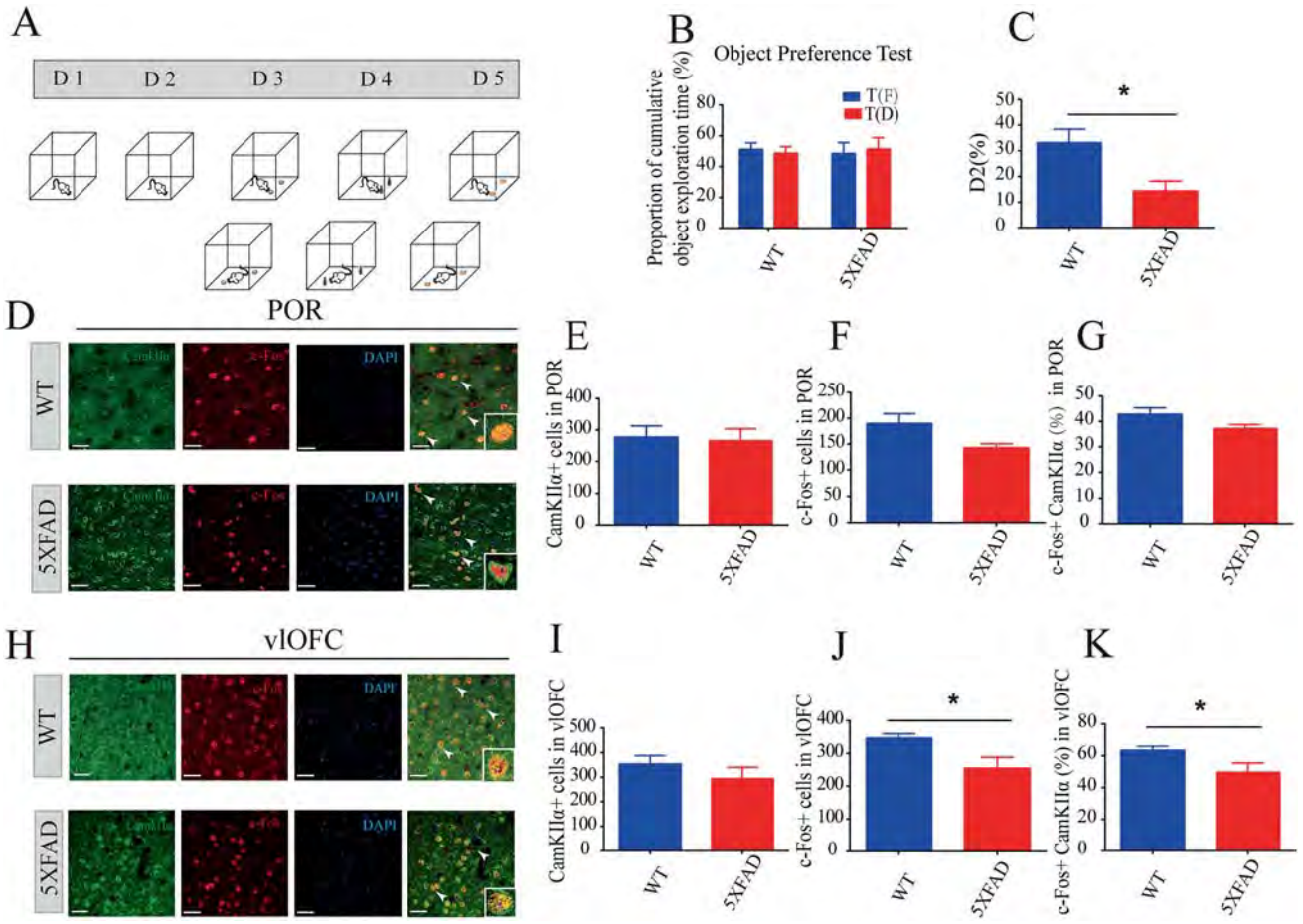

Fig. 1 CamKIIα activation in the POR and vlOFC regions of 6-month-old 5XFAD and WT mice during visuospatial memory retrieval. **A** Schematic of the novel object place recognition test. D1-D5, Day1-Day5; red, blue and orange dots in the boxes represent different objects that the mice explored. **B** There are no differences in T(f) and T(n) between WT and 5XFAD mice. **C** Compared to WT mice, 5XFAD mice show a reduced D2 during the recognition phase [5XFAD (n = 7) 14.41% ± 3.8% *vs* WT (n = 8) 33.20% ± 5.29%; independent sample t-tests, t = –2.807, P = 0.015]. **D**–**G** Representative images and statistics showing no significant differences between WT and 5XFAD mice in CamKIIα neurons, c-Fos+ cells, and c-Fos-activated CamKIIα neurons in the POR region (n_{5XFAD} = 4, n_{WT} = 5; independent sample t-tests, t = 0.237, P = 0.820; t = 2.099, P = 0.074; t = 1.039, P = 0.334). **H**–**K** Representative images and statistics showing that, compared to WT mice, 5XFAD mice show decreased c-Fos+ cells and c-Fos-activated CamKIIα neurons in the vlOFC region (n_{5XFAD} = 4, n_{WT} = 5; independent sample t-tests, t = 2.928, P = 0.022; t = 2.585, P = 0.042). However, no significant differences between the two groups were shown in the numbers of CamKIIα-positive neurons (independent sample t-tests, t = 1.023, P = 0.346). Data are presented as the mean ± SEM. Blue, DAPI; green, CamKIIα; red, c-Fos; scale bars, 50 μm; n = 64 sections of vlOFC and n = 36 sections of POR from four 5XFAD mice and n = 80 sections of vlOFC and n = 45 sections of POR from five WT mice; arrows indicate co-localization. WT, wild type; POR, postrhinal cortex; vlOFC, ventral lateral orbitofrontal cortex; T(f), time for the familiar object; T(n), time for the novel object; D2, discrimination index.

5XFAD-CamKIIα-ChR2-mCherry groups (Fig. 4E; P = 0.041, P = 0.021, $P < 0.001$). Furthermore, no significant difference in D2 was found between the 5XFAD-CamKIIα-ChR2-mCherry and WT-CamKIIα-mCherry or WT-CamKIIα-ChR2-mCherry groups (P = 0.162, P = 0.389).

Disruption of the OFC–PHG Circuit in aMCI-C Patients

As previously noted, the OFC–PHG circuit in humans is homologous to the POR–vlOFC circuit in rodents, so we further explored whether the OFC–PHG circuit is damaged in aMCI patients and whether this impairment can predict the conversion of aMCI to AD. At baseline, the analysis of MRI scans (GM volume and RSFC) showed significant "group" effects (FDR-corrected $P < 0.05$), and *post-hoc* comparisons showed that the volumes of the OFC and PHG ROIs were significantly smaller in aMCI-C patients than in aMCI-NC patients and HCs (Fig. 5B). No significant differences were found between aMCI-NC patients and HCs. Furthermore, compared to HCs, both aMCI-C and aMCI-NC patients showed significantly increased ALFF values in the PHG ROIs (Fig. 5C) with slightly higher

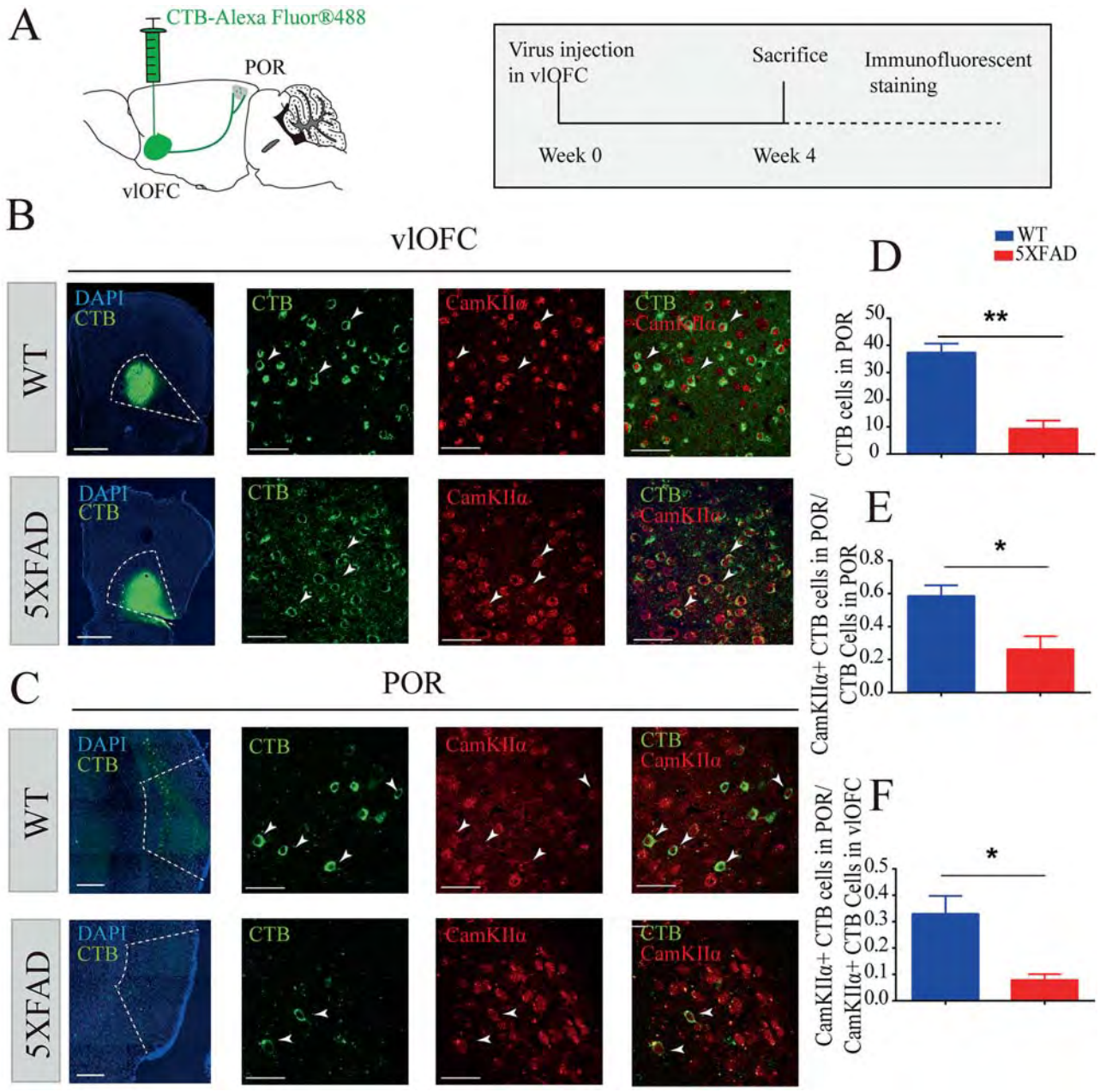

Fig. 2 CamKIIα+ POR inputs to the vlOFC region. **A** Retrograde tracing strategy using CTB and its experimental timeline. **B**–**C** Representative images showing retrograde labeling of CamKIIα+ POR input to the vlOFC region. Blue: DAPI; green: CTB - Alexa 488; red: CamKIIα; scale bars: 500 μm and 50 μm (**B**), 200 μm and 50 μm (**C**); arrows indicate co-localization; dashed outline indicate the vlOFC (**B**) and POR (**C**) regions; three mice each from 5XFAD and WT groups; n =27 sections of the POR and 48 sections of the vlOFC in each group. **D** Compared to WT mice, 5XFAD mice have significantly fewer CTB neurons in the POR [5XFAD (n = 3) 9.33 ± 2.96 *vs.* WT (n = 3) 37.33 ± 3.33; independent sample t-tests, t = 6.278, P = 0.003]. **E** 5XFAD mice have a significantly lower ratio of CamKIIα-positive CTB neurons to total CTB neurons in the POR compared to WT mice [5XFAD (n = 3) 26.28% ± 13.54% *vs* WT (n = 3) 58.28% ± 6.35%; independent sample t-tests, t = 3.208, P = 0.033]. **F** Compared to WT mice, 5XFAD mice have a slightly lower ratio of the CamKIIα-positive CTB neurons in the POR than in the vlOFC [5XFAD (n = 3) 7.85% ± 2.27% *vs* WT (n = 3) 32.90% ± 6.89%; non-parametric Mann-Whitney U test, U = 9, P = 0.05]. Data are presented as the mean ± SEM. WT, wild type; POR, postrhinal cortex; vlOFC, ventral lateral orbitofrontal cortex; CTB, cholera toxin B.

ALFF values in the PHG ROI (right TH) in aMCI-NC than in aMCI-C patients. In addition, aMCI-C patients showed decreased OFC-PHG connectivity compared to the HC and aMCI-NC groups (Fig. 5D) with slightly increased OFC–PHG connectivity in aMCI-NC patients compared to HCs. Finally, SVM classifiers for GM volume, ALFF, and connectivity were merged to distinguish between aMCI-C and aMCI-NC patients. Importantly, the merged classifier

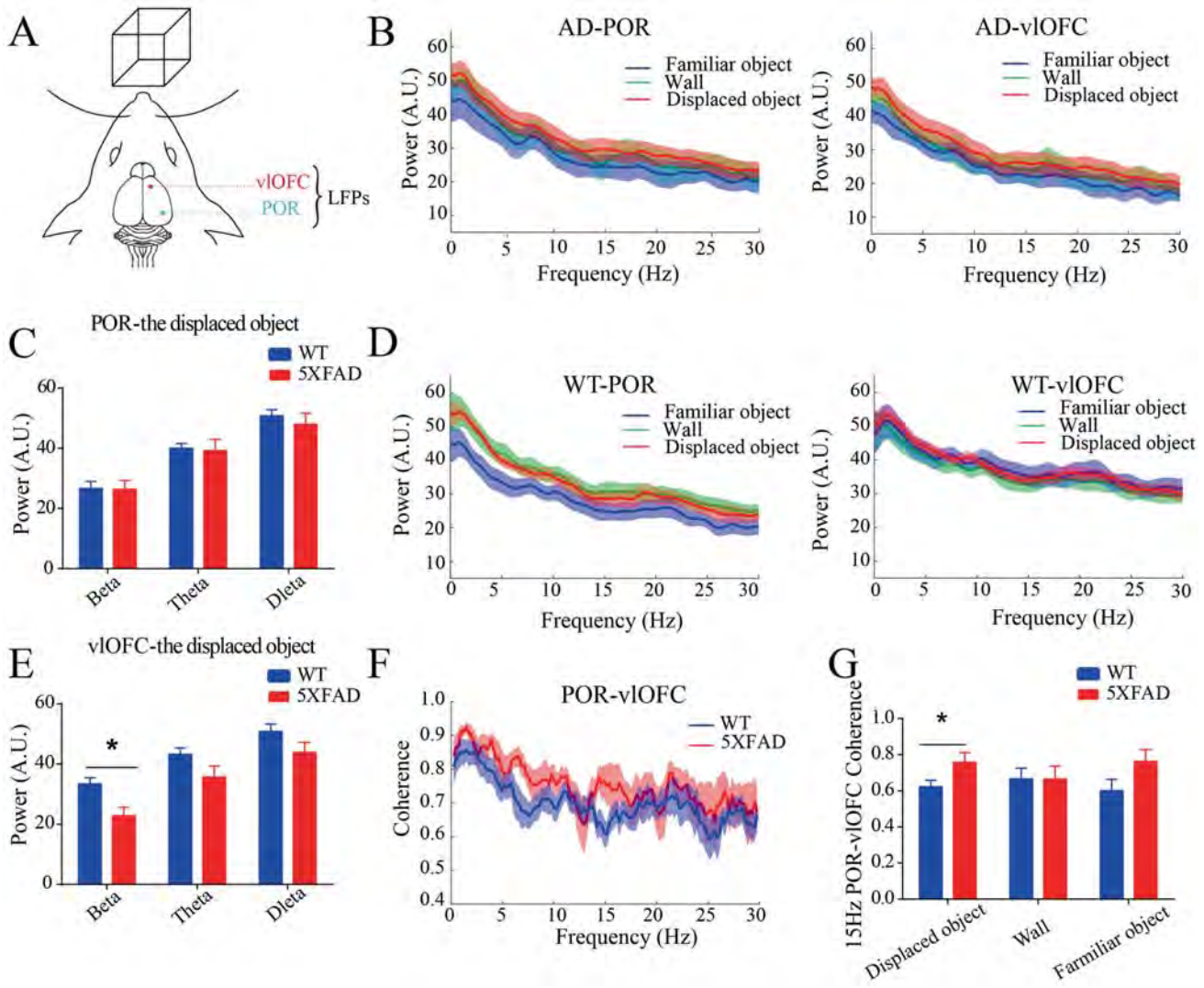

Fig. 3 Alterations of LFP functional connectivity in 5XFAD and WT mice. **A** Locations of recording electrodes in the POR and vlOFC regions. **B, D** Average power spectra of LFP recordings in the POR and vlOFC during exploration of a displaced object (red), a familiar object (blue), and a wall (green) (n_{WT} = 8, n_{5XFAD} = 6). **C** No significant differences are found between the two groups in the power of the beta (13–40 Hz), theta (4–7 Hz), and delta (<4 Hz) bands of the POR region (n_{WT} = 8, n_{5XFAD} = 6; two-way ANOVA, LSD *post-hoc* test, P >0.05 for all groups). **E** 5XFAD mice show reduced power of LFP signals in the beta band of the vlOFC region during exploration of the displaced object compared to WT mice (n_{WT} = 8, n_{5XFAD} = 6; two-way ANOVA, LSD *post-hoc* test, P = 0.013). **F, G** Coherence spectral analysis shows a significantly stronger functional connectivity between the two regions at 15 Hz in 5XFAD mice than in WT mice (n_{WT} = 8, n_{5XFAD} = 6, non-parametric Mann-Whitney U test, U = 6, P = 0.02). Data are presented as the mean ± SEM. WT, wild type; ANOVA, analysis of covariance; POR, postrhinal cortex; vlOFC, ventral lateral orbitofrontal cortex; LFP, local field potential.

had an accuracy of 77.33% (sensitivity 72.97%, specificity 81.58%) and an area under the curve of 0.8378 (Fig. 5E).

Our data indicated that the AC estimates (GM volume and RSFC) showed significant "group" effects (FDR-corrected, $P < 0.05$). The most important finding involved the annual change in GM atrophy, which was statistically significant in the OFC and PHG of only aMCI-C patients (Fig. 6A). Furthermore, a significant annual loss of OFC-PHG connectivity only occurred in the aMCI-C group (Fig. 6B). Interestingly, aMCI-NC patients conversely showed slightly increased ACs of OFC–PHG connectivity when compared to HCs. In addition, for aMCI-C-related ACs in GM volume and connectivity, the use of relevance vector regression permitted quantitative predictions of ACs in MMSE scores with statistically significant accuracy (r = 0.671, $P < 0.001$, Fig. 6C).

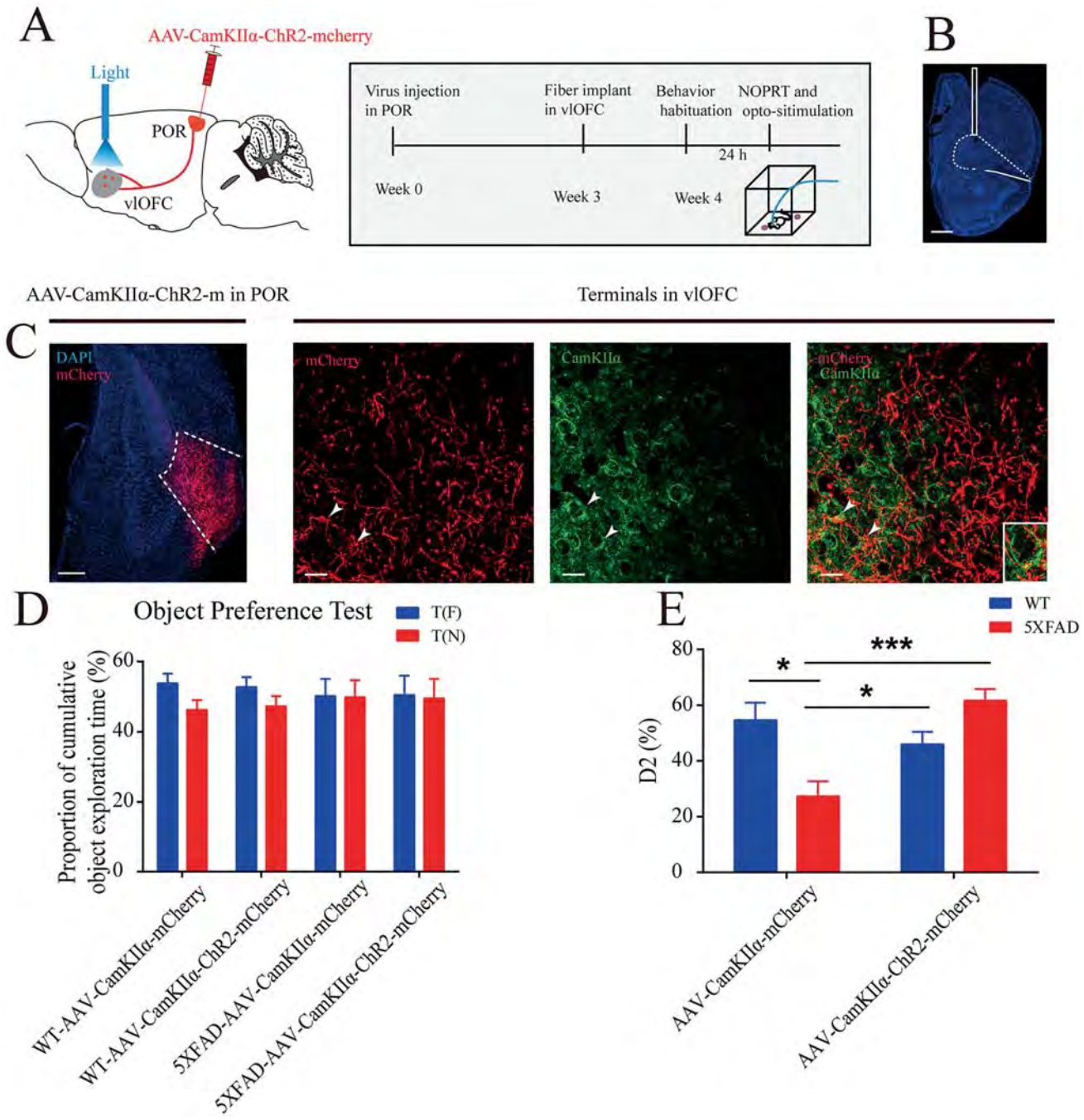

Fig. 4 Rescue of visuospatial memory deficit by opto-stimulation of CamKIIα:: POR-vlOFC terminals in 5XFAD mice. **A** Optogenetic strategy and experimental timeline for unilateral POR injections of AAV-CamKII-ChR2-mcherry or AAV-CamKIIα-mcherry virus and unilateral vlOFC optical activation. **B** Representative immunofluorescence image showing the position of the fiber track in the vlOFC (blue, DAPI; solid lines, fiber track; scale bar, 200 μm). **C** Representative images showing selective targeting of ChR2-mCherry to CamKIIα+ neurons in the POR and co-labeling of CamKIIα with mCherry-labeled POR terminals from POR CamKIIα+ neurons in the vlOFC (blue, DAPI; green, CamKIIα; red, mCherry; scale bars, 200 μm and 20 μm; arrowheads indicate co-localization). **D** There is no significant difference between T(f) and T(n) in each group ($n_{\text{WT-CamKIIα-mCherry}}$ = 9, $n_{\text{WT-CamKIIα-ChR2-mCherry}}$ = 11, $n_{\text{5XFAD-CamKIIα-mCherry}}$ = 9, $n_{\text{5XFAD-CamKIIα-ChR2-mCherry}}$ = 9; paired *t*-test, $P > 0.05$ for all groups). **E** D2 decreases in the 5XFAD-CamKIIα-mCherry group (n = 9) during the recognition phase with opto-stimulation compared to the WT-CamKIIα-mCherry (n = 9), WT-CamKIIα-ChR2-mCherry (n = 11), and 5XFAD-CamKIIα-ChR2-mCherry groups (two-way ANOVA by *post-hoc* Bonferroni multiple comparison tests, $^{*}P < 0.05$, $^{***}P < 0.001$). Data are presented as the mean ± SEM. WT, wild type; ANOVA, analysis of covariance; POR, postrhinal cortex; vlOFC, ventral lateral orbitofrontal cortex.

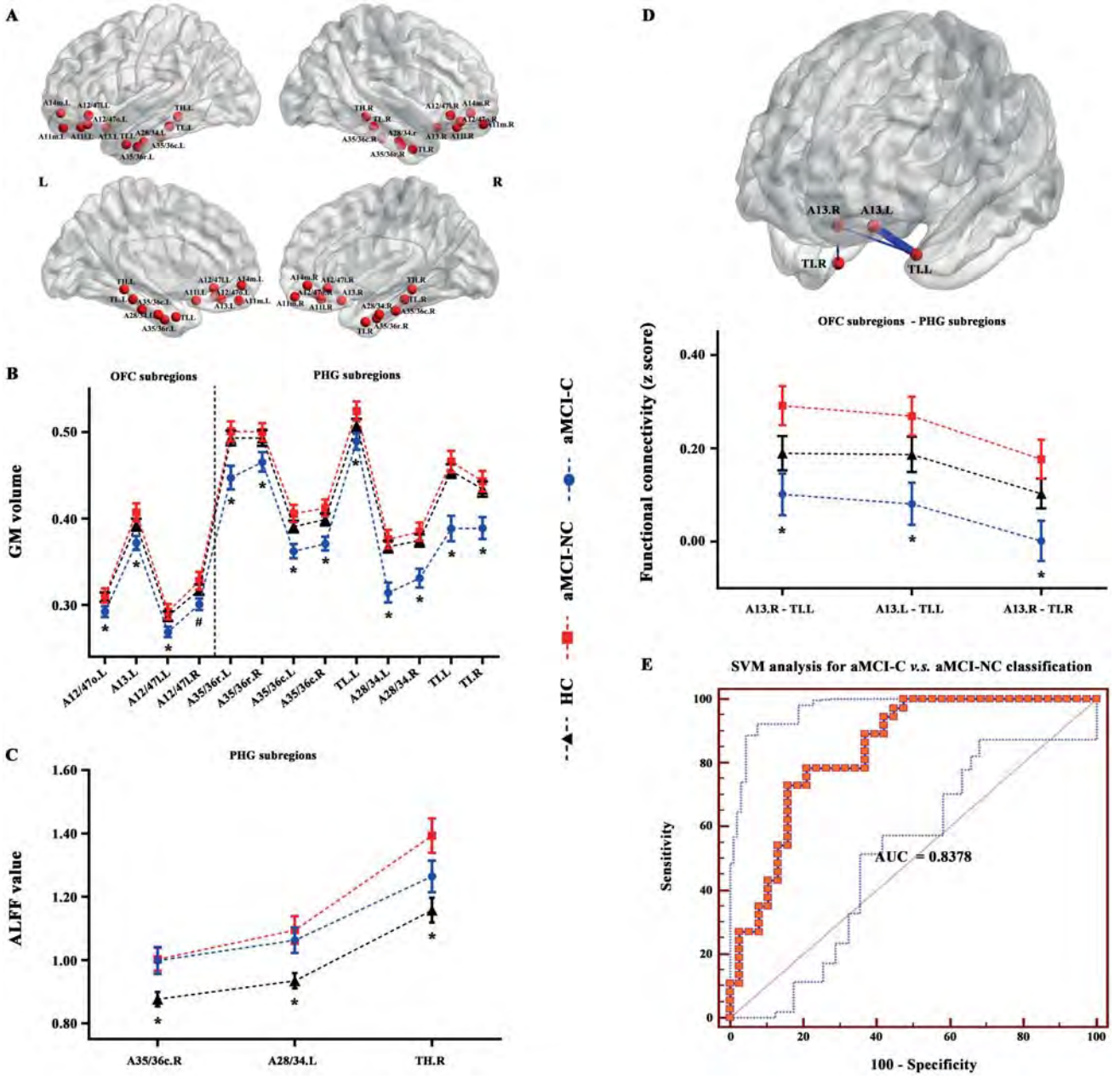

Fig. 5 Group differences in the OFC/PHG gray matter volume and OFC–PHG functional connectivity at baseline. **A** Bilateral OFC and PHG sub-regions according to the Brainnetome atlas. **B** Volumes of OFC and PHG sub-regions are significantly smaller in aMCI-C patients than in aMCI-NC patients and HCs at baseline (ANCOVAs; FDR-corrected, $P < 0.05$). **C** Compared to HCs, aMCI-C and aMCI-NC patients show increased ALFF values in the PHG ROIs (ANCOVAs; FDR-corrected, $P < 0.05$). aMCI-NC patients have higher ALFF values in the PHG ROI (i.e., right TH) than aMCI-C patients. **D** Compared to aMCI-NC patients and HCs, aMCI-C patients show decreased OFC-PHG functional connectivity (ANCOVAs; FDR-corrected, $P < 0.05$). Compared to HCs, aMCI-NC patients show higher OFC-PHG functional connectivity. **E** Merged SVM classifiers for GM volume, ALFF, and connectivity distinguish aMCI-C from aMCI-NC patients with an accuracy of 77.33% (sensitivity 72.97%, specificity 81.58%) and an area under the curve of 0.8378. Data are presented as the mean ± SEM. aMCI, amnestic mild cognitive impairment; aMCI-C, aMCI-converters; aMCI-NC, aMCI-non-converters; HC, healthy control; OFC, orbitofrontal cortex; PHG, para-hippocampal gyrus; GM, grey matter; ANCOVAs, analyses of covariance; AUC, area under the curve; ALFF, low-frequency fluctuations; ROIs, the regions of interest; FDR, false discovery rate; SVM, support vector machine; GM, grey matter. For the abbreviations of the OFC and PHG sub-regions, see Supplemental Table S1.

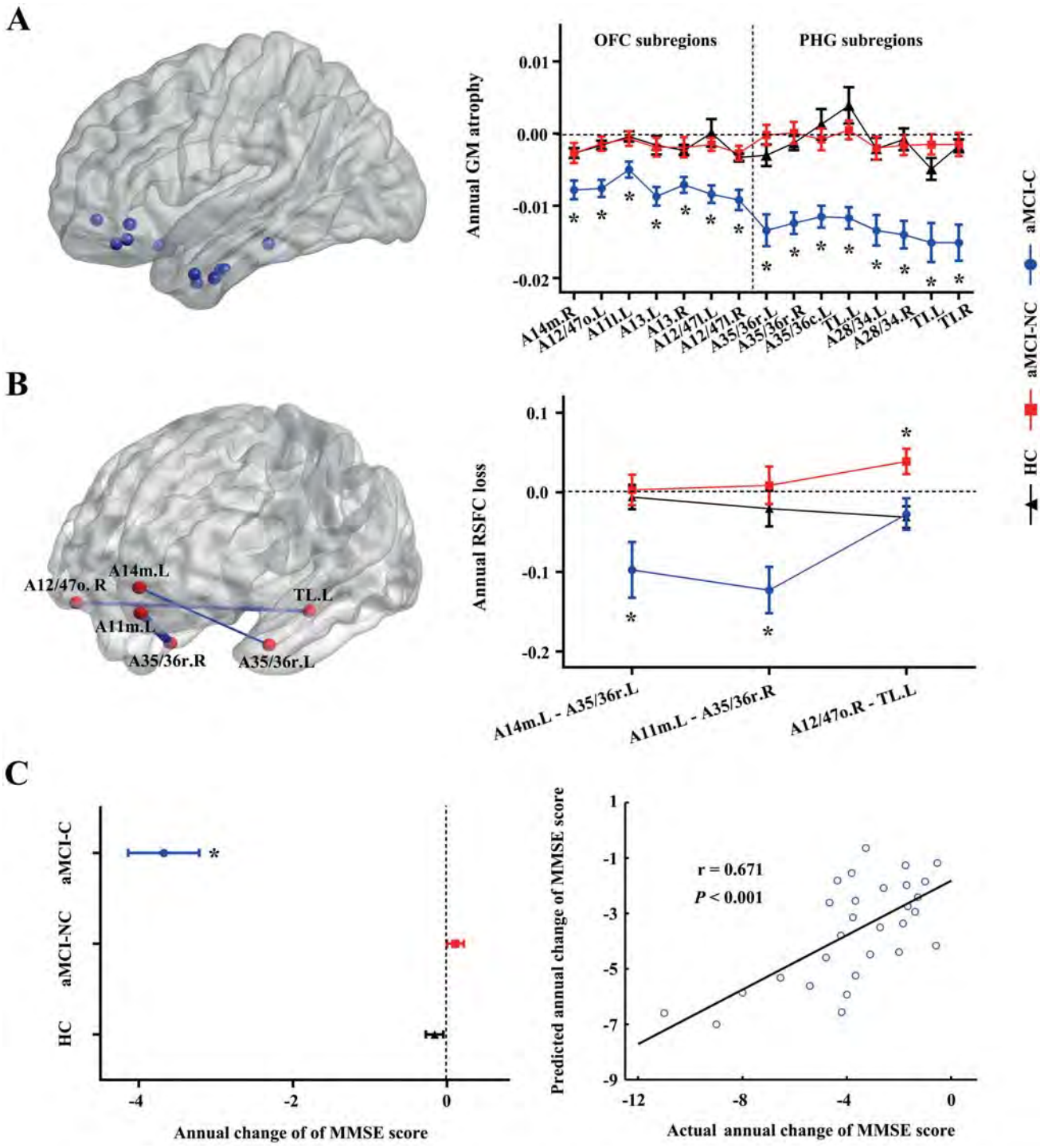

Fig. 6 Comparison of changes in annual GM volumes and RSFC in the aMCI-C, aMCI-NC, and HC groups. ANOVA analysis shows significant "group" effects on their AC estimates (FDR-corrected $P < 0.05$). **A**, **B** Significant annual GM atrophy in the OFC and PHG (**A**), and annual OFC-PHG connectivity loss (**B**) (A14m.L – A35/36r.L, A11m.L – A35/36r.R) of aMCI-C patients. **C** For aMCI-C-related ACs in GM volume and connectivity, the use of relevance vector regression permits prediction of ACs in MMSE scores with statistically significant accuracy ($r = 0.671$, $P < 0.001$). Data are presented as the mean ± SEM. aMCI, amnestic mild cognitive impairment; aMCI-C, aMCI-converters; aMCI-NC, aMCI-non-converters; OFC, orbitofrontal cortex; PHG, parahippocampal gyrus; GM, grey matter; MMSE, mini-mental state examination; RSFC, resting-state functional connectivity; ANOVA, analyses of variance; RVR, relevance vector regression; AC, annual change. For abbreviations of the OFC and PHG sub-regions, see Table S1.

Discussion

In the present study, we revealed visuospatial memory deficits early in 6-month-old 5XFAD mice with selectively impaired integrity of the glutamatergic POR–vlOFC pathway. Furthermore, opto-stimulating terminals in that specific neural circuit significantly improved the impaired visuospatial memory in 5XFAD mice. In addition, the progressively damaged PHG-OFC circuit measured by MRI distinguished aMCI-C from aMCI-NC patients and HCs, and AC estimates further confirmed the capacity of prediction for the progression of aMCI and AD conversion. Taken together, disruption of the glutamatergic POR–vlOFC circuit indicated an anatomical basis of visuospatial memory deficits, and the aggravating impairment of the PHG–OFC pathway in the aMCI group predicted the disease progression and AD conversion.

In our previous study [44, 45], we demonstrated that 1-month-old 5XFAD mice show memory impairment as measured by the Morris water maze test. This test is widely used to evaluate cognitive functions, including visuospatial memory, episodic memory, and working memory [46, 47]. Here, we mainly focused on visuospatial memory as measured by NOPRT, thereby taking advantage of the natural preference of rodents for new over familiar objects. However, visuospatial memory deficits appear in 5XFAD mice at the age of 6 months, when neuronal loss starts to occur in multiple regions of the brain [48]. In this study, a combination of NOPRT, cell-type-specific retrograde tracing, *in vivo* LFP recording, and optogenetic manipulation were used to determine the possible underlying mechanism of the glutamatergic POR–vlOFC circuit in visuospatial memory impairment in 6-month-old 5XFAD mice.

To our knowledge, this is the first example of disruption of the glutamatergic POR–vlOFC circuit in 5XFAD mice, which was directly related to deficient visuospatial memory retrieval. In both humans and rats, the OFC makes tight connections with the visual cortex [49] and temporal lobe structures [50–52], while the vlOFC is an efferent target of the POR in rats [53]. In a previous study, we have demonstrated that in wild-type mice, the vlOFC is one of the efferent targets of glutamatergic neurons in the POR [39], suggesting an anatomical foundation for the POR–vlOFC circuit in visuospatial memory. In addition, neurons in the POR of rats have been shown to encode representations that link locations and objects through *in vivo* recordings from postrhinal neurons and LFPs during visual discrimination tasks [54]. Neurons in the OFC are not only responsive to specific visual stimuli [55], but are also required for cognitive maps and task space in both humans [56] and rodents [57]. The data indicate that both the POR and OFC respond to visual stimuli and encode spatial information. Rats with injuries to the POR [17] and vlOFC [58] show impaired orientation to visual stimuli, while inhibition of the glutamatergic POR–vlOFC pathway reduces the retrieval deficit of visuospatial memory [39], indicating that lesions of the POR–vlOFC circuit result in visuospatial memory deficits. Using *in vivo* LFP recording, we found abnormal beta oscillation in the POR–vlOFC circuit in 5XFAD mice during NOPRT. These findings suggest that malfunction of the above circuit may contribute to visuospatial memory impairment in 5XFAD mice. Previous studies have shown that beta oscillations occur during learning, cognition, and cortical reorganization [59, 60]. A study by Quinn *et al*. showed that beta oscillations in the basal forebrain of rats are learning-dependent [59]. During an associative learning task, it has been reported that peak amplitudes are significantly greater around the novel object [59]. In a spatial exploration and memory-guided behavior task, beta oscillations in the hippocampus increase during memory retrieval [61]. In this study, 5XFAD mice showed decreased beta oscillation in the vlOFC during exploration of the displaced object, indicating that reduced beta oscillations contribute to visuospatial memory deficits. Moreover, increased FC between the POR and vlOFC regions in 5XFAD mice may compensate for visuospatial memory deficits. Taken together, in this study we demonstrated that anatomical and functional disruptions in the POR–vlOFC circuit in 5XFAD mice are associated with visuospatial memory retrieval deficits, which are significantly improved upon optogenetic activation.

Neuroimaging studies have shown that the PHG is a region with greater cortical thickness in individuals with normal cognition and is vulnerable to atrophy in AD, independent of amyloid load and the apolipoprotein E genotype [62]. In addition, reduced GM and FC of the PHG has been reported in aMCI [25, 63–65] and AD patients [26, 64, 66, 67]. Hypoperfusion of the PHG [68] and OFC [69] in AD patients is correlated with the MMSE scores, which indicates that they may be vulnerable hubs to maintain general cognition in AD patients, particularly for memory. In the current study, we focused on the PHG–OFC circuit in aMCI patients. In the AD spectrum, both decreased PHG–OFC activity and the ACs of PHG–OFC connectivity were only found in aMCI-C patients during follow-up, whereas an increased capacity of the neural circuit was found in aMCI-NC patients, suggesting that hyperactivation of the PHG–OFC circuit in aMCI-NC patients plays a role in memory preservation. Importantly, no significant differences were found in clinical cognitive performance between the two aMCI groups, which further indicated that the damaged neural circuit may be an early biomarker for the prediction of AD conversion. In addition, Mitolo and colleagues showed that MCI-C patients have

significantly reduced GM in the PHG compared to MCI-NC patients [70]. Mattsson and coworkers demonstrated that ^{18}F-AV-1451 in the PHG has 93% diagnostic accuracy for AD (prodromal or dementia) [71]. Initial metabolic impairment of AD converters has been shown in the OFC during the early stages of AD [72]. In this study, we demonstrated that anatomical and functional impairment of the PHG–OFC circuit had an accuracy of 77.33% to distinguish aMCI-C from aMCI-NC patients at baseline, and that aMCI-C-related ACs in GM volume and connectivity accurately predicted the ACs in MMSE scores. Taken together, our findings consistently showed that the impaired PHG–OFC circuit could serve as a potential biomarker for AD conversion.

This study had several limitations that should be addressed. The classical pathological biomarkers for AD and amyloid imaging should be applied for precise aMCI diagnosis. A task-functional MRI should be designed to track visuospatial memory-related changes in neural activity, and its complex underlying circuits should be elucidated through c-Fos mapping in the whole brain of mice [73]. Different subtypes of neurons in the POR–vlOFC circuit resulting in visuospatial memory impairment in 5XFAD mice should be clarified. Furthermore, the specific molecular regulatory mechanisms of the POR–vlOFC circuit require elucidation for application with PET in the clinic.

In conclusion, our findings indicated that impairment of the glutamatergic POR–vlOFC circuit contributes to visuospatial memory deficits in AD mice, which were significantly rescued by opto-stimulation of this specific neural circuit. Together, these findings suggested a potential target for intervention. The impaired PHG–OFC circuit as measured by MRI in aMCI patients is highlighted as a promising predictor of AD conversion.

Acknowledgements We thank all participants in the study, without whom this research would not have been possible. This work was supported by the National Natural Science Foundation of China (81420108012, 81671046, 91832000, and 31700936), the Program of Excellent Talents in Medical Science of Jiangsu Province, China (JCRCA2016006), a Special Project of Clinical Medicine Science and Technology in Jiangsu Province, China (BL2014077), a Guangdong Province Grant (2017A030310496), Key-Area Research and Development Program of Guangdong Province, China (2018B030331001), a National Special Support Grant (W02020453), and Guangdong Provincial Key Laboratory of Brain Connectome and Behavior (2017B030301017).

Compliance with Ethical Standards

Conflict of interest The authors declare that they have no conflict of interest.

References

1. Maharjan DM, Dai YY, Glantz EH, Jadhav SP. Disruption of dorsal hippocampal - prefrontal interactions using chemogenetic inactivation impairs spatial learning. Neurobiol Learn Mem 2018, 155: 351–360.
2. Viena TD, Linley SB, Vertes RP. Inactivation of nucleus reuniens impairs spatial working memory and behavioral flexibility in the rat. Hippocampus 2018, 28: 297–311.
3. Rajah MN, Wallace LMK, Ankudowich E, Yu EH, Swierkot A, Patel R, *et al.* Family history and APOE4 risk for Alzheimer's disease impact the neural correlates of episodic memory by early midlife. Neuroimage Clin 2017, 14: 760–774.
4. Ruggiero G, Iavarone A, Iachini T. Allocentric to egocentric spatial switching: Impairment in aMCI and Alzheimer's disease Patients? Curr Alzheimer Res 2018, 15: 229–236.
5. Good MA, Hale G. The "Swedish" mutation of the amyloid precursor protein (APPswe) dissociates components of object-location memory in aged Tg2576 mice. Behav Neurosci 2007, 121: 1180–1191.
6. Bianchini F, Di Vita A, Palermo L, Piccardi L, Blundo C, Guariglia C. A selective egocentric topographical working memory deficit in the early stages of Alzheimer's disease: a preliminary study. Am J Alzheimers Dis Other Demen 2014, 29: 749–754.
7. Allegri RF, Pertierra L, Cohen G, Chrem Mendez P, Russo MJ, Calandri I, *et al.* A biological classification for Alzheimer's disease - Amyloid, Tau and Neurodegeneration (A/T/N): results from the Argentine-Alzheimer's Disease Neuroimaging Initiative. Int Psychogeriatr 2019: 1–2.
8. Botha H, Mantyh WG, Murray ME, Knopman DS, Przybelski SA, Wiste HJ, *et al.* FDG-PET in tau-negative amnestic dementia resembles that of autopsy-proven hippocampal sclerosis. Brain 2018, 141: 1201–1217.
9. Jack CR, Jr., Bennett DA, Blennow K, Carrillo MC, Feldman HH, Frisoni GB, *et al.* A/T/N: An unbiased descriptive classification scheme for Alzheimer disease biomarkers. Neurology 2016, 87: 539–547.
10. Sills JB, Connors BW, Burwell RD. Electrophysiological and morphological properties of neurons in layer 5 of the rat postrhinal cortex. Hippocampus 2012, 22: 1912–1922.
11. Mishkin M, Ungerleider LG. Contribution of striate inputs to the visuospatial functions of parieto-preoccipital cortex in monkeys. Behav Brain Res 1982, 6: 57–77.
12. Ungerleider LG, Courtney SM, Haxby JV. A neural system for human visual working memory. Proc Natl Acad Sci U S A 1998, 95: 883–890.
13. Ungerleider LG, Haxby JV. 'What' and 'where' in the human brain. Curr Opin Neurobiol 1994, 4: 157–165.
14. Kravitz DJ, Saleem KS, Baker CI, Mishkin M. A new neural framework for visuospatial processing. Nat Rev Neurosci 2011, 12: 217–230.
15. Nyffeler T, Gutbrod K, Pflugshaupt T, von Wartburg R, Hess CW, Muri RM. Allocentric and egocentric spatial impairments in a case of topographical disorientation. Cortex 2005, 41: 133–143.
16. Ishii K, Koide R, Mamada N, Tamaoka A. Topographical disorientation in a patient with right parahippocampal infarction. Neurol Sci 2017, 38: 1329–1332.
17. Ramos JM. Differential contribution of hippocampus, perirhinal cortex and postrhinal cortex to allocentric spatial memory in the radial maze. Behav Brain Res 2013, 247: 59–64.
18. Qi X, Du ZJ, Zhu L, Liu X, Xu H, Zhou Z, *et al.* The glutamatergic postrhinal cortex-ventrolateral orbitofrontal cortex pathway regulates spatial memory retrieval. Neurosci Bull 2019, 35: 447–460.

19. Von Der Heide RJ, Skipper LM, Klobusicky E, Olson IR. Dissecting the uncinate fasciculus: disorders, controversies and a hypothesis. Brain 2013, 136: 1692–1707.
20. Farovik A, Place RJ, McKenzie S, Porter B. Orbitofrontal cortex encodes memories within value-based schemas and represents contexts that guide memory retrieval. J Neurosci 2015, 35: 8333–8344.
21. Chrastil ER, Sherrill KR, Hasselmo ME, Stern CE. Which way and how far? Tracking of translation and rotation information for human path integration. Hum Brain Mapp 2016, 37: 3636–3655.
22. Diehl B, Busch RM, Duncan JS, Piao Z, Tkach J, Lüders HO. Abnormalities in diffusion tensor imaging of the uncinate fasciculus relate to educed memory in temporal lobe epilepsy. Epilepsia 2008, 49:1409–1418.
23. Li XR, Ren YD, Cao B, Huang XL. Analysis of white matter characteristics with tract-based spatial statistics according to diffusion tensor imaging in early Parkinson's disease. Neurosci Lett 2018, 675: 127–132.
24. Raber J, Olsen RHJ, Su W, Foster S, Xing R, Acevedo SF, *et al.* CD44 is required for spatial memory retention and sensorimotor functions. Behav Brain Res 2014, 275: 146–149.
25. Wang Z, Dai Z, Shu H, Liu D, Guo Q, He Y, *et al.* Cortical thickness and microstructural white matter changes detect amnestic mild cognitive impairment. J Alzheimers Dis 2017, 56: 415–428.
26. Juh R, Suh T, Kim S. SU-E-I-73: SU-E-I-73: Gray matter atrophy and white matter tract abnormalities by voxel wise correlation analysis in patients with Alzheimer's disease. Med Phys 2012, 39: 3641.
27. Morikawa M, Kiuchi K, Taoka T, Nagauchi K, Kichikawa K, Kishimoto T. Uncinate fasciculus-correlated cognition in Alzheimer's disease: a diffusion tensor imaging study by tractography. Psychogeriatrics 2010, 10: 15–20.
28. Hiyoshi-Taniguchi K, Oishi N, Namiki C, Miyata J, Murai T, Cichocki A, *et al.* The uncinate fasciculus as a predictor of conversion from amnestic mild cognitive impairment to Alzheimer disease. J Neuroimaging 2015, 25: 748–753.
29. Bussey TJ, Duck J, Muir JL, Aggleton JP. Distinct patterns of behavioural impairments resulting from fornix transection or neurotoxic lesions of the perirhinal and postrhinal cortices in the rat. Behav Brain Res 2000, 111: 187–202.
30. Fujie S, Namiki C, Nishi H, Yamada M, Miyata J, Sakata D, *et al.* The role of the uncinate fasciculus in memory and emotional recognition in amnestic mild cognitive impairment. Dement Geriatr Cogn Disord 2008, 26: 432–439.
31. Metzler-Baddeley C, Hunt S, Jones DK, Leemans A, Aggleton JP, O'Sullivan MJ. Temporal association tracts and the breakdown of episodic memory in mild cognitive impairment. Neurology 2012, 79: 2233–2240.
32. Krogsrud SK, Fjell AM, Tamnes CK, Grydeland H, Due-Tonnessen P, Bjornerud A, *et al.* Development of white matter microstructure in relation to verbal and visuospatial working memory-A longitudinal study. PLoS One 2018, 13: e0195540.
33. Rombouts SA, Barkhof F, Witter MP, Machielsen WC, Scheltens P. Anterior medial temporal lobe activation during attempted retrieval of encoded visuospatial scenes: an event-related fMRI study. Neuroimage 2001, 14: 67–76.
34. Rosenbaum RS, Ziegler M, Winocur G, Grady CL, Moscovitch M. "I have often walked down this street before": fMRI studies on the hippocampus and other structures during mental navigation of an old environment. Hippocampus 2004, 14: 826–835.
35. Hohenfeld C, Nellessen N, Dogan I, Kuhn H, Muller C, Papa F, *et al.* Cognitive improvement and brain changes after real-time functional MRI neurofeedback training in healthy elderly and prodromal Alzheimer's disease. Front Neurol 2017, 8: 384.
36. Yetkin FZ, Rosenberg RN, Weiner MF, Purdy PD, Cullum CM. FMRI of working memory in patients with mild cognitive impairment and probable Alzheimer's disease. Eur Radiol 2006, 16: 193–206.
37. Jacobs HI, Gronenschild EH, Evers EA, Ramakers IH, Hofman PA, Backes WH, *et al.* Visuospatial processing in early Alzheimer's disease: a multimodal neuroimaging study. Cortex 2015, 64: 394–406.
38. Naber PA, Witter MP, Lopes da Silva FH. Differential distribution of barrel or visual cortex. Evoked responses along the rostrocaudal axis of the peri- and postrhinal cortices. Brain Res 2000, 877: 298–305.
39. Bucci DJ, Burwell RD. Deficits in attentional orienting following damage to the perirhinal or postrhinal cortices. Behav Neurosci 2004, 118: 1117–1122.
40. Lu Y, Zhu ZG, Ma QQ, Su YT, Han Y, Wang X, *et al.* A critical time-window for the selective induction of hippocampal memory consolidation by a brief episode of slow-wave sleep. Neurosci Bull 2018, 34: 1091–1099.
41. Duan J, Fu H, Zhang J. Activation of parvalbumin-positive neurons in both retina and primary visual cortex improves the feature-selectivity of primary visual cortex neurons. Neurosci Bull 2017, 33: 255–263.
42. Fan L, Li H, Zhuo J, Zhang Y, Wang J, Chen L, *et al.* The human brainnetome atlas: a new brain atlas based on connectional architecture. Cereb Cortex 2016, 26: 3508–3526.
43. Huang S, Cai N, Pacheco PP, Narrandes S, Wang Y, Xu W. Applications of Support Vector Machine (SVM) learning in cancer genomics. Cancer Genomics Proteomics 2018, 15: 41–51.
44. Tang X, Wu D, Yao Y, Gu L, Chen X, Ren Q, *et al.* Dorsal hippocampal changes in T2 relaxation times are associated with early spatial cognitive deficits in 5XFAD mice. Brain Res Bull 2019, 153: 150–161.
45. Wu D, Tang X, Gu LH. LINGO-1 antibody ameliorates myelin impairment and spatial memory deficits in the early stage of 5XFAD mice. CNS Neurosci Ther 2018, 24: 381–393.
46. Beracochea D, Krazem A, Henkouss N, Haccard G, Roller M, Fromentin E. Intake of wild blueberry powder improves episodic-like and working memory during normal aging in mice. Planta Med 2016, 82: 1163–1168.
47. Zhang M, Moon C, Chan GC, Yang L, Zheng F, Conti AC, *et al.* Ca-stimulated type 8 adenylyl cyclase is required for rapid acquisition of novel spatial information and for working/episodic-like memory. J Neurosci 2008, 28: 4736–4744.
48. Spangenberg EE, Lee RJ, Najafi AR, Rice RA, Elmore MR, Blurton-Jones M, *et al.* Eliminating microglia in Alzheimer's mice prevents neuronal loss without modulating amyloid-beta pathology. Brain 2016, 139: 1265–1281.
49. Rabbitt LR, Roberts DM, McDonald CG, Peterson MS. Neural activity reveals perceptual grouping in working memory. Int J Psychophysiol 2017, 113: 40–45.
50. Sharma A, Kesari KK, Saxena VK, Sisodia R. Ten gigahertz microwave radiation impairs spatial memory, enzymes activity, and histopathology of developing mice brain. Molecular and cellular biochemistry 2017, 435: 1–13.
51. Storbeck J, Watson P. Verbal makes it positive, spatial makes it negative: working memory biases judgments, attention, and moods. Emotion 2014, 14: 1072–1086.
52. Ring M, Gaigg SB, Altgassen M, Barr P, Bowler DM. Allocentric versus egocentric spatial memory in adults with autism spectrum disorder. J Autism Dev Disord 2018, 48: 2101–2111.
53. Hwang E, Willis BS, Burwell RD. Prefrontal connections of the perirhinal and postrhinal cortices in the rat. Behav Brain Res 2018, 354: 8–21.

54. Furtak SC, Ahmed OJ, Burwell RD. Single neuron activity and theta modulation in postrhinal cortex during visual object discrimination. Neuron 2012, 76: 976–988.
55. Funahashi S. The Contribution of the Orbitofrontal Cortex to the Preference for Visual Stimuli. Brain Nerve 2015, 67: 711–722.
56. Schuck NW, Cai MB, Wilson RC, Niv Y. Human orbitofrontal cortex represents a cognitive map of state space. Neuron 2016, 91: 1402–1412.
57. Maille A, Schradin C. Survival is linked with reaction time and spatial memory in African striped mice. Biol Lett 2016, 12: 20160346.
58. Farahmandfar M, Kadivar M, Naghdi N, Choopani S, Zarrindast M-R. Influence of pre-exposure to morphine on cannabinoid-induced impairment of spatial memory in male rats. Behav Brain Res 2013, 256: 157–164.
59. Quinn LK, Nitz DA, Chiba AA. Learning-dependent dynamics of beta-frequency oscillations in the basal forebrain of rats. Eur J Neurosci 2010, 32: 1507–1515.
60. Zanos S, Rembado I, Chen D, Fetz EE. Phase-locked stimulation during cortical beta oscillations produces bidirectional synaptic plasticity in awake monkeys. Curr Biol 2018, 28: 2515–2526.e2514.
61. Lopes-Dos-Santos V, van de Ven GM, Morley A, Trouche S, Campo-Urriza N, Dupret D. Parsing hippocampal theta oscillations by nested spectral components during spatial exploration and memory-guided behavior. Neuron 2018, 100: 940–952.e947.
62. Li C, Duara R, Loewenstein DA, Izquierdo W, Cabrerizo M, Barker W, *et al.* Greater regional cortical thickness is associated with selective vulnerability to atrophy in Alzheimer's disease, independent of amyloid load and APOE genotype. J Alzheimers Dis 2019, 69: 145–156.
63. Rami L, Sole-Padulles C, Fortea J, Bosch B, Llado A, Antonell A, *et al.* Applying the new research diagnostic criteria: MRI findings and neuropsychological correlations of prodromal AD. Int J Geriatr Psychiatry 2012, 27: 127–134.
64. Echavarri C, Aalten P, Uylings HB, Jacobs HI, Visser PJ, Gronenschild EH, *et al.* Atrophy in the parahippocampal gyrus as an early biomarker of Alzheimer's disease. Brain Struct Funct 2011, 215: 265–271.
65. Zhu L, Shu H, Liu D, Guo Q, Wang Z, Zhang Z. Apolipoprotein E epsilon4 Specifically Modulates the Hippocampus Functional Connectivity Network in Patients With Amnestic Mild Cognitive Impairment. Front Aging Neurosci 2018, 10: 289.
66. Hanyu H, Asano T, Kogure D, Sakurai H, Iwamoto T, Takasaki M. Relation between hippocampal damage and cerebral cortical function in Alzheimer's disease. Nihon Ronen Igakkai Zasshi. 2000, 37: 921–927.
67. Ferreira LK, Diniz BS, Forlenza OV, Busatto GF, Zanetti MV. Neurostructural predictors of Alzheimer's disease: a meta-analysis of VBM studies. Neurobiol Aging 2011, 32: 1733–1741.
68. Squarzoni P, Tamashiro-Duran J, Souza Duran FL, Santos LC, Vallada HP, Menezes PR, *et al.* Relationship between regional brain volumes and cognitive performance in the healthy aging: an MRI study using voxel-based morphometry. J Alzheimers Dis 2012, 31: 45–58.
69. Hreha K, Chaudhari A, Kong Y, Maduri P, Barrett AM. Illustrating where spatial perception versus memory-based representation: spatial neglect in a distinguished artist; a case report. Neurocase 2018, 24: 151–155.
70. Mitolo M, Stanzani-Maserati M, Capellari S, Testa C, Rucci P, Poda R, *et al.* Predicting conversion from mild cognitive impairment to Alzheimer's disease using brain (1)H-MRS and volumetric changes: A two- year retrospective follow-up study. Neuroimage Clin 2019, 23: 101843.
71. Mattsson N, Insel PS, Donohue M, Jogi J, Ossenkoppele R, Olsson T, *et al.* Predicting diagnosis and cognition with (18)F-AV-1451 tau PET and structural MRI in Alzheimer's disease. Alzheimers Dement 2019, 15: 570–580.
72. Salmon E, Lekeu F, Garraux G, Guillaume B, Magis D, Luxen A, *et al.* Metabolic correlates of clinical heterogeneity in questionable Alzheimer's disease. Neurobiol Aging 2008, 29: 1823–1829.
73. Wen P, Rao X, Xu L, Zhang Z, Jia F, He X, *et al.* Cortical organization of centrifugal afferents to the olfactory bulb: mono- and trans-synaptic tracing with recombinant neurotropic viral tracers. Neurosci Bull 2019, 35: 709–723.

Neurosci. Bull. August, 2020, 36(8):845–859
https://doi.org/10.1007/s12264-020-00489-4

www.neurosci.cn
www.springer.com/12264

ORIGINAL ARTICLE

Sirt1-ROS-TRAF6 Signaling-Induced Pyroptosis Contributes to Early Injury in Ischemic Mice

Weijie Yan[1] · Wei Sun[2] · Jiahui Fan[1] · Haiqing Wang[2] · Song Han[1] · Junfa Li[1] · Yanling Yin[1]

Received: 24 September 2019 / Accepted: 4 October 2019 / Published online: 6 April 2020

Abstract Stroke is an acute cerebro-vascular disease with high incidence and poor prognosis, most commonly ischemic in nature. In recent years, increasing attention has been paid to inflammatory reactions as symptoms of a stroke. However, the role of inflammation in stroke and its underlying mechanisms require exploration. In this study, we evaluated the inflammatory reactions induced by acute ischemia and found that pyroptosis occurred after acute ischemia both *in vivo* and *in vitro*, as determined by interleukin-1β, apoptosis-associated speck-like protein, and caspase-1. The early inflammation resulted in irreversible ischemic injury, indicating that it deserves thorough investigation. Meanwhile, acute ischemia decreased the Sirtuin 1 (Sirt1) protein levels, and increased the TRAF6 (TNF receptor associated factor 6) protein and reactive oxygen species (ROS) levels. In further exploration, both Sirt1 suppression and TRAF6 activation were found to contribute to this pyroptosis. Reduced Sirt1 levels were responsible for the production of ROS and increased TRAF6 protein levels after ischemic exposure. Moreover, N-acetyl-*L*-cysteine, an ROS scavenger, suppressed the TRAF6 accumulation induced by oxygen-glucose deprivation *via* suppression of ROS bursts. These phenomena indicate that Sirt1 is upstream of ROS, and ROS bursts result in increased TRAF6 levels. Further, the activation of Sirt1 during the period of ischemia reduced ischemia-induced injury after 72 h of reperfusion in mice with middle cerebral artery occlusion. In sum, these results indicate that pyroptosis-dependent machinery contributes to the neural injury during acute ischemia *via* the Sirt1-ROS-TRAF6 signaling pathway. We propose that inflammatory reactions occur soon after oxidative stress and are detrimental to neuronal survival; this provides a promising therapeutic target against ischemic injuries such as a stroke.

Keywords ROS · Stroke · Pyroptosis · TRAF6 · Sirt1

Introduction

Ischemic stroke is one of the main diseases with high mortality and disability worldwide [1]. The location and size of the cerebral ischemic region depend on the distribution of the occluded artery, after which metabolic and functional dysfunctions emerge [2]. Generally, two therapies are used to treat stroke: prompt blood restoration by thrombolysis and mechanical thrombectomy [3]. However, the effects of these treatments are modest [4]. Moreover, the loss of neuronal cells is the vital problem in stroke, making recovery difficult or even impossible at the late stage [5]. Therefore, novel neuro-protective strategies at the early stage with more positive effects deserve to be explored further.

Neuroinflammation is reported to be induced by cerebral ischemia; this is initiated by the accumulation of inflammatory cells and mediators in the ischemic region from

Weijie Yan and Wei Sun have contributed equally to this work.

Electronic supplementary material The online version of this article (https://doi.org/10.1007/s12264-020-00489-4) contains supplementary material, which is available to authorized users.

✉ Yanling Yin
yyling@ccmu.edu.cn

[1] Department of Neurobiology, Ministry of Education Key Laboratory for Neurodegenerative Disorders, Capital Medical University, Beijing 100069, China

[2] Department of Neurology, The Second Affiliated Hospital of Harbin Medical University, Harbin 150086, China

resident cerebral cells and infiltrating immune cells. Then, the following inflammatory injuries appear [6]. Recently, pyroptosis, a special kind of pro-inflammatory cell death, has been reported to occur in embryonic cortical neurons without interaction with glial cells under some specific conditions, such as poly-deoxyribonucleic acid (DNA) exposure [7]. The inflammatory reactions in neurons augment their susceptibility to injury, which aggravate neuronal damage and ultimately lead to death [8]. Protective therapies targeting neuro-inflammation have been considered as a promising area of research in recent years. Meanwhile, the key periods for treatment against inflammation are critical issues that require immediate investigation [9].

Members of the tumor necrosis factor (TNF) receptor associated factor (TRAF) subfamily serve as signaling adaptors in signaling events by coupling TNF receptor superfamily members [10]. To date, seven members of the TRAF family have been discovered, and are named TRAF1–7 in the order of their discovery. Among these members, TRAF6 has the least homology and the greatest difference in the C-terminal domain [11]. TRAF6 is distributed widely and abundantly in the central nervous system (CNS) and contributes to the inflammatory reactions in ischemic stroke [12]. Recently, the role of TRAF6 in the CNS has attracted increasing attention. It has been reported that down-regulation of TRAF6 is an effective target for improving the outcome of ischemic stroke in the cortex of rats [13].

Sirtuin1 (Sirt1) is a nicotinamide adenine dinucleotide-dependent deacetylase that is involved in many biological processes, including cellular metabolism, oxidative stress, gene transcription, and the cellular lifespan [14]. It has been reported that increased expression of Sirt1 in an Alzheimer's disease model contributes to neuronal survival [15]. Furthermore, the activation level of Sirt1 is associated with ischemia/reperfusion injury [16]. Also, increased Sirt1 expression plays a key role in the ischemic preconditioning-mediated protection against the subsequent ischemia/reperfusion injury in the mouse heart. Sirt1 is regarded as an anti-aging protein because its activation significantly delays the process of aging [17]. Further, since the Sirt1 protein level decreases in the brain of the elderly and a higher incidence of ischemic stroke is found in the elderly, there may be a possibility that Sirt1 is involved in the process of ischemic stroke [18]. However, due to the limitation of knowledge of signaling pathways involving Sirt1, its potential application is limited.

Oxidative stress and post-ischemic inflammatory responses are regarded as vital pathogenic mechanisms responsible for post-ischemic cerebral injury [19]. Oxygen and glucose levels change abruptly after ischemia, inducing subsequent inflammation, autophagy, oxidative stress, and apoptosis due to initial renal ischemia [20]. Emerging evidence indicates that there may be crosstalk between oxidative stress and inflammation in ischemic stroke [21]. However, the underlying scenario is obscure, requiring elucidation. In this current study, we found that the inflammatory reaction was pyroptotic, depending on up-regulated TRAF6, originating from the increased ROS burst after Sirt1 suppression. Sirt1-ROS-TRAF6 is responsible for the progress from oxidative stress to inflammation, which indicates that oxidative stress may be the onset of ischemic injury.

Methods

Animal Models

Experiments were performed at room temperature (RT, 18°C–22°C) on adult male C57BL/6J mice (Jackson Laboratory, Bar Harbor, ME) (weighing 18 g–22 g). All experimental procedures were approved by the Animal Research Committees of Capital Medical University and were carried out in accordance with the in-house guidelines for the care and use of laboratory animals of Capital Medical University. The middle cerebral artery occlusion (MCAO) surgery was carried out as previously reported [22].

N2a Cell Cultures and Treatments

Before experiments, N2a cells were differentiated with serum-deprivation for 12 h as reported previously [23]. Differentiated mouse neuroblastoma N2a cells were cultured in high-glucose DMEM (Dulbecco's modified Eagle's medium) supplemented with 10% (*v*/*v*) fetal bovine serum and 2 mmol/L *L*-glutamine at 37°C in a humidified incubator with 5% (*v*/*v*) CO_2. Cells were re-plated at low density (20,000 cells/cm^2), and cultured for 1 day prior to the experiment.

Primary Hippocampal Neuron Culture

Hippocampal neurons were cultured as described previously [24]. Pregnant Wistar rats were anesthetized and the brains of E18–19 embryos obtained by Cesarean section. The hippocampi were removed and incubated with 0.25% trypsin–EDTA for 15 min at 37°C and mechanically dissociated. The resulting single-cell suspension was diluted to a density of 2×10^5 cells/mL in high-glucose DMEM with 10% fetal bovine serum, 10% equine serum, and 2 mmol/L *L*-glutamine, then plated in 35-mm cell plates coated with poly-*L*-lysine (Sigma). Cells were kept at 37°C in a humidified incubator with 5% CO_2. After 4 h,

the medium was replaced by serum-free Neurobasal medium with B27 supplement and 0.5 mmol/L *L*-glutamine. Every 3 days half of the medium was replaced and the cells were used for experiments 10–14 days after plating.

Oxygen-Glucose Deprivation/Re-oxygenation (OGD/R) of N2a Cells

The OGD/R cellular model was used to simulate ischemia/reperfusion injury *in vitro*. N2a cells were exposed to OGD (glucose-free DMEM, 5% CO_2, 2% O_2 and 93% N_2 for 1 h)/R (high glucose DMEM supplemented with 10% (*v*/*v*) fetal bovine serum, 2 mmol/L *L*-glutamine, and 5% CO_2, 21% O_2, and 74% N_2 for 1 h or 24 h).

Thiazolyl Blue Tetrazolium Bromide (MTT) Assay

Ten microliters of MTT [3-(4,5-dimethyl-2-thiazolyl)-2,5-diphenyl-2-H-tetrazolium bromide, 5 mg/mL stock in phosphate-buffered saline (PBS)] was added into each well of a 96-well plate, and incubated at 37°C for 4 h. Dimethyl sulfoxide (100 μL) was used to solubilize the insoluble blue formazan, and OD values of the mixture were measured with a Bio-Rad microplate reader at 550 nm and 650 nm. All MTT assays involved no less than four separate samples, which were measured in triplicate. The viability of vehicle-treated control cells without OGD exposure was taken as 100% with values for the other groups expressed as a percentage of control.

Measurement of Reactive Oxygen Species (ROS) Production

After treatments and washing with HBSS (Hanks balanced salt solution, Gibco), ROS production was addressed by staining with 2′,7′-dichlorofluorescin diacetate (DCFDA; 5 μmol/L, Sigma) in HBSS for 30 min. The N2a cells were then washed and ROS production of DCFDA-preloaded cells was assessed under a fluorescence microscope (Leica, Germany). NAC (2 mmol/L, Sigma) was used as a scavenger of cytoplasmic ROS. Mito-Tempo (5 μmol/L, Sigma) was used as a scavenger of mitochondrial ROS.

Real-Time qPCR Assessment of Gene Expression

To evaluate the mRNA level of TRAF6, mRNA was isolated with TRIzol reagent from the different groups of N2a cells. The primer pairs for TRAF6 were 5′-CCACCCCTGGAAAGCAAGTA-3′ (forward) and 5′-ATGCAGGCTTTGCAGAACCT-3′(reverse) [25], and for GAPDH were 5’-CCTTCATTGACCTCAACTAC-3’ (forward) and 5’-GGAAGGCCATGCCAGTGAGC-3’ (reverse) [26].

Enzyme-Linked Immunosorbent Assay (ELISA)

The cerebral cortex in the penumbra was put into 1.0 mL PBS, pH 7.4, and immediately frozen on dry ice. Then, the tissue was stored at −80°C until use. To obtain the supernatant, the cortex was thawed on ice and centrifuged at 3,000 rpm for 20 min at 4°C. After that, the supernatant was placed in a new tube for use.

The IL-1β protein level in the supernatant was assessed using an IL-1β kit (R&D Systems, Inc., USA) according to the manufacturer’s protocols. The results were assessed by comparing the samples to the standard curve provided with the kit.

Immunofluorescence Staining

After OGD exposure, N2a cells were treated with anti-caspase-1 (Abcam Technology, Cambridge, MA). After washing, the cells were incubated with Alexa Fluor 594-conjugated goat anti-rabbit IgG (Molecular Probes, Eugene, OR) for 2 h at RT. Then the samples were counter-stained with DAPI (Sigma). Images were captured with a fluorescence microscope imaging system (Leica, Germany).

Evaluation of Superoxide Dismutase 2 (SOD_2) Enzyme Activity

SOD_2 enzymatic activity was measured using a SOD assay kit with WST-8 method (Beyotime Co., S0103) following the manufacturer’s instructions. To separate the activity of SOD_2, the inhibitors A and B were added to block the activity of SOD_1. The absorption at 450 nm was measured using a microplate reader.

Knock-Down of TRAF6 by Small-Interfering (si)RNA Transfection

N2a cells cultured in 6-well plates were transfected with 180 pmol of TRAF6-specific siRNAs (Santa Cruz Biotechnology, Inc., Santa Cruz, CA) using Lipofectamine™ 3000 transfection reagent (Invitrogen; Thermo Fisher Scientific, Inc.) according to the manufacturer’s instructions. The medium was replaced with growth culture medium 5 h after transfection. After the cells had been transfected for 72 h, they were harvested for OGD exposure and subsequent experiments.

Recombinant Lentiviral Vector

Lentiviruses containing sequences encoding rat TRAF6 (lenti-TRAF6, Weijin Biotechnologies Corp., Inc.) was constructed for *in vitro* studies of hippocampal neurons. The cultured neurons were infected for 72 h with lentiviruses at a multiplicity of infection of 50.

Sample Preparation and Western Blot Analysis

As reported previously [27], frozen samples were rapidly thawed and homogenized at 4°C in Buffer C [50 mmol/L Tris-Cl, pH 7.5, containing 2 mmol/L EDTA, 1 mmol/L EGTA, 100 mmol/L iodoacetamide (an SH-group blocker), 5 mg/mL each of leupeptin, aprotinin, pepstatin A, and chymostatin, 50 mmol/L potassium fluoride, 50 nmol/L okadaic acid, and 5 mmol/L sodium pyrophosphate]. The protein concentration was determined using a BCA kit (Pierce Co., Rockford, IL). Proteins (25 μg) from each sample were loaded for sodium dodecyl sulfate (SDS) polyacrylamide gel electrophoresis [10% (*w*/*v*) SDS gel]. Proteins were then electrophoresed and transferred onto poly-vinylidene difluoride membranes (GE Healthcare, UK) at 4°C. After several rinses with TTBS (20 mmol/L Tris-Cl, pH 7.5, 0.15 mol/L NaCl, and 0.05% Tween-20), the transferred membrane was blocked with 10% non-fat milk in TTBS for 1 h and then incubated with anti-TRAF6 (Abcam Technology, Cambridge, MA), anti-ASC (CST), anti-caspase-1 (Abcam), anti-interleukin 1β (Abcam), and anti-SQSTM1/p62 (Abcam) antibodies and the corresponding secondary antibodies (Stressgen Biotechnologies Corp., Victoria, BC, Canada) for 1 h. After incubation with the primary and secondary antibodies, an enhanced chemiluminescence kit (GE Healthcare, UK) was used to detect signals. To verify equal loading of protein, the blots were re-probed with primary monoclonal antibody against β-actin (Sigma), and GAPDH (CST). Quantitative analysis for immunoblotting was performed after scanning the X-ray film with Quantitative-One software (Gel Doc 2000 imaging system, Bio-Rad Co., CA).

Antibody Array Analysis

One hundred milligrams of cerebral cortex was thawed on ice with 1 mL RIPA (CST, 9806S) containing protease inhibitor and phosphatase inhibitor. Then, the lysate was centrifuged at 12,000 rpm for 10 min at 4°C and the supernatant was placed in a new tube. A BCA protein assay kit (Thermo Scientific) was used to quantify the total protein. Samples were obtained by diluting protein lysate $>$ 10-fold to 0.5 mg/mL with blocking buffer. The total volume was 1 mL for each of the protein samples for antibody array analysis.

Independent replicate antibody array assays were used and the RayBio AAM-INF-1 analysis tool software, provided with the array, was used to assess the signal intensities of identified proteins. Aligned data were normalized with background subtraction from the positive control densities. The positive control of the first sample was regarded as 100% and the signal intensities of other samples were calculated according to the formula: normalized intensity of signal spot = (signal intensity of spot) × (positive signal intensity on reference array/positive signal intensity on sample array) [28].

Statistical Analysis

Data are presented as the mean ± SD. Statistical analysis was conducted by one-way analysis of variance followed by all pair-wise multiple comparison procedures using the Bonferroni test (Sigmastat 10.0). A value of $P < 0.05$ was considered statistically significant.

Results

Ischemia Induces Pyroptosis in Cortical Regions of MCAO Mice

Pyroptosis is characterized as an inflammatory, caspase-1-dependent, and programmed form of cell death. It has been overwhelmingly accepted that pyroptosis is induced by the inflammasome, a multi-protein complex containing apoptosis-associated speck-like protein with a caspase recruitment domain (ASC), an adaptor protein, and caspase-1, an inflammatory cysteine-aspartic protease [7, 29]. To address whether pyroptosis occurs in cortical regions after acute ischemia (Fig. 1A, B), we assessed the levels of IL-1β, ASC, and cleaved caspase-1 in the ischemic rat cortex after MCAO using western blot assays (Fig. 1C–E). The data were collected from four groups: sham, MCAO 1 h, MCAO 1 h/reperfusion 1 h, and MCAO 1 h/reperfusion 24 h. After a 1-h ischemic insult, the mature IL-1β, ASC, and cleaved caspase-1 were all increased and remained at a higher level during the subsequent reperfusion compared with the sham group. Moreover, ASC oligomerization was detected by western blot analysis using a monoclonal antibody against ASC. Of note, ischemia or ischemia/reperfusion resulted in the production of multimers of ASC (Fig. S1). Further, the translocation of caspase-1 to the nuclei of neurons was observed with MAP2, caspase-1, and DAPI staining (Fig. S2) in the peri-ischemic region of MCAO mice, indicating that caspase-1 is activated in some neurons after 1 h of ischemia.

Antibody array analysis in the cerebral cortex of mice from the sham, naïve ischemia (1 h), or ischemia (1 h)/

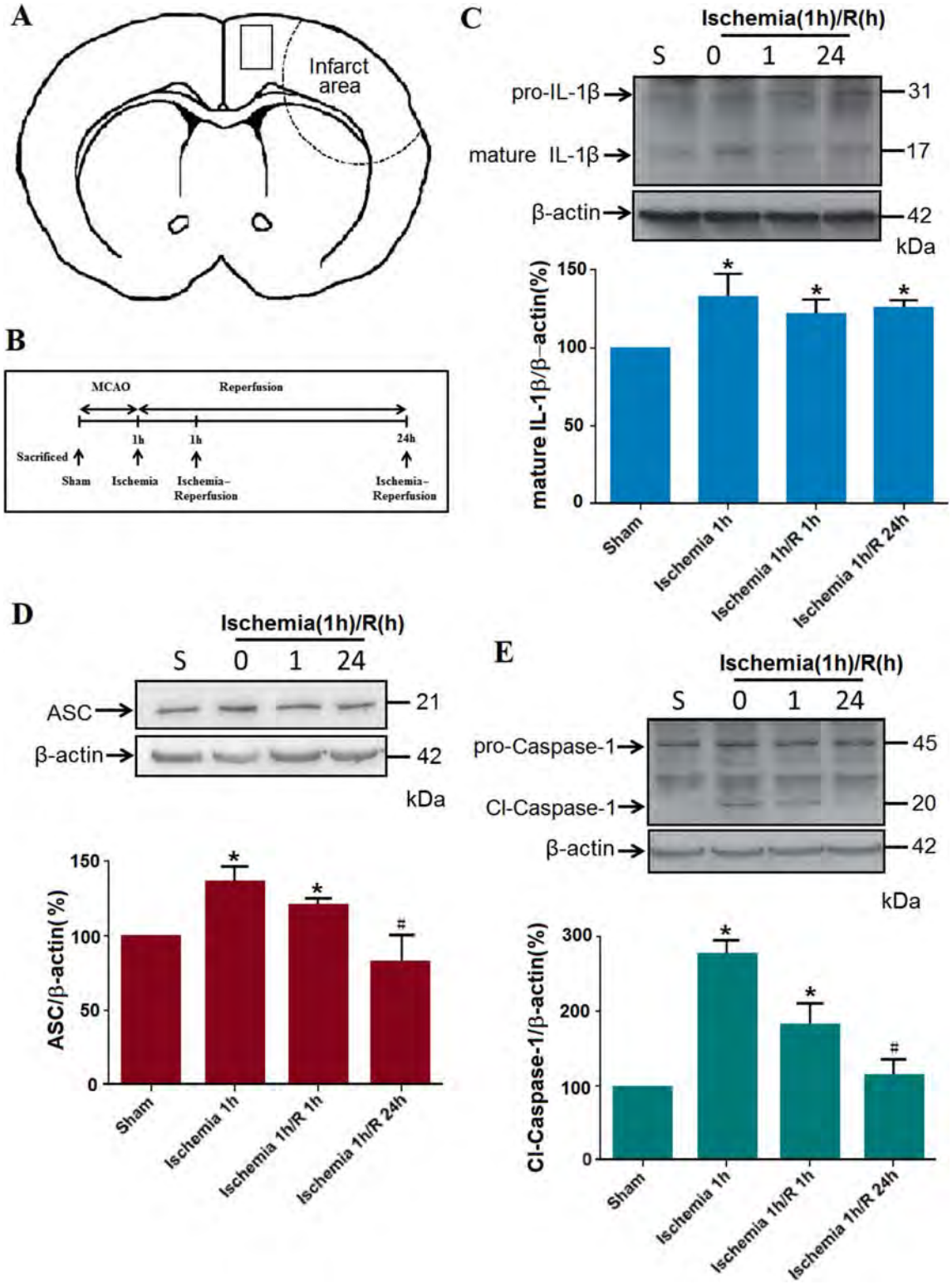

Fig. 1 MCAO-induced cerebral ischemia results in the pyroptosis of neural cells. **A** Schematic of the brain showing the areas of selected samples for the following experiments. **B** Illustration of the experimental protocol. **C** Representative blots and statistical results for mature IL-1β levels with western blot assay (β-actin was used as the loading control; $*P < 0.05$; $n = 5$/group). **D** Representative blots and statistical results for ASC protein levels ($*P < 0.05$; $n = 5$/group). **E** Representative blots and statistical results for cleaved-caspase-1 protein levels ($*P < 0.05$, $n = 5$/group).

reperfusion (1 h) groups was performed using the RayBio® Label–based array containing duplicate spots of 40 proteins. We emphasized 11 cytokines (Fig. 2A). Among the 10 identified cytokines, the expression of IL-1α, IL-1β, and TNF-α increased significantly after the ischemic insult and subsequent reperfusion ($P < 0.05$ *vs* control, $n = 3$/group; Fig. 2B). These results indicated that there was an inflammatory reaction in the ischemic stage. These results suggest an interesting phenomenon: the early inflammatory responses of neural cells are mainly in the pyroptotic mode, which may be the gateway to the subsequent injury.

TRAF6 Protein Levels Increase Due to Decreased Sirt1 Protein Levels in the Cortex of Naïve Ischemic Mice

TRAF6 is the only member of the TRAF subfamily to participate in Toll-like receptor signaling to the nuclear factor of kappa light polypeptide gene enhancer (NF-κB), which plays a vital role in inflammatory reactions [30, 31]. To explore whether TRAF6 is involved in this ischemia-induced inflammatory reaction, TRAF6 protein levels were assessed with western blot assays (Fig. 3A). We found that naïve ischemic or ischemia 1 h/R 1 h significantly increased the TRAF6 protein levels (Fig. 3A). Further, to determine whether the increased level of TRAF6 resulted from increased synthesis, qPCR was used to confirm the mRNA level of *traf6* (Fig. 3B). The *traf6* mRNA levels in the ischemia and ischemia 1 h/R 1 h groups were significantly higher than that in the sham group. Also, the Sirt1 protein levels were decreased by ischemic insults. And when the agonist of Sirt1, SRT1720, was injected intracerebroventricularly before surgery, no increase in TRAF6 protein levels was induced by cerebral ischemia, indicating that the Sirt1 activation may result in the activation of TRAF6 (Fig. 3C). Further, when TRAF6-specific siRNAs or SRT1720 were injected intracerebroventricularly before surgery, the increased IL-1β in the supernatant induced by ischemic insults was suppressed (Fig. 3D).

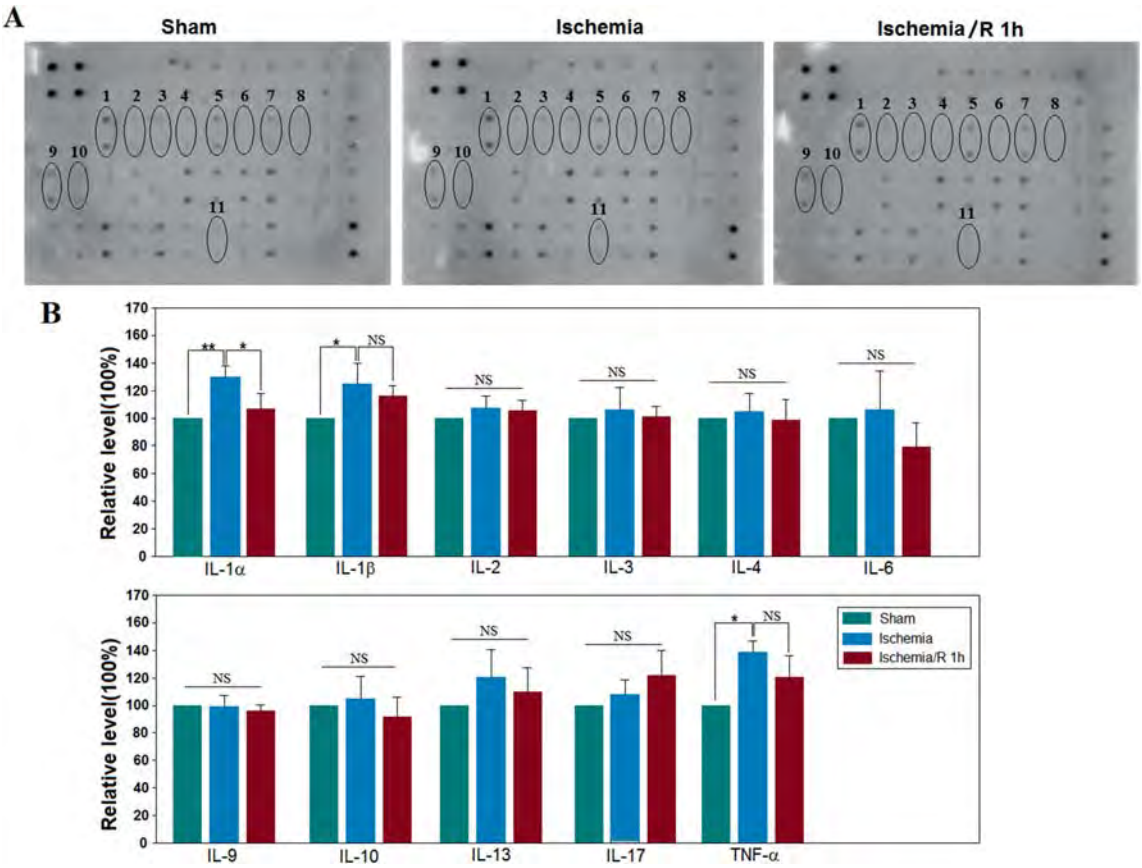

Fig. 2 MCAO-induced cerebral ischemia (1 h) increases the levels of IL-1α, IL-1β, and TNF-α, while the subsequent reperfusion (1 h) reduces the inflammatory cytokines. **A** Representative results of cerebral tissue influenced by MCAO-induced injury. The regions 1, 2, 3, 4, 5, 6, 7, 8, 9, 10, and 11 represent the blots of IL-1α, IL-1β, IL-2, IL-3, IL-4, IL-6, IL-9, IL-10, IL-13, IL-17, and TNF-α. **B** Statistical results showing that MCAO-induced ischemia increases the relative levels of IL-1α, IL-1β, and TNF-α (*$P < 0.05$ *vs* sham, $n = 3$/group). Meanwhile, the increased level of IL-1α, but not IL-1β and TNF-α, was reduced after the subsequent 1 h of reperfusion.

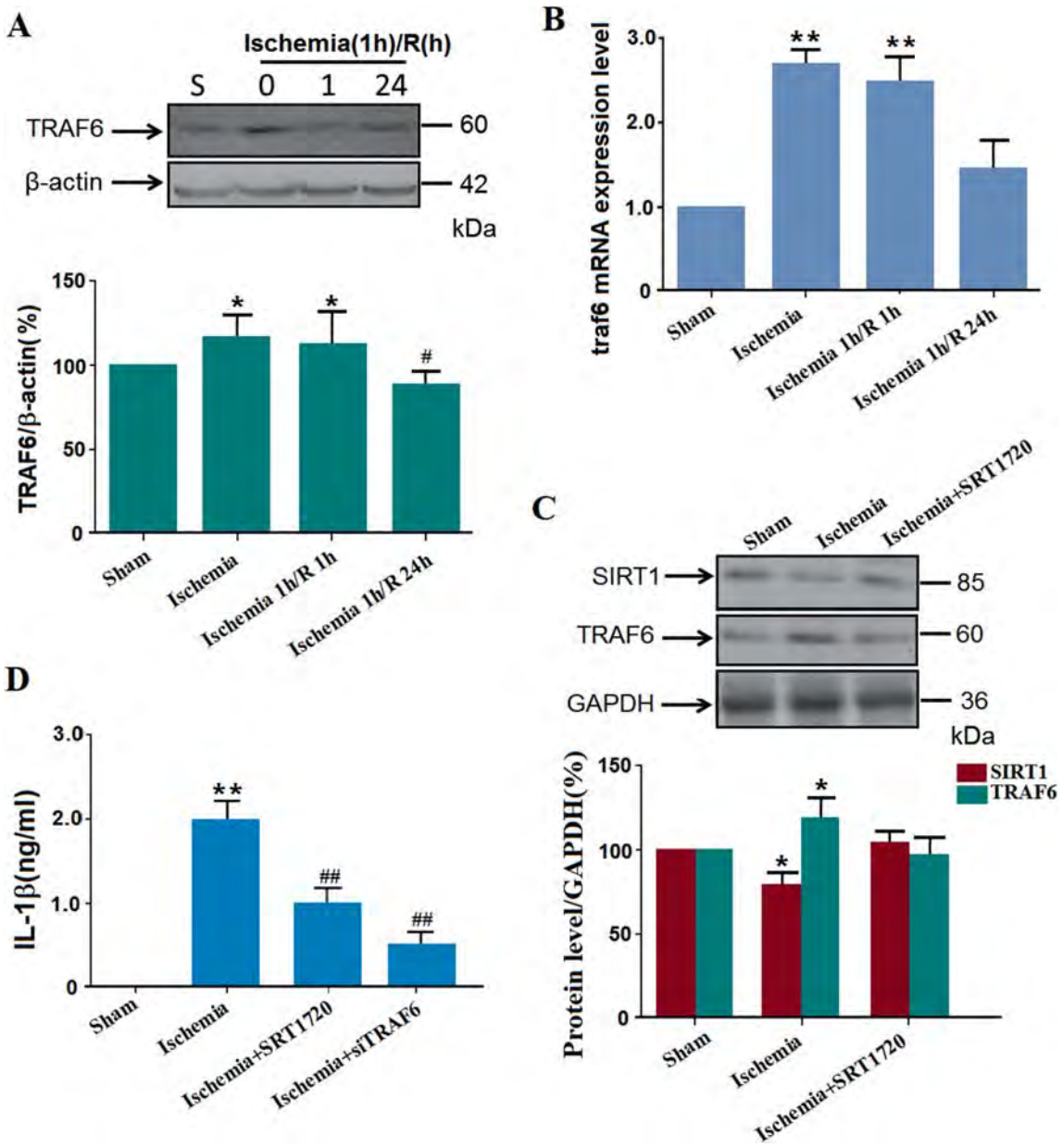

Fig. 3 MCAO-induced cerebral ischemia (1 h) increases the TRAF6 protein levels. **A** Representative blots and statistics for the TRAF6 protein levels in western blot assays ($^{*}P < 0.05$ *vs* sham; $^{\#}P < 0.01$ *vs* ischemia group; $n = 5$/group). **B** qPCR results showing the mRNA levels of TRAF6 in naïve ischemia, ischemia 1 h/R 1 h, and sham groups ($^{**}P < 0.01$; $n = 8$/group). **C** Salvage of the ischemia-increased TRAF6 protein level by intracerebroventricular injection of the Sirt1 activator SRT1720 (50 μg/kg) ($^{*}P < 0.05$, $n = 5$/group). **D** ELISA of supernatant IL-1β levels after ischemic insults and the effects of SRT1720 or TRAF6-specific siRNA ($^{**}P < 0.01$ *vs* sham; $n = 6$/group; $^{\#\#}P < 0.01$ *vs* ischemia group; $n = 6$/group; NC, negative control).

Suppression of TRAF6 or Increased Sirt1 Protein Levels in N2a Cells Decreased the Pyroptosis and Subsequent Death of OGD/R Cells

Based on the crucial role of TRAF6 in inflammation and the current *in vivo* results [32], we still needed to further explore the detailed mechanism of the Sirt1-TRAF6 signaling pathway in inflammatory reactions under ischemic stress. The following experiments were carried out in differentiated N2a cells (Fig. S3). First, pyroptosis in N2a cells under ischemic stress was assessed by the levels of pro-inflammatory IL-1β and activation of caspase-1. After 1 h OGD, mature IL-1β and the protein level of pro-IL-1β increased significantly (Figs. 4A and S4), while the cleaved caspase-1 translocated to the nuclei (Fig. 4B). Second, the TRAF6 protein levels increased after ischemia (Fig. 4C, D; statistical results of Sirt1 protein levels in Fig. S5). When the activator of Sirt1, SRT1720, or

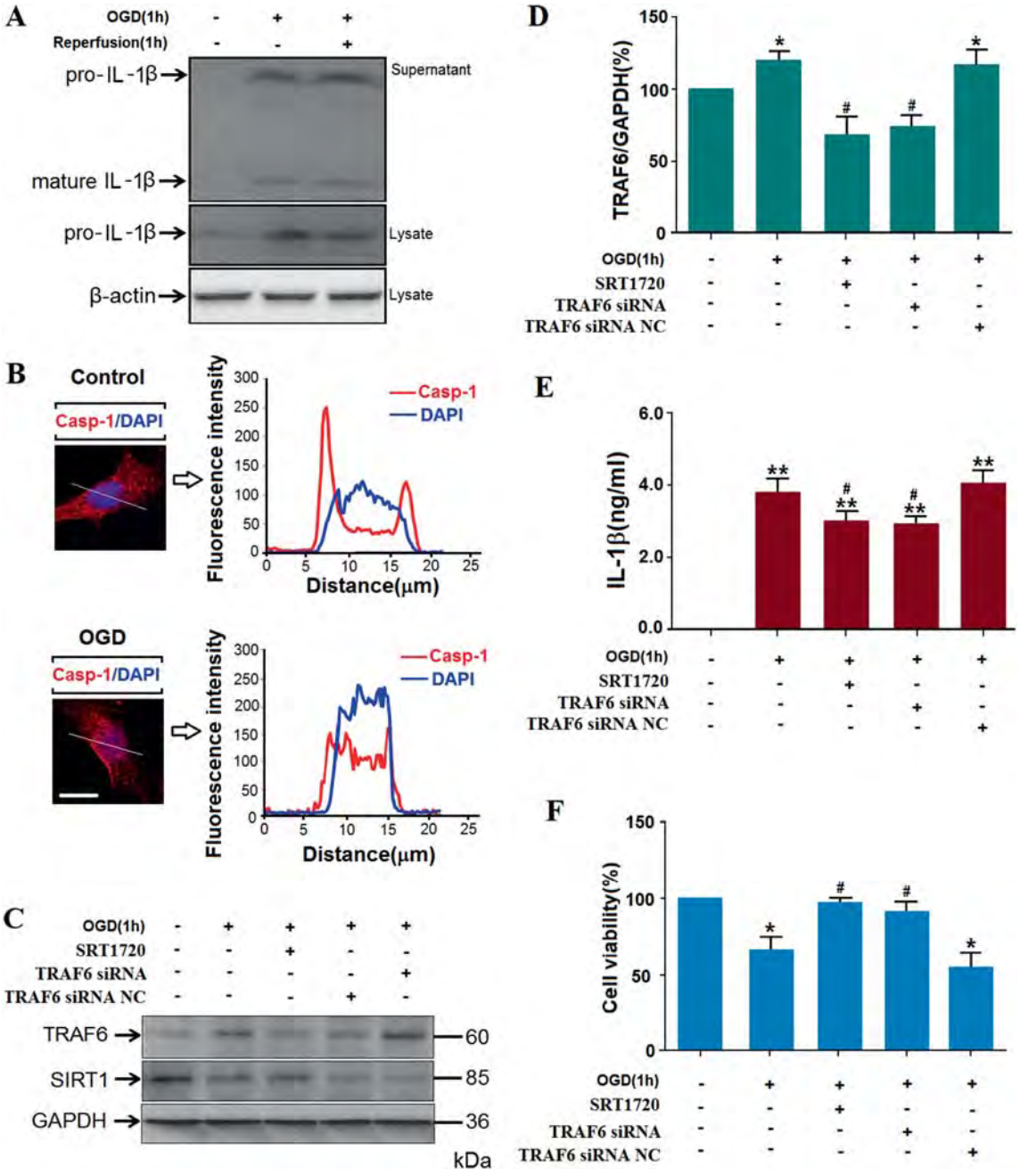

Fig. 4 Oxygen-glucose deprivation (OGD) causes pyroptosis in N2a cells. **A** Representative image showing pro-IL-1β protein levels in cells and mature IL-1β in supernatants after 1 h OGD and the subsequent re-oxygenation. **B** Representative images showing translocation of cleaved caspase-1 to the nucleus by confocal microscopy in N2a cells exposed to OGD (line tracings correspond to marked area; scale bar, 10 μm). **C** Representative blots of TRAF6 protein levels in N2a cells. **D** Analysis of TRAF6 protein levels as in **C** ($^{*}P < 0.05$ *vs* normoxia; $n = 5$ group). When the cells were transfected with TRAF6-specific siRNA or pretreated with SRT1720, the increased TRAF6 protein levels were reduced ($^{\#}P < 0.05$ *vs* OGD group; $n = 5$/group; NC, negative control). **E** ELISA of mouse IL-1β in supernatants of OGD-treated N2a cells and after transfection of TRAF6 siRNA or SRT1720 ($^{**}P < 0.01$ *vs* normoxia; $^{\#}P < 0.05$ *vs* OGD group; $n = 6$/group). **F** Quantitative analysis of MTT assay showed that OGD decreased cell viability ($^{*}P < 0.05$ *vs* control; $n = 6$/group). When the N2a cells were transfected with TRAF6 siRNA or pretreated with SRT1720, the viability was salvaged significantly ($^{\#}P < 0.05$ *vs* OGD/R group; $n = 6$/group).

TRAF6-specific siRNA was added before OGD, the increase in TRAF6 protein levels was reduced, indicating that Sirt1 is upstream of TRAF6. Third, both the increased TRAF6 and decreased Sirt1 protein levels resulted in IL-1β production in the supernatant of OGD-treated N2a cells (Fig. 4E). Fourth, cell viability measured with the MTT

assay was reduced after OGD and rescued after TRAF6 was knocked down or Sirt1 was activated (Fig. 4F). All these phenomena considered as a whole suggest the occurrence of pyroptosis of N2a cells *via* the Sirt1-TRAF6 signaling pathway after OGD. Since induced pyroptosis is deleterious and sustained cytokines are harmful, further study is warranted.

OGD-Induced Reduction of Sirt1 Contributes to ROS Production, Followed by TRAF6 Activation

It has been reported that there is a close relationship between ROS and inflammatory responses [33]. To explore whether ROS is involved in the relationship between Sirt1 and TRAF6 under our experimental conditions, the intercellular ROS level was assessed by DCF staining. N2a cells were pretreated with TRAF6-specific siRNAs before OGD. ROS production increased after OGD exposure, and remained at a similar level when the TRAF6-specific siRNAs were added. NAC, a ROS scavenger, was used as the positive control, and this significantly reduced the ROS level (Fig. 5A). Both NAC and TRAF6-specific siRNAs decreased OGD-induced neuronal death (Fig. 5B). Moreover, NAC treatment reversed the OGD-induced increase in TRAF6 protein level (Fig. 5C), indicating that ROS is upstream of TRAF6. Further, when Sirt1 was activated with SRT1720, the ROS level decreased, which had shown a burst after OGD exposure (Fig. 5A). Finally, when NAC and TRAF6-specific siRNAs were added to the medium before the ischemic insult, the increased IL-1β secretion was significantly suppressed (Fig. 5C). Besides, when the Sirt1 protein level was knocked down with siRNAs, the ROS production increased significantly (Fig. S6). Moreover, TRAF6 knockdown had no effect on the Sirt1 protein level (Fig. S5). The current results indicated that pyroptosis in N2a cells is induced by increased TRAF6 *via* the Sirt1-ROS signaling pathway.

To further explore the correlation between ROS and TRAF6, serial images of ROS and lenti-RFP-TRAF6 were recorded. The dynamic changes in ROS and TRAF6 were analyzed with Flash Sniper software and presented with ImageJ (Fig. 5D). To obtain precise signals of ROS and TRAF6, we measured the fluorescence intensities of ROS and TRAF6 in the dendritic processes of primary cultured hippocampal neurons where there were fewer overlapping signals and less noise. The neurons were subjected to OGD for 30 min, and then treated with NAC. The OGD-induced accumulation of TRAF6 was attenuated with the decay of the ROS burst. Based on the scavenging of ROS by NAC and the similar decay onset of the ROS burst and TRAF6 accumulation, it is likely that the ROS burst in the cytoplasm contributes to the TRAF6 accumulation.

Reduction of Sirt1 Increases ROS Levels in a SOD_2-Dependent Manner

SOD_2 plays a key role in the production of ROS as the vital mitochondrial oxidative scavenger [34]. To explore whether the Sirt1-induced ROS production depends on SOD_2, its activity was investigated under different experimental conditions. We found that OGD exposure suppressed the SOD_2 activity. However, SRT1720, the Sirt1 activator, salvaged the SOD_2-dependent actions. Moreover, EX527 (5 mmol/L; an inhibitor of Sirt1) decreased the SOD_2-mediated actions, and this served as a positive control here (Fig. 6A). To further strengthen our conclusion, we measured cytoplasmic ROS using DCF staining. OGD significantly increased the ROS level in the cytoplasm, and this was suppressed by pretreatment with 5 μmol/L SRT1720 or 200 μmolpyroptosis in long-term ischemic injury/L Mito-Tempo. Based on the scavenging of mitochondrial ROS by Mito-Tempo, it can be deduced that the OGD-induced ROS burst in the cytoplasm is derived from mitochondria (Fig. 6B). So, the decreased SOD_2-mediated activity contributes to the cytoplasmic ROS burst. Sirt1 plays a vital role in ROS production in a SOD_2-dependent manner under OGD. Now, there are two possibilities for the role of Sirt1 in SOD_2 modulation. One is that Sirt1 may translocate to mitochondria for its activity, but we did not find this in the current study. Another is that other molecules may be involved in the interaction between Sirt1 and SOD_2; this deserves to be thoroughly explored.

Anti-oxidative Stress Therapy Alleviates the Ischemic Injury in MCAO Mice

Neuronal injury starts from the acute stage of stroke, and then a second progressive injury occurs during the subacute period [35]. Among the mechanisms, the importance of early pyroptosis in long-term ischemic injury needs to be further elucidated. The following experiment was carried out on MCAO mice with ischemia for 1 h and reperfusion for 72 h. After the agonist of Sirt1 was injected intracerebroventricularly 30 min before the MCAO surgery (Fig. 7A), the infarct volume declined and the neurological score improved (Fig. 7B, C). Since the decreased action of Sirt1 occurred in the early onset of pyroptosis, gain-of-function of Sirt1 was thought to act *via* the early suppression of inflammation. Our results indicated that the mechanism responsible for the late ischemia-induced injury may 'hitch a ride' on the early inflammatory reactions, among which the early pyroptosis is especially worthy of note.

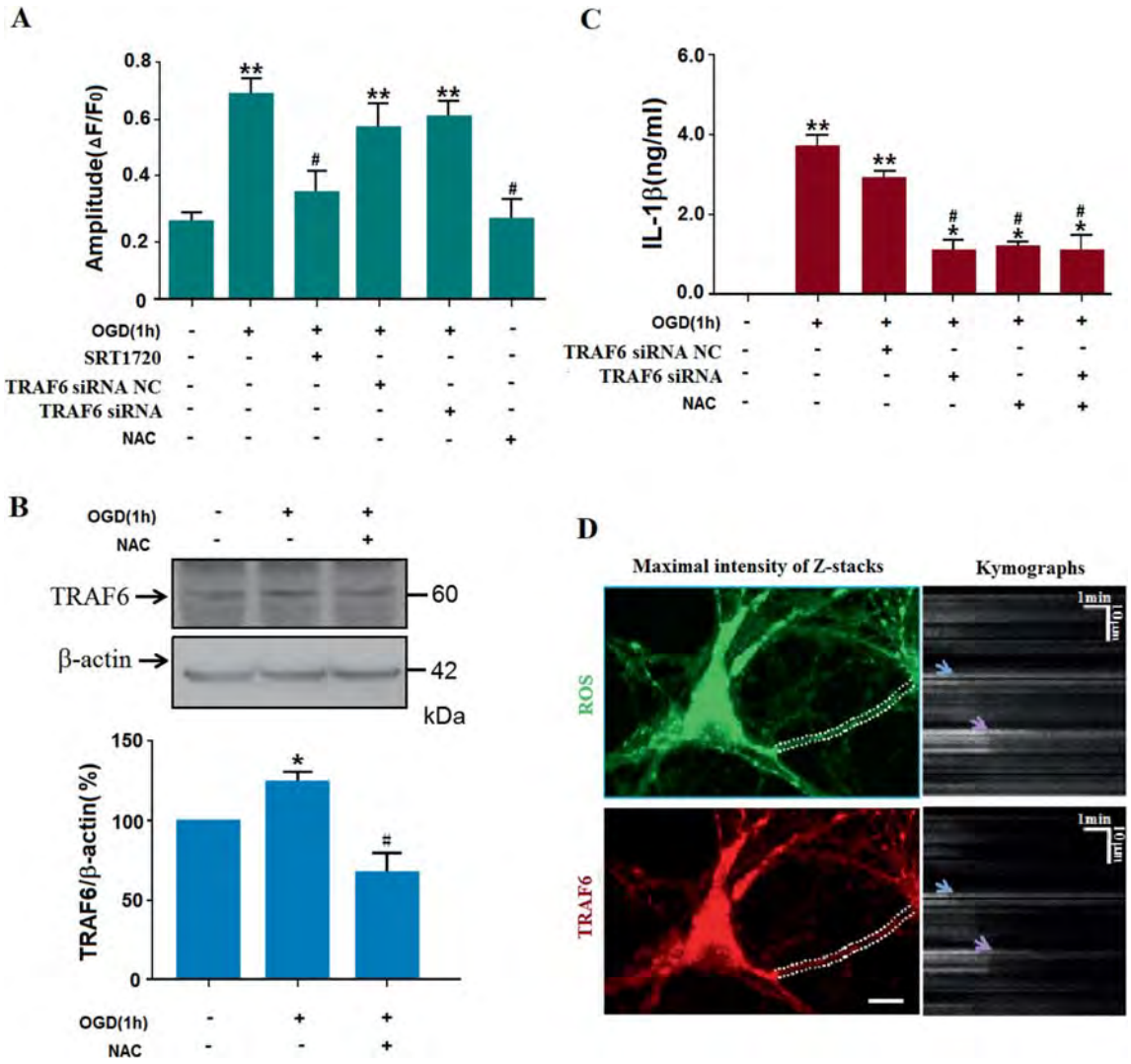

Fig. 5 ROS-mediated activation of TRAF6 plays an important role in OGD-induced injury. **A** OGD exposure increased the ROS production, which was reduced by NAC and SRT1720, but not TRAF6-specific siRNA (**$P < 0.01$ *vs* normoxia group, $^{\#}P < 0.05$ *vs* OGD group; n = 3/group). **B** Pretreatment with NAC suppressed OGD-induced activation of TRAF6 (*$P < 0.05$ *vs* normoxia group, $^{\#}P < 0.05$ *vs* OGD group; n = 5/group). **C** ELISA of mouse IL-1β in supernatants of OGD-treated N2a cells showing that OGD increased IL-1β secretion, which was blocked by treatment with NAC or TRAF6-specific siRNA (**$P < 0.01$ *vs* normoxia, $^{\#}P < 0.05$ *vs* OGD group; n = 6). **D** Representative images of a dendritic ROS burst and TRAF6 accumulation after OGD and subsequent NAC treatment. Left, DCF fluorescence revealing ROS and TRAF6 signals in a dendritic segment (dashed lines, boundaries of dendrite; scale bar, 10 μm); right, kymographs with ImageJ software show the two signals decayed at almost the same time (arrows) after 15–19 min after NAC treatment (because DCF is apt to enrichment in mitochondria, the images were acquired within 30 min after washes).

Discussion

Post-ischemic inflammation has been reported to be involved in neural cell death in the acute and sub-acute stages, along with the other mechanisms responsible for the pathogenesis of stroke [36]. Barrett *et al*. proposed that neuro-inflammation may be the main gateway to secondary cerebral injury in stroke [37]. Over the past years, many studies have emphasized the inflammatory responses induced by ischemic stroke for improving the outcome. However, initial treatments targeting inflammatory reactions against acute ischemic stroke have failed [38], and this is thought to be due to the nature of immune cells in stroke. Inflammatory reactions participate in the process of post-ischemic injury. Besides, they are also involved in post-stroke repair and regeneration [39]. Whether inflammatory responses constitute an initial event or consequence of ischemic stroke has been a frequent topic of debate; however, the increasing number of ischemic stroke-associated genes being addressed in inflammatory pathways indicates a causative role, at least in part. In the present study, we demonstrated a definite inflammatory burst as

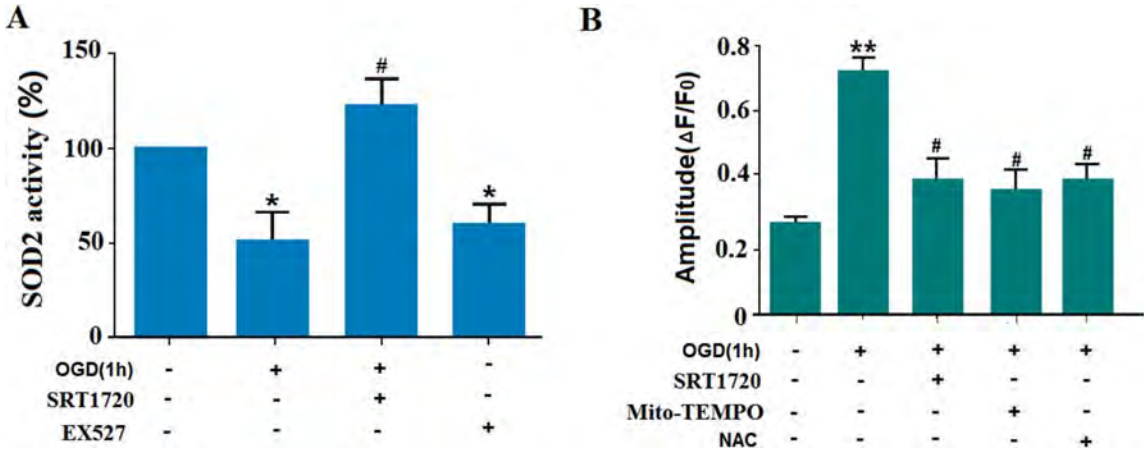

Fig. 6 OGD exposure increases ROS levels in the cytoplasm of N2a cells *via* the SIRT1-SOD_2 pathway. **A** SOD_2 activity was suppressed by OGD exposure, and salvaged by SRT1720, an activator of SIRT1 (EX527 treatment group served as a positive control). **B** ROS levels in the cytoplasm of N2a cells were increased by OGD exposure. SRT1720, Mito-Tempo, and NAC treatment decreased the OGD-induced ROS burst ($^{*}P < 0.05$ *vs* controls, $^{\#}P < 0.05$ *vs* OGD group). All experiments were repeated three times.

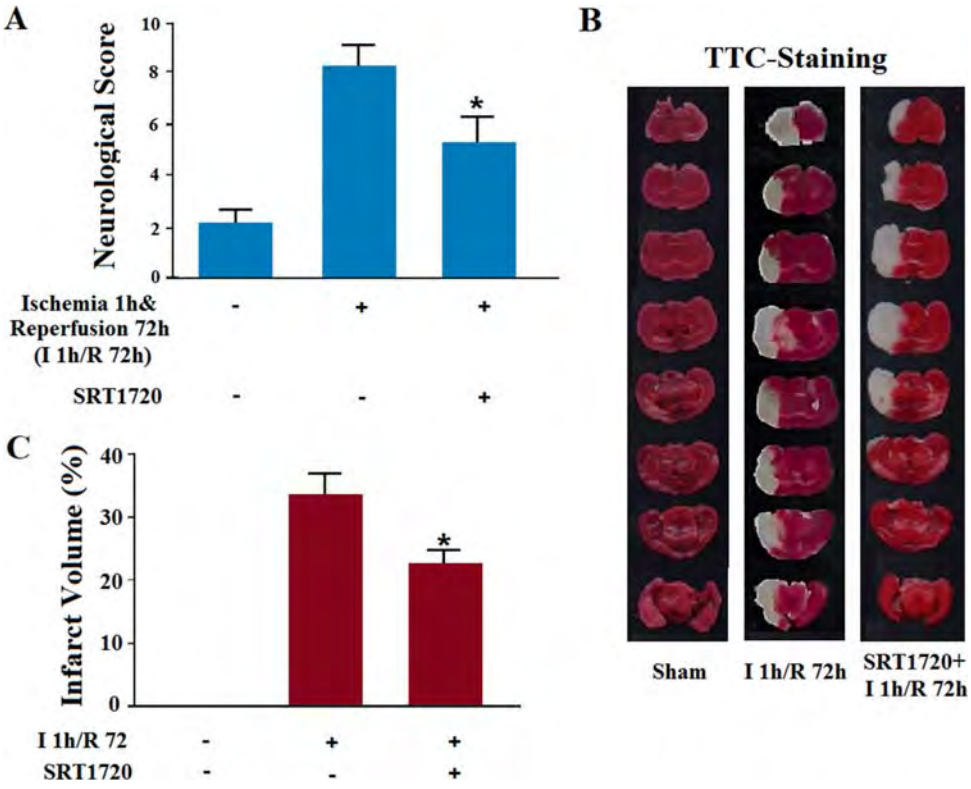

Fig. 7 Gain-of-function of Sirt1 alleviates ischemia-induced injury in MCAO mice (ischemia 1 h/reperfusion 72 h).**A** SRT1720 alleviated MCAO-increased neurological score ($^{*}P < 0.05$ *vs* ischemia group; $n = 6$/group).**B** Representative images of TTC-stained cerebral slices from mice subjected to sham, naïve ischemia, or ischemia 1 h/R 72 h. **C** SRT1720 alleviated MCAO-increased infarct volume ($^{*}P < 0.05$ *vs* ischemia group; $n = 6$/group).

pyroptosis at the early stage of stroke. Combined with the previous study, interventions in inflammatory reactions should be taken into consideration from the early to the late stages of stroke.

Sirt1, regarded as a bio-energetic regulator, serves as the onset of the subsequent oxidative stress in cerebral stroke [40]. Sirt1 warrants special interest since it is involved in both gene expression and cell metabolism under the cellular stress induced by cerebral ischemia [41]. The strategy of Sirt1 activation may alleviate stroke injury *via* the suppression of apoptosis and inflammation [42]. Based on its importance in ischemic stroke, the serum Sirt1 concentration is a promising means of evaluating functional outcomes, including dementia, anxiety, and depression in patients with acute ischemia [43]. Here, we found decreased Sirt1 protein levels both *in vivo* and *in vitro*, and this was followed by increased ROS and TRAF6 activation, indicating that Sirt1 indicates the onset of oxidative

stress and inflammatory responses follow. So, treatment by Sirt1 activation may be an effective strategy for ischemic stroke. Moreover, the relationship between Sirt1-induced pathological processes and its role at different stages of ischemic stroke deserves further study.

The activation of Sirt1 has been reported to play a key role in the anti-oxidative stress pathway *via* the Sirt1-FOXOs signaling pathway, which results in the release of high levels of ROS [44]. Then, an inflammatory response is elicited and systemic inflammation occurs [45]. In a rat model of traumatic brain injury, TRAF6 protein levels are significantly increased on day 7 after injury, in both neurons and astrocytes. These results show that TRAF6 is important for both neurons and astrocytes in stress injury [46]. Strikingly, in the present study, we found that the increase in TRAF6 was initiated by the ROS burst, suggesting that early inflammatory reactions may occur *via* the ROS-TRAF6 signaling pathway. Based on the current results, we determined that TRAF6-mediated pyroptosis occurs at the early stage of the post-ischemic period. Although it is a special kind of inflammation-induced programmed death, the same phenomena occurred, such as the increased level of TNF-α. Both our current results and those reported previously suggested that the TRAF6 protein level is important for neuronal survival and is an effective target for stroke treatment.

Oxidative stress is a crucial mechanism during I/R injury, and the production of ROS is an important contributor to cerebral I/R injury [47]. The increased ROS by I/R mainly results from the mitochondrial electron transport chain [48]. ROS has been reported to initiate and augment neuronal apoptosis after I/R. The current data suggest that cytoplasmic ROS is vital for cerebral damage-induced inflammation following I/R [49]. However, it remains obscure how Sirt1 regulates the ROS burst after ischemia. Our results indicated that the decrease of ROS level reduced ischemia-induced TRAF6 accumulation and the ischemia-induced injury. The Sirt1-mediated signaling pathway for ROS production may require deeper investigation.

During pyroptosis, proteolytic cleavage of caspase-1 transforms pro-IL-1β into its mature form, which further activates the NF-κB pathway to take part in cerebral innate immunity and inflammation *via* the production and action of other inflammatory cytokines [50]. IL-1 is a pro-inflammatory cytokine that is regarded as a vital mediator and the major effector of injury in experimental cerebral ischemic stroke or excitotoxicity in rodents [51]. Both IL-1α and IL-1β are produced soon after exposure to cerebral ischemia [52]. Inhibiting the actions of IL-1α and IL-1β with the IL-1 receptor antagonist (IL-1Ra) provides a protective strategy in experimental models of stroke [53]. Knock-out of both IL-1α and IL-1β significantly alleviates the ischemia-induced injury in response to experimental stroke [54]. Although IL-1α and IL-1β signal through a common receptor (IL-1RI), they have different actions in sterile inflammation [55]. And, different from IL-1β, the release of IL-1α is not caspase-1 dependent [56]. It has also been reported that IL-1α expression precedes IL-1β after cerebral ischemic insults [57]. In the present study, the expression of IL-1α and IL-1β increased after acute ischemia and IL-1α, but not IL-1β, declined after the subsequent reperfusion. Although the burst of mature IL-1β was determined to be consistent with the scenario of pyroptosis, the regulatory mechanism of IL-1α remains obscure and should be explored further.

Generally, inflammasomes are cytoplasmic supra-structured complexes that are formed after the signals of exogenous invasion or endogenous injury are sensed [58, 59]. Among these, the formation of NLRP3-centered complexes is vital for the activation of NLRP3 and the occurrence of pyroptosis. And, these complexes may derive from the combination of NLRP3 with ASC or NEK7 [60, 61]. Meanwhile, there is also a caspase recruitment domain in the structure of the ASC protein, resulting in caspase dimerization and activation [62, 63]. In our study, there may be a kind of ASC-centered complex with caspase-1 based on the activation of ASC and caspase-1. Due to the importance of supra-structured complexes in the inflammation, study of the formation of complexes and their gain-of-function should be emphasized in further studies.

N2a cells are derived from a mouse neuroblastoma cell line from a spontaneous tumor in an albino strain A mouse. Differentiated N2a cells possess many neuronal characteristics and express many neuronal markers [64]. Based on their neuronal characteristics, N2a cells have been widely used in many areas of study, including ischemia, amyotrophic lateral sclerosis, and Alzheimer's disease [19, 65, 66]. However, LePage *et al*. also reported that negative cytotoxicity data obtained using neuroblastoma cell lines should be viewed with caution because N2a cells are less sensitive to neurotoxicity than cerebellar granule neurons [67]. Here, we mainly used N2a cells to study neuro-inflammation. Although we demonstrated significant phenomena, the experimental conditions we used may not be suitable for primary neuronal cultures, which is a limitation of our study.

From the current findings, we can draw the following conclusions (Fig. 8). First, inflammatory reactions occur during the early stage of ischemic stroke. Second, the increased production of ROS that results from a decreased Sirt1 protein level plays an important role in the inflammatory reactions involving TRAF6. Third, there is cross-talk between oxidative stress and pyroptosis at the early stage of ischemic stroke. Fourth, the decreased Sirt1

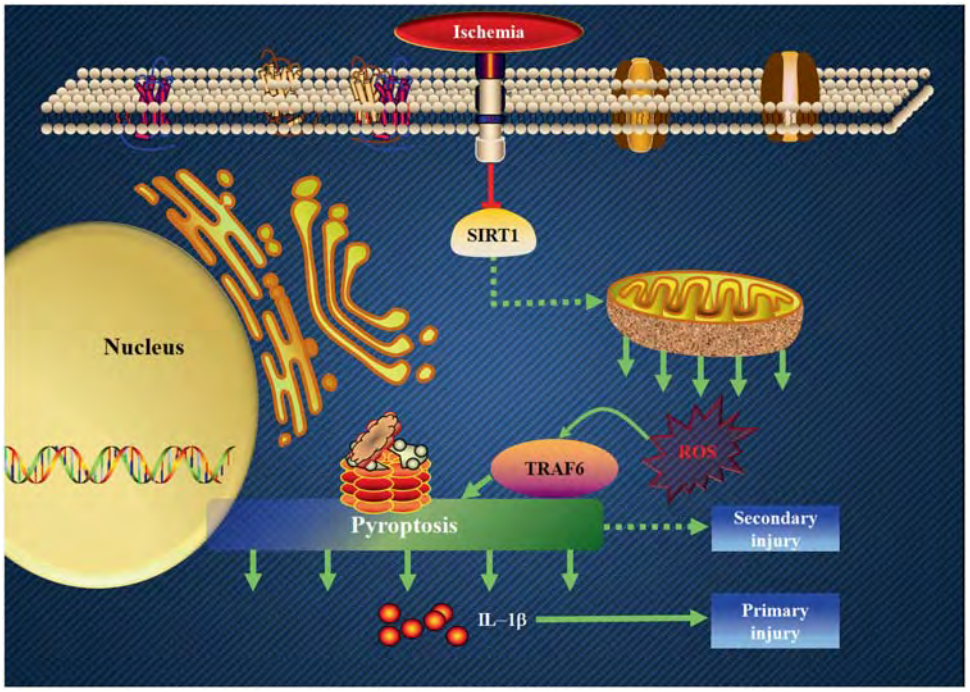

Fig. 8 Schematic of how Sirt1-ROS-TRAF6-induced pyroptosis contributes to the early neural injury after ischemia (red line, inhibitory effect; green arrows, positive correlations between members of the signaling cascade).

protein level is the onset of early inflammatory reactions. Fifth, pyroptosis is mediated by the Sirt1-ROS-TRAF6 signaling pathway. Sixth, the pyroptosis in neuronal cells is harmful, and can be suppressed in both an anti-oxidative stress manner and an anti-inflammation manner. Although we cannot disclose the whole scenario of the interaction between oxidative stress and inflammatory reactions during ischemic insults, the results suggest primarily that this is a promising prospect in further stroke research. In sum, based on our current results, we propose that the therapeutic strategies against inflammatory reactions should place emphasis on neuronal protection even at the early stage of ischemic stroke.

Acknowledgements This work was supported by the National Natural Science Foundation of China (31771292 and 31571162). We thank Professor Heping Cheng, Peking University, for kindly supporting the analytical methods for the fluorescence images.

Conflict of interest The authors declare that they have no conflict of interest.

References

1. Katan M, Luft A. Global burden of stroke. Semin Neurol 2018, 38: 208–211.
2. Stoll G, Jander S, Schroeter M. Inflammation and glial responses in ischemic brain lesions. Prog Neurobiol 1998, 56: 149–171.
3. Moskowitz MA. Brain protection: maybe yes, maybe no. Stroke 2010, 41: S85–86.
4. Del Zoppo GJ, Saver JL, Jauch EC, Adams HP, Jr., American Heart Association Stroke C. Expansion of the time window for treatment of acute ischemic stroke with intravenous tissue plasminogen activator: a science advisory from the American Heart Association/American Stroke Association. Stroke 2009, 40: 2945–2948.
5. Sekerdag E, Solaroglu I, Gursoy-Ozdemir Y. Cell death mechanisms in stroke and novel molecular and cellular treatment options. Curr Neuropharmacol 2018, 16: 1396–1415.
6. Shukla V, Shakya AK, Perez-Pinzon MA, Dave KR. Cerebral ischemic damage in diabetes: an inflammatory perspective. J Neuroinflammation 2017, 14: 21.
7. Adamczak SE, de Rivero Vaccari JP, Dale G, Brand FJ, 3rd, Nonner D, Bullock MR, *et al.* Pyroptotic neuronal cell death mediated by the AIM2 inflammasome. J Cereb Blood Flow Metab 2014, 34: 621–629.
8. Ceulemans AG, Zgavc T, Kooijman R, Hachimi-Idrissi S, Sarre S, Michotte Y. The dual role of the neuroinflammatory response after ischemic stroke: modulatory effects of hypothermia. J Neuroinflammation 2010, 7: 74.
9. Ahmad M, Graham SH. Inflammation after stroke: mechanisms and therapeutic approaches. Transl Stroke Res 2010, 1: 74–84.
10. Xie P. TRAF molecules in cell signaling and in human diseases. J Mol Signal 2013, 8: 7.
11. Lee NK, Lee SY. Modulation of life and death by the tumor necrosis factor receptor-associated factors (TRAFs). J Biochem Mol Biol 2002, 35: 61–66.
12. Lomaga MA, Henderson JT, Elia AJ, Robertson J, Noyce RS, Yeh WC, *et al.* Tumor necrosis factor receptor-associated factor 6 (TRAF6) deficiency results in exencephaly and is required for apoptosis within the developing CNS. J Neurosci 2000, 20: 7384–7393.
13. Zhang J, Fu B, Zhang X, Chen L, Zhang L, Zhao X, *et al.* Neuroprotective effect of bicyclol in rat ischemic stroke: down-regulates TLR4, TLR9, TRAF6, NF-kappaB, MMP-9 and up-regulates claudin-5 expression. Brain Res 2013, 1528: 80–88.
14. Rajendran R, Garva R, Krstic-Demonacos M, Demonacos C. Sirtuins: molecular traffic lights in the crossroad of oxidative

stress, chromatin remodeling, and transcription. J Biomed Biotechnol 2011, 2011: 368276.
15. Xu J, Jackson CW, Khoury N, Escobar I, Perez-Pinzon MA. Brain SIRT1 mediates metabolic homeostasis and neuroprotection. Front Endocrinol (Lausanne) 2018, 9: 702.
16. Duan J, Yin Y, Wei G, Cui J, Zhang E, Guan Y*, et al.* Chikusetsu saponin IVa confers cardioprotection *via* SIRT1/ERK1/2 and Homer1a pathway. Sci Rep 2015, 5: 18123.
17. Blokh D, Stambler I. Information theoretical analysis of aging as a risk factor for heart disease. Aging Dis 2015, 6: 196–207.
18. Meng X, Tan J, Li M, Song S, Miao Y, Zhang Q. Sirt1: Role under the condition of ischemia/hypoxia. Cell Mol Neurobiol 2017, 37: 17–28.
19. Wang CP, Shi YW, Tang M, Zhang XC, Gu Y, Liang XM*, et al.* Isoquercetin ameliorates cerebral impairment in focal ischemia through anti-oxidative, anti-inflammatory, and anti-apoptotic effects in primary culture of rat hippocampal neurons and hippocampal CA1 region of rats. Mol Neurobiol 2017, 54: 2126–2142.
20. Hadj Abdallah N, Baulies A, Bouhlel A, Bejaoui M, Zaouali MA, Ben Mimouna S*, et al.* Zinc mitigates renal ischemia-reperfusion injury in rats by modulating oxidative stress, endoplasmic reticulum stress, and autophagy. J Cell Physiol 2018, 233: 8677–8690.
21. Nasoohi S, Ismael S, Ishrat T. Thioredoxin-interacting protein (TXNIP) in cerebrovascular and neurodegenerative diseases: Regulation and implication. Mol Neurobiol 2018, 55: 7900–7920.
22. Zhang N, Yin Y, Han S, Jiang J, Yang W, Bu X*, et al.* Hypoxic preconditioning induced neuroprotection against cerebral ischemic injuries and its cPKCgamma-mediated molecular mechanism. Neurochem Int 2011, 58: 684–692.
23. Wang YP, Wang ZF, Zhang YC, Tian Q, Wang JZ. Effect of amyloid peptides on serum withdrawal-induced cell differentiation and cell viability. Cell Res 2004, 14: 467–472.
24. Evans MS, Collings MA, Brewer GJ. Electrophysiology of embryonic, adult and aged rat hippocampal neurons in serum-free culture. J Neurosci Methods 1998, 79: 37–46.
25. Sundar R, Gudey SK, Heldin CH, Landstrom M. TRAF6 promotes TGFbeta-induced invasion and cell-cycle regulation *via* Lys63-linked polyubiquitination of Lys178 in TGFbeta type I receptor. Cell Cycle 2015, 14: 554–565.
26. Muller L, Tokay T, Porath K, Kohling R, Kirschstein T. Enhanced NMDA receptor-dependent LTP in the epileptic CA1 area *via* upregulation of NR2B. Neurobiol Dis 2013, 54: 183–193.
27. Li Y, Sun W, Han S, Li J, Ding S, Wang W*, et al.* IGF-1-involved negative feedback of NR2B NMDA subunits protects cultured hippocampal neurons against NMDA-induced excitotoxicity. Mol Neurobiol 2017, 54: 684–696.
28. Yumnam S, Venkatarame Gowda Saralamma V, Raha S, Lee HJ, Lee WS, Kim EK*, et al.* Proteomic profiling of human HepG2 cells treated with hesperidin using antibody array. Mol Med Rep 2017, 16: 5386–5392.
29. Martinon F, Burns K, Tschopp J. The inflammasome: a molecular platform triggering activation of inflammatory caspases and processing of proIL-beta. Mol Cell 2002, 10: 417–426.
30. Newton K, Dixit VM. Signaling in innate immunity and inflammation. Cold Spring Harb Perspect Biol 2012, 4.
31. Abdullah M, Berthiaume JM, Willis MS. Tumor necrosis factor receptor-associated factor 6 as a nuclear factor kappa B-modulating therapeutic target in cardiovascular diseases: at the heart of it all. Transl Res 2018, 195: 48–61.
32. Ren M, Guo Y, Wei X, Yan S, Qin Y, Zhang X*, et al.* TREM2 overexpression attenuates neuroinflammation and protects dopaminergic neurons in experimental models of Parkinson's disease. Exp Neurol 2018, 302: 205–213.
33. Lee CW, Chi MC, Hsu LF, Yang CM, Hsu TH, Chuang CC*, et al.* Carbon monoxide releasing molecule-2 protects against particulate matter-induced lung inflammation by inhibiting TLR2 and 4/ROS/NLRP3 inflammasome activation. Mol Immunol 2019, 112: 163–174.
34. Kirby K, Hu J, Hilliker AJ, Phillips JP. RNA interference-mediated silencing of Sod2 in Drosophila leads to early adult-onset mortality and elevated endogenous oxidative stress. Proc Natl Acad Sci U S A 2002, 99: 16162–16167.
35. Andrabi SS, Ali M, Tabassum H, Parveen S, Parvez S. Pramipexole prevents ischemic cell death via mitochondrial pathways in ischemic stroke. Dis Model Mech 2019, 12. https://doi.org/10.1242/dmm.033860
36. Dirnagl U, Iadecola C, Moskowitz MA. Pathobiology of ischaemic stroke: an integrated view. Trends Neurosci 1999, 22: 391–397.
37. Barrett KM, Lal BK, Meschia JF. Stroke: advances in medical therapy and acute stroke intervention. Curr Cardiol Rep 2015, 17: 79.
38. del Zoppo GJ. Acute anti-inflammatory approaches to ischemic stroke. Ann N Y Acad Sci 2010, 1207: 143–148.
39. Drieu A, Martinez de Lizarrondo S, Rubio M. Stopping inflammation in stroke: Role of ST2/IL-33 signaling. J Neurosci 2017, 37: 9614–9616.
40. Kalaivani P, Ganesh M, Sathiya S, Ranju V, Gayathiri V, Saravana Babu C. Alteration in bioenergetic regulators, SirT1 and Parp1 expression precedes oxidative stress in rats subjected to transient cerebral focal ischemia: molecular and histopathologic evidences. J Stroke Cerebrovasc Dis 2014, 23: 2753–2766.
41. Petegnief V, Planas AM. SIRT1 regulation modulates stroke outcome. Transl Stroke Res 2013, 4: 663–671.
42. Lv H, Wang L, Shen J, Hao S, Ming A, Wang X*, et al.* Salvianolic acid B attenuates apoptosis and inflammation via SIRT1 activation in experimental stroke rats. Brain Res Bull 2015, 115: 30–36.
43. Liang X, Liu Y, Jia S, Xu X, Dong M, Wei Y. SIRT1: The value of functional outcome, stroke-related dementia, anxiety, and depression in patients with acute ischemic stroke. J Stroke Cerebrovasc Dis 2019, 28: 205–212.
44. Wang T, Gu J, Wu PF, Wang F, Xiong Z, Yang YJ*, et al.* Protection by tetrahydroxystilbene glucoside against cerebral ischemia: involvement of JNK, SIRT1, and NF-kappaB pathways and inhibition of intracellular ROS/RNS generation. Free Radic Biol Med 2009, 47: 229–240.
45. Settembre C, Annunziata I, Spampanato C, Zarcone D, Cobellis G, Nusco E*, et al.* Systemic inflammation and neurodegeneration in a mouse model of multiple sulfatase deficiency. Proc Natl Acad Sci U S A 2007, 104: 4506–4511.
46. Chen J, Wu X, Shao B, Zhao W, Shi W, Zhang S*, et al.* Increased expression of TNF receptor-associated factor 6 after rat traumatic brain injury. Cell Mol Neurobiol 2011, 31: 269–275.
47. Ten VS, Starkov A. Hypoxic-ischemic injury in the developing brain: the role of reactive oxygen species originating in mitochondria. Neurol Res Int 2012, 2012: 542976.
48. Hu S, Cheng D, Peng D, Tan J, Huang Y, Chen C. Leptin attenuates cerebral ischemic injury in rats by modulating the mitochondrial electron transport chain via the mitochondrial STAT3 pathway. Brain Behav 2019, 9: e01200.
49. Kalogeris T, Bao Y, Korthuis RJ. Mitochondrial reactive oxygen species: a double edged sword in ischemia/reperfusion vs preconditioning. Redox Biol 2014, 2: 702–714.
50. Zhang Y, Liu L, Peng YL, Liu YZ, Wu TY, Shen XL*, et al.* Involvement of inflammasome activation in lipopolysaccharide-induced mice depressive-like behaviors. CNS Neurosci Ther 2014, 20: 119–124.

51. Touzani O, Boutin H, Chuquet J, Rothwell N. Potential mechanisms of interleukin-1 involvement in cerebral ischaemia. J Neuroimmunol 1999, 100: 203–215.
52. Wang X, Yue TL, Barone FC, White RF, Gagnon RC, Feuerstein GZ. Concomitant cortical expression of TNF-alpha and IL-1 beta mRNAs follows early response gene expression in transient focal ischemia. Mol Chem Neuropathol 1994, 23: 103–114.
53. Brough D, Tyrrell PJ, Allan SM. Regulation of interleukin-1 in acute brain injury. Trends Pharmacol Sci 2011, 32: 617–622.
54. Boutin H, LeFeuvre RA, Horai R, Asano M, Iwakura Y, Rothwell NJ. Role of IL-1alpha and IL-1beta in ischemic brain damage. J Neurosci 2001, 21: 5528–5534.
55. Rider P, Carmi Y, Guttman O, Braiman A, Cohen I, Voronov E, *et al.* IL-1alpha and IL-1beta recruit different myeloid cells and promote different stages of sterile inflammation. J Immunol 2011, 187: 4835–4843.
56. Terlizzi M, Molino A, Colarusso C, Donovan C, Imitazione P, Somma P, *et al.* Activation of the absent in melanoma 2 inflammasome in peripheral blood mononuclear cells from idiopathic pulmonary fibrosis patients leads to the release of pro-fibrotic mediators. Front Immunol 2018, 9: 670.
57. Luheshi NM, Kovacs KJ, Lopez-Castejon G, Brough D, Denes A. Interleukin-1alpha expression precedes IL-1beta after ischemic brain injury and is localised to areas of focal neuronal loss and penumbral tissues. J Neuroinflammation 2011, 8: 186.
58. Lamkanfi M, Dixit VM. Mechanisms and functions of inflammasomes. Cell 2014, 157: 1013–1022.
59. Broz P, Dixit VM. Inflammasomes: mechanism of assembly, regulation and signalling. Nat Rev Immunol 2016, 16: 407–420.
60. Sharif H, Wang L, Wang WL, Magupalli VG, Andreeva L, Qiao Q, *et al.* Structural mechanism for NEK7-licensed activation of NLRP3 inflammasome. Nature 2019, 570: 338–343.
61. Stancu IC, Cremers N, Vanrusselt H, Couturier J, Vanoosthuyse A, Kessels S, *et al.* Aggregated Tau activates NLRP3-ASC inflammasome exacerbating exogenously seeded and non-exogenously seeded Tau pathology *in vivo*. Acta Neuropathol 2019, 137: 599–617.
62. Lu A, Magupalli VG, Ruan J, Yin Q, Atianand MK, Vos MR, *et al.* Unified polymerization mechanism for the assembly of ASC-dependent inflammasomes. Cell 2014, 156: 1193–1206.
63. Lu A, Li Y, Schmidt FI, Yin Q, Chen S, Fu TM, *et al.* Molecular basis of caspase-1 polymerization and its inhibition by a new capping mechanism. Nat Struct Mol Biol 2016, 23: 416–425.
64. Wang LJ, Colella R, Yorke G, Roisen FJ. The ganglioside GM1 enhances microtubule networks and changes the morphology of Neuro-2a cells *in vitro* by altering the distribution of MAP2. Exp Neurol 1996, 139: 1–11.
65. Kamelgarn M, Chen J, Kuang L, Jin H, Kasarskis EJ, Zhu H. ALS mutations of FUS suppress protein translation and disrupt the regulation of nonsense-mediated decay. Proc Natl Acad Sci U S A 2018, 115: E11904–E11913.
66. Reddy PH, Manczak M, Yin X. Mitochondria-division inhibitor 1 protects against amyloid-beta induced mitochondrial fragmentation and synaptic damage in Alzheimer's disease. J Alzheimers Dis 2017, 58: 147–162.
67. LePage KT, Dickey RW, Gerwick WH, Jester EL, Murray TF. On the use of neuro-2a neuroblastoma cells versus intact neurons in primary culture for neurotoxicity studies. Crit Rev Neurobiol 2005, 17: 27–50.

Neurosci. Bull. August, 2020, 36(8):860–874
https://doi.org/10.1007/s12264-020-00499-2

www.neurosci.cn
www.springer.com/12264

ORIGINAL ARTICLE

Prefrontal Nectin3 Reduction Mediates Adolescent Stress-Induced Deficits of Social Memory, Spatial Working Memory, and Dendritic Structure in Mice

Hong-Li Wang[1,2] · Ji-Tao Li[1] · Han Wang[1] · Ya-Xin Sun[1] · Rui Liu[1] · Xiao-Dong Wang[3] · Yun-Ai Su[1] · Tian-Mei Si[1]

Received: 17 July 2019 / Accepted: 16 December 2019 / Published online: 8 May 2020

Abstract Chronic stress may disrupt the normal neurodevelopmental trajectory of the adolescent brain (especially the prefrontal cortex) and contribute to the pathophysiology of stress-related mental illnesses, but the underlying molecular mechanisms remain unclear. Here, we investigated how synaptic cell adhesion molecules (e.g., nectin3) are involved in the effects of adolescent chronic stress on mouse medial prefrontal cortex (mPFC). Male C57BL/6N mice were subjected to chronic social instability stress from postnatal days 29 to 77. One week later, the mice exposed to chronic stress exhibited impaired social recognition and spatial working memory, simplified dendritic structure, and reduced spine density in the mPFC. Membrane localization of nectin3 was also altered, and was significantly correlated with behavioral performance. Furthermore, knocking down mPFC nectin3 expression by adeno-associated virus in adolescent mice reproduced the stress-induced changes in behavior and mPFC morphology. These results support the hypothesis that nectin3 is a potential mediator of the effects of adolescent chronic stress on prefrontal structural and functional abnormalities.

Keywords Adolescence · Chronic stress · Cell adhesion molecule · Prefrontal cortex · Social memory

Introduction

The prefrontal cortex (PFC) has long been implicated in the pathophysiology of stress-related psychiatric disorders such as depression and schizophrenia [1, 2]. As a late-maturing brain region, the PFC undergoes extensive structural remodeling during adolescence and early adulthood [3], including the pruning of initially over-produced excitatory synapses [4], and the maturation of inhibitory synapses [5]. Accompanying the structural development is the functional maturation of PFC-dependent behaviors, such as social behaviors and working memory [6, 7]. Chronic stress during adolescence has been shown to alter prefrontal dendritic architecture and to impair cognitive and social functions [8–10], but the neurobiological mechanisms have just started to be uncovered.

Synaptic cell adhesion molecules (CAMs) contain several families of proteins, such as N-cadherin, catenins, nectins, and neuroligins [11, 12]. These molecules are located at adherens and/or synaptic junctions, forming inter-neuronal connections and dynamically shaping synaptic plasticity by modulating synapse formation, maturation,

Hong-Li Wang and Ji-Tao Li have contributed equally to this work.

Electronic supplementary material The online version of this article (https://doi.org/10.1007/s12264-020-00499-2) contains supplementary material, which is available to authorized users.

✉ Ji-Tao Li
ljt_102124@163.com

✉ Tian-Mei Si
si.tian-mei@163.com

[1] National Clinical Research Center for Mental Disorders (Peking University Sixth Hospital/Institute of Mental Health) and the Key Laboratory of Mental Health, Ministry of Health (Peking University Sixth Hospital), Beijing 100191, China

[2] The National Clinical Research Center for Mental Disorders & Beijing Key Laboratory of Mental Disorders, Beijing Anding Hospital, Capital Medical University & the Advanced Innovation Center for Human Brain Protection, Capital Medical University, Beijing 100088, China

[3] Department of Neurobiology, Key Laboratory of Medical Neurobiology of The Ministry of Health of China, Zhejiang Province Key Laboratory of Neurobiology, Zhejiang University School of Medicine, Hangzhou 310003, China

and transmission [13–15]. Several CAMs are altered by stress, such as nectin3 [16, 17], nectin1 [18, 19], neuroligin2 [10, 20], β-catenin [21–23], and N-cadherin [22, 24]. Evidence also supports mediating roles of CAMs in the effects of stress on behavior and dendritic structure [16, 20, 25, 26], but the majority of these studies have focused on the hippocampus and postnatal/adult stress [16, 20, 25]. Only one study has reported the involvement of prefrontal neuroligin2 expression in adolescent stress-induced attention deficits [10]. Therefore, it remains unknown whether and how prefrontal CAM expression is associated with the behavioral and structural abnormalities induced by adolescent chronic stress.

In this study, we investigated the involvement of CAMs in chronic-stress-induced effects on the medial PFC (mPFC) in adolescent mice. Specifically, using the adolescent chronic social instability stress paradigm [27, 28], we first evaluated how adolescent chronic stress would affect mPFC-dependent social and spatial working memory behaviors and the mPFC dendritic architecture. We then tested the CAM involvement in these stress effects by examining whether adolescent stress would alter mPFC CAM expression and whether manipulating prefrontal CAM expression *via* adeno-associated virus (AAV) could reproduce the behavioral and structural consequences of chronic stress exposure.

Materials and Methods

Animals

Adolescent male C57BL/6N mice ($n = 72$, 21 ± 1 days old; Vital River Laboratories, Beijing, China) were housed in groups of 4 per cage under a 12L:12D cycle (lights on at 08: 00) and at a constant temperature (23 ± 1 °C) with free access to food and water. All experiments were carried out in accordance with the National Institute of Health's Guide for the Use and Care of Laboratory Animals and were approved by the Peking University Committee on Animal Care and Use.

Chronic Social Instability Stress

The chronic social instability stress paradigm was carried out as described previously [27] (Fig. 1A). After habituation in the vivarium for 7 days after arrival, mice were randomly divided into stress (ST) and control (CT) groups. In the ST group, cage-mates were changed twice a week for 7 weeks (postnatal days 29–77). To prevent the mice from developing stable social hierarchies, at each rotation 4 animals were regrouped in a cage such that an individual mouse was randomly introduced to 3 experimental mice that it had not encountered for at least one week. Cage-mates in the CT group remained unchanged. At the end of the chronic stress procedure, mice in both groups were separated and singly housed for 7 days and then subjected to behavioral tests. Body weight and fur state were monitored 24 h after each change of cage-mates.

Fig. 1 The paradigm, experimental design, and behavioral effects of adolescent chronic social instability stress. **A** The paradigm of adolescent chronic social instability stress. **B** The experimental timeline of the behavioral procedure and brain tissue acquisition after stress exposure. **C** The fur states of stressed mice worsen throughout stress exposure. **D** Adolescent stress increases the anxiety levels in the open field. **E–G** Adolescent stress does not affect social approach (**E**) and preference (**F**), but impairs social memory (**G**). **H** Stressed mice have a lower spontaneous alternation ratio in the Y-maze test than control mice. CT, control; ST, stress. Numbers in each bar indicate the number of animals in each group. Data represent the mean ± SEM. $^{*}P < 0.05$; $^{**}P < 0.01$; $^{***}P < 0.001$. PND, postnatal day. ▶

Fur state was scored independently by two experimenters on a 4-point scale (1, normal condition; 4, worst condition) [27, 29]. Three body parts were examined (body fur, whiskers, and conjunctivae). The scoring scheme was as follows: (1) smooth and shiny fur with no tousled and spiky patches; whiskers and conjunctivae normal; (2) slightly fluffy fur with some spiky patches; whiskers and conjunctivae normal; (3) fluffy fur on most of the body, slightly stained; whiskers and conjunctivae slightly abnormal; and (4) fluffy fur with some bald or wound patches; whisker lost and conjunctivae congested.

Experimental Design

This study contained two experiments. In Experiment 1 (Fig. 1B), we investigated the behavioral, morphological, and molecular effects of adolescent chronic stress. A total of 32 mice (16/group) were used for a series of behavioral tests (open field, social approach, social preference, social memory, and spontaneous alternation in the Y maze). Note that two mice in the stressed group died during stress exposure, leaving 14 mice for further analyses. On day 91 (24 h after the last behavioral test), each mouse was decapitated after anesthesia and the brain removed for morphological analyses ($n = 5$/group) and western blot ($n = 6$/group).

In Experiment 2, we investigated whether knocking down the prefrontal nectin3 expression (nectin3-KD) could mimic the effects of stress on behavior and mPFC morphology (Fig. 5A). A total of 35 mice were used (16 controls and 19 nectin3-KD mice). To match the stress schedule, AAV was injected into the mouse mPFC on day 29. Behavioral tests and neurobiological analyses were performed at the same time points as in Experiment 1. The

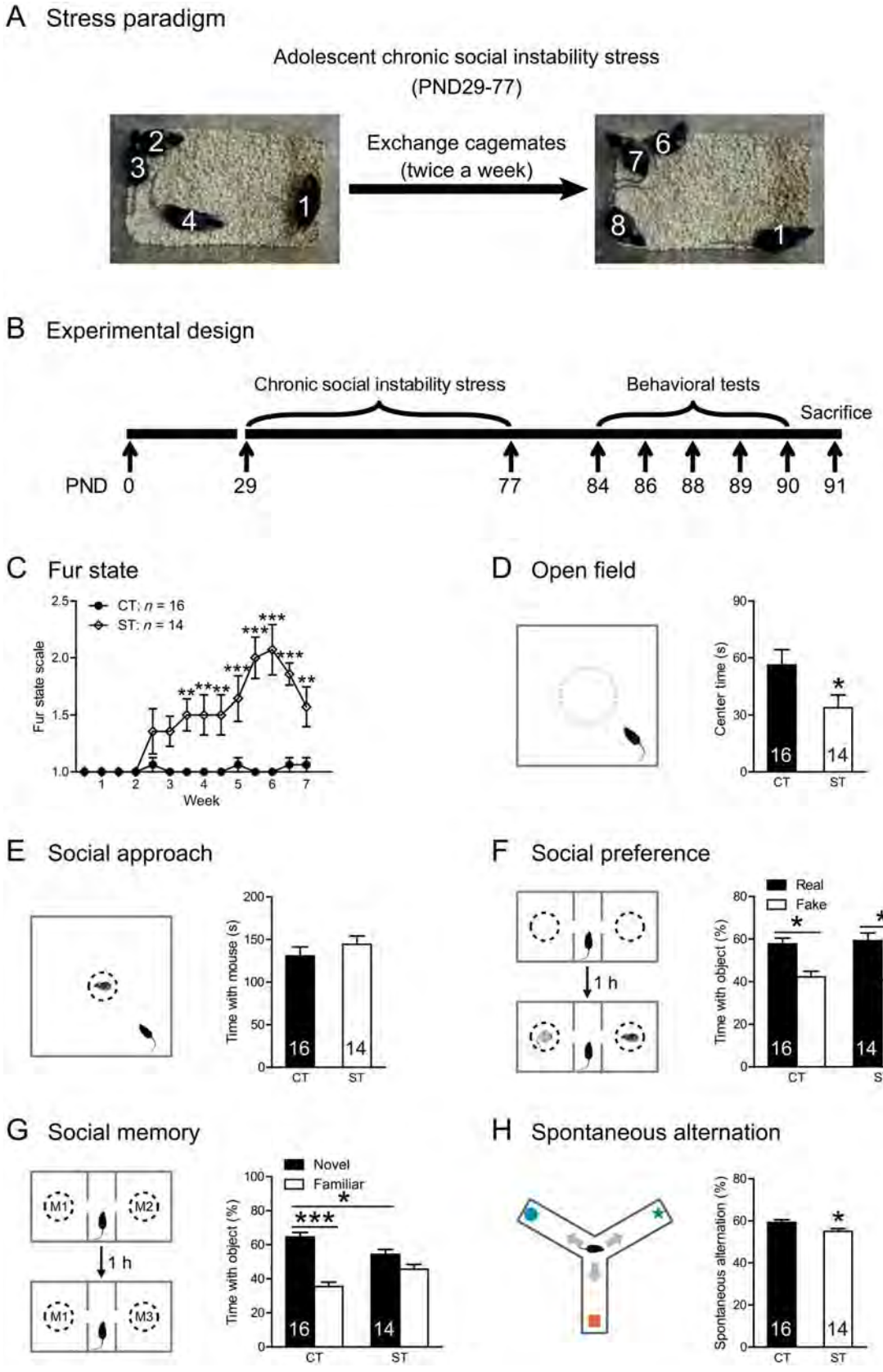
A Stress paradigm
Adolescent chronic social instability stress
(PND29-77)
Exchange cagemates
(twice a week)
B Experimental design
Chronic social instability stress
Behavioral tests
Sacrifice
PND 0 29 77 84 86 88 89 90 91
C Fur state
CT; n = 16
ST; n = 14
Fur state scale
Week
D Open field
Center time (s)
CT
ST
E Social approach
Time with mouse (s)
F Social preference
Real
Fake
1 h
Time with object (%)
G Social memory
M1
M2
M3
Novel
Familiar
H Spontaneous alternation
Spontaneous alternation (%)

sample sizes for the two experiments were based on previous studies [16, 25].

Behavioral Tests

All of the behavioral tests were carried out between 09:00 and 16:00 as described previously [28, 30, 31]. Behavior in the open field was analyzed using ANY-maze 4.98 (Stoelting, Wood Dale, IL). The social tests and Y-maze spontaneous alternation task were scored by an experimenter who was unaware of the aims of the study.

Open Field

The open field test was performed in an arena (50 cm × 50 cm × 50 cm, illuminated at 60 lux) made of gray polyvinyl chloride. During the test, a mouse was put in one corner and freely explored the arena for 10 min. To avoid residual olfactory traces, we cleaned the arena with 75% ethanol after each test. Using the ANY-maze software, we analyzed the following variables: total distance traveled during the test, time spent in the center zone (20 cm in diameter), and latency to the center zone. The number of fecal pellets was recorded by the experimenter as another index to reflex animals' anxiety levels.

Social Approach

This test was conducted in an open compartment made of gray polyvinyl chloride (50 cm × 50 cm × 50 cm, illuminated at 15 lux). A wire-mesh cylinder was fixed in the center with a stimulus mouse inside (male, 12 weeks old). During the test, another mouse was put in one corner of the compartment and allowed to interact with the stimulus mouse for 10 min. The time spent interacting with the stimulus mouse was recorded manually. Video tracking software was used to measure the latency to the central zone (15 cm in diameter).

Social Preference

Social preference was tested in a three-chambered box (50 cm × 25 cm × 50 cm) containing two side-compartments (20 cm × 25 cm × 50 cm), each with a wire-mesh cylinder in the center. During the acquisition session, each mouse was allowed to freely explore the box with empty cylinders for 10 min. An hour later, a fake mouse was put into one cylinder and a real mouse was put into the other. During the test trial, the test mouse was placed in the center chamber and allowed to habituate for 1 min. Then the doors to the side compartments were opened and the mouse allowed to freely explore the chambers for 10 min. A trained experimenter blind to the experimental conditions manually recorded the time the mouse spent sniffing each target (real *versus* fake mouse). The preference index was calculated as the time spent with each target divided by the total exploration time × 100%.

Social Memory

In the three-chambered box, the test started with a 10-min acquisition session, during which there was a male mouse in each cylinder and the test mouse was allowed to freely interact with them. The test session was carried out 1 h later, when the mouse in one cylinder was replaced by a new counterpart and the test mouse was given 10 min to interact with the two mice (one familiar and the other novel). The times spent interacting with the novel and familiar mice were recorded. The discrimination index was defined as the time spent with each mouse divided by the total exploration time × 100%.

Spontaneous Alternation

The Y-maze apparatus had three arms (30 cm × 10 cm × 15 cm, made of gray polyvinyl chloride), with the same angle (120°) between each of the arms. Intra-maze cues (blue circle, orange square, and green star) and some external cues were provided. The maze was illuminated at 15 lux during the test. Each mouse was placed in the center of the maze and allowed to freely explore the three arms for 8 min. The total distance traveled, the number of arm entries, and the spontaneous alternation ratio were recorded.

Golgi-Cox Staining and Morphological Analysis

Mice were transcardially perfused with 0.9% saline under anesthesia (pentobarbital sodium, 200 mg/kg, i.p.). The brains were quickly removed and immersed in Golgi-Cox solution for 2 weeks in the dark at room temperature. Then the brains were rinsed in 20 mL ddH_2O, transferred to 20 mL 30% sucrose, and left in the dark for 5 days. Serial coronal sections were cut at 120 μm on a Microm HM vibratome (Thermo Scientific, Walldorf, Germany) and collected in 6% sucrose in ddH_2O at 4 °C. The sections were then mounted on Superfrost plus slides (Thermo Scientific) and pre-processed according to a previously-described protocol [17, 32].

Pyramidal neurons in superficial (II/III) and deep (V) layers of the mPFC, fully impregnated with Golgi stain and minimally overlapped with other stained cells, were used for morphological analyses (6–8 neurons from each layer in each subregion per mouse; the number of neurons was chosen based on previous studies [16, 32]). For each neuron, the circumference of the cell body and the

dendritic branches in the x, y, and z directions were manually traced at ×400 with Neurolucida software (MicroBrightField Bioscience, Williston, VT).

Sholl analysis was used to assess the total dendritic length and dendritic complexity using NeuroExplorer software. For each neuron, the dendritic length was measured as the sum of the lengths of the apical main dendrite and branches. The apical main dendrite refers to the large apical dendrite that connects the soma to distal tuft dendrites. The apical branches included all the oblique dendrites that emanated from the apical main dendrite. Dendritic complexity was measured as the number of intersections per concentric circle (20 μm) of increasing distance from the cell body.

For dendritic spine analysis of mPFC pyramidal neurons, the inclusion criteria for segments to be analyzed were as follows [32]: (1) segments of apical main or oblique dendrites initiated at 120 μm from the soma; (2) segment length > 30 μm; (3) comparable segment diameter for each dendritic domain; and (4) no overlap with other segments, to prevent possible confusion in spine visualization. Bright-field z-series images of dendritic segments (6–8 segments from each dendritic domain per animal) were digitized at ×1000 using a CoolSNAP MP5 CCD camera (Roper Scientific, Tucson, AZ) mounted to an Olympus BX51 microscope (Tokyo, Japan). Dendritic spines in the mPFC were classified as thin, stubby, or mushroom types according to the criteria in the literature [33], and counted using NIH ImageJ software. Spine density is expressed as the number of spines per 10 μm of dendrite.

Western Blot

Based on a previous description [17], mice were anesthetized with isoflurane-O2 (4–5:100). The mPFC was rapidly dissected from the brain on ice, homogenized in ice-cold lysis buffer (137 mmol/L NaCl, 20 mmol/L Tris–HCl (pH 8.0), 1% NP-40, 10% glycerol, 1 mmol/L phenylmethylsulfonyl chloride, 10 mg/mL aprotinin, 1 mg/mL leupeptin, and 0.5 mmol/L sodium vanadate), sonicated, and centrifuged. The supernatants were stored at − 80 °C until use. Membrane proteins were collected using the ProteoExtract® Subcellular Proteome Extraction Kit (Cat#: 539790, Calbiochem, Darmstadt, Germany) according to the manufacturer's instructions. The mPFC of one hemisphere was used to assess total proteins, and that of the other hemisphere was used to measure membrane expression levels.

We prepared 5% sodium dodecyl sulfate polyacrylamide gel electrophoresis laminated gels and 10% separating gels for electrophoresis. Samples containing 20 μg protein were added to the gels and transferred electrophoretically to polyvinylidene difluoride membranes (Millipore, Bedford, MA). The membranes were then blocked with 5% non-fat milk diluted in Tris-buffered saline-Tween (TBST; containing 150 mmol/L NaCl, 10 mmol/L Tris-HCl, and 0.1% Tween, adjusted to pH 7.5) for 1 h at room temperature and labeled overnight at 4 °C with primary antibodies diluted in TBST containing 5% non-fat milk (nectin1: 1:5000, sc-28639, Santa Cruz; nectin3: 1:5000, sc-28637, Santa Cruz; N-cadherin: 1:5000, ab18203, Abcam; β-catenin: 1:50000, 281003, Synaptic Systems; neuroligin1: 1:10000, 129013, Synaptic Systems; neuroligin2: 1:10000, 129203, Synaptic Systems; GAPDH: 1:20000, 2118, Cell Signaling; Na, K-ATPase: 1:10000, 3010, Cell Signaling; β-actin: 1:20000, 3700S, Cell Signaling). After 2-h incubation with horseradish peroxidase-conjugated secondary antibodies (1:5000–10000, Zhongshan Gold Bridge Biotechnology, China, diluted in TBST) at room temperature, bands were visualized using the Amersham Imager 600 (GE Healthcare, PA) and analyzed using Quantity One 4.2 (Bio-Rad, Hercules, CA) by an investigator blind to the treatment conditions. The values were corrected based on their corresponding control protein levels. All results were normalized by taking the value of the vehicle group as 100%.

Immunofluorescence and Image Analysis

Mice were anesthetized with sodium pentobarbital (200 mg/kg, i.p.) and then transcardially perfused with 0.9% saline followed by 4% paraformaldehyde in 0.1 mol/L PBS. The brains were removed, post-fixed for 12 h in the same fixative, and then stored in 30% sucrose for 3 days at 4 °C. Next, the brains were quenched in N-hexane at − 60 °C and stored at − 80 °C until use. Following cryoprotection, serial coronal sections through the mPFC (1.98 mm–1.54 mm from bregma) were cut at 30 μm on a cryostat (Leica, Wetzlar, Germany). Sections at 180-μm intervals were blocked with 1% normal donkey serum for 1 h at room temperature and then incubated overnight at 4 °C with primary antibodies (nectin3: 1:1000, ab63931; nectin1: 1:1000; ab66985; NeuN: 1:5000, ab104225, all from Abcam, Cambridge, UK). The next day, the sections were rinsed 3 times in 0.1 mol/L PBS and then labeled with Alexa Fluor 594-conjugated secondary antibodies (1:500; Invitrogen, Carlsbad, CA) for 3 h at room temperature. The sections were rinsed, transferred onto slides, and coverslipped with Vectashield containing 4′,6-diamidino-2-phenylindole (DAPI; Vector Laboratories, Burlingame, CA).

The sections were assigned random numbers for analyses. Images were acquired from 4 sections per animal at 100× or 200× using an Olympus IX71 microscope equipped with a charge-coupled device camera (CoolSNAP

MP5, Roper Scientific Corp.). ImageJ software (NIH) was used to quantify the immunoreactivity of nectin1 and nectin3 and the density of NeuN-positive cells. Relative protein levels were calculated as differences in optical density between the mPFC and the corpus callosum (background). Results were normalized by taking the mean value of the control group as 100%. For co-localization analysis, images (1024 × 1024 pixel^2) were obtained at 200× (optical section thickness, 0.362 μm) or 600× (optical section thickness, 0.196 μm) using an Olympus IX81 laser-scanning confocal microscope (Olympus, Tokyo, Japan) with the Kalman filter and sequential scanning mode under identical settings for laser power, photomultiplier gain, and offset. The brightness and contrast of images were optimized using FV10-ASW 1.7 software (Olympus).

Stereotactic Surgery and Viral Microinjection

The adeno-associated virus (AAV) 2/8 vectors that were generated and purified by Obio Technology (Shanghai, China) were used to suppress the nectin3 protein levels. The short hairpin RNA (shRNA) sequence for nectin3 was 5′-TGTGTCCTGGAGGCGGCAAAGCACAACTT-3′. We used two types of virus: AAV-shNectin3 (AAV2/8-CMV-Nectin3.shRNA-terminator-CAG-EGFP-WPRE-BGH-polyA, 3.9 × 10^{12} viral genomes/mL) and control virus (AAV2/8-CMV-scrambled.shRNA-terminator-CAG-EGFP-WPRE-BGH-polyA, 3.5 × 10^{12} viral genomes/mL).

The procedures for stereotaxic surgery and microinjection were as previously described. After 7 days of habituation, adolescent mice (29 days old) were anesthetized (1.5%–1.8% isoflurane in 1 L/min air) with perioperative meloxicam analgesia (3 mg/kg, i.p.) and received viral microinjections into the bilateral mPFC (0.5 μL per side, 0.1 μL/min) through a glass micropipette. The injection coordinates (relative to bregma) were anterior + 1.8 mm, lateral ± 0.4 mm, and ventral − 1.8 mm. The micropipette was left in the site for a further 5 min. Mice were allowed to recover until the beginning of behavioral tests (day 84).

Fluorescent mRNA *In Situ* Hybridization

The mPFC mRNA expression was visualized using RNAscope (Advanced Cell Diagnostics). Following the manufacturer's guidelines, mouse brains were quickly dissected, dehydrated, and frozen. After cryoprotection, serial coronal sections through the mPFC (1.98 mm–1.54 mm from bregma) were cut at 15 μm on a cryostat (Leica). Slides at 180 μm intervals were dried at − 20 °C for 1 h and then stored at − 80 °C for up to one week. The slides were processed following the RNAscope protocol using a fluorescent multiplex reagent kit (ACD, catalog #323100) and probes for *Pvrl3* (Mm-Pvrl3-C1; ACD, catalog #300031), *Gad1* (Mm-Gad1-C2; ACD, catalog #400951), and *Slc17a7* (Mm-Slc17a7-C3; ACD, catalog #416631).

For co-localization analysis, images (1024 × 1024 pixel^2) were captured at 200× (optical section thickness, 5.4 μm) or 400× (optical section thickness, 2.64 μm) using a Nikon A1RHD25 laser-scanning confocal microscope (Tokyo, Japan). Images were then separated into multiple color channels and cell nuclei were identified in the DAPI channel. Signals in the red, green, and magenta channels were thresholded, identified, and filtered by the locations of nuclei. If a signal was found in a nucleus, the cell was defined as "positive" for the respective RNA species. Nuclei positive for *Gad1* or *Slc17a7* were finally filtered to determine whether they co-expressed nectin3.

Statistical Analyses

Data are presented as the mean ± standard error of the mean (SEM) in the figures. Independent samples *t*-tests were used for group comparisons. For body weight, fur state, and dendritic intersection, repeated measures analysis of variance was used, with time or distance as a within-subject factor and treatment as a between-subject factor, followed by the Bonferroni *post hoc* test when appropriate. The association between behavioral performance and fur state or CAM expression was quantified using Pearson's correlation. Differences with $P < 0.05$ were considered statistically significant.

Results

Adolescent Chronic Social Stress Impairs Social Memory and Spatial Working Memory

Adolescent chronic social stress had minimal influence on body weight (main effect of treatment: $F_{(1, 27)} = 0.177$, $P = 0.678$, Fig. S1A), but caused the fur state to deteriorate in the stressed group (Fig. 1C; main effect of treatment: $F_{(1, 28)} = 47.48$, $P < 0.0001$; treatment × time interaction: $F_{(13, 364)} = 7.576$, $P < 0.0001$), especially after the third week of stress exposure (all $t > 3.553$, Bonferroni-corrected all $P < 0.01$). Adolescent stress exposure also increased the anxiety-like behaviors in the open field ($t_{(28)} = 2.096$, $P = 0.045$, Figs. 1D and S1B). These results are consistent with previous findings using this paradigm [27].

Adolescent chronic stress did not significantly alter social approach and social preference. The stressed and control animals spent comparable times interacting with the stimulus mouse behind wire mesh in the social approach test ($t_{(28)} = 0.871$, $P = 0.391$; Figs. 1E and

S1C). Both groups exhibited clear social preference, as they spent significantly more time interacting with the real mouse than the fake one (CT: $t_{(15)} = 2.899$, $P = 0.011$; ST: $t_{(13)} = 2.580$, $P = 0.023$; Figs. 1F and S1D), and their preference indices were comparable ($t_{(28)} = 0.338$, $P = 0.738$).

In contrast, stressed animals exhibited impairments in the social memory test and spatial working memory assessed in the Y maze. In the social memory test (Fig. 1G), while control mice distinguished a novel from a familiar mouse ($t_{(15)} = 5.520$, $P < 0.001$), stressed mice failed to do so ($t_{(13)} = 1.558$, $P = 0.143$) and spent a significantly lower percentage of time interacting with a novel mouse compared with controls ($t_{(28)} = 2.633$, $P = 0.014$). The exploration time during the acquisition session was comparable in the two groups (Fig. S1E). In the Y-maze task, stressed animals had lower spontaneous alternation ratios than controls ($t_{(28)} = 2.389$, $P = 0.024$; Fig. 1H), despite the similar numbers of entries in the two groups (Fig. S1F).

Deterioration of fur state has been used as an indicator of stress experiences [34]. To determine whether behavioral alterations in the stressed group directly result from stress exposure, we correlated their fur state ratings with behavioral performances and found significant correlations in various behavioral measures (all $r > 0.532$, all $P < 0.05$, Fig. S2), confirming the association between stress adversity and behavioral changes.

Adolescent Chronic Social Stress Simplifies Apical Dendritic Structure and Decreases Spine Density of Pyramidal Neurons in Mouse mPFC

We examined the dendritic structure of pyramidal neurons in three mPFC subregions [cingulate (Cg), prelimbic (PrL), and infralimbic (IL) areas] using the Golgi-Cox staining method (Fig. 2A–C). Compared with controls, stressed mice showed reduced length and complexity of apical dendrites in each of these subregions (Cg: length: $t_{(8)} = 3.119$, $P = 0.014$; complexity: $F_{(1,\ 8)} = 5.772$, $P = 0.043$, Fig. 2D; PrL: length: $t_{(8)} = 5.845$, $P < 0.001$; complexity: $F_{(1,\ 8)} = 25.723$, $P = 0.001$, Fig. 2E; IL: length: $t_{(8)} = 7.828$, $P < 0.001$; complexity: $F_{(1,\ 8)} = 56.747$, $P < 0.001$, Fig. 2F). We further analyzed the superficial (II/III) and deep (V) layers of pyramidal neurons in each subregion and found a similar reduction in both layer types (Fig. S3).

The number of spines was also reduced by adolescent chronic stress. Spine loss was significant in stressed mice on both the main (all $t_{(8)} > 3.189$, all $P < 0.013$, Fig. 2G–I, left panel) and oblique apical dendrites (all $t_{(8)} > 3.055$, all $P < 0.016$, Fig. 2G–I, right panel) in all three subregions. The spine loss occurred in more than one spine type in each subregion (all $t_{(8)} > 2.337$, all $P < 0.048$). Examination of superficial and deep layers showed a general reduction in stressed animals, with various spine types affected (Fig. S4).

Together, these results demonstrated that adolescent chronic stress simplified apical dendritic structure and reduced spine density throughout the mPFC. We also counted the number of neurons positive for neuronal nuclei antigen ($NeuN^+$) in the three mPFC subregions (Fig. S5) and found comparable numbers in the stressed and control animals ($P > 0.449$), which indicated that the dendritic changes cannot be accounted for by neuronal loss.

Adolescent Chronic Social Stress Specifically Alters Nectin3 Membrane Expression in Mouse mPFC

In this experiment, we assessed whether and how adolescent chronic stress may influence the prefrontal expression of the synaptic CAMs nectin1, nectin3, N-cadherin, β-catenin, neuroligin1, and neuroligin2. At the total protein level (Fig. 3A), adolescent stress seemed to downregulate nectin1 and nectin3 expression, but the change did not reach statistical significance. At the membrane protein level (Fig. 3B), nectin3 was significantly reduced by adolescent chronic stress ($t_{(10)} = 3.327$, $P = 0.008$). The protein levels of the other CAMs were not affected at either the total or the membrane level (Fig. S6).

We then assessed the correlations between nectin3 membrane levels in the mPFC and behavioral performances. Nectin3 membrane expression did not correlate with anxiety-like behaviors, or performance in the social approach and preference tests (Fig. S7), but significantly correlated with the discrimination index in the social memory test (Fig. 3C) and with the Y-maze spontaneous alternation ratio (Fig. 3D), which indicates a possible association between nectin3 expression and stress-induced social and cognitive deficits.

Nectin3 Knockdown During Adolescence Reproduces Adolescent Stress-Induced Social and Working Memory Deficits, Dendritic Atrophy, and Spine Loss

To investigate how nectin3 downregulation may contribute to stress-induced behavioral and structural abnormalities, we examined the effects of adolescent nectin3 knockdown *via* AAV injection. We first confirmed that nectin3 mRNA (*Pvrl3*) is expressed in the mouse mPFC using the RNAscope technique (Figs. 4A and S8). The co-localization of *Pvrl3* with *Slc17a7* (the mRNA of vascular glutamate transporter 1, an excitatory neuron marker) and *Gad1* (the mRNA of GAD67, an inhibitory neuron marker) in the mPFC (Fig. 4B) revealed that the majority of $Pvrl3^+$ neurons co-localized with $Slc17a7^+$ neurons (1303 out of

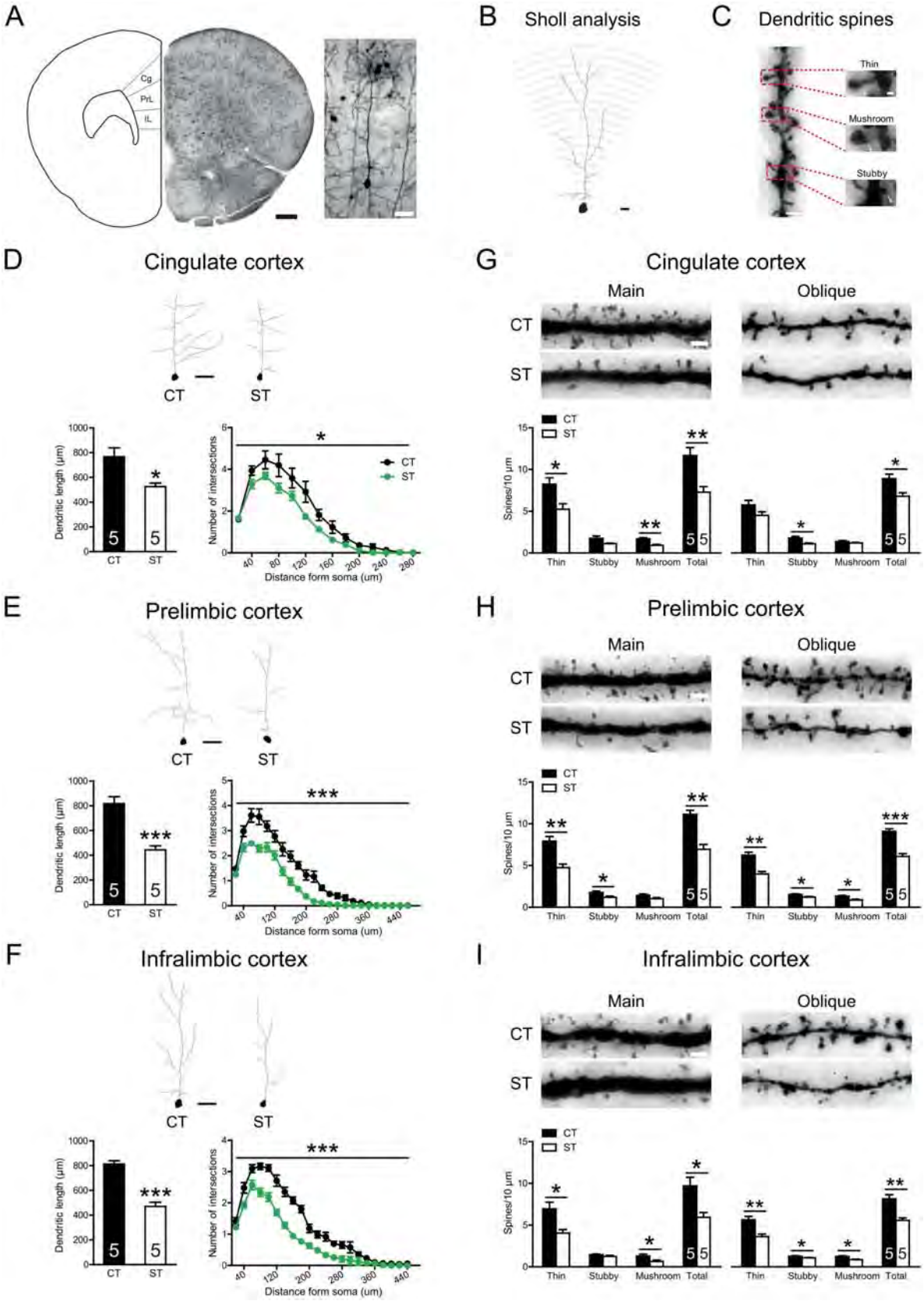
A
Cg
PrL
IL
B
Sholl analysis
C
Dendritic spines
Thin
Mushroom
Stubby
D
Cingulate cortex
CT
ST
Dendritic length (μm)
Number of intersections
Distance form soma (um)
E
Prelimbic cortex
F
Infralimbic cortex
G
Cingulate cortex
Main
Oblique
Spines/10 μm
Thin
Stubby
Mushroom
Total
H
Prelimbic cortex
I
Infralimbic cortex

◀**Fig. 2** Effects of adolescent chronic social instability stress on the dendritic architecture of the mouse medial prefrontal cortex (mPFC). **A** Diagrams of a coronal section (left) showing three regions of interest [dashed area; cingulate (Cg), prelimbic (PrL) and infralimbic (IL) cortex], a Golgi-stained coronal section (middle; scale bar, 500 μm), and a Golgi-impregnated mPFC pyramidal neuron from an adult mouse (right; scale bar, 50 μm). **B** Sholl analysis. Concentric circles (20 μm apart) are drawn on an apical dendrite. **C** Dendritic spines are categorized to three subtypes: thin (long, thin protrusions with a bulbous head), mushroom (protrusions with a small neck and a large head), and stubby (protrusions closely connected to the dendritic shaft and lacking a clear neck). **D–F** Adolescent stress reduces the length and complexity of apical dendrites of pyramidal neurons in cingulate (**D**), prelimbic (**E**), and infralimbic (**F**) cortex (scale bar, 50 μm). Six to eight neurons were analyzed for each layer in a given region per animal. **G–I** Adolescent stress reduces the spine density on apical main and oblique dendrites in cingulate (**G**), prelimbic (**H**), and infralimbic (**I**) cortex (scale bar, 5 μm). We analyzed 6–8 segments for each dendritic domain per animal. The total spine density was calculated as the sum of three spine types. CT, control; ST, stress. Numbers in each bar indicate the number of animals in each group. Data represent the mean ± SEM. $*P < 0.05$; $**P < 0.01$; $***P < 0.001$.

1536 *Pvrl3*$^+$ neurons, 84.83%, and out of 1391 *Slc17a7*$^+$ neurons, 93.67%). Some *Pvrl3*$^+$ neurons also co-localized with *Gad1*$^+$ neurons (172 out of 1536 *Pvrl3*$^+$ neurons, 11.20%, and out of 372 *Gad1*$^+$ neurons, 46.24%), indicating that nectin3 is expressed in both excitatory and inhibitory neurons in mouse mPFC.

Considering that stress-induced dendritic changes were evident throughout the mPFC, we injected AAV-shNectin3 into the mPFC (infection rate: 62.14%) to knock down nectin3 levels in adolescent mice (29 days old) without focusing on specific subregions and examined its impact at the same time point as in the stress experiment (day 84, Figs. 5A, B, and S9A). Compared with the controls, nectin3-KD mice showed significantly lower nectin3 immunoreactivity in the mPFC ($t_{(16)} = 3.341$, $P = 0.004$, Fig. 5C) and relatively unaltered nectin1 immunoreactivity levels (Fig. S9B). Western blot analyses further confirmed the reduction of nectin3, and not nectin1, expression levels (nectin3: $t_{(9)} = 3.338$, $P = 0.008$; nectin1: $t_{(9)} = 1.874$, $P = 0.090$; Fig. 5D).

The nectin3-KD and control mice exhibited comparable behaviors in the open field and social approach tests (all $P > 0.299$, Fig. S9C–D). Nevertheless, the nectin3-KD mice spent similar times interacting with the fake and real mice, which indicates impaired social preference (KD, $t_{(11)} = 0.014$, $P = 0.989$; CT, $t_{(11)} = 2.806$, $P = 0.017$, Figs. 5E and S9E). Nectin3-KD mice also failed to discriminate the novel from the familiar mouse in the social memory test ($t_{(16)} = 1.332$, $P = 0.210$, Fig. 5F), and their discrimination indices were significantly lower than those of controls ($t_{(22)} = 4.645$, $P < 0.001$), even though they showed a longer exploration time during the acquisition phase (Fig. S9F). In the Y-maze task, nectin3-KD mice had a significantly lower spontaneous alternation ratio than controls ($t_{(33)} = 2.145$, $P = 0.039$, Fig. 5G), despite similar numbers of entries in the two groups (Fig. S9G), suggesting an impairment in spatial working memory.

The morphological effects of prefrontal nectin3 knockdown during adolescence were largely consistent with the stress effects. Nectin3 knockdown decreased the length ($t_{(15)} = 12.885$, $P < 0.001$, Fig. 6A, middle panel) and complexity ($F_{(1,\ 15)} = 116.200$, $P < 0.001$, Fig. 6A, right panel) of the apical dendrites of mPFC pyramidal neurons, irrespective of the subregion (all $P < 0.001$, Fig. S10A–C) and layer (all $P < 0.001$, Fig. S10D–E). Nectin3 knockdown during adolescence also led to spine loss on the apical main and oblique dendrites in the mPFC (main: $t_{(15)} = 5.798$, $P < 0.001$; oblique: $t_{(15)} = 6.333$, $P < 0.001$; Fig. 6B). Detailed analyses showed that nectin3 knockdown specifically downregulated the number of thin spines (main: $t_{(15)} = 7.610$, $P < 0.001$; oblique: $t_{(15)} = 7.568$, $P < 0.001$), leaving stubby and mushroom spines relatively unaffected (all $t_{(15)} < 2.107$, all $P > 0.052$).

Discussion

In the present study, we investigated the involvement of CAMs in adolescent stress-induced alterations in mPFC-dependent behaviors and structural plasticity. We found that adolescent chronic social instability stress impaired social recognition and spatial working memory, and induced dendritic atrophy and spine loss in pyramidal neurons of the mPFC. Importantly, among the several CAMs tested, nectin3 may mediate these stress effects, as adolescent stress specifically downregulated nectin3 expression in the mPFC, which correlated with behavioral deficits. Furthermore, suppression of mPFC nectin3 levels during adolescence successfully reproduced the effects of stress. These results suggest that nectin3 plays an important role in adolescent chronic stress effects in the mouse PFC.

Our finding that adolescent social instability stress impaired social memory is consistent with previous work [28, 35]. This impairment cannot be explained by reduced sensitivity to social cues, as the stressed mice demonstrated clear social preference and social interactions similar to control mice. We also demonstrated for the first time that chronic social instability stress in adolescent mice impaired spatial working memory as measured by spontaneous alternation in the Y maze. Note that spontaneous alternation measures an animal's natural tendency to alternate choices on successive trials, which depends on several factors such as the anxiety level and spatial memory capacity and is mediated by many brain areas including the PFC [36]. Future studies are needed to validate the

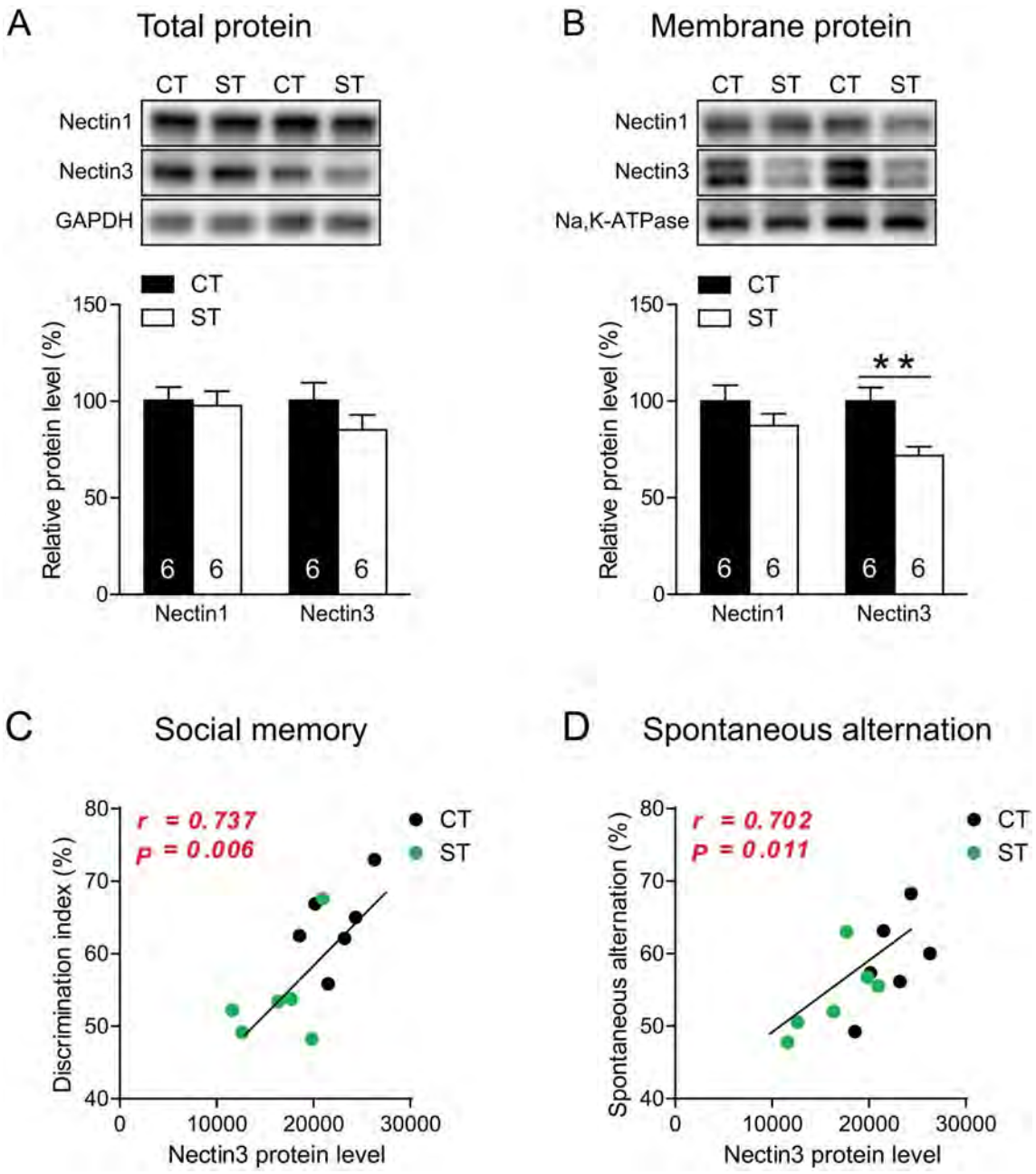

Fig. 3 Effects of adolescent chronic social instability stress on nectin1 and nectin3 expression in mouse medial prefrontal cortex (mPFC). **A** Adolescent stress does not change the total protein expression of nectin1 and nectin3. **B** Adolescent stress significantly reduces the membrane protein levels of nectin3, but not nectin1. **C**, **D** Nectin3 membrane protein levels are significantly correlated with the discrimination index in the social memory test (**C**) and with the spontaneous alternation ratio in the Y maze (**D**). CT, control; ST, stress. Numbers in each bar indicate the number of animals in each group. Data represent the mean ± SEM. $^*P < 0.05$.

deleterious effects of adolescent chronic stress on mPFC-mediated cognitive functions with other behavioral tasks such as temporal order memory and reversal learning tests. The behavioral deficits we found were significantly correlated with the deterioration in fur state resulting from stress exposure [27], which confirms the link between stressful experiences and behavioral deficits. We also found that social memory and spatial working memory were impaired following nectin3 knockdown in the adolescent mPFC. Together with social and attentional deficits following other types of adolescent chronic stressors [10], these results confirm that disrupting the adolescent brain has deleterious effects on the complex social and cognitive functions mediated by the mPFC.

Neuronal structural abnormalities may underlie synaptic plasticity changes and behavioral dysfunction [1, 37–39].

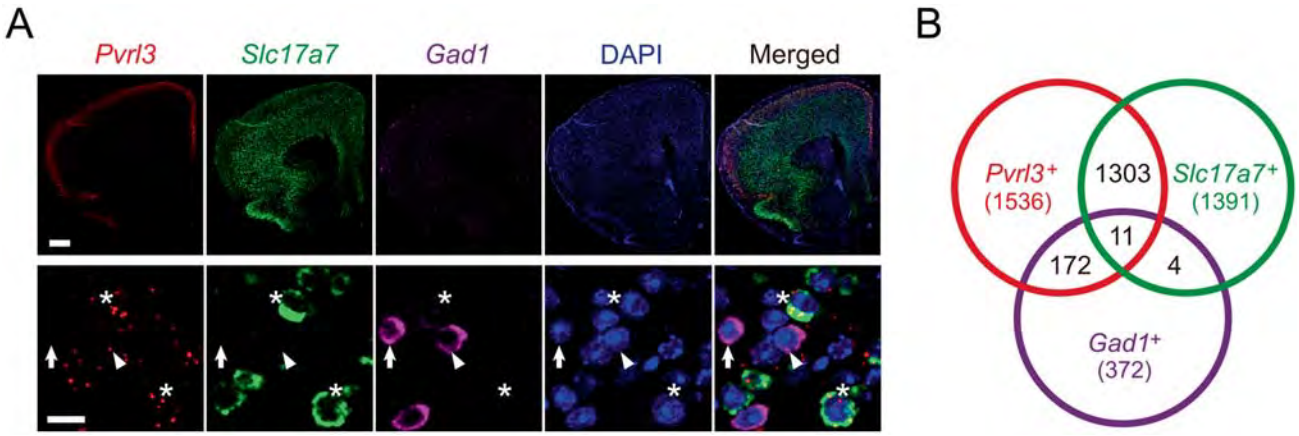

Fig. 4 Nectin3 expression in excitatory and inhibitory neurons in mouse medial prefrontal cortex. **A** Representative (upper, scale bar, 500 μm), and magnified (lower, scale bar, 20 μm) images showing the mRNA expression of *Pvrl3*, *Slc17a7,* and *Gad1* (stars, neurons that co-express *Pvrl3* and *Slc17a7*; arrowheads, neurons that co-express *Pvrl3* and *Gad1*; arrows, *Gad1*-expressing cells without detectable *Pvrl3* expression). **B** Numbers of neurons that co-express *Pvrl3* and *Slc17a7*, *Pvrl3* and *Gad1, Slc17a7* and *Gad1*, and *Pvrl3*, *Slc17a7*, and *Gad1*. Numbers in parentheses indicate the total number of neurons expressing the corresponding mRNA.

Previous studies have shown that the effects of adolescent chronic stress on prefrontal dendritic architecture vary with stressor type and other factors (for a review, see [8]). For instance, social isolation or chronic restraint stress leads to reductions in dendritic arborization [40], spine density [41], and apical dendritic length [42], whereas peer play deprivation by housing with adult females leads to increased dendritic length and complexity in the PFC [43, 44]. Here we showed that adolescent chronic instability stress simplifies the dendritic structure and reduces spine density in mouse mPFC. Given that peer play deprivation is often achieved by housing adolescent rodents with an adult female that is not socially threatening [43, 44], the results from studies adopting negative physical or social stressors (e.g., social instability in our study) are consistent in demonstrating that stressful life experiences during adolescence lead to a simplified dendritic structure of mPFC pyramidal neurons.

While the CAMs we examined have been found to be altered by postnatal or adult stress, only one study has focused on adolescent stress and the mPFC; it showed that a reduction in prefrontal neuroligin2 may mediate the attentional deficits induced by chronic exposure to fear-inducing stressors on postnatal days 28–42 [10]. Our findings point to the involvement of nectin3 in adolescent stress-induced alterations of social and spatial working memory and prefrontal dendritic architecture. Both studies highlight synaptic CAMs as potential targets of adolescent chronic stress in the rodent mPFC, but we did not find significant changes in neuroligin2 following long-term social instability stress. Given that several aspects of the stress paradigms differ between our study and the previous report (e.g., stress duration, stressor type, animal species), future studies are required to explicitly test whether and how the PFC responds to different stressors in different ways.

Nectin3 is a Ca^{2+}-independent immunoglobulin-like transmembrane protein that primarily anchors to the postsynaptic membrane at puncta adherentia junctions (PAJs)—the mechanical adhesion sites for neurotransmission [45]. Nectin3 forms heterophilic adhesions with presynaptic nectin1 and connects to the actin cytoskeleton *via* afadin, an actin filament-binding protein [46]. Nectin3 knockout has been shown to reduce the number of PAJs at mossy fiber–CA3 synapses and to change mossy fiber trajectories [47]. Our previous studies have linked hippocampal nectin3 to early-life stress-induced spine loss and cognitive deficits [16, 48]. As the first study to examine nectin3 in the PFC, we first confirmed that nectin3 is expressed in both excitatory and inhibitory neurons in mouse mPFC, similar to our findings in the hippocampus [30]. How nectin3 contributes to the stress effects on the neurodevelopment of the adolescent PFC is unknown. One possibility is that when nectin3 is downregulated by stress, the hetero-trans-dimers that it forms with nectin1 may be replaced by homo-trans-dimers, which have a lower affinity [49] and may result in weaker forms of PAJs and lead to the dying-back of dendrites due to the loss of a greater number of spines. Nectin3 may interact with other systems in the stress-induced effects on the structural development of the mPFC, such as the corticotropin-releasing hormone (CRH)-CRH receptor 1 signaling system [16, 50, 51], or other CAMs such as N-cadherins [52].

We also found some differences between adolescent stress and nectin3 knockdown. For example, nectin3 knockdown did not increase the anxiety-like behaviors as adolescent stress did. One explanation for these differences may be that the regions affected in nectin3 knockdown and

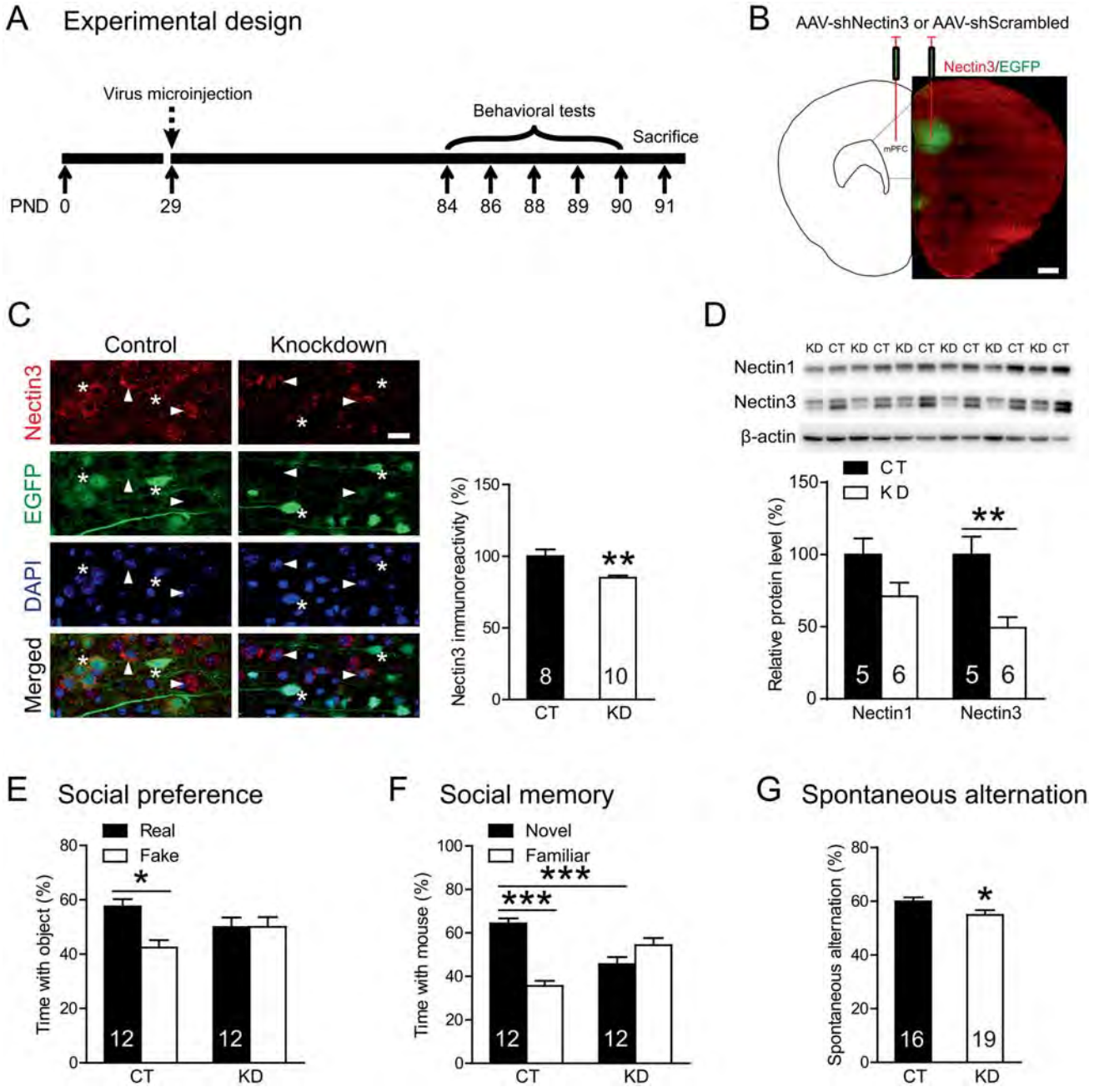

Fig. 5 Behavioral effects of adolescent nectin3 knockdown in the medial prefrontal cortex (mPFC) of adult mice. **A** The experimental timeline of the behavioral procedure and brain tissue acquisition after virus injection. **B** Left panel, schematic of AAV microinjection into the mPFC; right panel, an image showing region-specific expression of EGFP in the mPFC (scale bar, 500 μm). **C** Representative images showing the expression of nectin3, EGFP, and DAPI in the mPFC of control and nectin3-KD mice (scale bar, 20 μm). **D** Western blot analyses confirm the knockdown-induced reduction of nectin3, but not nectin1, expression in the mPFC. **E** In the social preference test, unlike control mice that spend significantly more time with the real than the fake mice, nectin3-KD mice spend similar time interacting with fake and real mice. **F** In the social memory test, compared with control mice that successfully distinguish the novel from the familiar mouse, nectin3-KD mice show impaired social memory. **G** In the Y-maze spontaneous alternation task, nectin3-KD mice show impaired spatial working memory. CT, control; KD, knockdown. Numbers in each bar indicate the number of animals in each group. Data represent the mean ± SEM. $^{*}P < 0.05$; $^{**}P < 0.01$; $^{***}P < 0.001$.

adolescent stress were different: while nectin3 knockdown was confined to the PFC, adolescent stress experiences may affect multiple stress-related regions such as the hippocampus [27], which may underlie the increased anxiety-like behaviors induced by chronic stress. As our study primarily focused on the mPFC, future studies are

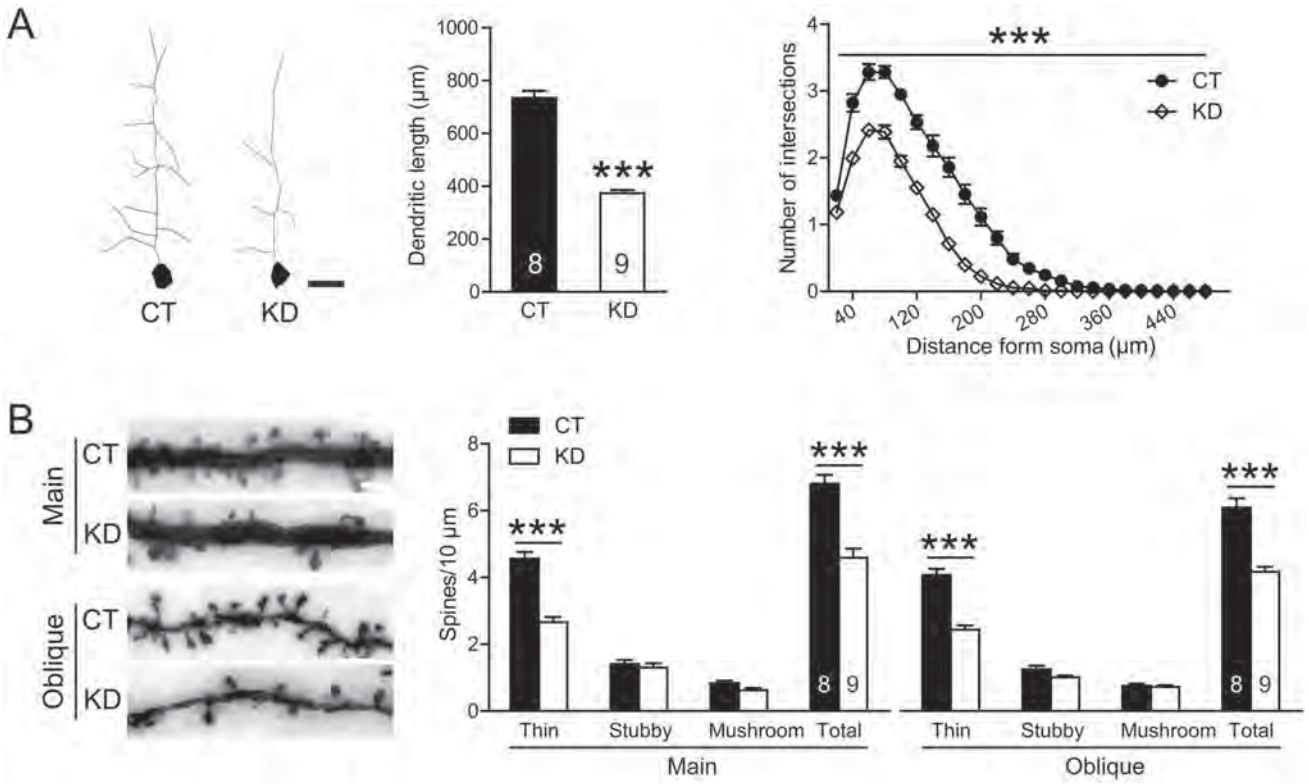

Fig. 6 Morphological effects of adolescent nectin3 knockdown in the medial prefrontal cortex (mPFC) of adult mice. **A** Adolescent nectin3 knockdown reduces the length and complexity of the apical dendrites of pyramidal neurons (scale bar, 50 μm). **B** In nectin3-KD mice, the spine density on apical main and oblique dendrites is significantly reduced (scale bar, 20 μm). Six to eight neurons or dendritic segments were analyzed in the deep and superficial layers of three mPFC subregions. Morphological measures were averaged across layers and subregions for individual mice and then compared between groups. CT, control; KD, knockdown. Numbers in each bar indicate the number of animals in each group. Data represent the mean ± SEM. ***$P < 0.001$.

warranted to investigate the effects of adolescent chronic stress on other stress-related regions and mPFC-related circuits [27, 53]. Structural plasticity was also altered differently by nectin3 knockdown and adolescent stress: while nectin3 knockdown caused a specific loss of thin spines, adolescent stress affected multiple spine types. The selective effects of nectin3 knockdown on thin spines have also been reported in the dentate gyrus [48], which may be related to spine-specific structural or functional properties (e.g., thin spines have smaller postsynaptic densities [54]).

In summary, our results support the hypothesis that nectin3 is a potential modulator of adolescent stress effects on the dendritic plasticity of mPFC pyramidal neurons and mPFC-dependent social recognition and spatial working memory. A better understanding of these pathophysiological mechanisms may promote the development of therapeutic targets for stress-related mental disorders.

Acknowledgements We thank Dr. Mathias V. Schmidt (Max Planck Institute of Psychiatry) for helpful discussions and suggestions, and Prof. Yi Rao (Peking University) for the use of the Neurolucida system. This work was supported by the National Natural Science Foundation of China (81401129, 81571321, 81630031, and 81571312), the Peking University Medicine Seed Fund for Interdisciplinary Research (BMU2017MX021), the National Key Basic Research Program of China (2015CB856401) and the Beijing Brain Project (Z171100000117016).

Conflict of interest The authors declare that they have no conflict of interest.

References

1. McEwen BS, Morrison JH. The brain on stress: vulnerability and plasticity of the prefrontal cortex over the life course. Neuron 2013, 79: 16–29.
2. Hoops D, Flores C. Making dopamine connections in adolescence. Trends Neurosci 2017, 40: 709–719.
3. Petanjek Z, Judas M, Simic G, Rasin MR, Uylings HB, Rakic P, *et al.* Extraordinary neoteny of synaptic spines in the human prefrontal cortex. Proc Natl Acad Sci U S A 2011, 108: 13281–13286.
4. Selemon LD. A role for synaptic plasticity in the adolescent development of executive function. Transl Psychiatry 2013, 3: e238.
5. Caballero A, Flores-Barrera E, Cass DK, Tseng KY. Differential regulation of parvalbumin and calretinin interneurons in the prefrontal cortex during adolescence. Brain Struct Funct 2014, 219: 395–406.
6. O'Donnell P. Adolescent onset of cortical disinhibition in schizophrenia: insights from animal models. Schizophr Bull 2011, 37: 484–492.
7. Spear LP. The adolescent brain and age-related behavioral manifestations. Neurosci Biobehav Rev 2000, 24: 417–463.
8. Watt MJ, Weber MA, Davies SR, Forster GL. Impact of juvenile chronic stress on adult cortico-accumbal function: Implications for cognition and addiction. Prog Neuropsychopharmacol Biol Psychiatry 2017, 79: 136–154.
9. Burke AR, McCormick CM, Pellis SM, Lukkes JL. Impact of adolescent social experiences on behavior and neural circuits implicated in mental illnesses. Neurosci Biobehav Rev 2017, 76: 280–300.
10. Tzanoulinou S, Garcia-Mompo C, Riccio O, Grosse J, Zanoletti O, Dedousis P, *et al.* Neuroligin-2 expression in the prefrontal cortex is involved in attention deficits induced by peripubertal stress. Neuropsychopharmacology 2016, 41: 751–761.
11. Shapiro L, Love J, Colman DR. Adhesion molecules in the nervous system: structural insights into function and diversity. Annu Rev Neurosci 2007, 30: 451–474.
12. Takai Y, Miyoshi J, Ikeda W, Ogita H. Nectins and nectin-like molecules: roles in contact inhibition of cell movement and proliferation. Nat Rev Mol Cell Biol 2008, 9: 603–615.
13. Dalva MB, McClelland AC, Kayser MS. Cell adhesion molecules: signalling functions at the synapse. Nat Rev Neurosci 2007, 8: 206–220.
14. Sudhof TC. Neuroligins and neurexins link synaptic function to cognitive disease. Nature 2008, 455: 903–911.
15. Xia QQ, Xu J, Liao TL, Yu J, Shi L, Xia J, *et al.* Neuroligins differentially mediate subtype-specific synapse formation in pyramidal neurons and interneurons. Neurosci Bull 2019, 35: 497–506.
16. Wang XD, Su YA, Wagner KV, Avrabos C, Scharf SH, Hartmann J, *et al.* Nectin-3 links CRHR1 signaling to stress-induced memory deficits and spine loss. Nat Neurosci 2013, 16: 706–713.
17. Liao XM, Yang XD, Jia J, Li JT, Xie XM, Su YA, *et al.* Blockade of corticotropin-releasing hormone receptor 1 attenuates early-life stress-induced synaptic abnormalities in the neonatal hippocampus. Hippocampus 2014, 24: 528–540.
18. van der Kooij MA, Grosse J, Zanoletti O, Papilloud A, Sandi C. The effects of stress during early postnatal periods on behavior and hippocampal neuroplasticity markers in adult male mice. Neuroscience 2015, 311: 508–518.
19. Gong Q, Su YA, Wu C, Si TM, Deussing JM, Schmidt MV, *et al.* Chronic stress reduces nectin-1 mrna levels and disrupts dendritic spine plasticity in the adult mouse perirhinal cortex. Front Cell Neurosci 2018, 12: 67.
20. Kohl C, Wang XD, Grosse J, Fournier C, Harbich D, Westerholz S, *et al.* Hippocampal neuroligin-2 links early-life stress with impaired social recognition and increased aggression in adult mice. Psychoneuroendocrinology 2015, 55: 128–143.
21. Chen YC, Tan QR, Dang W, Wang HN, Zhang RB, Li ZY, *et al.* The effect of citalopram on chronic stress-induced depressive-like behavior in rats through GSK3beta/beta-catenin activation in the medial prefrontal cortex. Brain Res Bull 2012, 88: 338–344.
22. de Azeredo LA, Wearick-Silva LE, Viola TW, Tractenberg SG, Centeno-Silva A, Orso R, *et al.* Maternal separation induces hippocampal changes in cadherin-1 (CDH-1) mRNA and recognition memory impairment in adolescent mice. Neurobiol Learn Mem 2017, 141: 157–167.
23. Sachs BD, Tran HL, Folse E, Caron MG. Brain-region-specific molecular responses to maternal separation and social defeat stress in mice. Neuroscience 2018, 373: 122–136.
24. Castaneda P, Munoz M, Garcia-Rojo G, Ulloa JL, Bravo JA, Marquez R, *et al.* Association of N-cadherin levels and downstream effectors of Rho GTPases with dendritic spine loss induced by chronic stress in rat hippocampal neurons. J Neurosci Res 2015, 93: 1476–1491.
25. van der Kooij MA, Fantin M, Rejmak E, Grosse J, Zanoletti O, Fournier C, *et al.* Role for MMP-9 in stress-induced downregulation of nectin-3 in hippocampal CA1 and associated behavioural alterations. Nat Commun 2014, 5: 4995.
26. Sandi C. Stress, cognitive impairment and cell adhesion molecules. Nat Rev Neurosci 2004, 5: 917–930.
27. Schmidt MV, Sterlemann V, Ganea K, Liebl C, Alam S, Harbich D, *et al.* Persistent neuroendocrine and behavioral effects of a novel, etiologically relevant mouse paradigm for chronic social stress during adolescence. Psychoneuroendocrinology 2007, 32: 417–429.
28. Saavedra-Rodriguez L, Feig LA. Chronic social instability induces anxiety and defective social interactions across generations. Biol Psychiatry 2013, 73: 44–53.
29. Mineur YS, Prasol DJ, Belzung C, Crusio WE. Agonistic behavior and unpredictable chronic mild stress in mice. Behav Genet 2003, 33: 513–519.
30. Li JT, Xie XM, Yu JY, Sun YX, Liao XM, Wang XX, *et al.* Suppressed Calbindin levels in hippocampal excitatory neurons mediate stress-induced memory loss. Cell Rep 2017, 21: 891–900.
31. Moy SS, Nadler JJ, Perez A, Barbaro RP, Johns JM, Magnuson TR, *et al.* Sociability and preference for social novelty in five inbred strains: an approach to assess autistic-like behavior in mice. Genes Brain Behav 2004, 3: 287–302.
32. Yang XD, Liao XM, Uribe-Marino A, Liu R, Xie XM, Jia J, *et al.* Stress during a critical postnatal period induces region-specific structural abnormalities and dysfunction of the prefrontal cortex via CRF1. Neuropsychopharmacology 2015, 40: 1203–1215.
33. Harris KM, Jensen FE, Tsao B. Three-dimensional structure of dendritic spines and synapses in rat hippocampus (CA1) at postnatal day 15 and adult ages: implications for the maturation of synaptic physiology and long-term potentiation. J Neurosci 1992, 12: 2685–2705.
34. Ducottet C, Belzung C. Behaviour in the elevated plus-maze predicts coping after subchronic mild stress in mice. Physiol Behav 2004, 81: 417–426.
35. Hodges TE, Baumbach JL, Marcolin ML, Bredewold R, Veenema AH, McCormick CM. Social instability stress in adolescent male rats reduces social interaction and social recognition performance and increases oxytocin receptor binding. Neuroscience 2017, 359: 172–182.

36. Lalonde R. The neurobiological basis of spontaneous alternation. Neurosci Biobehav Rev 2002, 26: 91–104.
37. Christoffel DJ, Golden SA, Russo SJ. Structural and synaptic plasticity in stress-related disorders. Rev Neurosci 2011, 22: 535–549.
38. Arnsten AF. Stress signalling pathways that impair prefrontal cortex structure and function. Nat Rev Neurosci 2009, 10: 410–422.
39. Forrest MP, Parnell E, Penzes P. Dendritic structural plasticity and neuropsychiatric disease. Nat Rev Neurosci 2018, 19: 215–234.
40. Pascual R, Zamora-Leon SP, Valero-Cabre A. Effects of postweaning social isolation and re-socialization on the expression of vasoactive intestinal peptide (VIP) and dendritic development in the medial prefrontal cortex of the rat. Acta Neurobiol Exp (Wars) 2006, 66: 7–14.
41. Silva-Gomez AB, Rojas D, Juarez I, Flores G. Decreased dendritic spine density on prefrontal cortical and hippocampal pyramidal neurons in postweaning social isolation rats. Brain Res 2003, 983: 128–136.
42. Eiland L, Ramroop J, Hill MN, Manley J, McEwen BS. Chronic juvenile stress produces corticolimbic dendritic architectural remodeling and modulates emotional behavior in male and female rats. Psychoneuroendocrinology 2012, 37: 39–47.
43. Burleson CA, Pedersen RW, Seddighi S, DeBusk LE, Burghardt GM, Cooper MA. Social play in juvenile hamsters alters dendritic morphology in the medial prefrontal cortex and attenuates effects of social stress in adulthood. Behav Neurosci 2016, 130: 437–447.
44. Bell HC, Pellis SM, Kolb B. Juvenile peer play experience and the development of the orbitofrontal and medial prefrontal cortices. Behav Brain Res 2010, 207: 7–13.
45. Mizoguchi A, Nakanishi H, Kimura K, Matsubara K, Ozaki-Kuroda K, Katata T, *et al.* Nectin: an adhesion molecule involved in formation of synapses. J Cell Biol 2002, 156: 555–565.
46. Takai Y, Nakanishi H. Nectin and afadin: novel organizers of intercellular junctions. J Cell Sci 2003, 116: 17–27.
47. Honda T, Sakisaka T, Yamada T, Kumazawa N, Hoshino T, Kajita M, *et al.* Involvement of nectins in the formation of puncta adherentia junctions and the mossy fiber trajectory in the mouse hippocampus. Mol Cell Neurosci 2006, 31: 315–325.
48. Wang XX, Li JT, Xie XM, Gu Y, Si TM, Schmidt MV, *et al.* Nectin-3 modulates the structural plasticity of dentate granule cells and long-term memory. Transl Psychiatry 2017, 7: e1228.
49. Satoh–Horikawa K, Nakanishi H, Takahashi K, Miyahara M, Nishimura M, Tachibana K, *et al.* Nectin-3, a new member of immunoglobulin-like cell adhesion molecules that shows homophilic and heterophilic cell-cell adhesion activities. J Biol Chem 2000, 275: 10291–10299.
50. Wang XD, Chen Y, Wolf M, Wagner KV, Liebl C, Scharf SH, *et al.* Forebrain CRHR1 deficiency attenuates chronic stress-induced cognitive deficits and dendritic remodeling. Neurobiol Dis 2011, 42: 300–310.
51. Uribe-Marino A, Gassen NC, Wiesbeck MF, Balsevich G, Santarelli S, Solfrank B, *et al.* Prefrontal cortex corticotropin-releasing factor receptor 1 conveys acute stress-induced executive dysfunction. Biol Psychiatry 2016, 80: 743–753.
52. Togashi H, Miyoshi J, Honda T, Sakisaka T, Takai Y, Takeichi M. Interneurite affinity is regulated by heterophilic nectin interactions in concert with the cadherin machinery. J Cell Biol 2006, 174: 141–151.
53. Qi X, Du ZJ, Zhu L, Liu X, Xu H, Zhou Z, *et al.* The glutamatergic postrhinal cortex-ventrolateral orbitofrontal cortex pathway regulates spatial memory retrieval. Neurosci Bull 2019, 35: 447–460.
54. Bourne J, Harris KM. Do thin spines learn to be mushroom spines that remember? Curr Opin Neurobiol 2007, 17: 381–386.

Neurosci. Bull. August, 2020, 36(8):875–894
https://doi.org/10.1007/s12264-020-00513-7

www.neurosci.cn
www.springer.com/12264

ORIGINAL ARTICLE

Blockade of HCN2 Channels Provides Neuroprotection Against Ischemic Injury *via* Accelerating Autophagic Degradation in Hippocampal Neurons

Cheng Chen[1] · Li Liu[3] · Ya-Qiao Shu[1] · Ping Jing[2] · Yun Lu[4] · Xiao-Xue Zhang[5] · Xian-Gang Zong[7] · Lian-Jun Guo[1,6] · Chang-Jun Li[2]

Received: 18 August 2019 / Accepted: 16 February 2020 / Published online: 10 June 2020

Abstract In the central nervous system, hyperpolarization-activated cyclic nucleotide-gated (HCN) channels are essential to maintain normal neuronal function. Recent studies have shown that HCN channels may be involved in the pathological process of ischemic brain injury, but the mechanisms remain unclear. Autophagy is activated in cerebral ischemia, but its role in cell death/survival remains controversial. In this study, our results showed that the HCN channel blocker ZD7288 remarkably decreased the percentage of apoptotic neurons and corrected the excessive autophagy induced by oxygen-glucose deprivation followed by reperfusion (OGD/R) in hippocampal HT22 neurons. Furthermore, in the OGD/R group, p-mTOR, p-ULK1 (Ser^{757}), and p62 were significantly decreased, while p-ULK1 (Ser^{317}), atg5, and beclin1 were remarkably increased. ZD7288 did not change the expression of p-ULK1 (Ser^{757}), ULK1 (Ser^{317}), p62, Beclin1, and atg5, which are involved in regulating autophagosome formation. Besides, we found that OGD/R induced a significant increase in Cathepsin D expression, but not LAMP-1. Treatment with ZD7288 at 10 μmol/L in the OGD/R group did not change the expression of cathepsin D and LAMP-1. However, chloroquine (CQ), which decreases autophagosome-lysosome fusion, eliminated the correction of excessive autophagy and neuroprotection by ZD7288. Besides, shRNA knockdown of HCN2 channels significantly reduced the accumulation of LC3-II and increased neuron survival in the OGD/R and transient global cerebral ischemia (TGCI) models, and CQ also eliminated the effects of HCN2-shRNA. Furthermore, we found that the percentage of LC3-positive puncta that co-localized with LAMP-1-positive lysosomes decreased in Con-shRNA-transfected HT22 neurons exposed to OGD/R or CQ. In HCN2-shRNA-transfected HT22 neurons, the percentage of LC3-positive puncta that co-localized with LAMP-1-positive lysosomes increased under OGD/R; however, the percentage was significantly decreased by the addition of CQ to HCN2-shRNA-transfected HT22 neurons. The present results demonstrated that blockade of HCN2 channels provides neuroprotection against OGD/R and TGCI by accelerating autophagic degradation attributable to the promotion of autophagosome and lysosome fusion.

Cheng Chen and Li Liu have contributed equally to this work.

✉ Lian-Jun Guo
gljyl1518@126.com

✉ Chang-Jun Li
hydlcj@163.com

1 Department of Pharmacology, School of Basic Medical Sciences, Tongji Medical College, Huazhong University of Science and Technology, Wuhan 430030, China

2 Department of Neurology, The Central Hospital of Wuhan, Tongji Medical College, Huazhong University of Science and Technology, Wuhan 430030, China

3 Office of Academic Research, The Central Hospital of Wuhan, Tongji Medical College, Huazhong University of Science and Technology, Wuhan 430030, China

4 Department of Pharmacy, Zhongnan Hospital of Wuhan University, Wuhan 430030, China

5 Department of Clinical Laboratory, Wuhan PuAi Hospital, Wuhan 430033, China

6 Key Laboratory of Drug Target Research and Pharmacodynamic Evaluation, Wuhan 430030, China

7 Center for Integrated Protein Science and Zentrum für Pharmaforschung, Department Pharmazie, Ludwig-Maximilians-Universität München, 80539 Munich, Germany

Keywords HCN2 channel · Autophagy · Neuroprotection · Oxygen-glucose deprivation/reperfusion · Transient global cerebral ischemia

Introduction

Stroke is a common cerebrovascular disease accompanied by high mortality and morbidity, imposing enormous social and economic burdens [1]. According to an epidemiological survey, cerebral ischemia accounts for approximately 87% of strokes [2]. Restoring blood flow to the affected area as early as possible is considered to be the most effective treatment of cerebral ischemia [3, 4]. However, restoration of the blood supply further aggravates ischemia-induced brain damage, which is termed ischemia/reperfusion (I/R) injury [5]. The pathophysiological mechanisms of cerebral I/R injury are not fully clarified yet, and more effective therapeutic strategies for cerebral ischemia still need to be explored.

Autophagy is a crucial lysosomal process for the degradation of damaged or unnecessary intracellular organelles, proteins, and other cell components to maintain homeostasis, and is involved in various basic physiological processes such as quality control of proteins and organelles, immunity, development, and differentiation [6]. Appropriate autophagic activity is necessary for the maintenance of normal intracellular homeostasis [7] and survival under certain environmental stress conditions [8]. However, excessive autophagy induced by various stressors may contribute to cell death [9, 10]. Increasing evidence has indicated that, although autophagy is activated in cerebral ischemia, its role in cell death or survival remains controversial [11]. Some studies have reported that autophagy protects against the neuronal injury induced by cerebral ischemia [12, 13]. Conversely, other studies have shown that the inhibition of autophagy protects against cerebral ischemia injury [14–17]. Thus, the role of autophagy in cerebral ischemia injury needs further investigation.

Hyperpolarization-activated cyclic nucleotide-gated (HCN) channels are encoded by a family of HCN1-4 genes and have four isoforms. HCN1 and HCN2 are abundantly expressed in the rodent hippocampus [18], but HCN3 and HCN4 are expressed at very low levels [19]. HCN channels are activated when the cell membrane is hyperpolarized and permeate K^+ and Na^+ ions to generate the inward I_h current in the nervous system [19]. I_h plays important roles in the stability of neuronal resting membrane potential [20], neuronal rhythmicity [19, 21], the periodicity of network oscillations [22], dendritic integration [23, 24], synaptic plasticity [25, 26], and neurotransmitter release [27, 28]. In general, I_h currents are activated at potentials negative to -50 mV to -60 mV [19]. In CA1 pyramidal cells, the mean resting membrane potential is -64 ± 2 mV, and oxygen–glucose deprivation (OGD) produces an initial hyperpolarization that ranges from 5 mV to 20 mV within 5 min after exposure [29], when I_h channels are activated. In a previous study, we have shown that the surface expression of HCN1 and HCN2 is dysregulated in the rat hippocampal CA1 area under chronic cerebral hypoperfusion [30]. Pavel Honsa *et al*. have reported that the expression of HCN channels is increased in reactive astrocytes following focal cerebral ischemia [31]. However, the biological effects of changes in HCN channel activation and expression during cerebral ischemia and possible mechanisms have yet to be revealed.

In this study, we investigated the regulation of autophagy by HCN channels and its effect on the neuronal ischemic injury induced by OGD followed by reperfusion (OGD/R) and transient global cerebral ischemia (TGCI).

Materials and Methods

Chemicals

Chloroquine (CQ) was from Sigma (St. Louis, MO); ZD7288 was from Tocris Cookson (Bristol, UK); and Dulbecco's modified Eagle's medium (DMEM) was from Gibco Invitrogen (Grand Island, NY). ZD7288 and CQ were prepared as stock solutions in sterile water and stored at -20 °C away from light. Subsequent solutions of specific concentrations (ZD7288: 1 μmol/L, 5 μmol/L, 10 μmol/L, and 20 μmol/L; CQ: 50 μmol/L) were made in culture medium or sterile water.

Cell Culture and OGD/R

The mouse HT22 hippocampal neuronal cell line was from Jennio Biotech Co., Ltd (Guangzhou, China). HT22 neurons were cultured in DMEM supplemented with 10% (*v*/*v*) fetal bovine serum, 100 U/mL penicillin, and 100 μg/mL streptomycin in a humidified incubator under 5% (*v*/*v*) CO_2 at 37 °C.

The method of OGD induction was described in detail in our previous publication [32], and its duration was 2 h, 4 h, 6 h, 8 h, or 12 h. At the end of these periods, cultures were returned to oxygenated, glucose-containing DMEM under normoxic conditions for 12 h (reperfusion). ZD7288 or CQ was added to the medium 2 h prior to OGD and left until the end of reperfusion.

Lentiviral Transduction

Small-hairpin (sh)RNA nucleotide (CGTGGTTTCGGATACTTTCTTCCTCA) against the *HCN2* gene (NM_053684) and a control sequence (TTCTCCGAACGTGTCACGT) were selected in accordance with previous publications [33–35]. The lentivirus-mediated shRNA for silencing HCN2 subunits (HCN2-shRNA) containing green fluorescence protein (GFP) and a non-targeting sequence as the negative control shRNA (Con-shRNA) were constructed by Genechem Corp., Ltd. (Shanghai, China). HCN2 expression in HT22 neurons was knocked down by lentivirus-mediated shRNA according to the manufacturer's instructions. For lentivirus transduction, HT22 neurons at $\sim$ 80% confluence were infected with lentivirus-bearing specific shRNAs in growth medium containing 8 μg/mL polybrene for 24 h, and then the infected neurons were subcultured for 48 h in growth medium. The transfection efficiency was further quantified by flow cytometric analysis. HCN2 immunofluorescence intensity and protein levels in HT22 neurons were measured 48 h after transduction.

Stereotaxic injection was performed as we described previously [36] under anesthesia with pentobarbital sodium (40 mg/kg, intraperitoneal injection, i.p.). Three weeks after shRNA infusion, we randomly selected half of the HCN2-shRNA-infected rats to determine the injection site and infection efficiency, and then carried out further studies as described below.

Cell Viability Assay [37]

HT22 neurons were seeded into 96-well plates. 10 μL CCK8 (Dojindo, Kumamoto, Japan) detection solution was added to each well and incubated at 37 °C for 1 h. The optical density values were recorded at 450 nm with an ELISA reader (Tecan, Männedorf, Switzerland) and then the survival rate in each group was calculated.

Flow Cytometric Analysis

HT22 neurons from each group were rinsed twice with phosphate-buffered saline (PBS), then re-suspended in 100 μL PBS (pH 7.4). The relative percentages of apoptotic and necrotic cells were calculated by fluorescence-activated cell sorting (FACS) analysis using Annexin V-PE/7-AAD or Annexin V-FITC/PI double staining. The final rate of apoptosis was measured on a BD FACSCantoII flow cytometer with BD FACSDiva software (BD Biosciences, San Jose, CA). These experiments were carried out following the manufacturer's instructions.

Establishment of the Transient Global Cerebral Ischemic Model

Adult male Sprague–Dawley rats of clean grade (approval number SCXK(E)2015-0018, No. 42000600032127), aged 2–3 months (weighing 220–250 g), were purchased from Hubei Provincial Laboratory Animal Public Service Center. The rats were given adaptive feeding (with a standard laboratory diet and water) for one week before experiments [30]. All experiments were approved by the Review Committee for the Care and Use of Laboratory Animals of Tongji Medical College, Huazhong University of Science and Technology. All efforts were made to minimize both the suffering and number of animals used. TGCI was induced *via* the 2-vessel occlusion model as described by Sun *et al*. [38]. Briefly, under anesthesia (pentobarbital sodium, 40 mg/kg, i.p.), blood was collected in a warmed heparinized syringe from the external jugular vein (2.5 mL/100 g), and then the bilateral common carotid arteries were temporarily occluded with small arterial clamps. After 20 min, the clamps were released and the extracted blood was slowly reinfused. Sham-operated animals received the same surgical procedures without blood extraction and occlusion. CQ was dissolved in sterile water and injected intracerebroventricularly (12.5 mg/kg) 2 h before TGCI through a 26-G needle at the following stereotaxic coordinates: 0.8 mm posterior to bregma, 1.5 mm lateral to the midline, and 3.6 mm ventral to the skull surface. Sterile saline was administered for vehicle control.

Water Maze Task

Three days after TGCI injury, we began Morris water maze training as described previously [30, 36], and recorded swim speed, latency to escape onto the hidden platform, proportion of time spent in the target quadrant, and amount of time spent in the quadrant of the former platform position with a video camera linked to a computer-based image analyzer (Morris water-maze tracking system MT-200; Chengdu Technology and Market Co., Ltd, Chengdu, China).

Western Blot Analysis

Total protein was extracted from cultured HT22 neurons and hippocampal CA1 tissue using RIPA lysis buffer (P0013B, Beyotime) as described in our reports [30, 39]. Protein concentration was determined using a BCA Protein Assay Kit (Pierce). For gel electrophoresis, total extracted protein from each sample (80 μg) was separated on 10% or 15% sodium dodecyl sulfate polyacrylamide gels and then transferred to polyvinylidene fluoride membranes

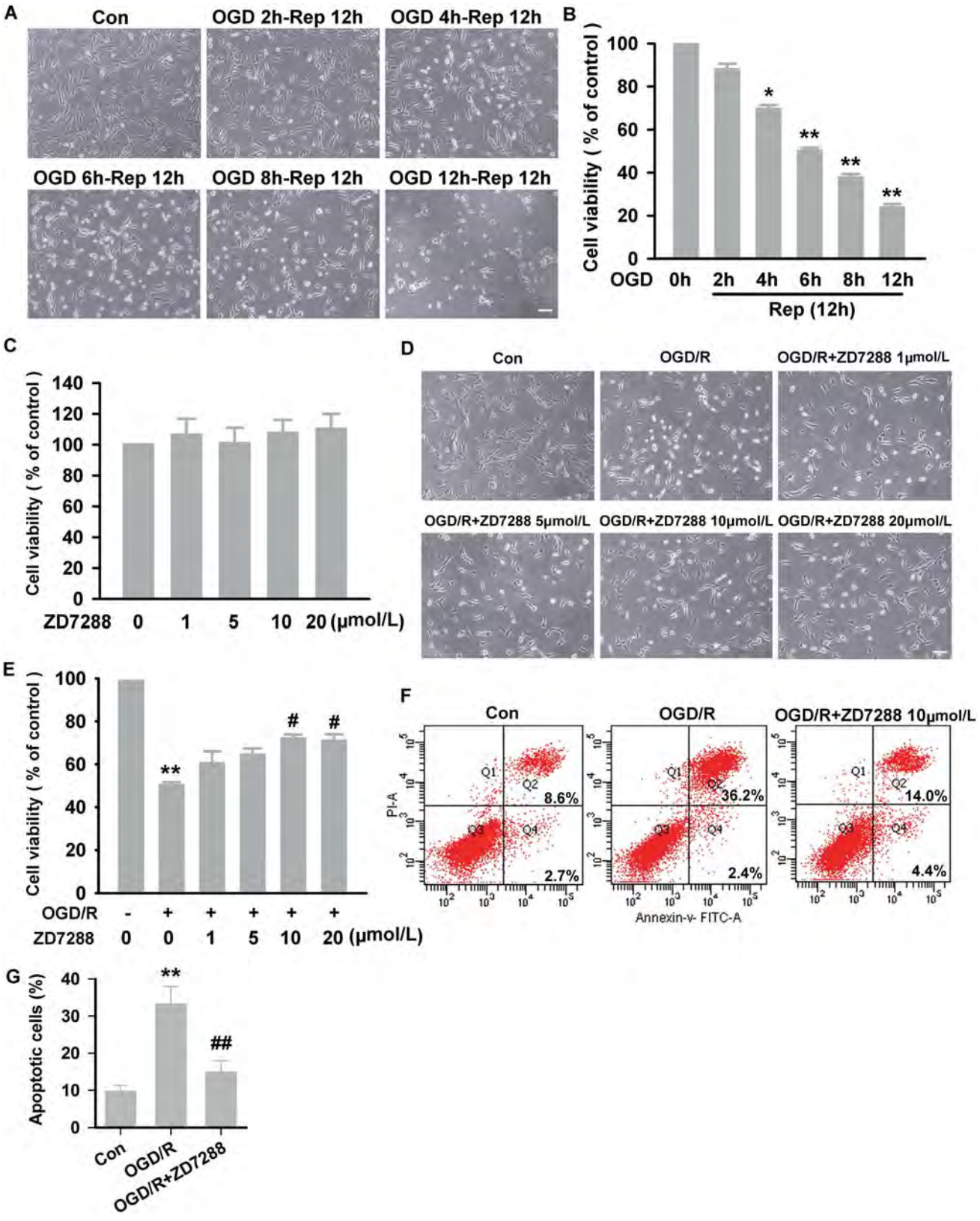
A
Con
OGD 2h-Rep 12h
OGD 4h-Rep 12h
OGD 6h-Rep 12h
OGD 8h-Rep 12h
OGD 12h-Rep 12h
B
Cell viability (% of control)
OGD 0h 2h 4h 6h 8h 12h
Rep (12h)
C
Cell viability (% of control)
ZD7288 0 1 5 10 20 (μmol/L)
D
Con
OGD/R
OGD/R+ZD7288 1μmol/L
OGD/R+ZD7288 5μmol/L
OGD/R+ZD7288 10μmol/L
OGD/R+ZD7288 20μmol/L
E
Cell viability (% of control)
OGD/R
ZD7288 0 0 1 5 10 20 (μmol/L)
F
Con
OGD/R
OGD/R+ZD7288 10μmol/L
PI-A
Annexin-v- FITC-A
8.6%
36.2%
14.0%
2.7%
2.4%
4.4%
G
Apoptotic cells (%)
Con
OGD/R
OGD/R+ZD7288

◀**Fig. 1** Neuroprotection against OGD/R injury by ZD7288. **A** Representative light microscopic live-cell images of HT22 neurons exposed to OGD insults of different durations (2 h, 4 h, 6 h, 8 h, or 12 h) followed by a further 12 h of reperfusion (× 200, scale bar, 200 μm). **B** Cell viability after OGD insults of the different durations followed by reperfusion (CCK8 assay). **C** ZD7288 at all concentrations used (1 μmol/L, 5 μmol/L, 10 μmol/L, and 20 μmol/L) did not affect the viability of normoxic neurons. **D** Representative light microscopy of HT22 neurons pretreated with ZD7288 at the different concentrations. **E** Effect of different concentrations of ZD7288 on HT22 neuronal viability after OGD/R (using CCK8). **F** Representative dot plots of flow cytometric analysis of cell death in HT22 neurons. **G** Quantitative analysis of the apoptotic rates by flow cytometry. Experiments were performed at least three times with similar results. $^{*}P < 0.05$ and $^{**}P < 0.01$ *versus* control group; $^{\#}P < 0.05$ and $^{\#\#}P < 0.01$ *versus* OGD/R group.

(Millipore, Billerica, MA, USA), followed by blocking with 5% non-fat milk for 2 h at room temperature. Subsequently, the membranes were incubated with the primary antibodies anti-LC3 (1:1000, PM036, MBL), anti-mTOR (1:1000, 2983, Cell Signaling Technology), anti-phospho-mTOR (Ser^{2448}) (1: 1000, 5536, Cell Signaling Technology), anti-ULK1 (1:1000, 8054, Cell Signaling Technology), anti-phospho-ULK1 (Ser^{317}) (1:1000, 6887, Cell Signaling Technology), anti-phospho-ULK1 (Ser^{757}) (1:1000, 6888, Cell Signaling Technology), anti-atg5 (1:500, NB110-53818, Novus), anti-p62 (1:1000, ab56416, Abcam), anti-beclin1 (1:1000, NB500-249, Novus), anti-HCN1 (1:800, NBP1-20250, Novus), anti-HCN2 (1:200, APC-030, Alomone Labs), anti-LAMP-1 (1:500, SC-20011, Santa Cruz Biotechnology), anti-cathepsin D (1:500, SC-377124, Santa Cruz Biotechnology), anti-neuronal nuclear antigen (NeuN) (1:2000, MAB377, Millipore), anti-GAPDH (1:5000, cw0100, Cwbiotech), or anti-alpha tubulin (1:5000, ab125267, Abcam). The antigen-antibody complexes were visualized with goat anti-rabbit or goat anti-mouse horseradish peroxidase (HRP)-conjugated secondary antibodies (1:5000; Proteintech Group Inc., China) by using Immobilon Western chemiluminescent HRP substrate (WBKLS0500, Millipore). The optical density of bands was measured using NIH ImageJ software, and results were normalized to GAPDH or alpha tubulin in each sample lane. All assays were performed at least three times.

Immunofluorescence and Hematoxylin & Eosin (H&E) Staining

HT22 neurons and rat brain sections were prepared for immunofluorescence as previously described [30, 40]. Subsequently, HT22 neurons were incubated with the primary antibody against anti-LC3 and/or anti-LAMP-1, anti-HCN1, or anti-HCN2 for 2 h at 37 °C, then with DyLight 488 Affinipure goat anti-rabbit IgG (H+L) (A23220, Abbkine, CA), DyLight 549 Affinipure goat anti-mouse IgG (H+L) (A23310, Abbkine), or DyLight 549 Affinipure rabbit anti-sheep IgG (H+L) (313-505-003, Jackson) for 2 h at 37 °C. Immunohistochemical staining of sections was sequentially performed following incubation with anti-LC3 (1: 500, PM036, MBL) overnight at 4 °C and Fluorescein (FITC)-conjugated Affinipure donkey anti-rabbit IgG(H+L) (SA00003-8, Proteintech Group Inc., China) for 2 h. And the images were recorded and analyzed using an Olympus FluoView 1200 confocal microscope system (Olympus Corp., Tokyo, Japan). LC3-postitive puncta and LAMP-1-positive lysosomes were then analyzed using ImageJ. LC3-positive puncta were expressed as a percentage of the total puncta within the indicated size ranges or co-localized with LAMP-1-positive lysosomes. The fluorescence intensity of LC3 staining in the rat hippocampal CA1 area was estimated using ImageJ. H&E staining was performed according to a protocol described previously [30] and photographed under the microscope. The number of neurons was counted using ImageJ and neuronal density was calculated as the ratio of viable neuron counts to the area of view in a section.

Statistical Analysis

All data are presented as the mean ± SD. Statistical analyses were calculated by one- or two-way analysis of variance (ANOVA, Tukey's HSD [honestly significant difference] test) using SPSS 22 .0 software (SPSS Inc., USA). Differences between two groups were evaluated by the *t*-test. $P < 0.05$ was considered statistically significant.

Results

ZD7288 Protects HT22 Neurons Against OGD/R Injury

Compared with the control group, the degree of neuronal damage was gradually aggravated after exposure to OGD insults of different durations (2 h, 4 h, 6 h, 8 h, or 12 h) followed by a further 12 h of reperfusion; the viability of HT22 neurons decreased from 100% to 88.28% ± 2.29%, 70.00% ± 1.38%, 50.50% ± 1.02%, 38.07% ± 1.28%, and 24.16% ± 1.25%, respectively (Fig. 1A, B). And the appropriate model was determined to be 6-h OGD followed by 12-h reperfusion because this caused nearly half of the neurons to die.

To determine whether ZD7288 protects HT22 neurons from damage induced by OGD/R, the neurons were pretreated with ZD7288 at different concentrations

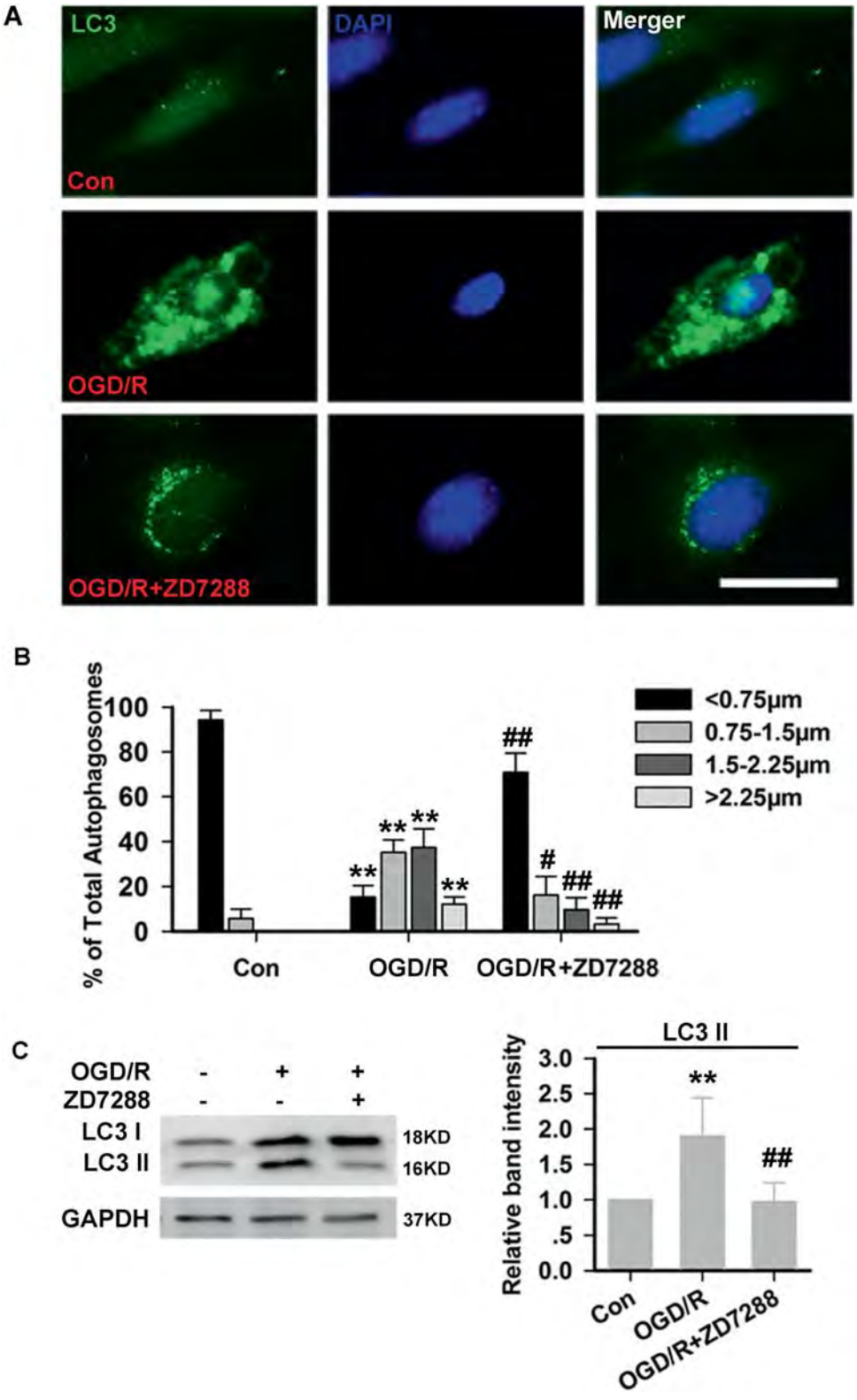

Fig. 2 ZD7288 corrects the excessive autophagy induced by OGD/R injury in HT22 neurons. **A** Representative photomicrographs of immunohistochemical staining with anti-LC3 antibody in HT22 neurons (scale bar, 50 μm). **B** Size distributions of autophagosome vacuoles (percentages of diameters within the indicated ranges of all LC3-positive puncta per neuron). **C** Expression of LC3-II protein in HT22 neurons. Experiments were performed at least four times with similar results. $^{**}P < 0.01$ *versus* control group; $^{\#}P < 0.05$, $^{\#\#}P < 0.01$ *versus* OGD/R group.

(1 μmol/L, 5 μmol/L, 10 μmol/L and 20 μmol/L) 2 h before OGD, and cell viability was measured at the end of OGD/R. At all these concentrations, ZD7288 had no effect on the viability of normoxic neurons as assayed by CCK-8 (Fig. 1C). Compared to OGD/R alone (50.53% ± 1.02%), the neuronal viability increased with ZD7288 concentration (1 μmol/L, 5 μmol/L, and 10 μmol/L) (60.69% ± 5.29%, 64.63% ± 2.71%, and

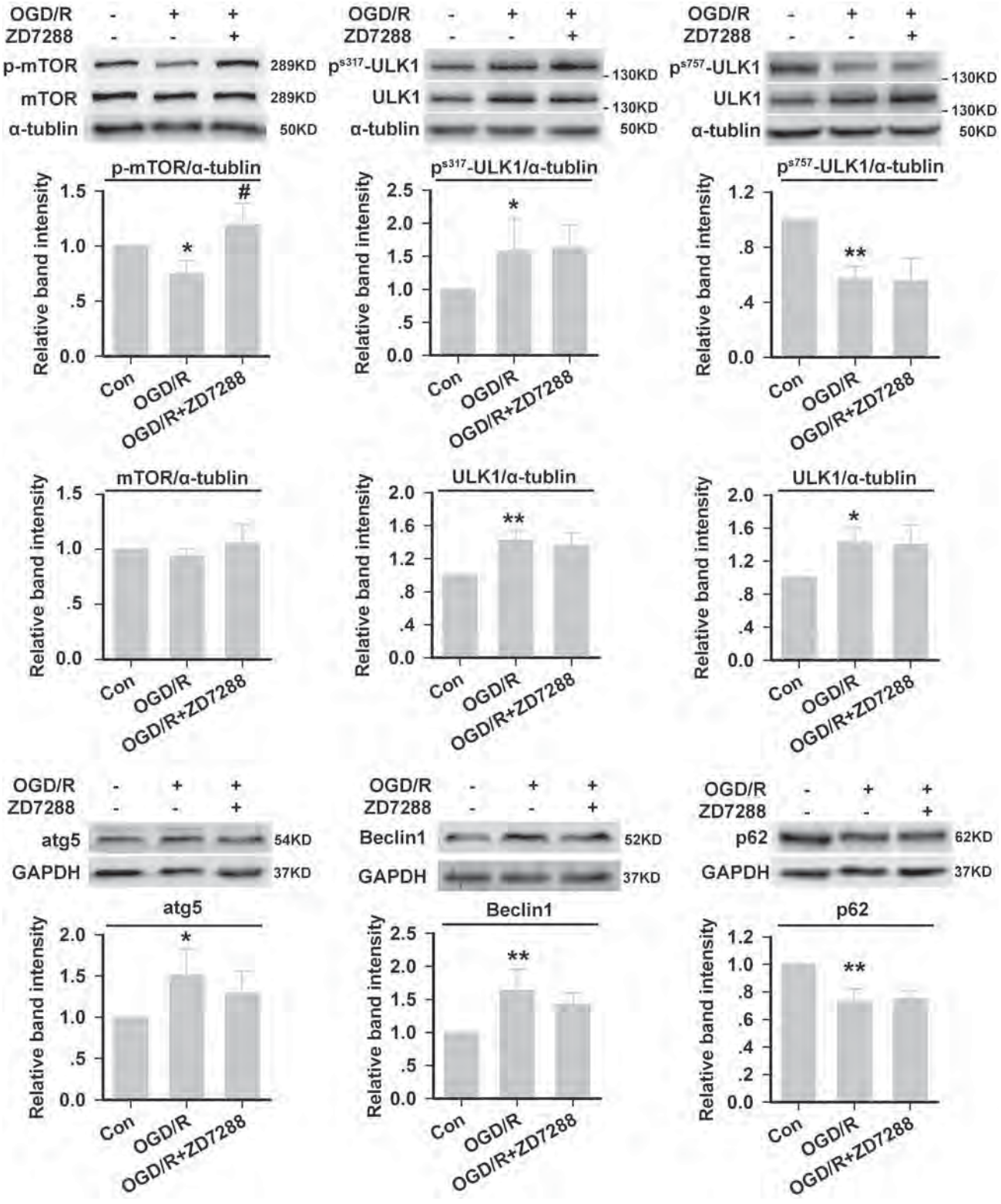

Fig. 3 The expression of autophagic proteins in HT22 neurons. The experiments were performed at least four times with similar results. $^{*}P < 0.05$ and $^{**}P < 0.01$ *vs* control group; $^{\#}P < 0.05$ *versus* OGD/R group.

72.27% ± 1.58%); ZD7288 at 20 μmol/L did not further increase the viability (71.19% ± 2.74%) (Fig. 1D, E). Thus, 10 μmol/L ZD7288 was used in the subsequent experiments. Next, necrosis and/or apoptosis of neurons

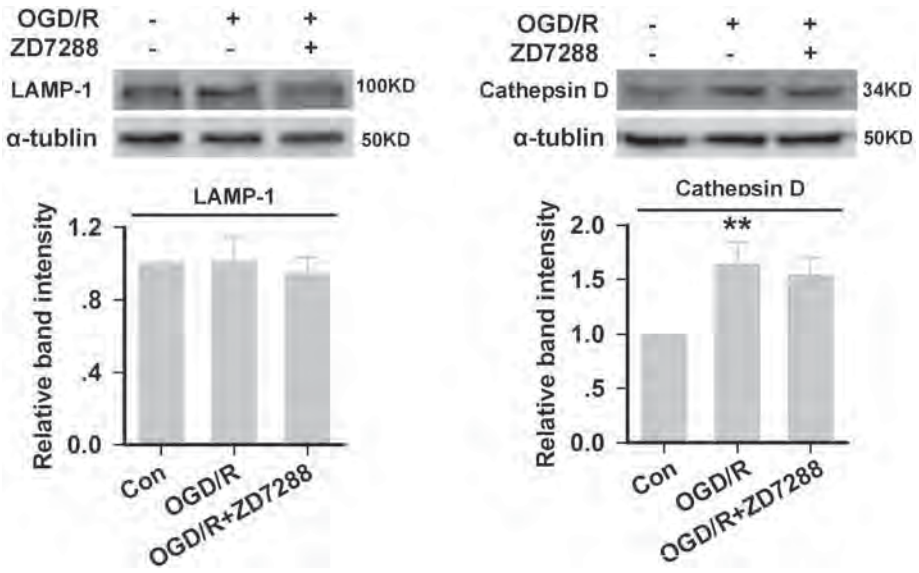

Fig. 4 The expression of LAMP-1 and cathepsin D in HT22 neurons. Experiments were performed at least four times with similar results. $^{**}P < 0.01$ *versus* control group.

was analyzed by flow cytometry. After OGD/R, HT22 neurons were stained with propidium iodide (PI) and FITC-labeled Annexin V (AV-FITC). Our results showed that OGD/R resulted in a significant increase in the percentage of apoptotic neurons (AV^+/PI^- and AV^+/PI^+) from a control value of 11.3% to 38.6%. ZD7288 (10 μmol/L) remarkably decreased the percentage of apoptotic neurons (18.4%) induced by OGD/R (Fig. 1F, G).

ZD7288 Corrects the Excessive Autophagy Induced by OGD/R Injury in HT22 Neurons

Compared with the control group, LC3 immunoreactivity was robustly elevated in the OGD/R group, whereas in the ZD7288 (10 μmol/L)+OGD/R group, the LC3 immunoreactivity declined towards basal levels (Fig. 2A, B). To further confirm that ZD7288 corrected OGD/R-induced autophagy, LC3-II (a marker of autophagosomes) was detected by Western blot analysis. Our results showed that the LC3-II levels were significantly increased in the OGD/R group. However, in the ZD7288 (10 μmol/L)+OGD/R group, the levels of LC3-II were remarkably decreased compared with the untreated OGD/R group (Fig. 2C).

Influence of ZD7288 on the Regulation of Autophagosome Formation, Lysosomal Enzymes, and Numbers of Lysosomes

To determine how ZD7288 regulates autophagy, we first analyzed the expression of regulators of autophagosome formation. Our results showed that, in the OGD/R group, p-mTOR, p-ULK1 (Ser^{757}), and p62 were significantly decreased, while p-ULK1 (Ser^{317}), Beclin1, and atg5 were significantly increased. ZD7288 (10 μmol/L) reversed the change in p-mTOR expression, but did not change the expression of p-ULK1 (Ser^{757}), p-ULK1 (Ser^{317}), p62, beclin1, or atg5 compared with OGD/R alone (Fig. 3). Next, we investigated the influence of ZD7288 on lysosomes and lysosomal enzymes, and found that OGD/R induced a significant increase in cathepsin D expression, but not LAMP-1. Treatment of the OGD/R group with ZD7288 at 10 μmol/L did not change the expression of cathepsin D or LAMP-1 (Fig. 4).

ZD7288 Accelerates Autophagic Degradation in HT22 Neurons During OGD/R Injury

To determine whether the correction of excessive autophagy by ZD7288 is due to the promotion of autophagic degradation, we further examined changes in autophagy-related proteins after co-incubation with CQ (50 μmol/L), which inhibits autophagosome–lysosome fusion. First, LC3 immunostaining was assessed in the presence of CQ with or without ZD7288. CQ increased the LC3 puncta in the control and OGD/R groups, and ZD7288 failed to correct the excessive autophagy in the presence of

Fig. 5 ZD7288 accelerates autophagic degradation in HT22 neurons during OGD/R injury. **A** Representative photomicrographs of immunohistochemical staining with anti-LC3 antibody in HT22 neurons (scale bar, 50 μm). **B** Size distributions of autophagosome vacuoles (percentages of diameters within the indicated ranges of all LC3-positive puncta per neuron). **C** Protein expression of LC3-II and p62 in HT22 neurons. **D** Representative dot plots of flow cytometric analysis of cell death in HT22 neurons. **E** Quantitative analysis of the apoptosis rates by flow cytometry. The experiments were performed at least three times with similar results. $^{**}P < 0.01$ *versus* control group, $^{\#\#}P < 0.01$ *versus* OGD/R group, $^{\&}P < 0.05$, $^{\&\&}P < 0.01$ *versus* Con+CQ group.

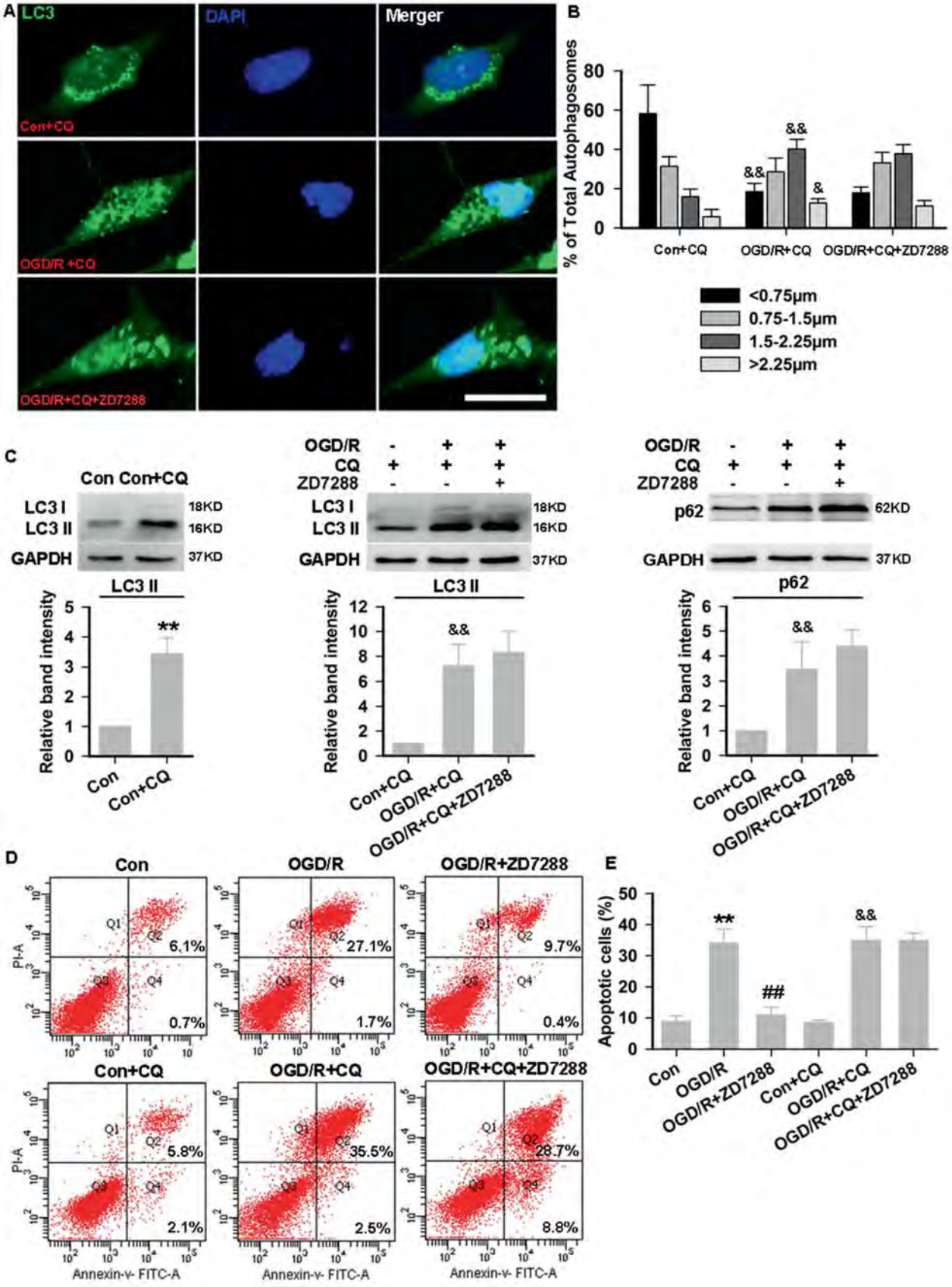
A
LC3
DAPI
Merger
Con+CQ
OGD/R +CQ
OGD/R+CQ+ZD7288
B
% of Total Autophagosomes
Con+CQ
OGD/R+CQ
OGD/R+CQ+ZD7288
<0.75μm
0.75-1.5μm
1.5-2.25μm
>2.25μm
C
Con Con+CQ
LC3 I
LC3 II
GAPDH
18KD
16KD
37KD
OGD/R
CQ
ZD7288
p62
62KD
Relative band intensity
D
Con
OGD/R
OGD/R+ZD7288
Con+CQ
OGD/R+CQ
OGD/R+CQ+ZD7288
PI-A
Annexin-v- FITC-A
6.1%
0.7%
27.1%
1.7%
9.7%
0.4%
5.8%
2.1%
35.5%
2.5%
28.7%
8.8%
E
Apoptotic cells (%)

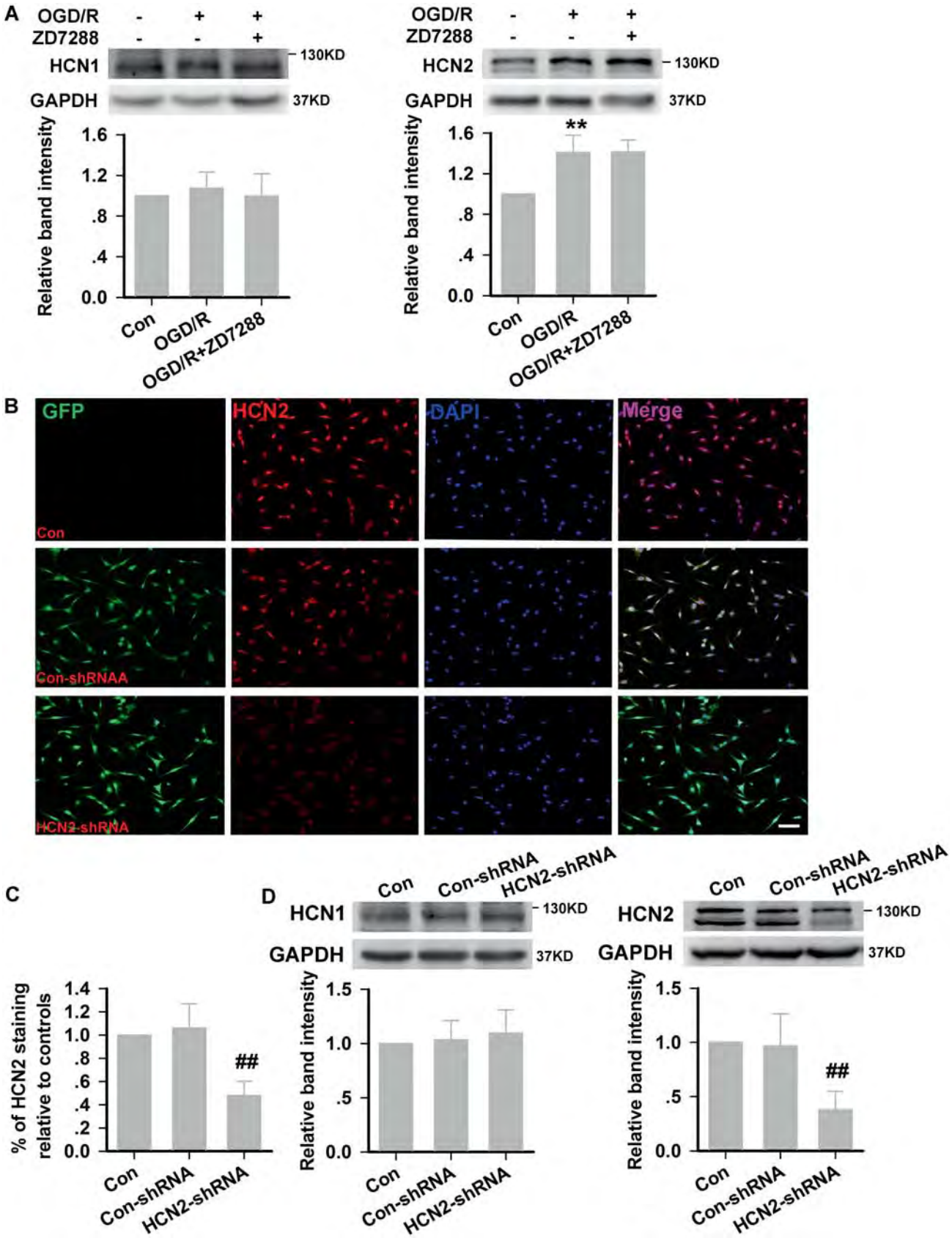
A
OGD/R - + +
ZD7288 - - +
HCN1
130KD
GAPDH
37KD
Relative band intensity
1.6
1.2
.8
.4
0.0
Con
OGD/R
OGD/R+ZD7288
OGD/R - + +
ZD7288 - - +
HCN2
130KD
GAPDH
37KD
**
Relative band intensity
1.6
1.2
.8
.4
0.0
Con
OGD/R
OGD/R+ZD7288
B
GFP
HCN2
DAPI
Merge
Con
Con-shRNAA
HCN2-shRNA
C
% of HCN2 staining relative to controls
1.4
1.2
1.0
.8
.6
.4
.2
0.0
##
Con
Con-shRNA
HCN2-shRNA
D
Con
Con-shRNA
HCN2-shRNA
HCN1
130KD
GAPDH
37KD
Relative band intensity
1.5
1.0
.5
0.0
Con
Con-shRNA
HCN2-shRNA
Con
Con-shRNA
HCN2-shRNA
HCN2
130KD
GAPDH
37KD
Relative band intensity
1.5
1.0
.5
0.0
##
Con
Con-shRNA
HCN2-shRNA

◀**Fig. 6** HCN2 subunit knockdown in HT22 neurons. **A** HCN1 and HCN2 expression in HT22 neurons after OGD/R injury (experiments were performed at least four times with similar results). **B** Representative photomicrographs of fluorescence produced by EGFP and immunohistochemical staining with anti-HCN2 antibody in HT22 neurons (× 200, scale bar, 200 μm). **C** Quantitative analysis of HCN2 immunoreactivity (experiments were performed at least three times with similar results). **D** Relative expression of HCN1 and HCN2 channels at the protein level in Con-shRNA and HCN2-shRNA cells (experiments were performed at least four times with similar results) $^{**}P < 0.01$ *versus* control group; $^{\#\#}P < 0.01$ *versus* Con-shRNA group.

CQ (Fig. 5A, B). Consistent with the immunocytochemical data, the addition of CQ increased the levels of LC3-II in controls, representing the maximal autophagic flux. In the OGD/R group, CQ increased the LC3-II levels to a greater extent. However, in the presence of CQ, treatment with ZD7288 at 10 μmol/L in the OGD/R group did not change the excessive expression of LC3-II and p62 (Fig. 5C). In order to further explore whether neuroprotection against OGD/R injury by ZD7288 is due to the acceleration of autophagic degradation, we measured the numbers of vital, apoptotic, and necrotic neurons in the presence of CQ by flow cytometry. CQ at 50 μmol/L had no significant effect on apoptosis or necrosis in HT22 neurons. However, it eliminated the neuroprotection by ZD7288 against OGD/R injury (Fig. 5D, E).

Neuroprotection Against OGD/R Injury by Blocking HCN2 Channels Using Genetic Knockdown is Due to Promotion of Autophagic Degradation in HT22 Neurons

At the end of OGD/R injury, HCN1 channels remained unchanged, while HCN2 channels were significantly increased in HT22 neurons (Fig. 6A). To further confirm that ZD7288 accelerated the autophagic degradation by blocking HCN channels, we next blocked HCN2 channels by genetic knockdown, and assessed the expression of EGFP in the lentivirus using confocal laser scanning microscopy. As shown in Fig. 5B, the cell morphology in each group did not differ significantly. EGFP was strongly expressed in HT22 neurons transfected with the lentivirus. The percentage of EGFP-positive cells exceeded 90% in the HCN2- or empty vector-transfected (HCN2-shRNA or Con-shRNA) HT22 neurons, as determined by flow cytometry (data not shown). HCN2-shRNA significantly reduced the fluorescence intensity of HCN2 (Fig. 6B, C) but not HCN1 (data not shown). Consistent with the immunocytochemistry, the relative expression of HCN2 channels at the protein level was inhibited by 63.39% ± 3.46% in HCN2-shRNA cells relative to Con-shRNA cells, and there was no effect on HCN1 channel expression (Fig. 6D).

Our results showed that Con-shRNA had no significant effect on apoptosis in HT22 neurons. OGD/R resulted in a significant increase in the percentage of apoptotic neurons from a control value of 6.2% to 32.1% in Con-shRNA-transfected HT22 neurons. The percentage of apoptotic neurons induced by OGD/R remarkably decreased in HCN2-shRNA-transfected neurons (8.0%). However, CQ (50 μmol/L) eliminated the neuroprotection by HCN2 channel knockdown (Fig. 7A, B). Next, we evaluated the effect of HCN2 channel knockdown on autophagic flux. A slight increase in LC3-II levels occurred in Con-shRNA-transfected neurons, but the difference from normal neurons was not significant (Fig. 7C). Under normal culture conditions, HCN2-shRNA decreased the LC3-II level, and CQ significantly increased the LC3-II level to a great extent. Besides, in the presence of CQ, HCN2-shRNA did not reverse the excessive expression of LC3-II (Fig. 7D). In Con-shRNA-transfected HT22 neurons, western blot analysis revealed that exposure to OGD/R resulted in an increase in the LC3-II level, while knockdown of HCN2 channels corrected the excessive expression of LC3-II. However, in the presence of CQ, knockdown of HCN2 channels did not reverse the excessive expression of LC3-II induced by OGD/R (Fig. 7E). In HCN2-shRNA-transfected neurons, ZD7288 (10 μmol/L) decreased the LC3-II level to a lesser extent at the end of OGD/R, and did not significantly differ from that of HCN2-shRNA transfection alone (Fig. 7F).

HCN2-shRNA Promotes Autophagosome–Lysosome Fusion in HT22 Neurons

In order to further evaluate the effect of HCN2-shRNA on the fusion of autophagosomes and lysosomes, we used immunohistochemical co-staining with antibodies against LC3 and LAMP-1 in HT22 neurons. As shown in Fig. 8, consistent with the western blot results, exposure of Con-shRNA-transfected neurons to OGD/R resulted in an increase in LC3 puncta, while knockdown of HCN2 channels significantly reduced them. However, in the presence of CQ, knockdown of HCN2 channels did not reverse the excessive autophagy induced by OGD/R. Besides, the expression of LAMP-1 did not change significantly in each group. Furthermore, we found that the percentage of LC3-positive puncta co-localized with LAMP-1-positive lysosomes decreased in Con-shRNA-transfected neurons exposed to OGD/R or CQ. In HCN2-shRNA-transfected HT22 neurons, the percentage of LC3-positive puncta that co-localized with LAMP-1-positive lysosomes increased under OGD/R; however, this percentage was significantly decreased by addition of CQ to the

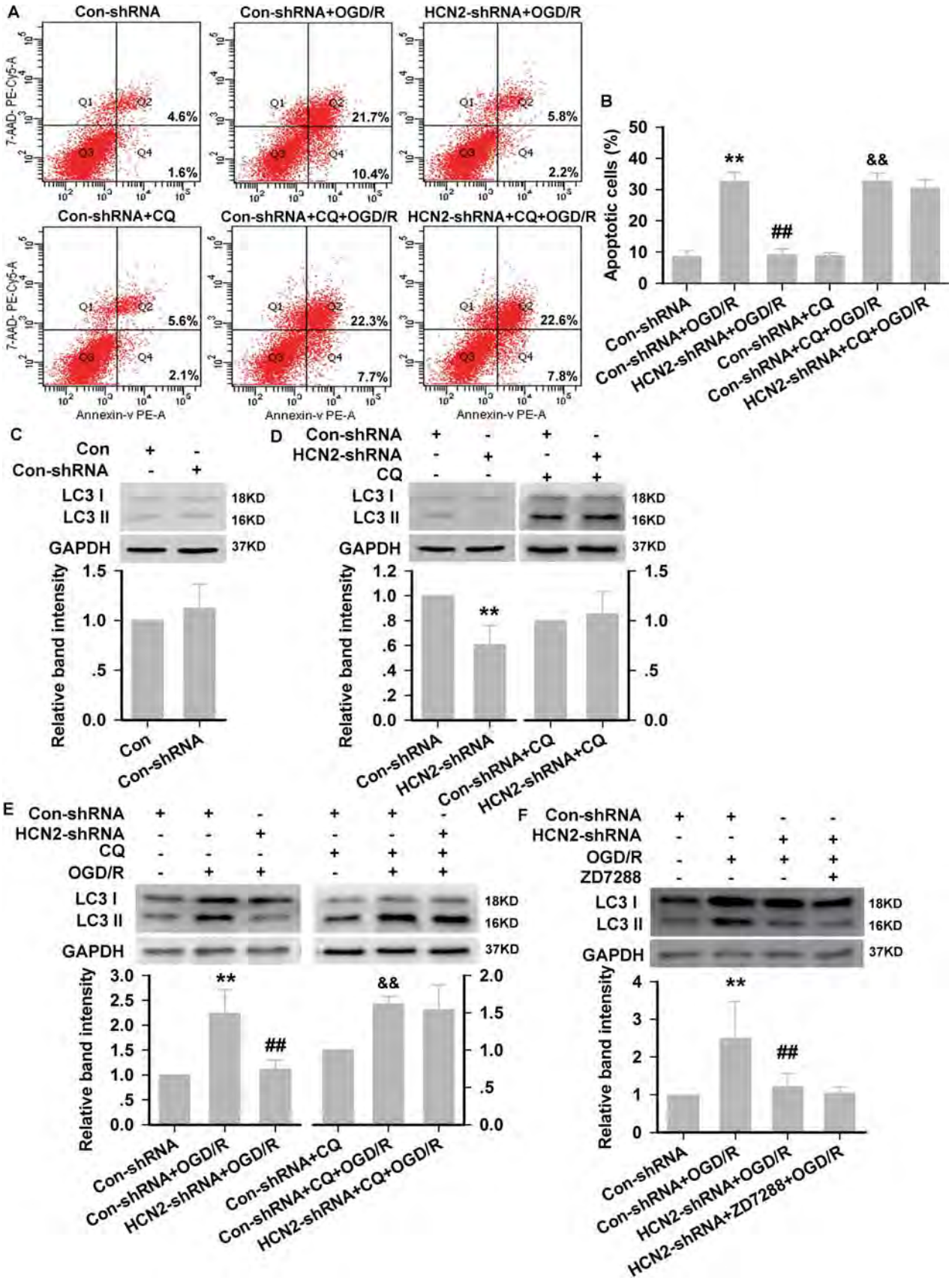
A
Con-shRNA
Con-shRNA+OGD/R
HCN2-shRNA+OGD/R
Con-shRNA+CQ
Con-shRNA+CQ+OGD/R
HCN2-shRNA+CQ+OGD/R
7-AAD- PE-Cy5-A
Annexin-v PE-A
Q1
Q2
Q3
Q4
4.6%
1.6%
21.7%
10.4%
5.8%
2.2%
5.6%
2.1%
22.3%
7.7%
22.6%
7.8%
B
Apoptotic cells (%)
**
##
&&
Con-shRNA
Con-shRNA+OGD/R
HCN2-shRNA+OGD/R
Con-shRNA+CQ
Con-shRNA+CQ+OGD/R
HCN2-shRNA+CQ+OGD/R
C
Con
Con-shRNA
LC3 I
LC3 II
GAPDH
18KD
16KD
37KD
Relative band intensity
D
Con-shRNA
HCN2-shRNA
CQ
E
OGD/R
F
ZD7288
HCN2-shRNA+ZD7288+OGD/R

◀**Fig. 7** Neuroprotection against OGD/R injury by blocking HCN2 channels using genetic knockdown is due to promotion of autophagic degradation. **A** Representative dot plots of flow cytometry analysis of cell death in HT22 neurons. **B** Quantitative analysis of the apoptosis rates by flow cytometry (experiments were performed at least three times with similar results). **C–F** Protein expression of LC3-II in each group (experiments were performed at least four times with similar results). $^{**}P < 0.01$ *versus* Con-shRNA group; $^{\#\#}P < 0.01$ *versus* Con-shRNA+OGD/R group; $^{\&\&}P < 0.01$ *versus* Con-shRNA+CQ group.

HCN2-shRNA-transfected neurons. Our results suggested that HCN2-shRNA promotes the fusion of autophagosomes and lysosomes in HT22 neurons.

Blocking HCN2 Channels by Genetic Knockdown Protects Against TGCI in Rats

After TGCI, HCN1 channels remained unchanged, however, HCN2 channels were significantly increased in the rat hippocampal CA1 area (Fig. 9A). To further evaluate the potential protective effects against TGCI, we next blocked HCN2 channels by genetic knockdown. The relative expression of HCN2 channels at the protein level was inhibited by 54.92% ± 1.37% in CA1 compared with Con-shRNA rats, and it had no effect on HCN1 channel expression (Fig. 9C).

Then, we examined the effect of blocking HCN2 channels on performance in the Morris water maze task and found no significant difference in swimming speed between groups (Fig. 10C). The latency to find the platform of TGCI rats was longer than the rats in the Con-shRNA group (Fig. 10D). The HCN2-shRNA+TGCI group showed a learning latency similar to that of the Con-shRNA group. However, in the presence of CQ, knockdown of HCN2 channels did not reverse the prolongation of latency to find the platform of TGCI rats (Fig. 10E). Furthermore, the rats in the Con-shRNA group spent longer in the target quadrant than TGCI rats (Con-shRNA group: 23.46% ± 3.08%, TGCI rats: 12.32% ± 4.22%). HCN2-shRNA improved the TGCI-induced deficit of acquisition in the water maze (HCN2-shRNA+TGCI group: 22.08% ± 4.12%), and CQ (12.5 mg/kg) eliminated the effect of HCN2-shRNA (HCN2-shRNA+CQ+TGCI group: 14.87% ± 3.07%, Fig. 10E).

In the present study, H&E staining and Western blotting were used to assess the influence of HCN2-shRNA on degenerative changes in the hippocampal CA1 area. Forty-eight hours after TGCI, significant neuronal loss in CA1 was detected on H&E staining (Fig. 10F, G), and HCN2-shRNA markedly diminished this neuronal loss. Consistent with the above results, Western blotting showed that HCN2-shRNA reversed the TGCI-induced reduction of NeuN protein in CA1. However, in the presence of CQ, knockdown of HCN2 channels did not reverse the TGCI-induced neuronal loss in CA1 (Fig. 10H).

HCN2-shRNA Corrects Excessive Autophagy Induced by TGCI in Rats

To investigate whether autophagy is involved in the neuroprotection by blocking HCN2 channels under TGCI, we examined the activation of autophagy in the hippocampal CA1 area. Forty-eight hours after TGCI, the LC3 immunoreactivity was significantly increased in CA1 (Fig. 11A, B), consistent with the protein expression of LC3-II (Fig. 11C). Knockdown of HCN2 channels corrected the excessive expression of LC3-II. However, in the presence of CQ, knockdown of HCN2 channels did not reverse the excessive expression of LC3-II induced by TGCI (Fig. 11A–C).

Discussion

In the present study, we demonstrated for the first time that blocking HCN channels by genetic knockdown or pharmacology protects hippocampal neurons from the damage induced by OGD/R and TGCI, and this might be attributed to the accelerated autophagic degradation.

Our results showed that, compared to untreated OGD/R, pretreatment with ZD7288 (10 μmol/L) significantly increased neuronal viability as assayed by CCK-8. However, OGD/R not only resulted in neuronal necrosis and/or apoptosis, but also decreased the HT22 cell proliferation rate. So we further analyzed the necrosis and apoptosis of neurons by flow cytometry. Our results showed that ZD7288 (10 μmol/L) also remarkably decreased the percentage of apoptotic neurons induced by OGD/R. The present results suggested that ZD7288 has protective effects against OGD/R-induced injury in hippocampal HT22 neurons.

Many reports have shown that the excessive or uncontrolled autophagy induced by ischemic injury leads to autophagic cell death, which is a form of non-apoptotic programmed cell death characterized by the presence of intense autophagy [41–43], and the correction of excessive autophagy can attenuate cerebral ischemia-associated neuronal damage [14–17]. Consistent with these studies, we found that ZD7288 corrected the excessive autophagy induced by OGD/R injury in HT22 neurons. To determine how ZD7288 regulates autophagy, we first analyzed the expression of regulators of autophagosome formation. Our results showed that ZD7288 (10 μmol/L) remarkably increased the phosphorylation of mTOR (Ser^{2448}) under OGD/R conditions in HT22 neurons. However, ZD7288

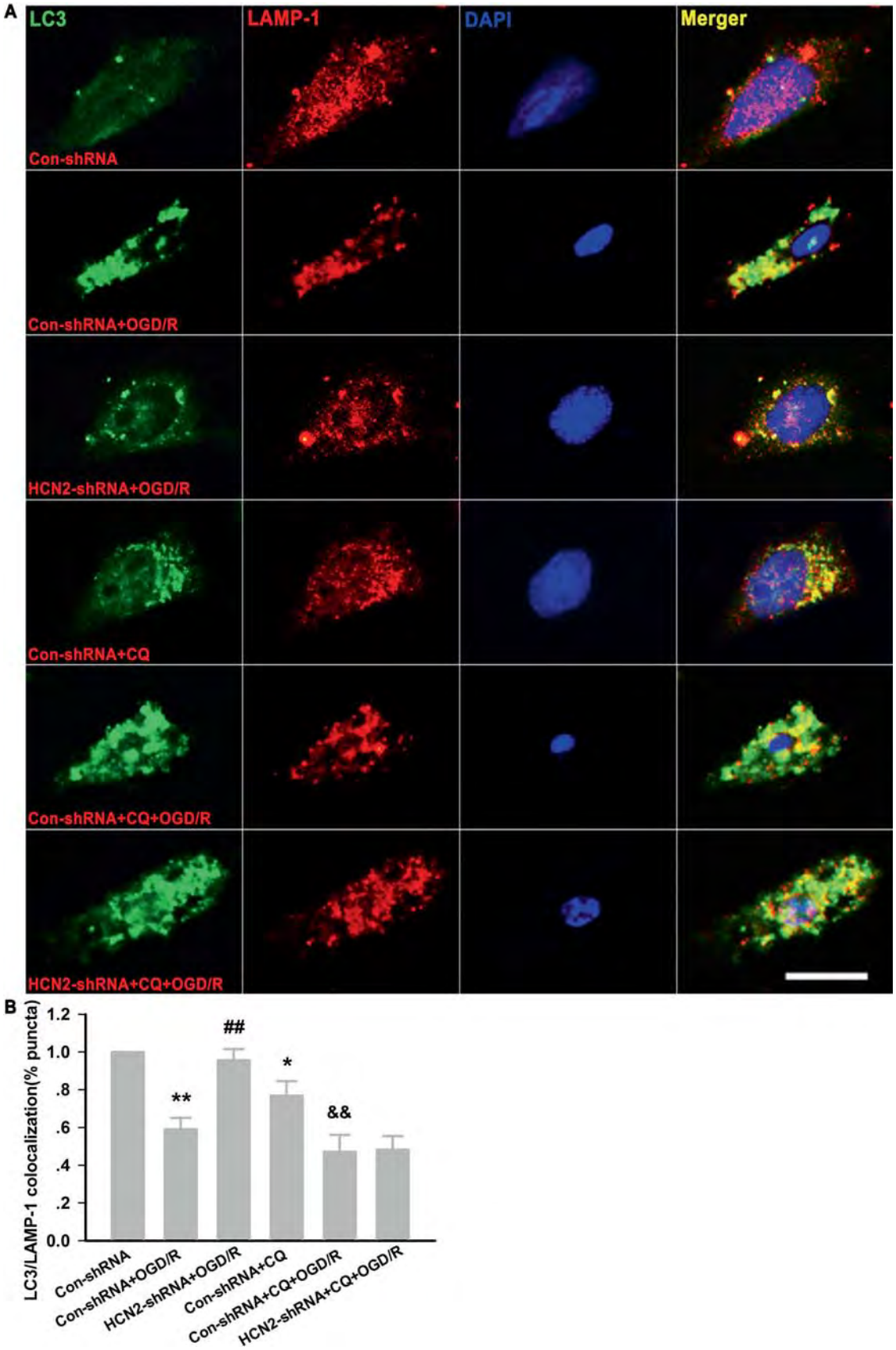
A
LC3
LAMP-1
DAPI
Merger
Con-shRNA
Con-shRNA+OGD/R
HCN2-shRNA+OGD/R
Con-shRNA+CQ
Con-shRNA+CQ+OGD/R
HCN2-shRNA+CQ+OGD/R
B
LC3/LAMP-1 colocalization(% puncta)
1.2
1.0
.8
.6
.4
.2
0.0
**
##
*
&&
Con-shRNA
Con-shRNA+OGD/R
HCN2-shRNA+OGD/R
Con-shRNA+CQ
Con-shRNA+CQ+OGD/R
HCN2-shRNA+CQ+OGD/R

◀**Fig. 8** HCN2-shRNA promotes autophagosome-lysosome fusion in HT22 neurons. **A** Representative images of immunohistochemical staining with anti-LC3 and anti-LAMP-1 in HT22 neurons (scale bar, 50 μm). **B** Analysis of the percentages of LC3-positive puncta that co-localize with LAMP-1-positive lysosomes in each group. $^{*}P < 0.05$, $^{**}P < 0.01$ *versus* Con-shRNA group, $^{\#\#}P < 0.01$ *versus* Con-shRNA+OGD/R group, $^{\&\&}P < 0.01$ *versus* Con-shRNA+CQ group.

(10 μmol/L) did not reverse the OGD/R-induced decrease in phosphorylation of ULK1 at Ser^{757}. Previous reports have shown that high mTOR activity prevents ULK1 activation by phosphorylating ULK1 Ser^{757} [44] and the subsequent inhibition of autophagy [45]. We hypothesized that upregulation of p-mTOR (Ser^{2448}) might act as a rescue mechanism to counter ZD7288-mediated effects in the HT22 neurons. A decrease in the phosphorylation of ULK-1 at Ser^{757} promotes its release from mTOR and association with AMPK, which enables the phosphorylation of ULK-1 at Ser^{317} by AMPK, and then activates beclin1, accelerating LC3-I transformation into an active lapidated form (LC3-II) [46]. Therefore, we further analyzed the expression of phosphorylation of ULk1 at Ser^{317}, beclin1, and atg5, and found that OGD/R increased the expression of all three, and treatment with ZD7288 at 10 μmol/L did not change their expression compared with the OGD/R group. These results are consistent with our hypothesis that p-mTOR levels are upregulated as a feedback mechanism to counter ZD7288-mediated effects in HT22 neurons, which means that ZD7288 is not involved in the regulation of autophagosome formation through activation of p-AMPK and p-AMPK.

Studies have shown that brain ischemia causes a late-stage block of autophagy, which prevents the autophagic degradation during autophagic flux [47], and leads to the accumulation of intracellular protein aggregates and damaged organelles, and delayed neuronal death. For autophagy, ubiquitination of the cargo is the prerequisite for its degradation. p62/SQSTM1, an adaptor protein, simultaneously binds to ubiquitinated cargo and LC3, which enables the degradation of itself and cargo in the lysosome [48]. Since the induction of autophagy is usually accompanied

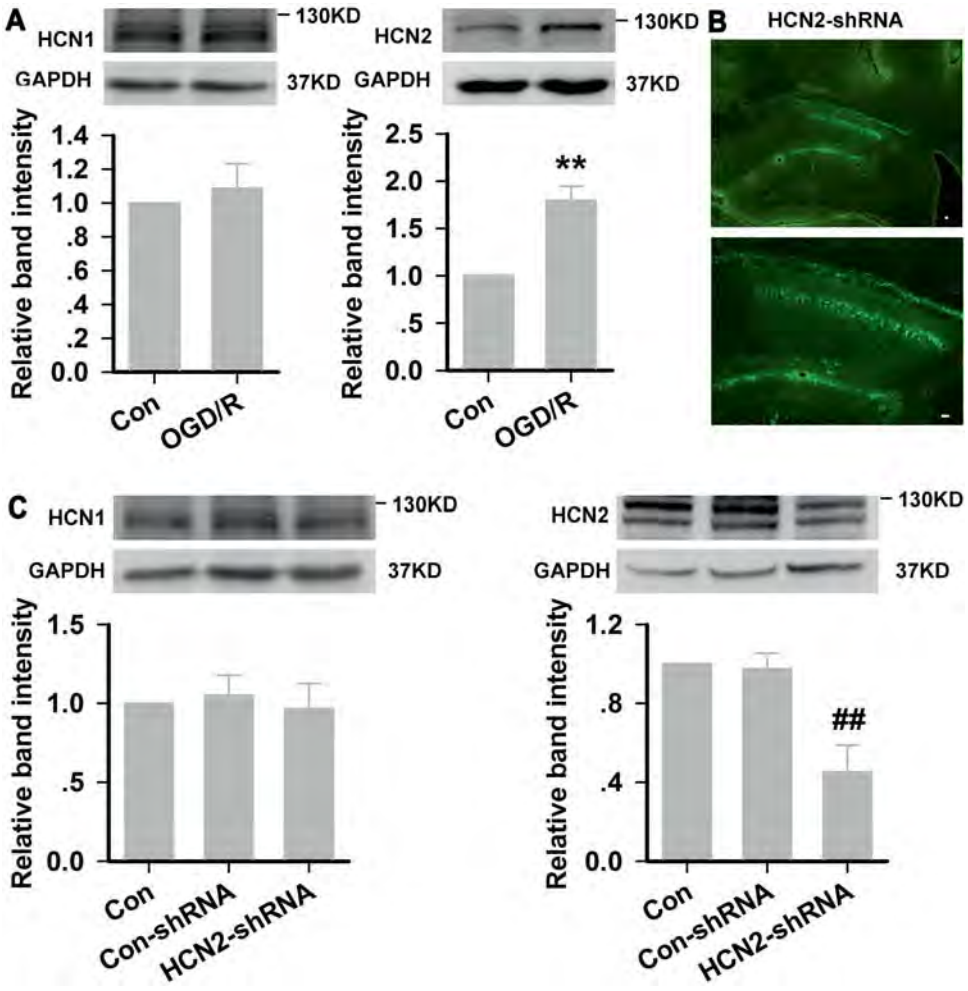

Fig. 9 HCN2 subunit knockdown in rat hippocampal CA1 region. **A** HCN1 and HCN2 expression in CA1 after TGCI (experiments were performed at least four times with similar results). **B** Distribution of lentivirus in the dorsal hippocampal CA1 region (green; × 40, × 100, scale bars, 100 μm). **C** Relative expression of HCN1 and HCN2 channels at the protein level in Con-shRNA and HCN2-shRNA rats (experiments were performed at least four times with similar results). $^{**}P < 0.01$ *versus* Con group; $^{\#\#}P < 0.01$ *versus* Con-shRNA group.

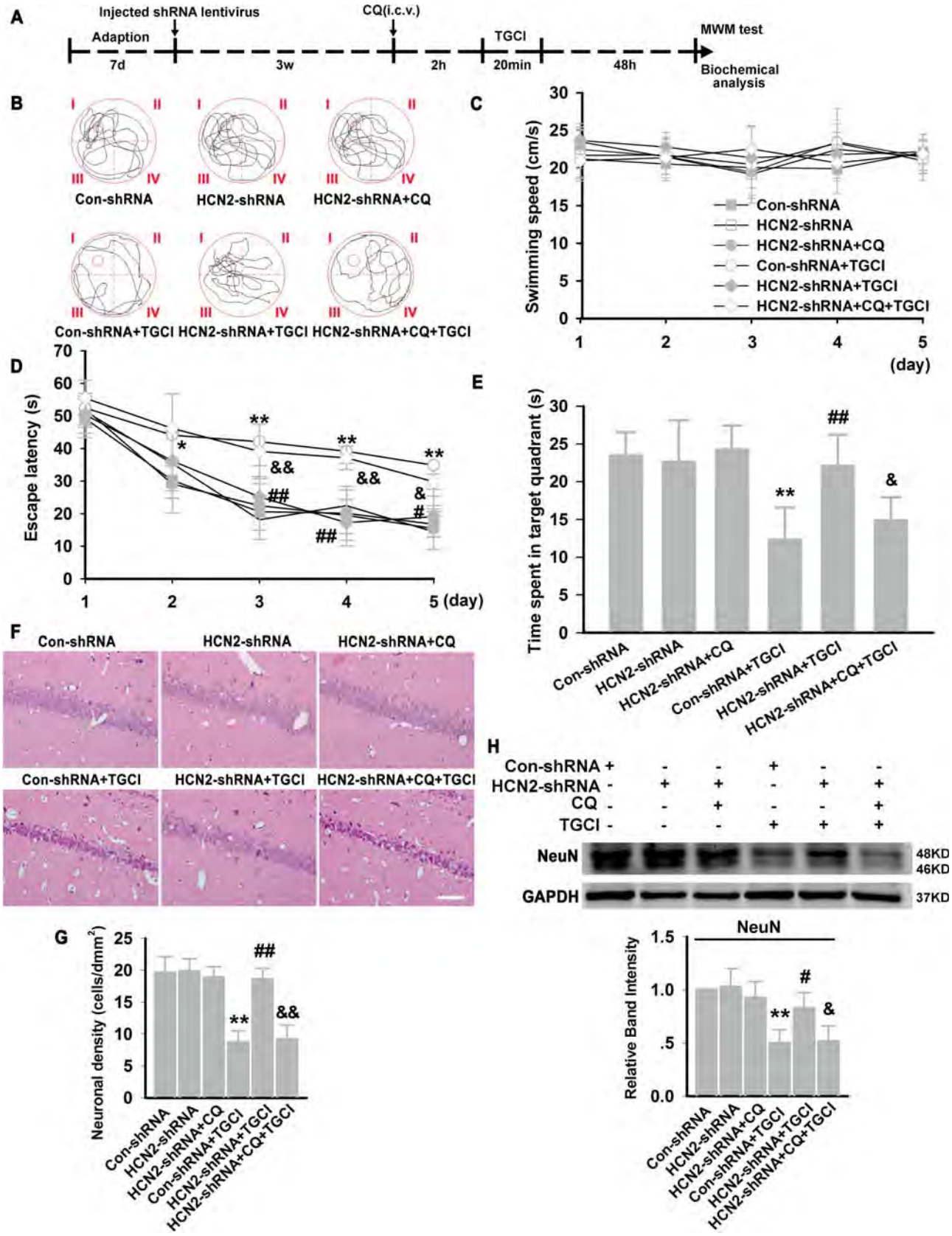
A
Injected shRNA lentivirus
CQ(i.c.v.)
Adaption
7d
3w
2h
TGCI
20min
48h
MWM test
Biochemical analysis
B
Con-shRNA
HCN2-shRNA
HCN2-shRNA+CQ
Con-shRNA+TGCI
HCN2-shRNA+TGCI
HCN2-shRNA+CQ+TGCI
C
Swimming speed (cm/s)
(day)
Con-shRNA
HCN2-shRNA
HCN2-shRNA+CQ
Con-shRNA+TGCI
HCN2-shRNA+TGCI
HCN2-shRNA+CQ+TGCI
D
Escape latency (s)
5 (day)
E
Time spent in target quadrant (s)
F
Con-shRNA
HCN2-shRNA
HCN2-shRNA+CQ
Con-shRNA+TGCI
HCN2-shRNA+TGCI
HCN2-shRNA+CQ+TGCI
G
Neuronal density (cells/dmm²)
H
Con-shRNA +
HCN2-shRNA -
CQ -
TGCI -
NeuN
GAPDH
48KD
46KD
37KD
NeuN
Relative Band Intensity

◀**Fig. 10** Neuroprotection against TGCI by blocking HCN2 channels with genetic knockdown. **A** Experimental design. **B** Typical swimming paths of each group. **C** Average speed from day 1 to day 5 (n = 8 per group). **D** Escape latency to find the hidden platform from day 1 to day 5. **E** Percentage of quadrant dwell time in the target quadrant on training day 6. **F** Example of H&E-stained sections of the hippocampus in each group (scale bar, 100 μm). **G** Quantification of neuronal density in CA1. **H** Protein expression of NeuN in CA1 of each group (n = 4 per group). $^{*}P < 0.05$, $^{**}P < 0.01$ *versus* Con-shRNA group; $^{\#}P < 0.05$, $^{\#\#}P < 0.01$ *versus* Con-shRNA+TGCI group; $^{\&}P < 0.05$, $^{\&\&}P < 0.01$ *versus* HCN2-shRNA+TGCI group. w, weeks.

by a decrease in p62, and accumulation of p62 occurs after autophagy is inhibited, p62 may be used to monitor autophagic flux [49]. We found that OGD/R reduced the abundance of p62. Unexpectedly, treatment with ZD7288 at 10 μmol/L did not change the expression of p62 compared with OGD/R alone. If ZD7288 had no effect on autophagosome formation, its correction of excessive autophagy might be due to the acceleration of autophagic degradation, and would decrease p62 expression, which contradicts our results. Sahani *et al*. have reported that the expression level of p62 depends on

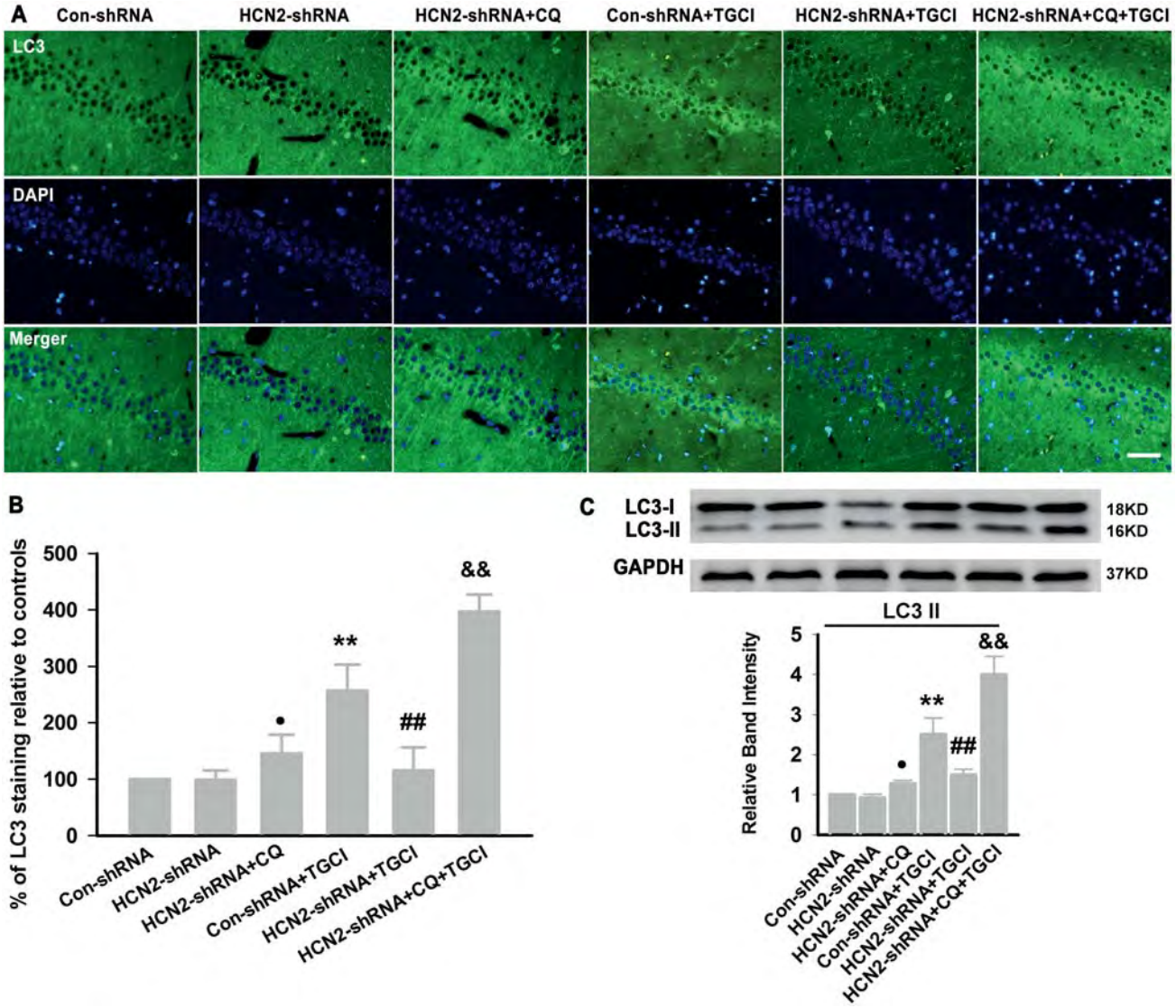

Fig. 11 HCN2-shRNA corrects the excessive autophagy induced by TGCI in rats. **A** Representative photomicrographs of immunohistochemical staining with anti-LC3 antibody in the hippocampal CA1 area (scale bar, 100 μm). **B** Quantitative analysis of the LC3 immunoreactivity (n = 4 per group). **C** Protein expression of LC3-II in CA1 of each group (n = 4 per group). $^{\bullet}P < 0.05$ *versus* HCN2-shRNA group, $^{**}P < 0.01$ *versus* Con-shRNA group; $^{\#\#}P < 0.01$ *versus* Con-shRNA+TGCI group; $^{\&\&}P < 0.01$ *versus* HCN2-shRNA+TGCI group.

autophagic degradation, changes in transcription and translation, and the availability of lysosome-derived amino-acids, so the p62 level is not always inversely related to autophagic activity [50]. Thus, p62 cannot be used as an indicator of the effect of ZD7288 on autophagic flux.

The accumulation of autophagic vacuoles can have three sources, selective impairment of autophagosome–lysosome fusion, dysfunction of lysosomal proteolysis, or a decrease in the number of lysosomes. The most widely used chemicals that inhibit the last stage of autophagy are CQ, bafilomycin A1 (BafA1), and lysosomal protease inhibitor cocktails. BafA1 inhibits the degradative capacity of lysosomes by decreasing their acidity, but it also impairs fusion between autophagosomes and lysosomes [51, 52]. In contrast, Mauthe *et al*. have reported that CQ inhibits autophagic flux by decreasing autophagosome–lysosome fusion, but not the degradative capacity of lysosomes [53, 54]. So we used CQ to evaluate whether ZD7288 affects the fusion of autophagosomes and lysosomes. Our results showed that, in the presence of CQ, treatment with ZD7288 at 10 μmol/L in the OGD/R group did not change the excessive expression of LC3-II compared with OGD/R alone, which meant that disrupting the fusion of autophagosomes and lysosomes cancelled the effect of ZD7288. On the other hand, if ZD7288 promoted or inhibited autophagosome formation, the accumulation of LC3-II in the OGD/R+CQ+ZD7288 group would be increased or decreased compared with the OGD/R+CQ group. Furthermore, we examined the expression of LAMP-1 and cathepsin D by Western blot analysis. Consistent with previous research [55], we found that the expression of LAMP-1 did not change significantly after ischemia, but cathepsin D expression was remarkably increased. However, treatment with ZD7288 at 10 μmol/L in the OGD/R group did not change the expression of LAMP-1 and cathepsin D, suggesting that ZD7288 had no effect on lysosomal proteolysis and the number of lysosomes. Thus, our findings demonstrated that ZD7288 has no effect on autophagosome formation, and it provides neuroprotection against OGD/R by accelerating autophagic degradation, which might be attributed to the promotion of autophagosome and lysosome fusion.

Studies have reported that ZD7288 may interact with Na^+ and Ca^{2+} channels [56, 57], and is not an isoform-selective blocker of the HCN channel [58]. In the present study, we found that OGD/R injury resulted in significantly increased HCN2 channels but not HCN1 channels in HT22 neurons. shRNA knockdown of HCN2 channels increased neuronal survival in the OGD/R model of HT22 neurons. However, CQ eliminated the neuroprotective effect of HCN2-shRNA. We further demonstrated that, in OGD/R injury, HCN2-shRNA significantly reduced the accumulation of LC3-II in neurons. However, in the presence of CQ, HCN2-shRNA failed to reduce this accumulation, and the level of LC3-II did not significantly differ from OGD/R+CQ. Similarly, if HCN2-shRNA promoted or inhibited autophagosome formation, the accumulation of LC3-II would be increased or decreased compared with the OGD/R+CQ group. Thus, our findings demonstrated that knockdown of HCN2 channels also had no effect on autophagosome formation; it corrected the excessive autophagy induced by OGD/R injury due to the acceleration of autophagic degradation that might be attributed to the promotion of autophagosome and lysosome fusion. In HCN2-shRNA-transfected HT22 neurons, ZD7288 did not further reduce LC3-II accumulation, which suggested that the neuroprotection against OGD/R injury by ZD7288 is due to blockade of HCN2 channels. In order to further evaluate the effect of HCN2-shRNA on the fusion of autophagosomes and lysosomes, we performed immunohistochemical co-staining with antibodies against LC3 and LAMP-1 in HT22 neurons. We found that the percentage of LC3-positive puncta that co-localized with LAMP-1-positive lysosomes decreased in Con-shRNA-transfected neurons exposed to OGD/R or CQ. In HCN2-shRNA-transfected neurons, the percentage of LC3-positive puncta that co-localized with LAMP-1-positive lysosomes increased under OGD/R, but the percentage was significantly decreased by the addition of CQ to HCN2-shRNA-transfected neurons. Our results suggested that HCN2-shRNA promotes the fusion of autophagosomes and lysosomes in HT22 neurons.

Next, we performed experiments in the rat TGCI model to validate our findings. Consistent with the above results, shRNA knockdown of HCN2 channels markedly diminished TGCI-induced neuronal loss in the hippocampal CA1 area and ameliorated the cognitive impairment in rats. Besides, in the presence of CQ, HCN2-shRNA did not offer neuroprotection against TGCI injury. Furthermore, in the TGCI model, HCN2-shRNA also significantly reduced the accumulation of LC3-II in neurons, and CQ abolished the effects of HCN2-shRNA. These results further indicated that disrupting autophagic degradation eliminates the neuroprotective effect of HCN2-shRNA on the TGCI model in rats.

Although the present study has yielded some preliminary findings, several limitations to this pilot study need to be acknowledged. First, although HT22 cells are widely used, the data obtained from this cell line might differ from primary hippocampal neurons and animal studies. Second, our results indicated that ZD7288 had no significant effect on cell viability. In addition, ZD7288 (OGD/R+ZD7288) had no significant effect on the expression of autophagy-related proteins. So we did not further measure the effect of ZD7288 alone on the expression of autophagy-associated

proteins in HT22 neurons. Third, the mechanisms underlying the OGD/R-induced increase of HCN2 channels in HT22 cells need further evaluation. Fourth, it is necessary to find an appropriate method to further investigate the effect of HCN2 channels on autophagosome and lysosome fusion in the case of cerebral ischemia *in vivo*. Fifth, we cannot rule out the possibility that ZD7288 regulates autophagy *via* other HCN channels, Na^+ or Ca^{2+} channels. Further investigations are under way in our laboratory.

In conclusion, our present results demonstrated that blockade of HCN2 channels provides neuroprotection against OGD/R and TGCI injury by accelerating autophagic degradation, which might be attributed to the promotion of autophagosome and lysosome fusion in hippocampal neurons.

Acknowledgements This work was supported by grants from the National Natural Science Foundation of China (85100929), the Natural Science Foundation of Hubei Province, China (2018CFB302 and 2019CFB446), and the Youth Fund of Health and Family Planning Commission of Wuhan Municipality, Hubei Province, China (WX18Q13 and WX18Q22).

Conflict of interest The authors declare that they have no conflict of interest.

References

1. Benjamin EJ, Blaha MJ, Chiuve SE, Cushman M, Das SR, Deo R, *et al.* Heart Disease and Stroke Statistics-2017 Update: A Report From the American Heart Association. Circulation 2017, 135: e146–e603.
2. Kurisu K, Yenari MA. Therapeutic hypothermia for ischemic stroke; pathophysiology and future promise. Neuropharmacology 2018, 134: 302–309.
3. Dong Z, Pan K, Pan J, Peng Q, Wang Y. The possibility and molecular mechanisms of cell pyroptosis after cerebral ischemia. Neurosci Bull 2018, 34: 1131–1136.
4. Yang J, Liang H, Song Y, Shen L, Wang S. Analysis of the efficacy and safety of recombinant tissue plasminogen activator for chinese patients over 80 years of age with acute ischemic stroke: a pilot study. Neurosci Bull 2016, 32: 202–203.
5. Gomis M, Davalos A. Recanalization and reperfusion therapies of acute ischemic stroke: what have we learned, what are the major research questions, and where are we headed? Front Neurol 2014, 5: 226.
6. Lee KM, Hwang SK, Lee JA. Neuronal autophagy and neurodevelopmental disorders. Exp Neurobiol 2013, 22: 133–142.
7. Uchiyama Y, Shibata M, Koike M, Yoshimura K, Sasaki M. Autophagy-physiology and pathophysiology. Histochem Cell Biol 2008, 129: 407–420.
8. Steiger-Barraissoul S, Rami A. Serum deprivation induced autophagy and predominantly an AIF-dependent apoptosis in hippocampal HT22 neurons. Apoptosis 2009, 14: 1274–1288.
9. Yorimitsu T, Klionsky DJ. Atg11 links cargo to the vesicle-forming machinery in the cytoplasm to vacuole targeting pathway. Mol Biol Cell 2005, 16: 1593–1605.
10. Shen S, Kepp O, Kroemer G. The end of autophagic cell death? Autophagy 2012, 8: 1–3.
11. Nabavi SF, Sureda A, Sanches-Silva A, Pandima Devi K, Ahmed T, Shahid M, *et al.* Novel therapeutic strategies for stroke: The role of autophagy. Crit Rev Clin Lab Sci 2019: 1–18.
12. Gurusamy N, Lekli I, Gorbunov NV, Gherghiceanu M, Popescu LM, Das DK. Cardioprotection by adaptation to ischaemia augments autophagy in association with BAG-1 protein. J Cell Mol Med 2009, 13: 373–387.
13. Su J, Zhang T, Wang K, Zhu T, Li X. Autophagy activation contributes to the neuroprotection of remote ischemic perconditioning against focal cerebral ischemia in rats. Neurochem Res 2014, 39: 2068–2077.
14. Wen YD, Sheng R, Zhang LS, Han R, Zhang X, Zhang XD, *et al.* Neuronal injury in rat model of permanent focal cerebral ischemia is associated with activation of autophagic and lysosomal pathways. Autophagy 2008, 4: 762–769.
15. Puyal J, Vaslin A, Mottier V, Clarke PG. Postischemic treatment of neonatal cerebral ischemia should target autophagy. Ann Neurol 2009, 66: 378–389.
16. Shi R, Weng J, Zhao L, Li XM, Gao TM, Kong J. Excessive autophagy contributes to neuron death in cerebral ischemia. CNS Neurosci Ther 2012, 18: 250–260.
17. Dong F, Yao R, Yu H, Liu Y. Neuroprotection of Ro25-6981 against ischemia/reperfusion-induced brain injury via inhibition of autophagy. Cell Mol Neurobiol 2017, 37: 743–752.
18. Bender RA, Brewster A, Santoro B, Ludwig A, Hofmann F, Biel M, *et al.* Differential and age-dependent expression of hyperpolarization-activated, cyclic nucleotide-gated cation channel isoforms 1-4 suggests evolving roles in the developing rat hippocampus. Neuroscience 2001, 106: 689–698.
19. Biel M, Wahl-Schott C, Michalakis S, Zong X. Hyperpolarization-activated cation channels: from genes to function. Physiol Rev 2009, 89: 847–885.
20. Doan TN, Kunze DL. Contribution of the hyperpolarization-activated current to the resting membrane potential of rat nodose sensory neurons. J Physiol 1999, 514: 125–138.
21. Wahl-Schott C, Biel M. HCN channels: structure, cellular regulation and physiological function. Cell Mol Life Sci 2009, 66: 470–494.
22. Leresche N, Lightowler S, Soltesz I, Jassik-Gerschenfeld D, Crunelli V. Low-frequency oscillatory activities intrinsic to rat and cat thalamocortical cells. J Physiol 1991, 441: 155–174.
23. Nolan MF, Malleret G, Dudman JT, Buhl DL, Santoro B, Gibbs E, *et al.* A behavioral role for dendritic integration: HCN1 channels constrain spatial inputs to distal dendrites memory and plasticity at of CA1 pyramidal neurons. Cell 2004, 119: 719–732.
24. Harnett MT, Magee JC, Williams SR. Distribution and function of HCN channels in the apical dendritic tuft of neocortical pyramidal neurons. J Neurosci 2015, 35: 1024–1037.
25. Huang CC, Hsu KS. Reexamination of the role of hyperpolarization-activated cation channels in short- and long-term

plasticity at hippocampal mossy fiber synapses. Neuropharmacology 2003, 44: 968–981.
26. Masi A, Narducci R, Resta F, Carbone C, Kobayashi K, Mannaioni G. Differential contribution of Ih to the integration of excitatory synaptic inputs in substantia nigra pars compacta and ventral tegmental area dopaminergic neurons. Eur J Neurosci 2015, 42: 2699–2706.
27. Mellor J, Nicoll RA, Schmitz D. Mediation of hippocampal mossy fiber long-term potentiation by presynaptic Ih channels. Science 2002, 295: 143–147.
28. Huang Z, Li G, Aguado C, Lujan R, Shah MM. HCN1 channels reduce the rate of exocytosis from a subset of cortical synaptic terminals. Sci Rep 2017, 7: 40257.
29. Shimizu H, Mizuguchi A, Aoki M. Differential responses between CA1 pyramidal cells and granule cells to ischemic insult in rat hippocampal slices. Neurosci Lett 1996, 203: 195–198.
30. Li CJ, Lu Y, Zhou M, Zong XG, Li C, Xu XL, *et al.* Activation of GABAB receptors ameliorates cognitive impairment via restoring the balance of HCN1/HCN2 surface expression in the hippocampal CA1 area in rats with chronic cerebral hypoperfusion. Mol Neurobiol 2014, 50: 704–720.
31. Honsa P, Pivonkova H, Harantova L, Butenko O, Kriska J, Dzamba D, *et al.* Increased expression of hyperpolarization-activated cyclic nucleotide-gated (HCN) channels in reactive astrocytes following ischemia. Glia 2014, 62: 2004–2021.
32. Pan LN, Zhu W, Li C, Xu XL, Guo LJ, Lu Q. Toll-like receptor 3 agonist Poly I:C protects against simulated cerebral ischemia *in vitro* and *in vivo*. Acta Pharmacol Sin 2012, 33: 1246–1253.
33. Noori-Daloii MR, Mojarrad M, Rashidi-Nezhad A, Kheirollahi M, Shahbazi A, Khaksari M, *et al.* Use of siRNA in knocking down of dopamine receptors, a possible therapeutic option in neuropsychiatric disorders. Mol Biol Rep 2012, 39: 2003–2010.
34. Zhang Q, Huang A, Lin YC, Yu HG. Associated changes in HCN2 and HCN4 transcripts and I(f) pacemaker current in myocytes. Biochim Biophys Acta 2009, 1788: 1138–1147.
35. Yang C, Zhang JR, Chen L, Ge SN, Wang JL, Yan ZQ, *et al.* Decreased HCN2 expression in STN contributes to abnormal high-voltage spindles in the cortex and globus pallidus of freely moving rats. Brain Res 2015, 1618: 17–28.
36. Lu Y, Li CJ, Chen C, Luo P, Zhou M, Li C, *et al.* Activation of GABAB2 subunits alleviates chronic cerebral hypoperfusion-induced anxiety-like behaviours: A role for BDNF signalling and Kir3 channels. Neuropharmacology 2016, 110: 308–321.
37. Su F, Guo AC, Li WW, Zhao YL, Qu ZY, Wang YJ, *et al.* Low-dose ethanol preconditioning protects against oxygen-glucose deprivation/reoxygenation-induced neuronal injury by activating large conductance, Ca(2+)-activated K(+) channels *in vitro*. Neurosci Bull 2017, 33: 28–40.
38. Sun D, Wang W, Wang X, Wang Y, Xu X, Ping F, *et al.* bFGF plays a neuroprotective role by suppressing excessive autophagy and apoptosis after transient global cerebral ischemia in rats. Cell Death Dis 2018, 9: 172.
39. Powell KL, Ng C, O'Brien TJ, Xu SH, Williams DA, Foote SJ, *et al.* Decreases in HCN mRNA expression in the hippocampus after kindling and status epilepticus in adult rats. Epilepsia 2008, 49: 1686–1695.
40. Li C, Lu Q, Huang P, Fu T, Li C, Guo L, *et al.* Activity-dependent downregulation of M-Type (Kv7) K(+) channels surface expression requires the activation of iGluRs/Ca(2)(+)/PKC signaling pathway in hippocampal neuron. Neuropharmacology 2015, 95: 154–167.
41. Codogno P, Meijer AJ. Autophagy and signaling: their role in cell survival and cell death. Cell Death Differ 2005, 12 Suppl 2: 1509–1518.
42. Rami A, Langhagen A, Steiger S. Focal cerebral ischemia induces upregulation of Beclin 1 and autophagy-like cell death. Neurobiol Dis 2008, 29: 132–141.
43. Li WL, Yu SP, Chen D, Yu SS, Jiang YJ, Genetta T, *et al.* The regulatory role of NF-kappaB in autophagy-like cell death after focal cerebral ischemia in mice. Neuroscience 2013, 244: 16–30.
44. Mizushima N. The role of the Atg1/ULK1 complex in autophagy regulation. Curr Opin Cell Biol 2010, 22: 132–139.
45. Gabryel B, Kost A, Kasprowska D. Neuronal autophagy in cerebral ischemia–a potential target for neuroprotective strategies? Pharmacol Rep 2012, 64: 1–15.
46. Leidal AM, Levine B, Debnath J. Autophagy and the cell biology of age-related disease. Nat Cell Biol 2018, 20: 1338–1348.
47. Liu C, Gao Y, Barrett J, Hu B. Autophagy and protein aggregation after brain ischemia. J Neurochem 2010, 115: 68–78.
48. Zheng YT, Shahnazari S, Brech A, Lamark T, Johansen T, Brumell JH. The adaptor protein p62/SQSTM1 targets invading bacteria to the autophagy pathway. J Immunol 2009, 183: 5909–5916.
49. Bjorkoy G, Lamark T, Pankiv S, Overvatn A, Brech A, Johansen T. Monitoring autophagic degradation of p62/SQSTM1. Methods Enzymol 2009, 452: 181–197.
50. Sahani MH, Itakura E, Mizushima N. Expression of the autophagy substrate SQSTM1/p62 is restored during prolonged starvation depending on transcriptional upregulation and autophagy-derived amino acids. Autophagy 2014, 10: 431–441.
51. Yamamoto A, Tagawa Y, Yoshimori T, Moriyama Y, Masaki R, Tashiro Y. Bafilomycin A1 prevents maturation of autophagic vacuoles by inhibiting fusion between autophagosomes and lysosomes in rat hepatoma cell line, H-4-II-E cells. Cell Struct Funct 1998, 23: 33–42.
52. Jahreiss L, Menzies FM, Rubinsztein DC. The itinerary of autophagosomes: from peripheral formation to kiss-and-run fusion with lysosomes. Traffic 2008, 9: 574–587.
53. Mauthe M, Orhon I, Rocchi C, Zhou X, Luhr M, Hijlkema KJ, *et al.* Chloroquine inhibits autophagic flux by decreasing autophagosome-lysosome fusion. Autophagy 2018, 14: 1435–1455.
54. Klionsky DJ, Abdelmohsen K, Abe A, Abedin MJ, Abeliovich H, Acevedo Arozena A, *et al.* Guidelines for the use and interpretation of assays for monitoring autophagy (3rd edition). Autophagy 2016, 12: 1–222.
55. Zhan L, Chen S, Li K, Liang D, Zhu X, Liu L, *et al.* Autophagosome maturation mediated by Rab7 contributes to neuroprotection of hypoxic preconditioning against global cerebral ischemia in rats. Cell Death Dis 2017, 8: e2949.
56. Sanchez-Alonso JL, Halliwell JV, Colino A. ZD 7288 inhibits T-type calcium current in rat hippocampal pyramidal cells. Neurosci Lett 2008, 439: 275–280.
57. Wu X, Liao L, Liu X, Luo F, Yang T, Li C. Is ZD7288 a selective blocker of hyperpolarization-activated cyclic nucleotide-gated channel currents? Channels (Austin) 2012, 6: 438–442.
58. Sartiani L, Mannaioni G, Masi A, Novella Romanelli M, Cerbai E. The hyperpolarization-activated cyclic nucleotide-gated channels: from biophysics to pharmacology of a unique family of ion channels. Pharmacol Rev 2017, 69: 354–395.

Neurosci. Bull. August, 2020, 36(8):895–906
https://doi.org/10.1007/s12264-020-00500-y

www.neurosci.cn
www.springer.com/12264

ORIGINAL ARTICLE

Neurocognitive Correlates of Statistical Learning of Orthographic–Semantic Connections in Chinese Adult Learners

Xiuhong Tong[1] · Yi Wang[2] · Shelley Xiuli Tong[3]

Received: 7 August 2019 / Accepted: 11 February 2020 / Published online: 12 May 2020

Abstract We examined the neural correlates of the statistical learning of orthographic–semantic connections in Chinese adult learners. Visual event-related potentials (ERPs) were recorded while participants were exposed to a sequence of artificial logographic characters containing semantic radicals carrying low, moderate, or high levels of semantic consistency. The behavioral results showed that the mean accuracy of participants' recognition of previously exposed characters was 63.1% that was significantly above chance level (50%), indicating the statistical learning of the regularities of semantic radicals. The ERP data revealed a temporal sequence of the neural process of statistical learning of orthographic-semantic connections, and different brain indexes were found to be associated with this processing, i.e., a clear N170–P200–N400 pattern. For N170, the larger negative amplitudes were evoked by the high and moderate consistency than the low consistency. For P200, the mean amplitudes elicited by the moderate and low consistency were larger than the high consistency. In contrast, a larger N400 amplitude was observed in the low than moderate and high consistency; and more negative amplitude was elicited by the moderate than high consistency. We propose that the initial potential shifts (N170 and P200) may reflect orthographic or graphic form identification, while the later component (N400) may be associated with semantic information analysis.

Keywords Orthography–semantic connection · Statistical learning · N170 · P200 · N400

The human brain possesses a powerful computational ability to automatically extract the regularities of a language from the statistical patterns embedded in linguistic input (e.g., English speakers learn that the syllable /lang/ is more likely to be followed by /uage/ than by /sage/) [1]. This ability is simply defined as statistical learning, which occurs without conscious awareness [2, 3]. Statistical learning has been found to play a crucial role in various domains of perception and cognition [4, 5] and is particularly important for the development of language (for reviews, see [6–8]). For example, contemporary theories and growing empirical evidence on children's orthographic learning, which refers to a mental process of storing the concrete orthographic representations of words in memory [9], suggest that statistical learning helps children to learn the hidden orthographic regularities of a language [10, 11]. However, the neural process of statistical learning of orthographic regularities remains unknown. In the present study, we employed the event-related potential (ERP) approach to examine the neural signatures of statistical learning of orthographic regularities in Chinese, with a particular focus on the learning of orthographic-semantic connections (i.e., semantic radical) of Chinese character orthography.

Given its unique logographic features, Chinese is a fascinating language for exploring the role of statistical learning in orthographic learning [10]. Chinese is a

✉ Shelley Xiuli Tong
xltong@hku.hk;
https://slrlab.edu.hku.hk/about-us/director/

[1] Department of Psychology, The Education University of Hong Kong, Hong Kong, China

[2] Institute of Psychological Sciences, Hangzhou Normal University, Hangzhou 310000, China

[3] Human Communication, Development, and Information Sciences, Faculty of Education, The University of Hong Kong, Hong Kong, China

morphosyllabetic writing system in which the basic writing unit, the character, maps on to the syllable and also the morpheme [12]. Approximately 80% of Chinese characters are phonetic-semantic compound characters comprising a phonetic and a semantic radicals. The radicals exhibit certain positional and functional regularities. Phonetic radicals usually occur on the left or the top while semantic radicals localize on the right or at the bottom for the left-right or top-bottom structured characters, respectively. Phonetic radicals provide sound cues while semantic radicals give a clue as to the meaning of the character [13]. However, semantic regularities are not absolutely systematic, but are more quasi-regular and exhibit certain distributional statistics, such as frequency and variability. Semantic consistency has been proposed to reflect how frequently a semantic radical indicates a given meaning [10]. For example, according to a corpus analysis of Chinese characters taught in primary schools, 44 of 55 characters contain the semantic radical 车/che1/, resulting in a semantic consistency of 80% (44/55) [12].

Most psycholinguistic models of visual character recognition explicitly emphasize the role of semantic radicals in Chinese character processing[14–16]. For example, the facilitative effects of the semantic relatedness of embedded radicals on character recognition have been reported in various studies using different behavioral paradigms [16–18]. Children begin acquiring knowledge of semantic radicals from grade 1 [19] and the usage of semantic radicals in Chinese character reading increases with grade [20]. Furthermore, semantic radicals have also been found to be significantly correlated with children's word reading and sentence comprehension [19].

However, it remains unclear about how Chinese readers acquire the regularities of semantic radicals. A recent behavioral study revealed that Chinese children might use the statistical properties present in Chinese characters to extract the regularities of semantic radicals [10] and use them in their subsequent character recognition [10]. More specifically, He *et al.* used a modified classical statistical learning paradigm, artificial orthography learning, in which a set of Chinese-like logographic characters was created using an ideographic Dongba script and a syllabic Geba script. After a short exposure to a subset of novel logographic characters, school-aged Chinese children were able to statistically learn semantic regularities and integrated the learned sematic consistency into their orthographic representations, which they used in subsequent character encoding [10].

Although increasing numbers of studies have revealed the role of statistical learning in orthographic learning [13, 20–22], no neurophysiological research to date has examined how the human brain discovers orthographic regularities using statistical information embedded in learned materials and what neural processes are involved in the online statistical learning of Chinese orthographic regularities. One way to address these questions is to apply the ERP approach, which provides a continuous recording of brain activity at millisecond resolution [23]. Since ERPs are time-locked to the onset of stimuli, we were able to disentangle statistical learning processes that cannot be predicted from behavioral data alone, such as when statistical learning occurs [24].

Although no ERP studies have directly examined the neural process of orthographic statistical learning, some neural indicators have been shown to be associated with orthographic processing during word recognition. For example, the N170 or N1 component, a negative-going ERP component peaking at around 200 ms after stimulus onset with localization over the left occipital-temporal cortex in skilled readers, has been found to be a neural indicator of online orthographic processing in both children and adults [24, 25]. It has been proposed that perceptual expertise for orthographic regularities is associated with a larger N1 for word and word-like stimuli than for visual controls [26–28]. In addition, the available ERP studies on Chinese character processing with adults have demonstrated that semantic and phonetic radical activation occur at P200 and N400 during Chinese character recognition, suggesting that orthographic and phonological analyses are involved in the early stages of radical activation and in the later stages of lexical identification for character recognition [29–32]. The P200 component is believed to be sensitive to early orthographic processing during word recognition [33, 34]. A variety of cognitive processes contribute to the N400 effect, except for semantic inconsistency and unexpected sentence endings [35, 36].

In fact, some recent ERP studies have examined the neural process of statistical learning in speech and artificial grammar learning (for a review, see [35]). For example, Kooijman and colleagues [37] showed that 10-month-old pre-linguistic infants are sensitive to word boundaries in continuous speech, indexed by an N400-like component at the neural level. Also, Teinonen and colleagues [38] reported that even sleeping newborns are able to use the statistical patterns of speech input to detect word boundaries in a continuous stream of syllables containing no morphological cues. This sensitivity is reflected by a late negativity in the time-window from 340 to 390 ms [38]. Similarly, another ERP study with adults revealed that a larger N100 was elicited in the initial than the medial and final syllables of pseudowords for pre- and post-training phases in high learners but not low learners. A similar effect has also been found in the N400 component [39].

The present study applied the ERP approach to examine the neural correlates of orthographic statistical learning of

orthographic-semantic connection (i.e., semantic radicals) in Chinese. We manipulated semantic consistency, which is defined as the frequency of meaning indicated by a target semantic radical, using three consistency levels: low, moderate, and high. Since semantic radicals embody both positional regularities and functional regularities, we expect to find a semantic consistency effect in early ERP components, such as N170 or P200, which reflect the initial orthographic processing of visual features and the activation of sublexical units [24, 27, 31, 32], and at the later well-known semantic processing-related component, N400 [34, 35, 40]. More specifically, we hypothesized that (1) the most negative N170 occurs with high semantic consistency followed by moderate and low semantic consistency; (2) the mean amplitude for low semantic consistency is more positive than the other two levels in the P200 time-window; and (3) low semantic consistency produces a more negative N400 amplitude than the other two levels. These hypotheses were tested in the present study with native Mandarin-speaking Chinese adults using a visual statistical learning paradigm described below.

Methods

Participants

Nineteen native Mandarin Chinese speaking adults (12 females and 7 males) aged 18 to 26 were recruited to participate in the experiment. None of the participants had engaged in similar experiments before, and none had any neurological disease. All had normal or corrected-to-normal vision. Sixty Yuan ($\sim$9 U.S. dollars) was given to each participant to express our gratitude for his or her participation. Two participants' ERP data were excluded from the final data analysis, one because of excessive α wave activity, and the other because the accuracy in the learning phase was $<$50%. Ethical approval for this study was obtained from the Research Ethics Committee of Hangzhou Normal University, China.

Materials and Design

An ERP experiment was designed to investigate the neural processes involved in the online statistical learning of semantic regularities of radicals in Chinese. Statistical information in this experiment was manipulated by varying the semantic consistency of target radicals embedded in pseudocharacters. The learning stimuli comprised 15 artificial logographic characters and 15 matched pictures representing the meanings of the characters. These items were modified from a recent study by He *et al.* [10]. The 15 logographic characters were created by combing 3 target radicals with 5 control radicals. They were all left-right structures with a target radical (the semantic radical) located on the left and a control radical located on the right. Semantic radicals were selected from Dongba script, and control radicals were selected from Geba scrip, both of which are used by the Naxi minority in Western China [41]. The semantic radicals were manipulated to carry three levels of semantic consistency: high (100%), moderate (80%), and low (60%). At the high consistency level, all semantic radicals in five artificial characters represented meanings in the same semantic category (i.e., the five sense organs), which were illustrated by the pictures. For the moderate consistency, four of five semantic radicals represented the same semantic category while the fifth one indicated a different meaning (e.g., animals in four pictures and a specific animal body part in one picture). At the low semantic consistency level, three semantic radical represent different types of food, whereas the other two semantic radicals represent different food containers (e.g., a bowl and a cup). Examples of stimuli for each condition are shown in Table 1.

Procedure

Each participant was individually tested in a sound-attenuated EEG lab at the Huangzhou Normal University. Before the experiment, each participant was presented with and signed a written consent form, which had been approved by the Hangzhou Normal University research ethics committee. Participants were asked to complete two parts of the experiment consisting of a learning phase and a recognition test with a 2-min break in-between. Participants' neural activity was recorded only in the learning phase, while their response accuracy and reaction time were recorded in both phases.

In the learning phase, we used a modified statistical learning paradigm, which has been successfully used in previous studies [10], to record participants' statistical learning process. The stimuli were shown on a monitor using E-Prime 2.0 software (Psychology Software Tools, Pittsburgh, PA). Participants were exposed to a sequence of paired stimuli on the screen: an artificial logographic character on the left and a picture on the right. Fifteen pairs of stimuli were presented in a pseudorandomized sequence. Each of the 15 pairs was repeated 24 times for a total of 360 trials. At the beginning of each trial, a fixation "+" lasting 500 ms appeared on the monitor. Next, a blank screen appeared for 500 ms, followed by a character-picture pair for 2000 ms. After each stimulus presentation, a blank screen appeared for 1000 ms as the interstimulus interval. Participants were asked to respond to the consecutive identical pairs of stimuli by pressing the SPACEBAR key. With four consecutive repetitions for each pair, a total of 60 responses was required.

Table 1 Examples of experimental stimuli across three consistency conditions

Experimental condition	Description	Examples
100% semantic consistency	All five pictures describe five sense organs	
80% semantic consistency	Four pictures among five are animals, and the other is a specific animal body part	
60% semantic consistency	Three pictures among the five depict types of food, but the other two are food-related feelings	

In the recognition test, participants were shown each character from the learning phase with two pictures underneath (one correct and one unrelated). They were asked to select the picture that best represented the meaning of the presented character. The unrelated picture represented the meaning of another semantic radical. Fifteen test trials were presented in a pseudorandomized sequence. Stimuli remained visible until participants pressed the space bar. The procedures in the two phases are shown in Fig. 1.

Electroencephalography (EEG) Acquisition and Data Analysis

The EEG was recorded using the Brain Product 32-channel Ag/AgCl system (Brain Products GmbH) while participants performed the statistical learning task in the learning section. The EEG was continuously recorded at a sampling rate of 500 Hz with the FCz electrode as the online reference. Active electrode impedances were kept below 5 kΩ. The EEG was acquired with a 0.05–100 Hz band-pass. The EEG data were preprocessed using the EEGLAB toolbox [42]. The offline data were re-referenced to the average reference. Eye-blink artifacts were corrected using independent component analysis. The continuous EEG was segmented into epochs of –100 ms to 600 ms and time-locked to the target stimuli with an offline band-pass filter of 2–30 Hz. The ERPs were baseline-corrected at –100 ms pre-stimulus. Separate ERPs were averaged within each condition. We used the mean amplitude rather than peak amplitude to index the ERP components because this approach has many advantages over the peak amplitude approach [43]. For example, it has been suggested that mean amplitude is more reliable than peak amplitude

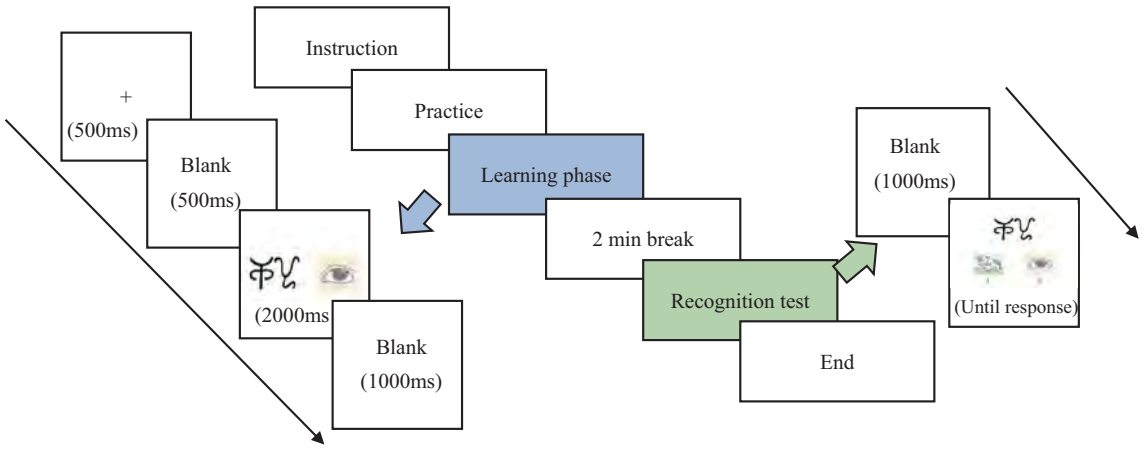

Fig. 1 Procedures of the visual statistical learning experiment.

because the latter is easily influenced by noise. In contrast, the mean amplitude filters out noise at high and intermediate frequencies [43]. In addition, the peak occurs at different times at different electrode sites, which conflicts with the hypothesis that an ERP component in the brain has the same timing at every electrode side. Furthermore, mean amplitude is insensitive to trial-to-trial latency variability, while peak amplitude is strongly influenced by such variability [43].

Consistency effects were assessed *via* comparisons of the mean amplitudes in three temporal windows of interest: N170 (150–210 ms), posterior P2 (210–280 ms), and N400 (220–400 ms). The components analyzed were obtained based on visual inspection, the peak of the component, and scalp map analysis. More specifically, for the N170 component, the time-window 180–240 ms was selected based on visual inspection of data and the peak in the grand average waveform (peaking $\sim$210 ms after the onset of the stimuli), and then the time-window was determined $\pm$30 ms from the peak. For the P200 component, we analyzed the scalp map for every 50-ms window and found clear topographic maxima in the positive field on the occipital-temporal area at both 250–300 ms and 300–350 ms, thus, the time-window analyzed for posterior P200 was from 250 to 350 ms. Finally, for the N400 component, the time-window 250–400 ms was based on visual inspection of the data and previous studies on N400 [44].

For the N170 component, four electrodes (P7, P8, O1, and O2) in the occipital-temporal areas were selected according to the topographic maxima in the negative field over both hemispheres across experimental conditions. The N170 amplitude was analyzed with repeated measures ANOVA with three within-subjects factors: experimental condition (low, moderate, and high consistency levels), laterality (left, right), and electrode (P7, P8, O1, and O2). For the P200 component, the same our electrodes were selected according to the topographic maxima in the positive field over both hemispheres across experimental conditions. The P200 amplitude was analyzed with repeated measures ANOVA using the same three within-subjects factors as for N170. The N400 amplitude was computed at nine electrodes (F3, Fz, F4, C3, Cz, C4, P3, Pz, and P4) and analyzed with repeated measures ANOVA with three within-subject factors: experimental condition (low, moderate, and high consistency levels), laterality (in the frontal, central, and parietal regions), and electrode (F3, Fz, F4, C3, Cz, C4, P3, Pz, and P4). For each ANOVA, the Greenhouse-Geisser adjustment to the degrees of freedom was used to correct for the violation of sphericity associated with repeated measures and Bonferroni adjustments was used for *post hoc* comparisons. The mean amplitudes and the topographic maps for N170, P200, and N400 are shown in Figs 2–6.

Results

Behavioral Results

In the learning phase, participants' response accuracy ranged from 76.7% to 100% with a mean of 94.9%, suggesting that all participants attended to the stimuli during the learning phase.

In the recognition test, participants' overall mean recognition accuracy was 63.1%, and it was significantly higher than chance [50%; t (16) = 2.58, $P < 0.05$]. One-sample t-tests revealed that recognition accuracy at the high consistency level was significantly higher than chance [Mean = 72.90%; t (16) = 4.75, $P < 0.001$]. However, there was no significant difference between recognition accuracy and chance at the moderate consistency level [Mean = 56.5%; t (16) = 0.86, $P = 0.40$], and at the low consistency level [Mean = 60.0%; t (16) = 1.37, $P = 0.19$]. These results show that participants might use statistical properties to extract the semantic consistency of semantic radicals embedded in the artificial logographic characters.

Two separate repeated measures ANOVAs with the experimental condition as a within-subject factor were conducted on accuracy rate and reaction time for the recognition test to further examine participants' sensitivity to the semantic consistency of radicals. For accuracy, the consistency effect was marginally significant [F (2, 32) = 2.72, $P = 0.08$, $\eta^2 = 0.15$]. Follow-up analyses revealed that the differences between the high and moderate consistency conditions ($P = 0.19$), between the high and low conditions ($P = 0.43$), and between the moderate and low conditions were not significant ($P = 1.00$). Furthermore, no significant difference was found among all three conditions in the reaction time [F (2, 32) = 0.12, $P = 0.89$, $\eta^2 = 0.01$].

ERP Results

N170

Repeated measures ANOVAs, with consistency level (low, moderate, and high), laterality (left and right) and electrode (P, O) as within-subjects factors, showed that the effect of consistency level was significant [F (2, 32) = 25.61, $P < 0.001$, $\eta^2 = 0.62$]. The follow-up comparisons showed that the mean amplitude for high (Mean = – 0.26 μV) and moderate consistency (Mean = – 0.47 μV) was significantly more negative than for low consistency (Mean = 0.63 μV) ($P < 0.001$); however, there was no significant difference between high and moderate consistency ($P = 0.89$). Neither the effect of laterality [F (1, 16) = 0.09, $P = 0.77$, η^2 =

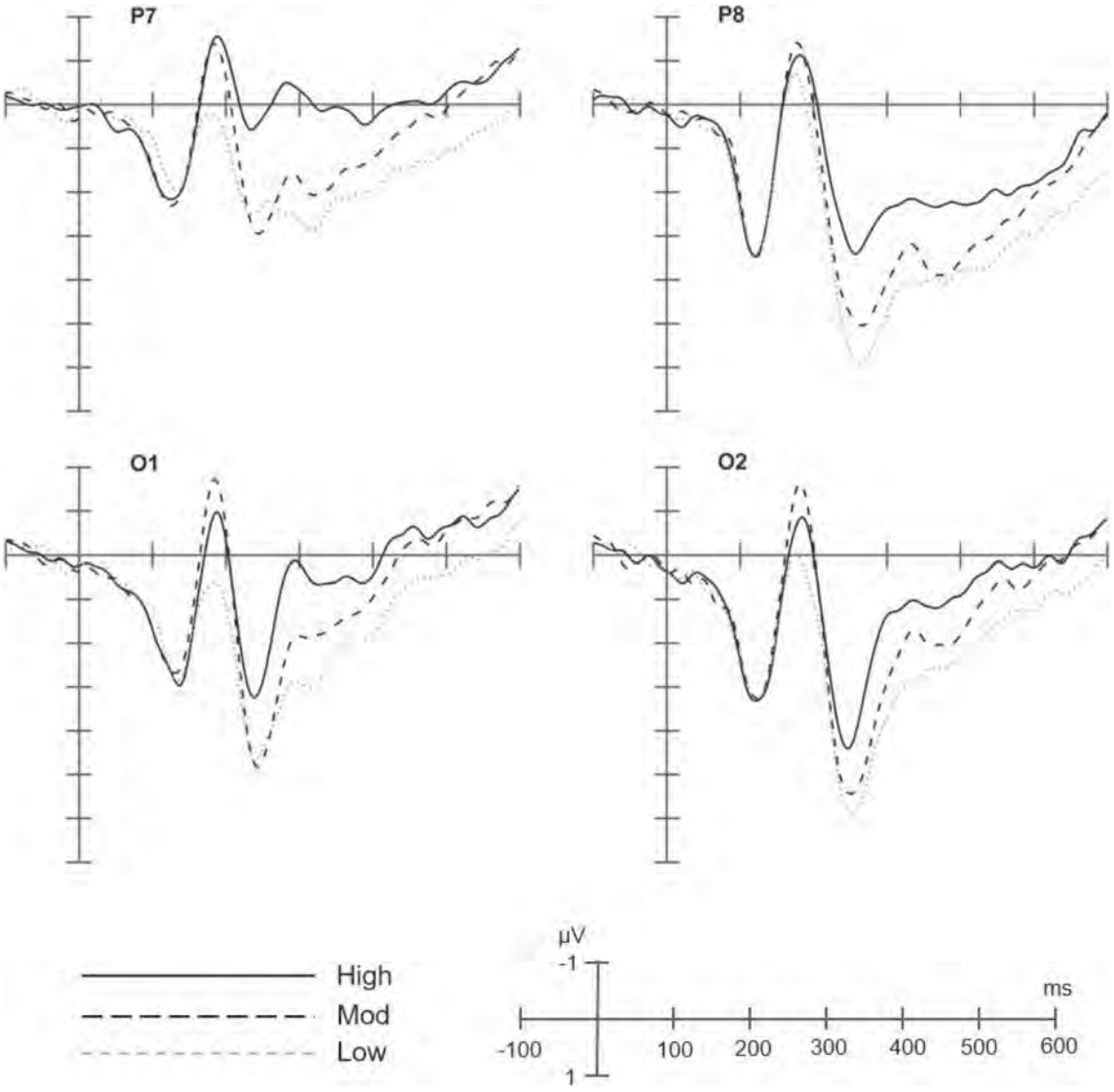

Fig. 2 Grand averaged ERP waveforms of low, moderate, and high consistency conditions at the P7, O1, P8, and O2 electrodes.

0.01] nor that of electrode [F (1, 16) = 1.77, P = 0.20, η^2 = 0.10] was significant.

The interaction of electrode by consistency level was significant [F (2, 32) = 14.48, $P < 0.001$, η^2 = 0.48], and the consistency effects were significant in both pairs of electrodes [P7/8: F (2, 32) = 27.40, $P < 0.001$, η^2 = 0.63; O1/2: F (2, 32) = 22.76, $P < 0.001$, η^2 = 0.59]. The follow-up contrasts revealed that, at the P7/8 electrodes, the mean

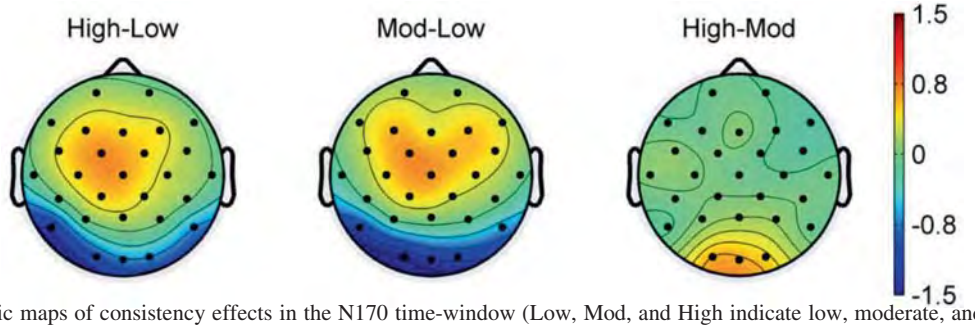

Fig. 3 Topographic maps of consistency effects in the N170 time-window (Low, Mod, and High indicate low, moderate, and high consistency levels).

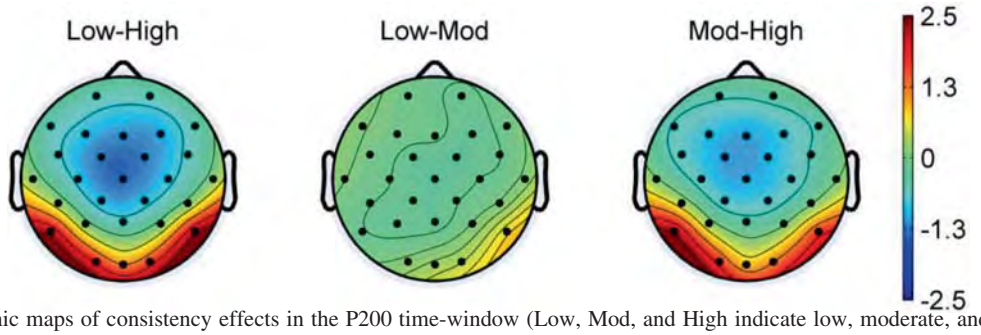

Fig. 4 Topographic maps of consistency effects in the P200 time-window (Low, Mod, and High indicate low, moderate, and high consistency levels).

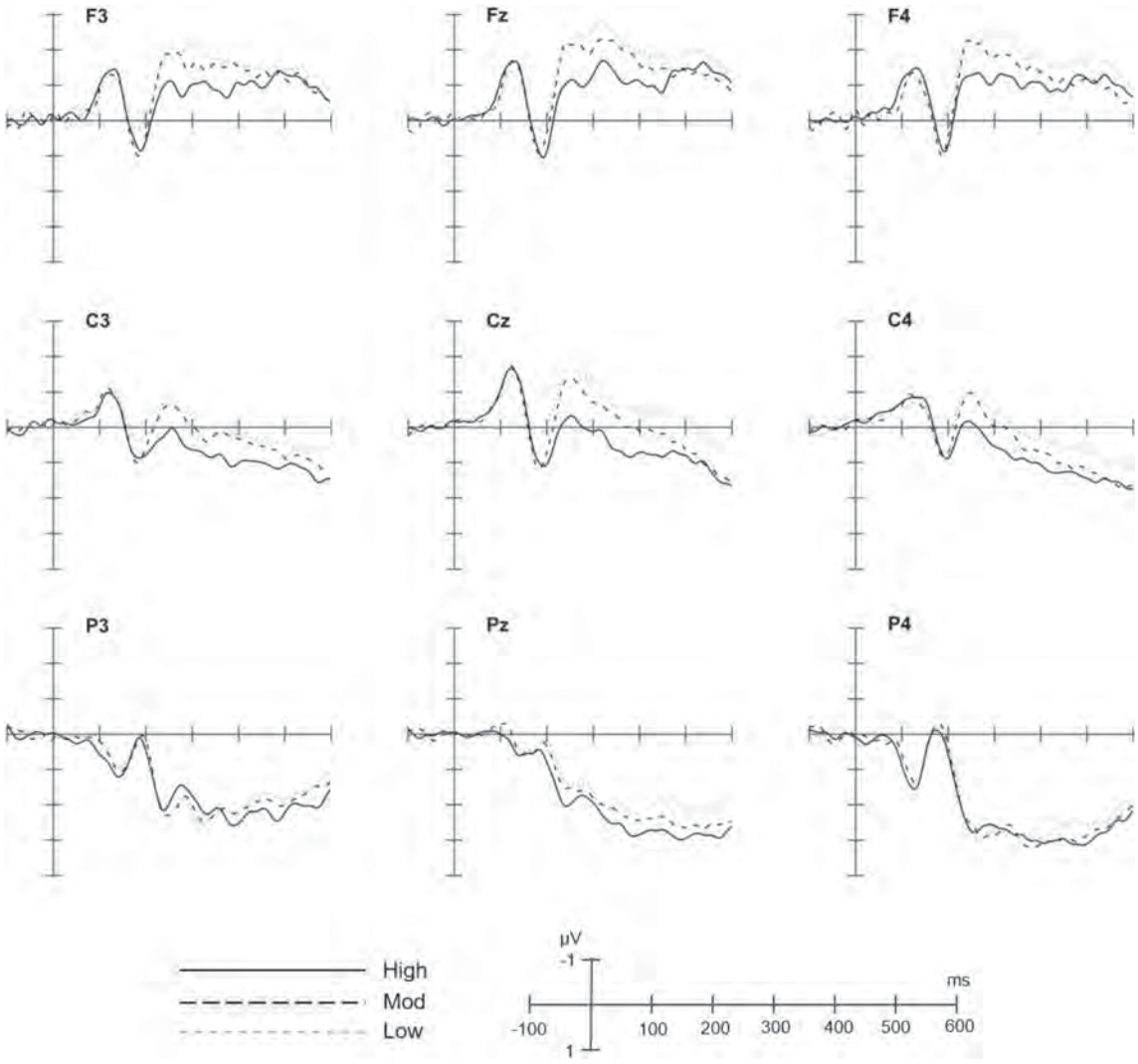

Fig. 5 Grand averaged ERP waveforms of low, moderate, and high consistency conditions at nine representative electrodes.

amplitudes for high and moderate consistency were more negative than for low consistency ($P < 0.001$), and the difference between high and moderate consistency was not significant ($P = 1.00$); at the O1/2 electrodes, the mean amplitudes for high and moderate consistency were more negative than for low consistency ($P < 0.001$), and the difference between high and moderate consistency was not significant ($P = 0.12$). No other effect was significant ($P > 0.11$).

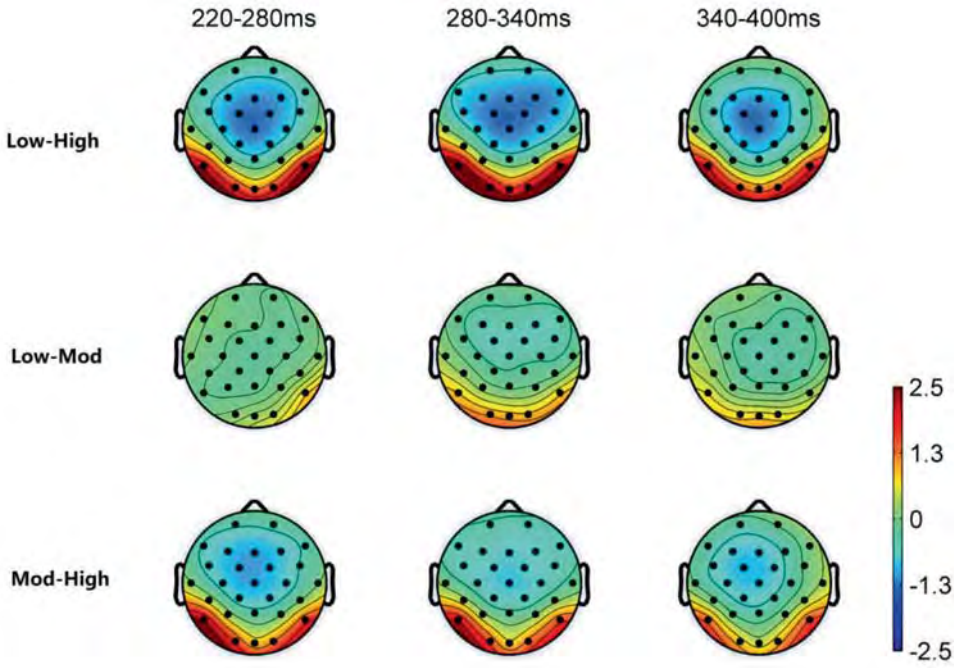

Fig. 6 Topographic maps of consistency effects in the N400 time-window (Low, Mod, and High indicate low, moderate, and high consistency levels).

Posterior P2

Repeated measures ANOVAs with consistency level (low, moderate, and high), laterality (left, right), and electrode (P, O) as within-subjects factors revealed that the consistency effect was significant [F (2, 32) = 50.14, $P < 0.001$, $\eta^2 = 0.76$]. Follow-up comparisons showed that the mean amplitudes for low (Mean = 4.18 μV) and moderate consistency (Mean = 3.91 μV) were more positive than for high consistency (mean, 2.24 μV) ($P < 0.001$), and the difference between low and moderate consistency was not significant $P = 0.34$). The main effect of laterality was significant [F (1, 16) = 9.38, $P < 0.01$, $\eta^2 = 0.37$], the mean amplitude in the right hemisphere was more positive than in the left hemisphere. The main effect of electrode was significant [F (1, 16) = 10.83, $P < 0.01$, $\eta^2 = 0.40$]; the mean amplitudes at the O1/2 electrodes were more positive than at the P7/8 electrodes.

The interaction of electrode by consistency level was significant [F (2, 32) = 7.89, $P < 0.01$, $\eta^2 = 0.33$]. The consistency effects were significant at both pairs of electrodes [P7/8: F (2, 32) = 51.02, $P < 0.001$, $\eta^2 = 0.76$; O1/2: F (2, 32) = 37.07, $P < 0.001$, $\eta^2 = 0.69$]. Follow-up contrasts revealed that, at the P7/8 and O1/2 electrodes, the mean amplitudes for low and moderate consistency were more positive than for high consistency ($P < 0.001$ for both pairs), and the difference between low and moderate consistency was not significant ($P = 0.41$ and 0.39). The interaction of laterality by electrode was significant [F (1, 16) = 7.50, $P < 0.05$, $\eta^2 = 0.32$]. In the right hemisphere, the effect of electrode was not significant [F (1, 16) = 1.18, $P = 0.29$, $\eta^2 = 0.07$], while in the left hemisphere it was significant [F (1, 16) = 16.05, $P < 0.01$, $\eta^2 = 0.50$], the mean amplitude in O1 was more positive than in P7. No other effect was significant ($P > 0.11$).

N400

Repeated measures ANOVAs with consistency level (low, moderate, and high), laterality (left, midline and right) and electrode (frontal, central, and parietal) as within-subjects factors revealed that the consistency effect was significant [F (2, 32) = 34.21, $P < 0.001$, $\eta^2 = 0.68$]. The follow-up comparisons showed that the mean amplitudes for low (mean, –0.14 μV) and moderate consistency (mean, 0.07 μV) were more negative than for high consistency (mean, 0.57 μV) ($P < 0.001$), and the mean amplitude for low consistency was more negative than for moderate consistency ($P = 0.05$). The main effect of laterality was not significant [F (2, 32) = 3.05, $P = 0.06$, $\eta^2 = 0.16$]. The mean amplitude in the midline region was not significantly more negative than in the left region ($P = 0.18$), and more negative than in the right region (marginally significant, $P = 0.07$). The main effect of electrode was significant [F (2, 32) = 50.52, $P < 0.001$, $\eta^2 = 0.76$]. The mean amplitudes for the frontal and central electrodes were more negative than for the parietal electrodes, and the mean amplitude for the frontal electrodes was more negative than for the central electrodes ($P < 0.001$).

The interaction of laterality by consistency level was significant [F (4, 64) = 4.29, $P < 0.01$, $\eta^2 = 0.21$]. In the left region, the effect of consistency level was significant [F (2,

32) = 12.47, $P < 0.001$, $\eta^2 = 0.44$]. The mean amplitudes for low and moderate consistency were more negative than for high consistency ($P < 0.01$), and the difference between low and moderate consistency was not significant ($P = 0.82$). In the midline region, the effect of consistency level was significant [F (2, 32) = 32.51, $P < 0.001$, $\eta^2 = 0.67$]. The mean amplitudes for low and moderate consistency were more negative than for high consistency ($P < 0.001$), and the difference between low and moderate consistency was not significant ($P = 0.06$). In the right region, the effect of consistency was significant [F (2, 32) = 20.93, $P < 0.001$, $\eta^2 = 0.57$]. The mean amplitude for low consistency was more negative than for high consistency ($P < 0.001$), the mean amplitude for moderate consistency was more negative for high consistency ($P < 0.01$), and the mean amplitude for low consistency was more negative than for moderate consistency ($P < 0.05$).

The interaction of electrode by consistency level was significant [F (4, 64) = 12.64, $P < 0.001$, $\eta^2 = 0.44$]. In frontal electrodes, the effect of consistency was significant [F (2, 32) = 28.21, $P < 0.001$, $\eta^2 = 0.64$]. The mean amplitudes for low and moderate consistency were more negative than for high consistency ($P < 0.001$), and the difference between low and moderate consistency was not significant ($P = 0.20$). In central electrodes, the effect of consistency was significant [F (2, 32) = 44.18, $P < 0.001$, $\eta^2 = 0.73$]. The mean amplitudes for low and moderate consistency were more negative than for high consistency ($P < 0.001$), and the mean amplitude for low consistency was more negative than for moderate consistency ($P < 0.05$). In parietal electrodes, the effect of consistency was not significant [F (2, 32) = 0.39, $P = 0.68$, $\eta^2 = 0.02$].

The interaction of laterality by electrode was significant [F (4, 64) = 3.77, $P < 0.01$, $\eta^2 = 0.19$]. In frontal electrodes, the effect of laterality was not significant [F (2, 32) = 1.94, $P = 0.16$, $\eta^2 = 0.11$], as was the case in central electrodes [F (2, 32) = 2.71, $P = 0.08$, $\eta^2 = 0.15$]. In parietal electrodes, the effect of laterality was significant [F (2, 32) = 4.65, $P < 0.05$, $\eta^2 = 0.23$]. The mean amplitude in the midline region was more negative than in the right region ($P < 0.05$), and the difference between midline and left regions was not significant ($P = 1.00$).

Discussion

In the present study, we used an ERP approach to examine the neural process of statistical learning of orthographic–semantic connections in Chinese adult learners by manipulating the consistency levels of semantic radicals embedded in artificial logographic characters. The behavioral results were consistent with previous studies showing that Chinese adult learners can use the statistical information to extract the regularities of semantic radicals. The ERP results revealed that semantic consistency had two early ERP effects in the posterior N170 and P200 time-windows, and one late ERP effect in the N400 time-window. More specifically, the high and moderate consistency levels produced more negative amplitudes than the low consistency level at N170, and the mean amplitudes for moderate and low consistency were more positive than for high consistency at P200. Consistency also modulated the N400 amplitude with low consistency producing more negative amplitudes than moderate and high consistency, and moderate consistency eliciting more negative amplitudes than high consistency.

Our findings extend previous behavioral and computational modeling studies by providing neurophysiological evidence that statistical learning plays an important role in Chinese learners' acquisition of orthographic–semantic connections. The results also revealed that the process of statistical learning of semantic radical regularities involved different neural processes, namely, the N170-P200-N400 pattern. Although no empirical studies have directly examined the neural process of statistical learning of Chinese orthographic regularities, research on the consistency effect in Chinese visual word recognition has reported a similar ERP pattern. Lee *et al*. [39] investigated the neural locus of the consistency effect of phonetic radicals of Chinese characters and reported that the low-consistency characters produce a greater N170 amplitude in the temporal–occipital region and a greater P200 amplitude in the frontal region than the high-consistency characters, and that high-consistency characters elicit a greater N400 amplitude than low-consistency characters. The authors concluded that low-consistency characters and high-consistency characters might be associated with different neural processes in which a greater activation reflects the initial analysis of the orthographic and phonological representations for low-consistency characters while a greater lexical competition occurs in the later stage for the high-consistency characters.

Similar to the N170 effect found in the study of Lee *et al*. [45], the high and moderate consistency levels in the present study elicited a more negative N170 than the low consistency level. The occipital–temporal N170 has been confirmed to be associated with visual word form identification at the early stages of visual word recognition [24, 26, 27, 45] with familiar words eliciting a more negative N170 than unfamiliar words or visual controls [24, 25, 46]. Our findings extended the N170 effect in orthographic identification to orthographic learning. Here, we manipulated the semantic radicals embedded in the artificial characters. Semantic radicals in Chinese not only have a functional role to indicate the meaning of the characters, but they also possess positional regularities with

location at the left in left-right structured characters or at the top in top-bottom structured characters [13]. During the learning process, it is highly likely that learners might first analyze the positional information of semantic radicals after repeated exposure to the learned stimuli, which then activates the neural process associated with early orthographic form identification, indexed in this study by the N170 component.

The consistency effect was also reflected in the P200 component with distribution over the posterior brain region. P200 has been suggested to indicate selective attention [46], a visual feature-detection process [47], and graphic processing [32], and has also been interpreted as reflecting both orthographic and phonological processing at the sublexical level in visual word recognition [31]. For example, previous studies have shown that a syllable-frequency effect is found at the P200 time-window with a more positive amplitude for a low syllable frequency than for a high syllable frequency at the frontal brain region [31, 47]. In the present study, the P200 effect may reflect the learning process for semantic forms that require attention or temporary memory. More specifically, the differences across high, moderate, and low semantic consistency levels were in the number of pictures representing meanings associated with a given semantic radical. At the high consistency level, all pictures represented meanings in the same semantic category; at the moderate consistency level, four pictures represented animals and one picture represented a specific animal body part; and at the low semantic consistency level, three pictures depicted types of food, whereas two depicted different food containers (e.g., bowl and cup). The differences across conditions might lead to greater activation for low consistency than for high and moderate consistency during the early stage of analyzing the orthographic or semantic representation of the given semantic radicals, which was indicated by the greater positivity at the P200 component.

The consistency levels also modulated the N400 component in the present study. N400 is a stable neural indicator related to semantic processing, and its amplitude is modulated by semantic associations in which a less negative amplitude is found for words having many semantic associations in the sentence context [35]. In addition, N400 is sensitive to repetition and semantic priming [33, 40]. The N400 component has also been reported in a few studies to be involved in the neural process of statistical learning in speech or word segmentation [39, 48, 49]. This component is interpreted as reflecting a possible lexical search process triggered by segmental words in word segmentation [39]. In another study, Abla *et al*. [49] found a significant group effect on the N400 component with a larger word-onset effect in the early learning session in high learners and in the later session in middle learners, but with no such effect in low learners. They thus suggest that the N400 component may also reflect the degree of on-line statistical learning. In the present study, the low consistency level produced the most negative N400 amplitude followed by the moderate and high consistency levels. We propose that N400 reflects the semantic processing of semantic radicals during online statistical learning of semantic radicals.

The present findings offer unique contributions to the modeling of orthographic learning and provide neurophysiological evidence supporting the connectionist orthographic learning model of Chinese [10]. Similar to the triangle network of connectionist models proposed, the connectionist orthographic learning model of Chinese assumes that word representation is presented by a triangular network of three interrelated structural components (orthography, phonology, and semantics), as well as the connections between the three components. This model also suggests that statistical learning facilitates the formation of both orthography–phonology and orthography–semantic correspondences, and then helps to construct orthographic representations during word learning [10]. Using an implicit learning task with the ERP technique, we further identified the robust role of statistical learning that underlines orthographic learning. We extended previous behavioral studies by showing that statistical learning of orthographic–semantic connections in Chinese involves different neural responses at different stages, revealing that N170, P200, and N400 index the learning from visual word form to sub-lexical orthography and then to the meaning process.

Taken together, the ERP evidence can be considered as further empirical support for the hypothesis that statistical learning is a robust mechanism that accounts for orthographic learning in Chinese. That is, Chinese adult learners rapidly acquire the regularities of semantic radicals by using statistical information. More importantly, the findings provide a temporal sequence of the neural process of statistical learning of orthographic–semantic connections in Chinese and different brain indexes associated with this learning process, i.e., a clear N170–P200–N400 pattern. The initial potential shifts (N170 and P200) may reflect orthographic or graphic form identification located in posterior brain regions [49], while the later component (N400) may be associated with semantic information analysis. Furthermore, our findings corroborate the importance of the N170–P200–N400 components as ERP indexes of visual word processing and their involvement in fast orthographic–semantic regularity learning, suggesting that ERPs might reflect the implicit statistical learning of orthographic regularities more accurately than do behavioral assessments.

Acknowledgements This work was supported, in part, by the General Research Fund of the Hong Kong Government Research Grant Council (17609518), the Early Career Scheme of the Hong Kong Grants Council (28606419), and the National Natural Science Foundation of China (31600903).

Conflict of interest The authors claim that there are no conflicts of interest.

References

1. Meltzoff AN, Kuhl PK, Movellan J, Sejnowski TJ. Foundations for a new science of learning. Science 2009, 325: 284–288.
2. Arciuli J, Simpson IC. Statistical learning in typically developing children: The role of age and speed of stimulus presentation. Dev Sci 2011, 14: 464–473.
3. Turk-Browne NB, Scholl BJ, Chun MM, Johnson MK. Neural evidence of statistical learning: Efficient detection of visual regularities without awareness. J Cogn Neurosci 2009, 21: 1934–1945.
4. Brady TF, Oliva A. Statistical learning using real-world scenes: Extracting categorical regularities without conscious intent. Psychol Sci 2008, 19: 678–685.
5. Nissen MJ, Bullemer P. Attentional requirements of learning: Evidence from performance measures. Cogn Psychol 1987, 19: 1–32.
6. Chater N, Manning CD. Probabilistic models of language processing and acquisition. Trends Cogn Sci 2006, 10: 335–344.
7. Kuhl PK. Early language acquisition: cracking the speech code. Nat Rev Neurosci 2004, 5: 831–843.
8. Erickson LC, Thiessen ED. Statistical learning of language: Theory, validity, and predictions of a statistical learning account of language acquisition. Dev Rev 2015, 37: 66–108.
9. Share DL. Orthographic learning at a glance: On the time course and developmental onset of self-teaching. J Exp Child Psychol 2004, 87: 267–298.
10. He X, Tong X. Statistical learning as a key to cracking Chinese orthographic codes. Sci Stud Read 2017, 21: 60–75.
11. Yang J, McCandliss BD, Shu H, Zevin JD. Simulating language-specific and language-general effects in a statistical learning model of Chinese reading. J Mem Lang 2009, 61: 238–257.
12. Shu H, Chen X, Anderson RC, Wu N, Xuan Y. Properties of school Chinese: Implications for learning to read. Child Dev 2003, 74: 27–47.
13. Tong X, McBride C. Chinese children's statistical learning of orthographic regularities: Positional constraints and character structure. Sci Stud Read 2014, 18: 291–308.
14. Perfetti CA, Liu Y, Tan LH. The lexical constituency model: some implications of research on Chinese for general theories of reading. Psychol Rev 2005, 112: 43–59.
15. Taft M, Zhu X, Peng D. Positional specificity of radicals in Chinese character recognition. J Mem Lang 1999, 40: 498–519.
16. Zhou X, Marslen-Wilson W. The nature of sublexical processing in reading Chinese characters. J Exp Psychol Learn Mem Cogn 1999, 25: 819–837.
17. Chen MJ, Weekes BS. Effects of semantic radicals on Chinese character categorization and character decision. Chin J Psychol 2004, 46: 181–196.
18. Williams C, Bever T. Chinese character decoding: a semantic bias? Read Writ 2010, 23: 589–605.
19. Ho CS, Ng TT, Ng WK. A "radical" approach to reading development in Chinese: The role of semantic radicals and phonetic radicals. J Lit Res 2003, 35: 849–878.
20. Tong X, Tong X, McBride C. Radical sensitivity is the key to understanding Chinese character acquisition in children. Read Writ 2017, 30: 1251–1265.
21. Wang M, Liu Y, Perfetti CA. The implicit and explicit learning of orthographic structure and function of a new writing system. Sci Stud Read 2004, 8: 357–379.
22. Yin L, McBride C. Chinese kindergartners learn to read characters analytically. Psychol Sci 2015, 26: 424–432.
23. Molfese DL, Molfese VJ, Espy KA. The predictive use of event-related potentials in language development and the treatment of language disorders. Dev Neuropsychol 1999, 16: 373–377.
24. Howard-Jones PA, Varma S, Ansari D, Butterworth B, De Smedt B, Goswami U, *et al*. The principles and practices of educational neuroscience: comment on bowers. Psychol Rev 2016, 123: 620–627.
25. Maurer U, Zevin JD, McCandliss BD. Left-lateralized N170 effects of visual expertise in reading: evidence from Japanese syllabic and logographic scripts. J Cogn Neurosci 2008, 20: 1878–1891.
26. Bentin S, Mouchetant-Rostaing YO, Giard MH, Echallier JF, Pernier J. ERP manifestations of processing printed words at different psycholinguistic levels: time course and scalp distribution. J Cogn Neurosci 1999, 11: 235–260.
27. Lin SE, Chen HC, Zhao J, Li S, He S, Weng XC. Left-lateralized N170 response to unpronounceable pseudo but not false Chinese characters—the key role of orthography. Neuroscience 2011, 190: 200–206.
28. Wong AC, Gauthier I, Woroch B, Debuse C, Curran T. An early electrophysiological response associated with expertise in letter perception. Cogn Affect Behav Neurosci 2005, 5: 306–318.
29. Hsiao JH, Shillcock R, Lee CY. Neural correlates of foveal splitting in reading: Evidence from an ERP study of Chinese character recognition. Neuropsychologia 2007, 45: 1280–1292.
30. Hsu CH, Tsai JL, Lee CY, Tzeng OJ. Orthographic combinability and phonological consistency effects in reading Chinese phonograms: an event-related potential study. Brain Lang 2009, 108: 56–66.
31. Lee CY, Tsai JL, Huang HW, Hung DL, Tzeng OJ. The temporal signatures of semantic and phonological activations for Chinese sublexical processing: An event-related potential study. Brain Res 2006, 1121: 150–159.
32. Liu Y, Perfetti CA, Hart L. ERP evidence for the time course of graphic, phonological, and semantic information in Chinese meaning and pronunciation decisions. J Exp Psychol Learn Mem Cogn 2003, 29: 1231–1247.
33. Kong L, Zhang B, Zhang JX, Kang C. P200 can be modulated by orthography alone in reading Chinese words. Neurosci Lett 2012, 529: 161–165.
34. Perfetti CA, Liu Y. Orthography to phonology and meaning: Comparisons across and within writing systems. Read Writ 2005, 18: 193–210.
35. Kutas M, Hillyard SA. Reading senseless sentences: Brain potentials reflect semantic incongruity. Science 1980, 207: 203–205.
36. Daltrozzo J, Conway CM. Neurocognitive mechanisms of statistical-sequential learning: what do event-related potentials tell us? Front Hum Neurosci 2014, 8: 437.
37. Kooijman V, Hagoort P, Cutler A. Electrophysiological evidence for prelinguistic infants' word recognition in continuous speech. Brain Res Cogn Brain Res 2005, 24: 109–116.
38. Teinonen T, Fellman V, Näätänen R, Alku P, Huotilainen M. Statistical language learning in neonates revealed by event-related brain potentials. BMC Neurosci 2009, 10: 21.
39. Sanders LD, Newport EL, Neville HJ. Segmenting nonsense: an event-related potential index of perceived onsets in continuous speech. Nat Neurosci 2002, 5: 700–703.
40. Holcomb PJ, Neville HJ. Auditory and visual semantic priming in lexical decision: A comparison using event-related brain potentials. Lang Cogn Process 1990, 5: 281–312.

41. Li X. Study on He Hong's dongba manuscripts collected by American Harvard-Yenching Library. Adv in Anth 2014, 4: 13–17.
42. Delorme A, Makeig S. EEGLAB: an open source toolbox for analysis of single-trial EEG dynamics including independent component analysis. J Neurosci Methods 2004, 134: 9–21.
43. Luck SJ. An Introduction to the Event-Related Potential Technique. 2nd ed. MIT Press, 2014.
44. Lau EF, Phillips C, Poeppel D. A cortical network for semantics:(de) constructing the N400. Nat Rev Neurosci 2008, 9: 920–933.
45. Lee CY, Tsai JL, Chan WH, Hsu CH, Hung DL, Tzeng OJ. Temporal dynamics of the consistency effect in reading Chinese: an event-related potentials study. Neuroreport 2007, 18: 147–151.
46. Maurer U, Brandeis D, McCandliss BD. Fast, visual specialization for reading in English revealed by the topography of the N170 ERP response. Behavl Brain Funct 2005, 1:13.
47. Hackley SA, Woldorff M, Hillyard SA. Cross-modal selective attention effects on retinal, myogenic, brainstem, and cerebral evoked potentials. Psychophysiology 1990, 27: 195–208.
48. Cunillera T, Toro JM, Sebastián-Gallés N, Rodríguez-Fornells A. The effects of stress and statistical cues on continuous speech segmentation: an event-related brain potential study. Brain Res 2006, 1123: 168–178.
49. Abla D, Katahira K, Okanoya K. On-line assessment of statistical learning by event-related potentials. J Cogn Neurosci 2008, 20: 952–964.

Neurosci. Bull. August, 2020, 36(8):907–918
https://doi.org/10.1007/s12264-020-00509-3

www.neurosci.cn
www.springer.com/12264

ORIGINAL ARTICLE

Responses of Primary Afferent Fibers to Acupuncture-Like Peripheral Stimulation at Different Frequencies: Characterization by Single-Unit Recording in Rats

Ran Huo[1,2,3,4] · Song-Ping Han[1,2,3] · Feng-Yu Liu[1,2,3] · Xiao-Jing Shou[1,2,3] · Ling-Yu Liu[1,2,3] · Tian-Jia Song[1,2,3] · Fu-Jun Zhai[1,2,3] · Rong Zhang[1,2,3,5] · Guo-Gang Xing[1,2,3,5] · Ji-Sheng Han[1,2,3]

Received: 16 June 2019 / Accepted: 18 January 2020 / Published online: 11 May 2020

Abstract The pain-relieving effect of acupuncture is known to involve primary afferent nerves (PANs) *via* their roles in signal transmission to the CNS. Using single-unit recording in rats, we characterized the generation and transmission of electrical signals in Aβ and Aδ fibers induced by acupuncture-like stimuli. Acupuncture-like signals were elicited in PANs using three techniques: manual acupuncture (MAc), emulated acupuncture (EAc), and electro-acupuncture (EA)-like peripheral electrical stimulation (PES). The discharges evoked by MAc and EAc were mostly in a burst pattern with average intra-burst and inter-burst firing rates of 90 Hz and 2 Hz, respectively. The frequency of discharges in PANs was correlated with the frequency of PES. The highest discharge frequency was 246 Hz in Aβ fibers and 180 Hz in Aδ fibers. Therefore, EA in a dense-disperse mode (at alternating frequency between 2 Hz and 15 Hz or between 2 Hz and 100 Hz) best mimics MAc. Frequencies of EA output >250 Hz appear to be obsolete for pain relief.

Keywords Acupuncture · Peripheral electrical stimulation · Dorsal root · Primary afferent fiber · Electrophysiology · Single unit recording

Ran Huo and Song-Ping Han have contributed equally to this work.

Electronic supplementary material The online version of this article (https://doi.org/10.1007/s12264-020-00509-3) contains supplementary material, which is available to authorized users.

✉ Guo-Gang Xing
ggxing@bjmu.edu.cn

✉ Ji-Sheng Han
hanjisheng@bjmu.edu.cn

[1] Neuroscience Research Institute, Peking University, Beijing 100191, China

[2] Department of Neurobiology, Peking University School of Basic Medical Sciences, Beijing 100191, China

[3] Key Laboratory for Neuroscience, Ministry of Education/ National Health and Family Planning Commission, Peking University, Beijing 100191, China

[4] Department of Radiology, Peking University Third Hospital, Beijing 100191, China

[5] Department of Integration of Chinese and Western Medicine, Peking University School of Basic Medical Sciences, Beijing 100191, China

Introduction

As an important technique in Traditional Chinese Medicine, acupuncture may be the most frequently used alternative and complimentary technique world-wide due to its prominent therapeutic effects. However, the consistency and reproducibility of these effects need further improvement. A better understanding of the mechanisms underlying the current technology and concepts is critical to making this thousand-year old technique more effective. We designed the present study to explore the production, processing, and transmission of acupuncture-like signals from the periphery to the CNS where various neurotransmitters and neuropeptides are released to activate descending analgesic pathways [2, 12, 14].

Manipulation techniques such as lifting, inserting, and twisting are considered to be critical in acupuncture therapy [4, 7]. Previous studies have shown that various manipulation styles produce distinctive patterns of brain activity [1, 8, 18, 26, 28]. Three techniques were used in the present study to elicit acupuncture-like signals: manual acupuncture (MAc), electro-acupuncture (EA), and EA-like peripheral electrical stimulation (PES).

It has been shown that the discharge activity in the sciatic nerve tract, a fine nerve bundle in the spinal dorsal root, and wide dynamic range neurons, is elevated in response to MAc or EA applied to the Zusanli acupoint (ST36) in the leg [16, 25, 36]. However, compound action potentials recorded in a nerve bundle do not permit the characterization and analysis of activity in an individual afferent fiber. Using single-unit recording from the dorsal root (DR) of lumbar segments 4 and 5 (L4/5), we set out to determine how acupuncture-induced electrical signals in primary fibers (acupuncture signals) are transmitted from the terminals of PANs to the CNS.

It is controversial as to which type of PAN is involved in transmitting acupuncture signals to the CNS. In the present work, we focused on Aβ and Aδ fibers since we have shown that they are the most important types of PAN in transmitting the acupuncture signal at least in the context of anti-nociception. Some investigators have shown that all the four populations of afferent fibers, including C-fibers, are activated by acupuncture-like stimulation [19, 20, 37]; however, the C-fiber activation usually requires very strong stimulation and is accompanied by an uncomfortable sensation.

An important finding in our previous studies of EA therapy was the frequency-dependence, which might be more critical than any other parameters. For example, the types of opioid peptides released and the analgesic effect produced by EA are all frequency-dependent [11]. Low (2 Hz)- and high (100 Hz)-frequency EA activates different neural pathways, releases different endorphins, causes binding to different receptors, and has different therapeutic effects [13, 15, 32, 33]. However, information is limited on how the signal is produced and processed in PANs by acupuncture-like stimulation at various frequencies. This information is critical in our efforts to further optimize EA parameters.

In the present study, we set out to accomplish three goals: (1) to characterize the firing patterns in Aβ- and Aδ-fibers in response to various forms of mechanical stimulation at the ST36 acupoint; (2) to explore how PES signals at the optimal frequency, pulse-width, and intensity are processed in PAN fibers; and (3) to assess the conduction efficiency of PAN fibers in response to PES over the whole range of clinically-relevant frequencies (100 Hz–1000 Hz).

Materials and Methods

Animals

Male Sprague-Dawley rats weighing 250 g–350 g were obtained from the Department of Experimental Animal Sciences, Peking University Health Science Center. They were housed no more than 4 per cage and maintained on artificial light 07:00–19:00 day/night cycles at a room temperature of 20°C–25°C, 50% relative humidity, and food and water freely available. All the animal experimental procedures were in line with the National Institutes of Health Guide for the Care and Use of Laboratory Animals, and were approved by Peking University Animal Use and Care Committee.

Neurophysiological Experiments

Single-Unit Recording

Each rat was anesthetized with urethane (1.4 g/kg, i.p.) and maintained with supplemental doses as needed. A tracheostomy was performed to keep the airway unobstructed. The left external jugular vein was cannulated for the slow administration of fluids and the arterial O_2 saturation was maintained at >90%. Heart rate (375 bpm–450 bpm) was monitored by a small animal vital signs monitor. Rectal temperature was maintained at 36.5°C–37.5°C throughout the experiments with cotton under the body and a heating lightbulb overhead. The pupil size, corneal reflex, skin color, and skeletal muscle reflexes were closely monitored during experiments. An experiment would be terminated if these physiological indicators appeared abnormal.

The erector spinae was separated from both sides of the spinous process and partially resected. In the prone position, a lumbosacral laminectomy was performed to expose the L4/5 DR. The roots were covered with warm paraffin oil at 37°C in a pool formed by skin flaps. The temperature of the paraffin oil was maintained at 36.5°C–37.5°C to avoid the influence of temperature on nerve fiber conduction velocity (CV).

The DR of the L4/5 spinal nerve on the left side was cut close to its entry into the spinal cord, teased from the DR using fine forceps, and mounted on a platinum wire electrode (0.2 mm in diameter) for recording, with the reference electrode connected to nearby tissue (Fig. 1A). Only nerve bundles without spontaneous activity or evoked firing by applying brush to the skin were further studied. Most of the data were collected from the L5 spinal nerve and a small proportion from the L4 spinal nerve; we pooled the two together for analysis. Data were captured and analyzed using Micro 1401 mk II coupled to a Pentium computer with Spike2 software (Cambridge Electronic Design, Cambridge, UK). Only neural signals with signal-to-noise ratios >1.5 were accepted for further analysis.

Measurement of Conduction Velocity of Single-Unit Afferent Fibers

In some of the PES experiments, the peripheral receptive located on the glabrous skin of the hind paw was identified

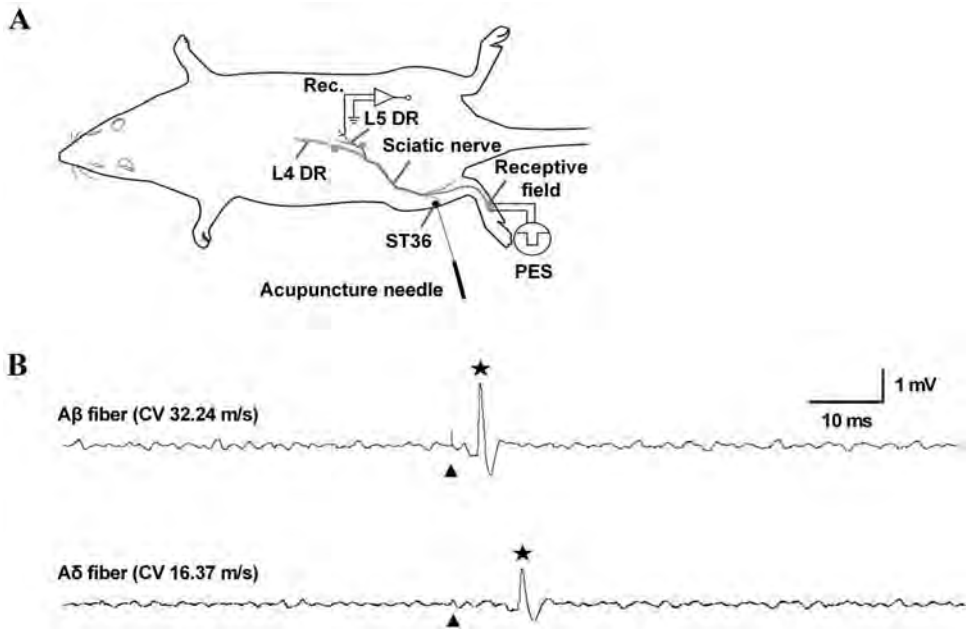

Fig. 1 Experimental setup for *in vivo* single-unit recording in the L4/5 DR. **A** Recording site on the left L4/5 DR and stimulating site at the ipsilateral ST36 (for MAc or EAc) or in the corresponding receptive field (for PES). **B** Example traces of evoked discharges (indicated by a star) recorded in an Aβ-fiber (conduction distance, 113 mm; latency, 3.30 ms; CV, 34.24 m/s) and an Aδ-fiber (conduction distance, 131 mm; latency. 8.00 ms; CV, 16.37 m/s) following a single square-wave stimulus applied to the corresponding receptive field. The single stimulus intensity (artifacts indicated by arrowheads) was 1.5 times the threshold of the afferent fiber. L4/5 DR, lumbar 4 or 5 dorsal root; ST36, Zusanli acupoint; MAc, manual acupuncture; EAc, emulation acupuncture PES, peripheral electrical stimulation; CV, conduction velocity.

using von Frey hairs after the target single-unit afferent fiber was identified. After locating the most sensitive point in the receptive field of the single-unit afferent fiber, the latency of the evoked discharge in the dissected dorsal root fiber was measured by stimulation with a negative square-wave (100 μs pulse width for Aβ fibers and 500 μs for Aδ fibers) at 1.5 times the threshold current delivered by a pair of electrodes inserted under the skin in parallel and centripetally (Fig. 1A) [5]. The CV of each afferent fiber was calculated as the distance between the stimulating and recording electrodes divided by the latency of the evoked discharge. Based on CV (without temperature correction), target fibers were classified as myelinated Aβ fibers (CV, 25 m/s–72 m/s) or thin myelinated Aδ fibers (CV, 2 m/s–24 m/s) (Fig. 1B) [17, 21].

Experimental Protocols

MAc and Emulated Acupuncture (EAc) at Human ST36 in Rats

After the hair of the left hind limb was shaved and before teasing out the single-unit fiber, a stainless-steel acupuncture needle (0.25 mm in diameter) was inserted into the site equivalent to human ST36 (5 mm lateral to the anterior tubercle of the tibia) (Fig. 1A). A rubber plug on the needle was positioned 7 mm from the tip to standardize the depth of insertion. Fiber types were not identified in these experiments.

In MAc, a target single-unit afferent fiber was identified if evoked discharges were recorded during MAc around ST36. Evoked discharges of the target fiber were continuously recorded when the acupuncture needle was twisted manually at a frequency of once or twice per second for 60 s (Fig. 2A).

Due to the high variation and low reproducibility of the needle manipulation parameters in MAc, a novel EAc apparatus (ZSF-I) was developed at Shanghai University of Traditional Chinese Medicine. The twirling angle (90°, 180°, or 360°) and number of times per second of needle twisting (one, two, or three times per second) can be set in any combination. A uniform speed of rotation was maintained during most of the time in one cycle of needle manipulation. The range of lifting and inserting the needle (up and down movement of the needle) was 3 mm to a maximum depth of 7 mm. The evoked discharges in the target fiber in response to EAc around ST36 were continuously recorded with various combinations of twirling angle and times per second of twisting in 60 s.

Data were collected with the aid of Spike2 software, and the firing rates and patterns of evoked discharges were analyzed off-line.

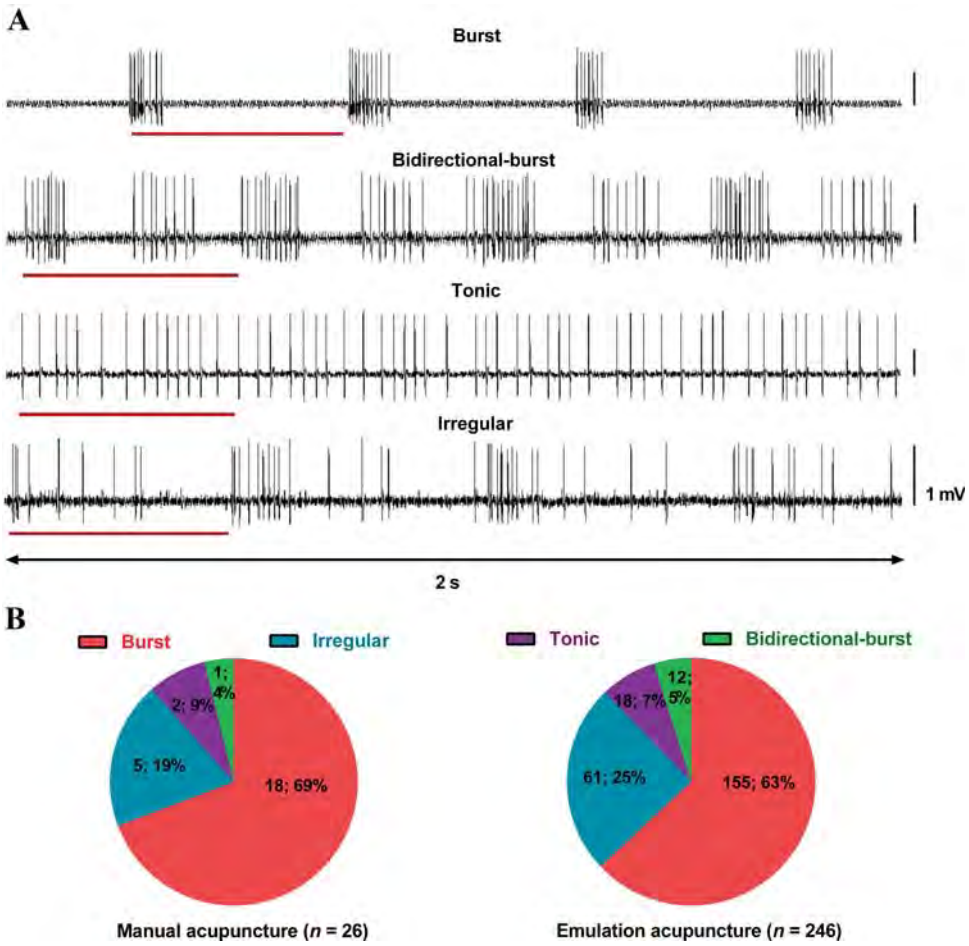

Fig. 2 Patterns of evoked discharges in single-unit afferent fibers of the L4/5 DR in response to MAc and EAc at ST36. **A** Representative traces of the four discharge patterns of single-units in response to MAc and EAc. The lines below traces represent one cycle of needle twisting (One time per second). **B** Distribution of the four types of discharge following MAc and EAc stimulation (number of recorded fibers; percentage). Note that the distributions are similar following MAc and EAc stimulation. L4/5 DR, lumbar 4 or 5 dorsal root; MAc, manual acupuncture; EAc, emulated acupuncture; ST36, Zusanli acupoint.

PES at Frequencies not Exceeding 100 Hz Delivered to the Receptive Fields of Afferent Fibers

Single-unit activity was recorded from a fiber in the dorsal root of the L4/5 spinal nerve on the left side when PES was delivered to its receptive field after measuring the latency of its evoked discharge. A pair of stimulating electrodes were connected to a constant-current stimulator (HANS-200A, Nanjing Jesen Co., Nanjing, China) (Fig. 1A). Alternating positive and negative rectangular square-wave pulses were delivered at various frequencies including single frequency (2 Hz, 15 Hz, and 100 Hz) and alternating frequency, also called a dense-disperse mode (EA or PES at alternating frequency between 2 Hz and 15 Hz [2/15 Hz] for 3 s each, or between 2 Hz and 100 Hz [2/100 Hz] for 3 s each) (Table 1). When the stimulation threshold of a target single-unit afferent fiber had been identified and then the current gradually increased, the responses to PES at the above frequencies were recorded. The activity of the target fiber was recorded continuously for 30 min during PES (intensity: 1–2 times the threshold current) at randomly-selected frequencies ($\leq$100 Hz). Data were analyzed using spike2 software. The response ratio was calculated as the ratio of the number of evoked discharges to the number of electrical stimuli delivered multiplied by 100.

PES at Frequencies Up to 1000 Hz Delivered to the Receptive Fields of Afferent Fibers in Rats

In these experiments, 100-Hz PES (negative square wave, pulse width, 100 μs; intensity, 2× threshold current) delivered to the receptive field for 60 s served as the positive control. Only single-unit afferent fibers with a 100% response ratio following PES at 100 Hz were studied further.

The activity of single units in response to PES (parameters as above) delivered to the receptive field at random frequencies (100 Hz, 200 Hz, 300 Hz, 400 Hz, 500 Hz, 600 Hz, 700 Hz, 800 Hz, 900 Hz, and 1000 Hz) was recorded continuously for 60 s. If the response ratio at any frequency was <100%, the results were validated by the presence of a normal response (response ratio, 100%) to PES at 100 Hz after the fiber was allowed to rest for 5 min. This procedure helped to exclude the artifact that the reduced response ratio was due to neuronal damage rather than the PES frequency exceeding the transduction capacity (i.e. the refractory period) of the fiber.

Table 1 Parameters of the HANS-200A stimulator.

Frequency (Hz)	Pulse Width (μs)	Wave-form
2	600	2 Hz as an example: 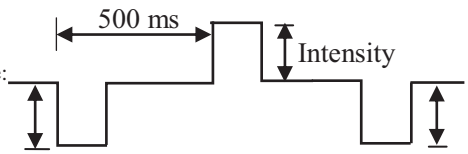
15	400	
100	200	
2/15	Alternating 2 Hz and 15 Hz for 3 s each	
2/100	Alternating 2 Hz and 100 Hz for 3 s each	

The data were collected and analyzed using the method described for PES at frequencies not exceeding 100 Hz.

Data Analysis

Statistical analysis was performed using SPSS ver. 19 (IBM Inc., Chicago, IL) and graphs were generated using Prism 6.0 (GraphPad Software Inc., San Diego, CA). Data from some of the EAc experiments were analyzed using non-parametric tests (Kruskal–Wallis test followed by Dunn's multiple comparisons test) and are presented as the median ± interquartile range for a non-normal distribution. Comparisons of response ratio–stimulus frequency between Aβ and Aδ fibers were analyzed by repeated measures ANOVA. Other comparisons between or among different groups used the unpaired *t* test or one-way ANOVA and values are expressed as the mean ± SEM unless otherwise specified. Differences with *P* values <0.05 (two-tailed) were considered significant.

Results

Characterization of Evoked Discharges in PAN Fibers by Mechanical Stimulation at Acupoint ST36

Characteristics of the Patterns of Evoked Discharges

All single-unit afferent fibers recorded in the present study were silent with no spontaneous discharges in the absence of mechanical acupuncture stimulation. The results showed four distinct firing patterns of discharge in fibers in response to MAc and/or EAc, summarized as follows (Fig. 2A, B):

1. Burst firing: recurring, abrupt discharges when the needle was rotated clockwise. There was no evoked discharge during anticlockwise rotation. This pattern was most common under all experimental conditions, accounting for 69% with MAc and 63% with EAc. Note that almost all the burst firing occurred when the needle was rotated to near its maximum angle (90°, 180°, or 360°).
2. Bidirectional-burst firing: burst firing when the needle was rotated both clockwise and anticlockwise. They made up 4% during MAc and 5% during EAc.
3. Tonic firing: a continuous and irregular pattern during needle manipulation. There was no clear difference among the inter-spike intervals (ISIs) of evoked discharges of a fiber. They constituted ∼9% in MAc and ∼7% in EAc.
4. Irregular firing: no particular pattern. All firing was included in this category except for the three types above. Again, more evoked discharges occurred when the needle was rotated clockwise than anticlockwise. They made up 19% in MAc and 25% in EAc.

Activity Level (Number of Evoked Spikes per Second) of PAN Fibers

Single-unit afferent fibers of the L4/5 spinal dorsal root in rats were activated by acupuncture-like mechanical stimulation at ST36. Only initially silent afferent bundles were examined in order to eliminate interference from spontaneous discharges.

In MAc, the discharge activity of 26 bundles from 11 rats was randomly divided into two groups: a one twist per second group (n = 12) and a two twists per second group (n = 14). There were more evoked spikes in the two-twists than in the one-twist group (7.7 ± 0.8 spikes/s *vs* 14.9 ± 1.5 spikes/s, $P < 0.001$, unpaired *t* test; Fig. 3A(a), B).

In the EAc experiments, the needle was inserted into the ST36 acupoint. In order to quantify the effects of various manipulation styles on discharge activity in PAN fibers, the needle rotation angle was preset to 90°, 180°, or 360°. At each rotation angle, the number of twists per second was delivered once, twice, or three times.

In the 90° EAc group, 84 bundles were recorded from 21 rats, and they were randomized into three groups with one, two, or three twists per second (n = 28, 27, and 29, respectively). The numbers of evoked spikes increased with the number of twists per second and the medians were 8.05, 14.80, and 20.00, respectively (Fig. 3A(b), C).

In the 180° EAc study, 81 bundles (28, 27, and 26 per group) were recorded from 22 rats, and in the 360° EAc study, 81 bundles (26, 28, and 27 per group) were recorded from 19 rats. Similar increases were found in the

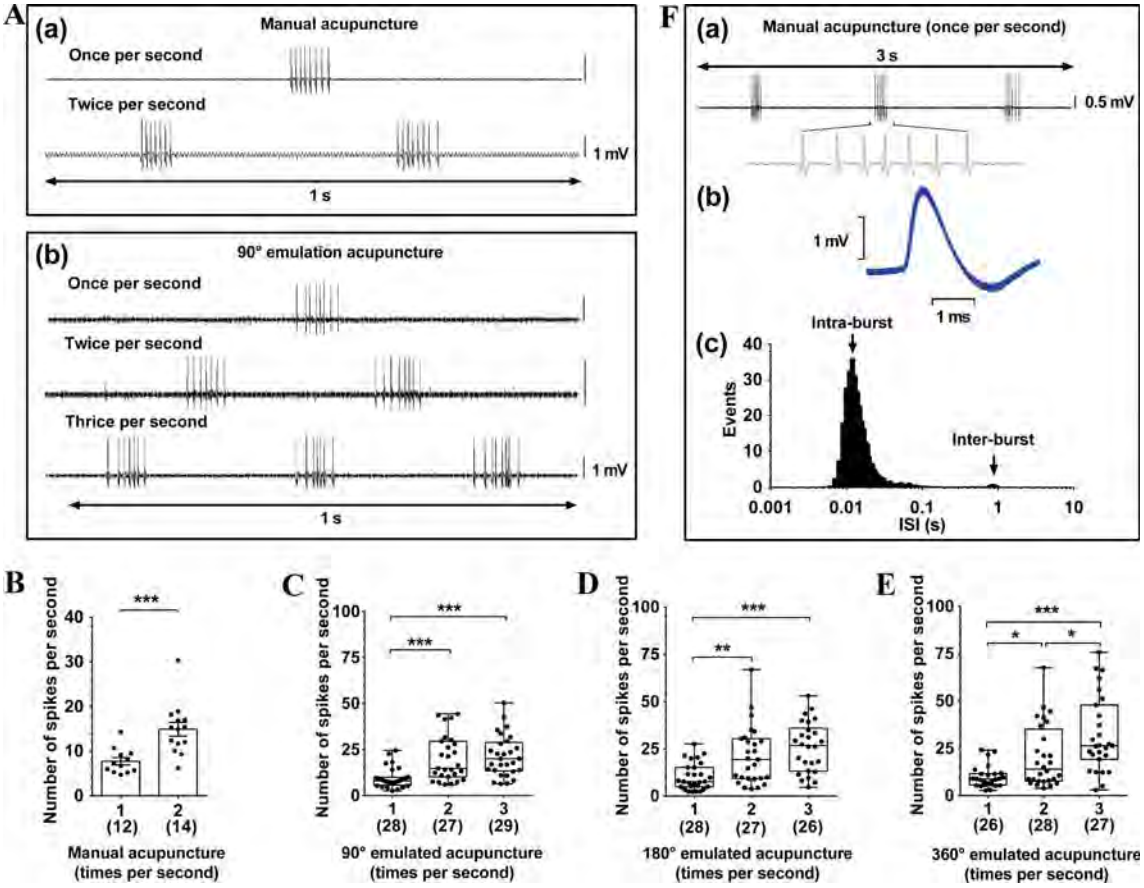

Fig. 3 Evoked discharges of single-unit afferent fibers in the L4/5 dorsal root in response to MAc and EAc at ST36. **A** Representative recordings from fibers in response to MAc and EAc at an angle of 90°. **B–E** More discharges were evoked with increasing numbers of twists per second with MAc (**B**) and EAc (**C–E**). **F** Representative recordings and ISI histogram of evoked burst firing in the same fiber in response to MAc (once/second). **(a)** Three-second recording during MAc. **(b)** Superimposed wavelet plot of all the evoked discharges in the fiber shown in **A** during MAc for 60 s (once per second). **(c)** ISI distribution within a burst (0.01 s–0.02 s, arrow) and between bursts (~1 s, arrow) (binwidth, 1 ms; a log scale (abscissa) was used to show all intervals). Data are expressed as the mean ± SEM (**B**, unpaired *t* test) or median and 25–75th percentiles (**C–E**, outliers beyond the 1.5 interquartile ranges were removed, non-parametric tests). Digits in brackets are the number of fibers. $*P < 0.05$, $**P < 0.01$, and $***P < 0.001$. ISI, inter-spike interval; MAc, manual acupuncture; EAc, emulated acupuncture; ST36, Zusanli acupoint.

180° (median, 7.65, 19.30, and 26.75; $P < 0.01$ or $P < 0.001$, Kruskal-Wallis test followed by Dunn's multiple comparisons test; Fig. 3D) and 360° groups (median, 8.75, 14.00, and 26.40; $P < 0.05$ or $P < 0.001$, test as for 180°; Fig. 3E).

There were no significant differences in the numbers of evoked spikes per second between the EAc groups with 90°, 180°, or 360° rotation (Fig. S1).

These data suggest that the number of times per second in a certain range of manipulating the needle is the most important factor affecting the level of the evoked response (spikes per second) to mechanical acupuncture. Furthermore, these data suggest that increases in the rotation angle of the needle under experimental conditions do not result in a higher level of activation of the afferent fibers in response to mechanical acupuncture.

ISIs of Evoked Discharges of PAN Fibers During MAc at Once per Second

Having demonstrated above that burst firing (Fig. 2B) was the most common pattern of evoked discharges in response to MAc at once per second, and given that MAc is used widely in clinical settings, we next focused on characterizing the firing pattern in MAc at once per second.

Twelve single-unit afferent fibers (11 burst firing and 1 irregular firing) were recorded from 5 rats in response to MAc at once per second. We examined the ISIs of evoked discharges of target fibers to explore the discharge distribution. Typical fiber recordings showed that the ISIs within a burst ranged from 0.01 s to 0.02 s. The mean frequency of evoked discharges within a burst was between 50 Hz and 100 Hz (frequency = 1/ISI) with a peak at 83 Hz (Fig. 3F).

Considering the limited number of non-bursting fibers, we focused the ISI analysis on burst firing (11 fibers). The results revealed that the evoked discharges could be further classified into two categories: burst firing and sporadic firing (Fig. 4A). A burst was defined by the following criteria: (1) a maximum ISI within a burst $\leq$0.019 s; (2) an ISI between bursts >0.1 s; and (3) $\geq$3 spikes per burst. Among the 11 bursting fibers, most of the ISIs were <0.02 s with a peak at 0.012 s and a minimum of 0.005 s (Fig. 4B). The results showed that the number of intra-burst spikes was 5.55 ± 0.43 (mean ± SEM), the frequency of evoked intra-burst discharges was 89.77 Hz ± 2.08 Hz, and the frequency of evoked inter-burst discharges was 2.36 Hz ± 0.30 Hz (Fig. 4C).

PES at Frequencies not Exceeding 100 Hz Delivered to the Receptive Fields of PAN Fibers

A total of 72 Aβ fibers were recorded from 21 rats and randomized into 2-Hz (n = 14), 15-Hz (n = 14), 2/15-Hz (n = 15), 100-Hz (n = 15), and 2/100-Hz groups (n = 14) (Fig. 5A). For Aδ fibers, 67 bundles were recorded from 32 rats with 14, 12, 13, 16, and 12 bundles in each of the frequency groups as described for Aβ fibers. The response ratio was used to describe the responses of neurons to a series of stimuli, and showed no significant differences between Aβ fibers and Aδ fibers in the response ratio to PES at each of the frequencies, at least in the initial 60 s of simulation (Aβ: 100% ± 0%, 100% ± 0%, 99.48% ± 0.52%, 99.27% ± 0.73%, and 99.44% ± 0.57%; Aδ: 100% ± 0%, 100% ± 0%, 100% ± 0%, 97.83% ± 1.51%, and 100% ± 0%; one-way ANOVA; Fig. 5B, C). Similarly, in studies with a longer stimulation/recording period (30 min), Aβ fibers retained an almost 100% response ratio during PES at the various specified frequencies (97.49% ± 2.50%, 97.85% ± 1.65%, 99.61% ± 0.39%, 93.43% ± 2.93%, and 93.21% ± 3.25%; one-way ANOVA; Fig. 5D). In contrast, the response ratio in Aδ fibers following 100-Hz PES was only 80.17% ± 6.11%, significantly lower than that in response to other frequencies (2 Hz, 100% ± 0%; 15 Hz, 97.99% ± 2.01%; 2/15, 100% ± 0%, and 2/100 Hz, 97% ± 1.97%; $P < 0.01$, one-way ANOVA; Fig. 5E).

These results suggest that conduction failure occurs when PES is continuously applied at 100 Hz, and PES at alternating frequency between 2 Hz and 100 Hz (2/100 Hz) for 3 s each improves the situation (details in Fig. S2).

PES at Frequencies from 100 to 1000 Hz Delivered to the Receptive Fields of Afferent Fibers

The discharges evoked in Aβ and Aδ fibers in response to high-frequency stimulation were in various forms – irregular, proportional, burst, and sporadic (Fig. S3)

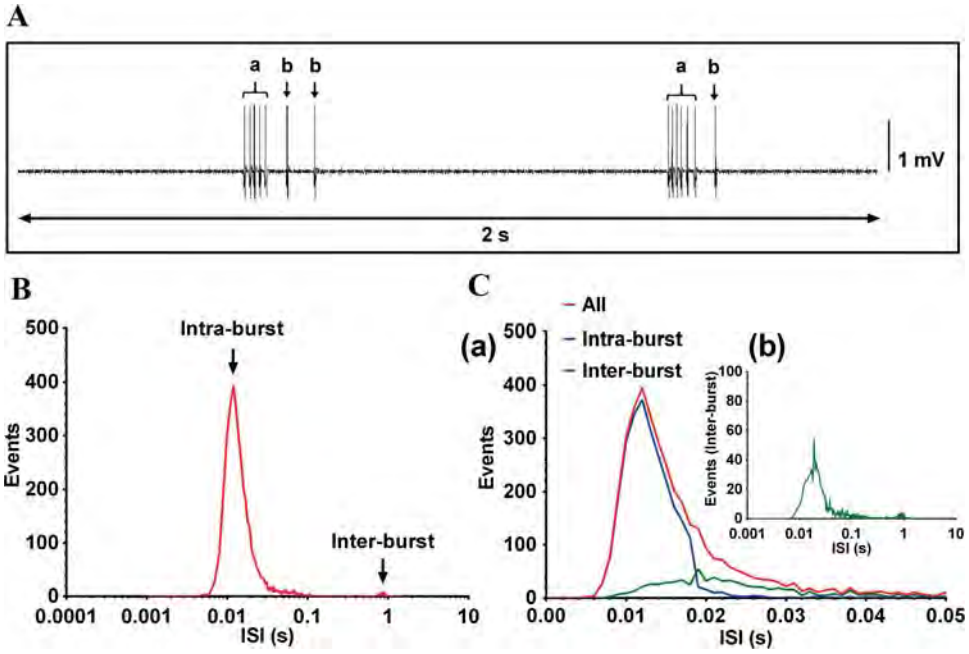

Fig. 4 ISI distribution of evoked discharges of PAN fibers in response to MAc at once per second. **A** Examples of burst firing (**a**) and sporadic firing (**b**) of evoked discharges. **B** Distribution of ISIs of evoked discharges in all 11 recorded burst-firing fibers in response to MAc at once per second. Note log scale on abscissa. **C (a)** Distribution of burst firing (intra-burst) and sporadic firing (inter-burst) of all 11 recorded burst-firing fibers according to the burst criteria (maximum intra-burst ISI $\leq$0.019 s; minimum inter-burst ISI >0.1 s; and minimum number of spikes in a burst $\geq$3). The intra-burst ISI peak within a burst was ~0.012 s (arrow) and the inter-burst ISI was ~1 s (arrow). (**b**) Distribution of sporadic firing (inter-burst and intra-burst) of all 11 fibers. PAN, primary afferent nerve; MAc, manual acupuncture; ISI, inter-spike interval.

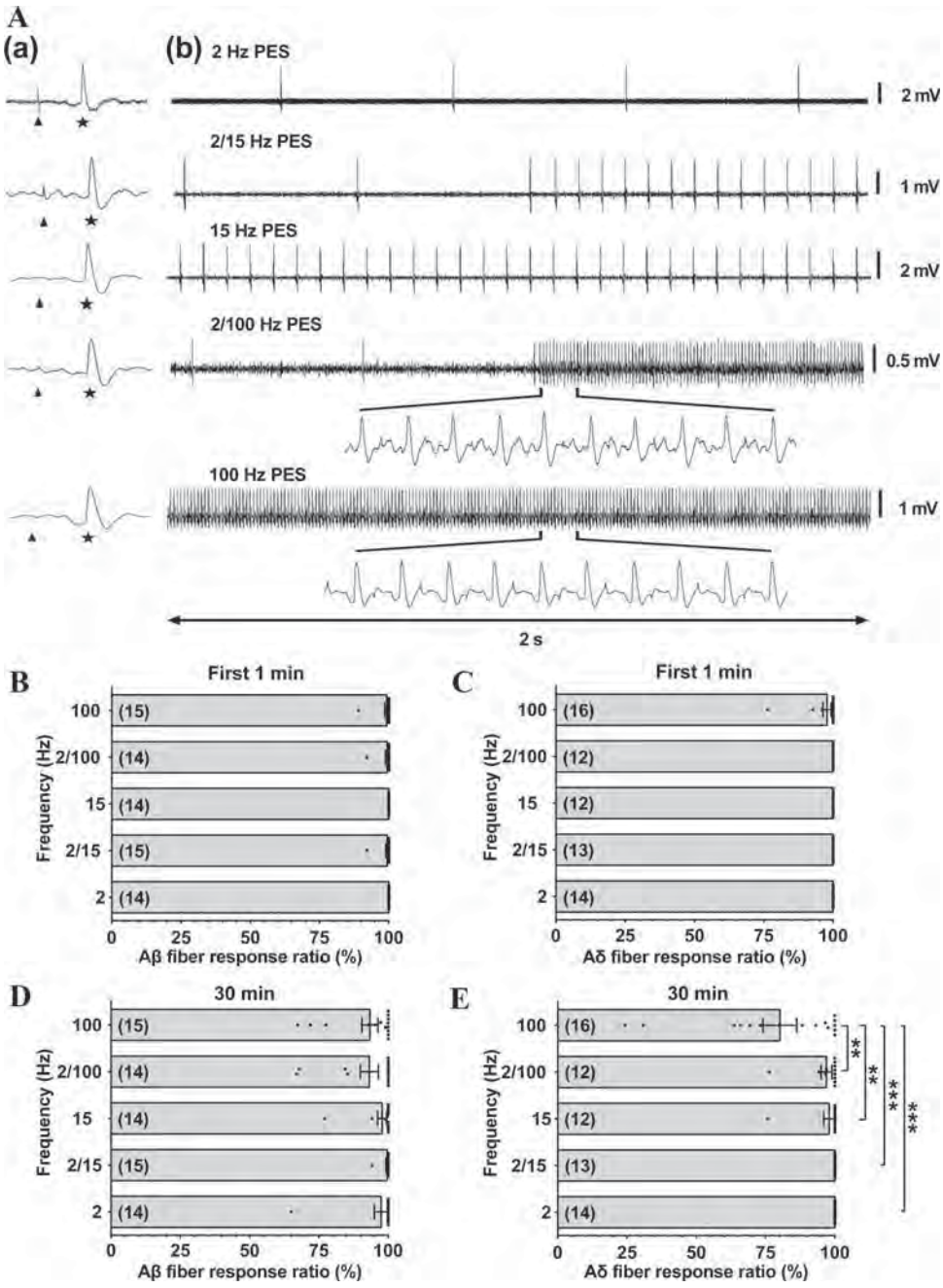

Fig. 5 Spike traces and response ratios of single-unit afferent fibers in response to PES at optimal frequencies. **A (a)** Evoked discharges (stars) of Aβ fibers (conduction velocities 31.06, 30.60, 30.00, 26.48, and 26.81 m/s) induced by negative square-wave pulses (width 100 μs, 1.5× threshold current, stimulus artifact indicated by arrow) at their receptive fields; and **(b)** examples of one-to-one responses of the fibers in (**a**). **B**, **C** No difference in the response ratios during the initial 60 s among the different frequency groups in Aβ or Aδ fibers in response to PES at the optimal frequencies. **D**, **E** A significantly lower response ratio is found only in Aδ fibers at 100 Hz in response to 30 min PES. Digits in brackets are the numbers of recorded fibers. Data are expressed as the mean ± SEM. $^{**}P < 0.01$ and $^{***}P < 0.001$; one-way ANOVA. PES, peripheral electrical stimulation.

Changes in Response Ratio of Afferent Fibers with Increasing Frequency of PES (100 to 1000 Hz)

In these experiments, 32 Aβ single-unit afferent fibers were recorded from 7 rats, and 30 Aδ fibers were recorded from 11 rats. Each fiber received PES using at least one of the following randomly-selected frequencies: 100 Hz, 200 Hz, 300 Hz, 400 Hz, 500 Hz, 600 Hz, 700 Hz, 800 Hz, 900 Hz, and 1000 Hz. The corresponding numbers of Aβ fibers were 17, 17, 17, 14, 15, 13, 14, 16, 14, and 12, and the numbers of Aδ fibers were 18, 21, 14, 10, 14, 8, 12, 9, 13, and 14. The response ratios of Aβ and Aδ fibers declined gradually with increasing frequency of PES above 100 Hz (Fig. 6A, B), reaching a plateau 20 s after PES started. The response ratios of Aβ and Aδ fibers in the last 10 s of 60-s stimulation at various frequencies were relatively stable and used for analysis. The response ratios of both Aβ and Aδ fibers dramatically deteriorated as the frequency of PES approached 1000 Hz. Furthermore, the response ratio in Aδ fibers deteriorated more quickly than that in Aβ fibers under the same experimental conditions ($P < 0.001$, repeated measures ANOVA; Fig. 6C).

Changes in Frequency of Evoked Discharges of Afferent Fibers with Increasing Frequency of PES (100 Hz–1000 Hz)

Changes in the frequency of evoked discharges in response to PES at given frequencies serve as another way to describe the frequency-conduction relationship in neurons. We found that the number of evoked discharges per second in Aβ fibers increased with an increase in the frequency of PES between 100 Hz and 300 Hz (Fig. 6D). However, the number of evoked discharges per second remained at 246 in Aβ fibers in spite of PES frequency further increasing from 300 to 1000 Hz.

A similar decrease in evoked discharges was found in Aδ fibers; the maximum number of evoked discharges per second was <200 at 200-Hz PES. There was a steady decrease in the evoked discharges with an increase in the frequency; in fact, there was a significant negative correlation between the number of evoked discharges and the frequency of PES in the range of 200 Hz–1000 Hz (r = –0.875, P = 0.002; Fig. 6E).

These data demonstrate the limit of efficiency in PAN fibers in transmitting high-frequency signals. The response ratio decreases dramatically when the frequency of peripheral stimulation exceeds a certain level in term of the axon diameter and the refractory period of afferent nerve fibers. These PANs function as a frequency filter to prevent signals >300 Hz in Aβ fibers or 200 Hz in Aδ fibers from entering the CNS.

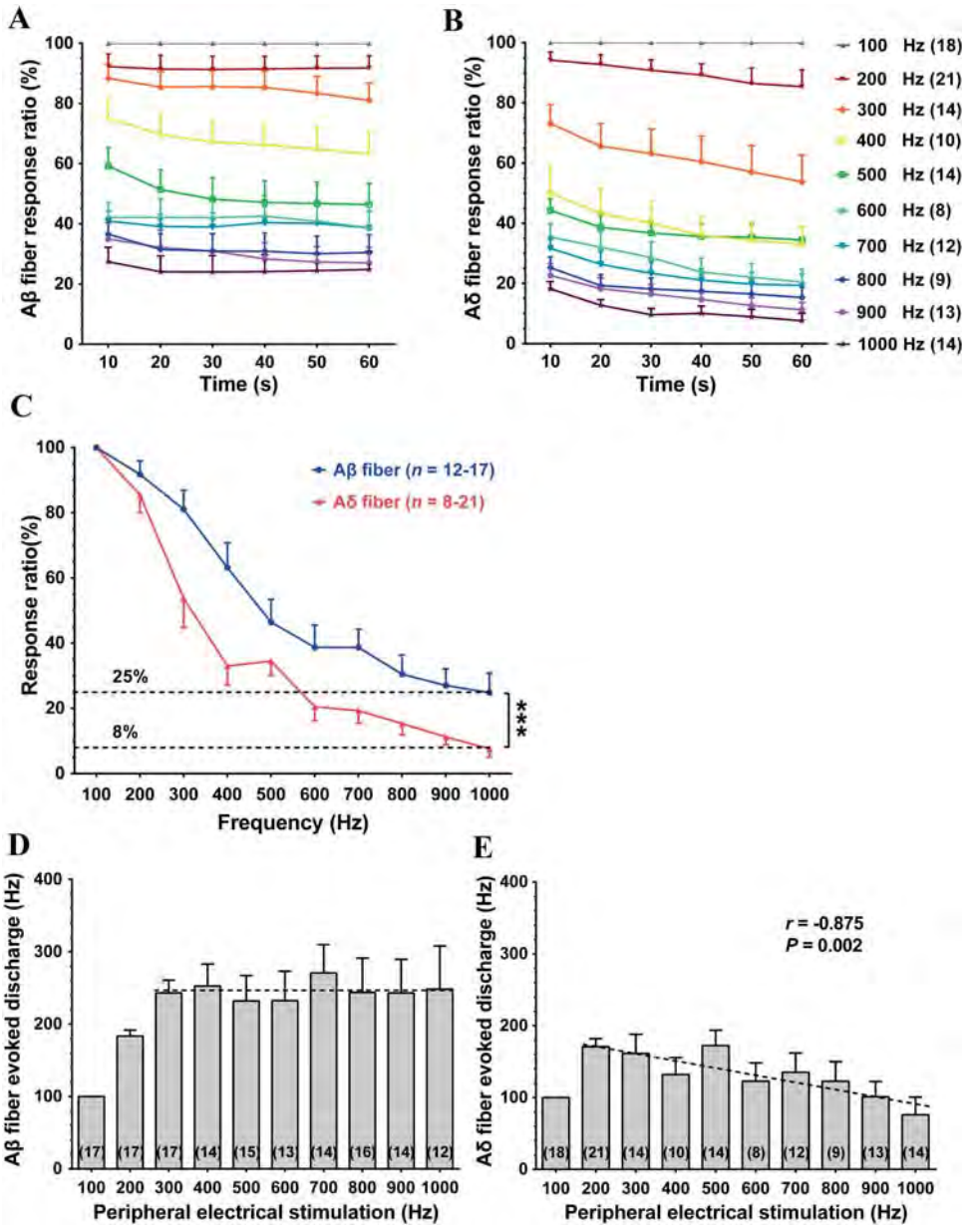

Fig. 6 Response ratios and evoked discharge rates of Aβ and Aδ fibers in response to PES at various frequencies. **A**, **B** Response ratios of Aβ and Aδ fiber remain relatively stable after 20-s PES. **C** Response ratios gradually decrease with increasing stimulus frequency in both Aδ and Aβ fibers in the last 10 s of 60-s PES, and the curve is steeper in Aδ than in Aβ fibers (***$P < 0.001$, repeated measures ANOVA). **D**, **E** The discharge rates of Aβ fibers do not change in response to PES at 300 Hz–1000 Hz; and the discharge rates of Aδ fibers are negatively correlated with PES frequency at 200 Hz–1000 Hz. Digits in brackets are the numbers of recorded fibers. Data are expressed as the mean ± SEM. PES, peripheral electrical stimulation.

Discussion

We have demonstrated previously that at least some of the therapeutic effects of acupuncture such as pain relief are mediated by activity in the brain and spinal cord [15]. It is known that multiple types of PAN fibers are activated by peripheral stimulation. For example, Kagitani *et al*. reported that all the four populations of afferent fibers are activated by acupuncture and 5–7 spikes per second occur in A-fibers induced by manual twisting once per second [19]. This is in good agreement with our data. However, we suggest that the analgesic acupuncture signal from the periphery to the CNS appears to be mediated primarily by the large-diameter myelinated Aβ and Aδ fibers of PANs since the anti-nociceptive effect is lost after the afferents being blocked by local anesthetics [29] but not by capsaicin [2], which selectively blocks C-fibers.

Chang *et al.* also reported distinct and persistent burst discharges from pressing or manipulating needles in the receptive fields [3]. Our results showed that MAc induced four different patterns of evoked discharges in Aβ and Aδ fibers. They can be simplified into two categories: burst firing and sporadic firing. Burst firing was the dominant pattern of evoked discharges in MAc at a frequency of once per second, which induced ∼6 spikes per burst on average. The frequency of evoked intra-burst discharges was ∼90 Hz, which occurred mostly when the needle started moving from zero to the maximum angular velocity. Distortion of the nerve terminal near the needle is assumed to be responsible. The sporadic firing mainly consisted of tonic and irregular patterns; the ISIs varied dramatically. The average frequency of sporadic firing was ∼2 Hz, lower than in the burst firing (90 Hz). The two types of firing pattern in PANs can be viewed as two types of acupuncture signals: high frequency and low frequency signals.

To avoid inconsistent MAc, we used an EAc device that provided precise and reproducible rotation angle, rotation speed, and up-down movement. The data further showed that increasing the rotation angle from 90° to 360° did not further increase the number of evoked discharges per second. In contrast, there was a frequency-dependent increase in the evoked discharges when the twisting frequency was increased from one cycle per second to three cycles per second.

PES in the receptive field of the PANs mimics the EA effect. Different stimulus thresholds were found at different frequencies. For example, the threshold was lower at 2 Hz than at 100 Hz. This difference was most likely due to the greater pulse width used at 2 Hz (Fig. S4). A wider pulse was used in 2-Hz stimulation during the dense-disperse mode in order to deliver more energy per pulse to offset the difference in the total energy delivered between low and high frequencies during a given period of time. Otherwise the sensation would be too weak during 2 Hz stimulation compared with the 100 Hz stimulation.

It is generally accepted that low- and high-frequency stimulation have distinct neural transmission pathways and activate different neurotransmitter/neuropeptide systems in different parts of the CNS resulting in different therapeutic effects [11, 32, 33, 38]. For example, we have previously demonstrated that 2-Hz EA stimulates the release of beta endorphin in the brain which acts on mu and delta opioid receptors [13, 15]. In contrast, 100-Hz EA stimulates the release of spinal dynorphin which acts on kappa opioid receptors [15]. Based on these findings, an EA stimulator capable of delivering dense-disperse mode between 2 Hz and 100 Hz, for 3 s each, appears to have a better pain-relieving effect [6]. It is interesting that MAc also produced low- (2 Hz) and high (90 Hz)-frequency discharges in PANs. These two frequencies are almost the same as those recommended for use in electroacupuncture (2 Hz and 100 Hz) [11]. From the above results it is clear that the MAc signal is transmitted into the CNS by PAN fibers with a 100% transmission response ratio. In addition, the 2 Hz and 100 Hz alternating stimulation pattern recommended for use in EA appears to mimic the signal produced by MAc in PANs (2 Hz and 90 Hz).

The therapeutic effects of acupuncture for many disorders appear to be frequency-dependent. For example, low-frequency EA has been shown to be better than high-frequency in improving ovary function in reproductive medicine [34]. Low-frequency is also better at improving behavioral symptoms in autistic children [35], while high-frequency is more effective than low-frequency for the treatment of myospasm and arthritic pain [24]. Therefore, the appropriate acupuncture manipulation style in MAc or frequency parameters in EA would be selected for a better therapeutic effect for a particular disorder. Based on our data, an acupuncturist requiring more high-frequency or burst signals in MAc would choose twisting with short strokes and frequent turning back and forth rather than long strokes, since burst firing mostly occurs at the beginning of each twist.

One of the purposes of the present study was to provide information to facilitate the establishment of a limit on the maximum output frequency for EA stimulators to be published by the International Organization for Standardization. The results showed that the EA signal is in the physiological range when reaching the dorsal horn after the high-frequency signal had been filtered by the PANs. Some EA stimulators on the market deliver very high frequencies which are certainly beyond the physiological range of signals that a neuron can transmit. Very high frequencies should not be recommended since they do not have

therapeutic advantages and may expose the patients to unnecessary risks associated with high energy output. Therefore, we examined the transmission capacity of PAN fibers over a wide range of frequencies of PES and concluded that the Aβ and Aδ fibers in PANs transmit the EA-like signal faithfully when the frequency is <100 Hz. The response ratio was reduced in a frequency-dependent manner when PES was between 100 Hz and 300 Hz. The induced discharges in Aβ-fibers stabilized at 246 per second even when the PES frequency was raised to 1000 Hz. However, the number of evoked discharges gradually decreased from a peak when PES was between 200 Hz and 1000 Hz in Aδ fibers. The dropping of evoked spikes (i.e. the response ratios of the PANs) at higher frequencies is presumably due to the diameter and the refractory period of the PAN axons, because the smaller the diameter of the afferent nerve fibers, the slower conduction velocity and the longer the refractory period of excitation, and therefore the lower the frequency of response to peripheral stimuli such as EA and PES. Other factors such as the presence or absence of myelin sheath around the fibers also have influence on the response ratios of the PANs to the PES frequency. This phenomenon has also been reported by others [10, 23, 30, 31] including Gasser and Grundfest who found the refractory period to be ~0.4 ms in rabbit alpha fibers, imposing a maximum frequency of evoked discharge to be ~250 Hz [9]. Furthermore, the transmission efficiency of both Aβ and Aδ fibers dropped further during prolonged stimulation at higher frequencies. Here, we found that the decrease in response ratio appeared to be reversible, suggesting that temporary intracellular imbalance of electrolytes or ions may be responsible [27]. Using the radiant heat/tail-flick latency method to measure changes in nociception threshold in rats, our previous studies have shown that EA stimulation at ST36 and SP6 at 2000 Hz has an anti-nociceptive effect [22] which can be partially reversed by a high dose of naloxone capable of blocking all opioid receptors (mu, delta, and kappa). Our present findings suggest that the EA signal is in the physiological range when reaching the dorsal horn after high-frequency signals are filtered out by the PAN. However, our study also had limitations. We did not examine the evoked responses in different fiber types in the manual and emulated acupuncture experiments. It cannot be ruled out that different fibers respond differently, for example, bursting might be preferentially associated with Aβ rather than Aδ fibers. To our knowledge, the present study is the first to quantitatively describe the response ratio and the rate of evoked discharges in Aβ and Aδ fibers in response to PES at various frequencies. Unlike another study [30], the intensity of PES used in our study was double the activation threshold current of the afferent fibers, closer to that used in clinical practice. Furthermore, a positive control (100-Hz PES) was included after each testing frequency to ensure that the fibers responded to PES normally with no shift in the baseline.

Although Aβ and Aδ fibers cannot follow very high frequency stimulation (>100 Hz), such stimulation may still have analgesic effects in terms of spinal cord stimulation. Future studies are encouraged to study acupuncture and single-unit recordings in animals with inflammatory pain or neuropathic pain.

Conclusions

The present findings suggest the coexistence of high-frequency and low-frequency evoked firing and frequency-dependent responses occur in PANs following MAc and PES. Aβ and Aδ fibers may serve as filters to prevent very high frequency signals from entering the CNS. Therefore, EA therapy with frequencies >250 Hz appears to be ineffective at least for the purpose of pain relief.

Acknowledgments We wish to thank JY Wei of the University of California at Los Angeles and Zhi-Qi Zhao of Fudan University for their suggestions throughout the study. Special thanks go to Hua-Yuan Yang, Yi-Ming Zhang, and Gang Xu of Shanghai University of Traditional Chinese Medicine for their generosity in providing equipment for emulation acupuncture. In addition, we thank Xiao-Ping Kang, Yao Huang, Chang-Xi Xu, Zhi-Jun Lv, and Zhen-Chen Liu for their help with part of the data analysis. This work was supported by the National Key Research and Development Program of the Ministry of Science and Technology, China (2016YFC0105501, 2019YFC1712104 and 2016YFF0202802) and the National Natural Science Foundation of China (81974169, 81671085 and 61527815).

Conflict of interest The authors declare no conflicts of interest.

References

1. Bäcker M, Hammes MG, Valet M, Deppe M, Conrad B, Tölle TR, *et al.* Different modes of manual acupuncture stimulation differentially modulate cerebral blood flow velocity, arterial blood pressure and heart rate in human subjects. Neurosci Lett 2002, 333: 203–206.
2. Bao H, Zhou Z, Yu Y, Han J. C fiber is not necessary in electro-acupuncture analgesia, but necessary in diffuse noxious inhibitory controls (DNIC). Zhen Ci Yan Jiu 1991, 16: 120–124.
3. Chang SC, Wei JY, Mao CP. Deep innervation of sural nerve. Brain Res 1983, 279: 262–265.
4. Chang XB, Wang S, Meng ZH, Fan XN, Yang X, Shi XM. Study on acupuncture parameters impacting on the acupuncture effect using cluster analysis in a rat model with middle cerebral artery occlusion. Chin J Integr Med 2014, 20: 130–135.
5. Chen W, Chi YN, Kang XJ, Liu QY, Zhang HL, Li ZH, *et al.* Accumulation of Cav3.2 T-type calcium channels in the uninjured sural nerve contributes to neuropathic pain in rats with spared nerve injury. Front Mol Neurosci 2018, 11: 24.

6. Chen XH, Guo SF, Chang CG, Han JS. Optimal conditions for eliciting maximal electroacupuncture analgesia with dense-and-disperse mode stimulation. Am J Acupunct 1994, 22: 47–53.
7. Choi YJ, Lee JE, Moon WK, Cho SH. Does the effect of acupuncture depend on needling sensation and manipulation? Complement Ther Med 2013, 21: 207–214.
8. Fang JL, Krings T, Weidemann J, Meister IG, Thron A. Functional MRI in healthy subjects during acupuncture: different effects of needle rotation in real and false acupoints. Neuroradiology 2004, 46: 359–362.
9. Gasser HS, Grundfest H. Axon diameter in relation to the spike dimensions and the conduction velocity in mammalian A fibers. Am J Physiol 1939, 127: 393–414.
10. Gee MD, Lynn B, Cotsell B. Activity-dependent slowing of conduction velocity provides a method for identifying different functional classes of C-fibre in the rat saphenous nerve. Neuroscience 1996, 73: 667–675.
11. Han JS. Acupuncture: neuropeptide release produced by electrical stimulation of different frequencies. Trends Neurosci 2003, 26: 17–22.
12. Han JS. Acupuncture and endorphins. Neurosci Lett 2004, 361(1–3): 258–261.
13. Han JS, Sun SL. Differential release of enkephalin and dynorphin by low and high frequency electroacupuncture in the central nervous system. Acupunct Sci Int 1990, 1: 19–27.
14. Han JS, Terenius L. Neurochemical basis of acupuncture analgesia. Annu Rev Pharmacol Toxicol 1982, 22: 193–220.
15. Han JS, Wang Q. Mobilization of specific neuropeptides by peripheral stimulation of identified frequencies. Physiology 1992, 7: 176–180.
16. Hong S, Ding S, Wu F, Xi Q, Li Q, Liu Y, *et al*. Strong manual acupuncture manipulation could better inhibit spike frequency of the dorsal horn neurons in rats with acute visceral nociception. Evid Based Complement and Alternat Med 2015, 2015: 675437.
17. Hunt CC. Relation of function to diameter in afferent fibers of muscle nerves. J Gen Physiol 1954, 38: 117–131.
18. Jiang Y, Wang H, Liu Z, Dong Y, Dong Y, Xiang X, *et al*. Manipulation of and sustained effects on the human brain induced by different modalities of acupuncture: an fMRI study. PLoS One 2013, 8: e66815.
19. Kagitani F, Uchida S, Hotta H, Aikawa Y. Manual acupuncture needle stimulation of the rat hindlimb activates group I, II, III and IV single afferent nerve fiber in the dorsal spinal roots. Jpn J Physiol 2005, 55: 149–155.
20. Kim SA, Lee BH, Bae JH, Kim KJ, Steffensen SC, Ryu YH, *et al*. Peripheral afferent mechanisms underlying acupuncture inhibition of cocaine behavioral effects in rats. PLoS One 2013, 8: e81018.
21. Kress M, Koltzenburg M, Reeh PW, Handwerker HO. Responsiveness and functional attributes of electrically localized terminals of cutaneous C-fibers *in vivo* and *in vitro*. J Neurophysiol 1992, 68: 581–595.
22. Lin JG, Chen XH, Han JS. Antinociception produced by 2 and 5 KHz peripheral stimulation in the rat. Int J Neurosci 1992, 64: 15–22.
23. Littlefield PD, Vujanovic I, Mundi J, Matic AI, Richter CP. Laser stimulation of single auditory nerve fibers. Laryngoscope 2010, 120: 2071–2082.
24. Liu HX, Tian JB, Luo F, Jiang YH, Deng ZG, Xiong L, *et al*. Repeated 100 Hz TENS for the treatment of chronic inflammatory hyperalgesia and suppression of spinal release of substance P in monoarthritic rats. Evid Based Complement Alternat Med 2007, 4: 65–75.
25. Li WM, Chen YB, Wang XY. Characteristics of peripheral afferent nerve discharges evoked by manual acupuncture and electroacupuncture of "Zusanli" (ST 36) in rats. Zhen Ci Yan Jiu 2008, 33: 65–70.
26. Li X, Li Y, Chen J, Zhou D, Liu Y, Li Y, *et al*. The influence of skin microcirculation blood perfusion at zusanli acupoint by stimulating with lift-thrust reinforcing and reducing acupuncture manipulation methods on healthy adults. Evid Based Complement and Alternat Med 2013, 2013: 452697.
27. Lüscher C, Streit J, Lipp P, Lüscher HR. Action potential propagation through embryonic dorsal root ganglion cells in culture. II. Decrease of conduction reliability during repetitive stimulation. J Neurophysiol 1994, 72: 634–643.
28. Min S, Lee H, Kim SY, Park JY, Chae Y, Lee H, *et al*. Local changes in microcirculation and the analgesic effects of acupuncture: a laser doppler perfusion imaging study. J Alternat Complement Med 2015, 21: 46–52.
29. Research Group of Acupuncture Anesthesia, Peking Medical College. Effect of acupuncture on the pain threshold of human skin. Chin Med J 1973, 3: 151–157.
30. Tang JS, Shi WC, Hou ZL. Effect of electroacupuncture stimulation (EAS) of different frequencies on the excitability of fibers of various groups. Zhen Ci Yan Jiu 1987, 12: 68–72.
31. Torebjörk HE, Hallin RG. Responses in human A and C fibres to repeated electrical intradermal stimulation. J Neurol Neurosurg Psychiatry 1974, 37: 653–664.
32. Wang Q, Mao L, Han J. The arcuate nucleus of hypothalamus mediates low but not high frequency electroacupuncture analgesia in rats. Brain Res 1990, 513: 60–66.
33. Wang Q, Mao L, Han J. The role of parabrachial nucleus in high frequency electroacupuncture analgesia in rats. Chin J Physiol Sci 1991, 7: 363–367.
34. Zhang R, Feng XJ, Guan Q, Cui W, Zheng Y, Sun W, *et al*. Increase of success rate for women undergoing embryo transfer by transcutaneous electrical acupoint stimulation: a prospective randomized placebo-controlled study. Fertil Steril 2011, 96: 912–916.
35. Zhang R, Jia MX, Zhang JS, Xu XJ, Shou XJ, Zhang XT, *et al*. Transcutaneous electrical acupoint stimulation in children with autism and its impact on plasma levels of arginine-vasopressin and oxytocin: A prospective single-blinded controlled study. Res Dev Disabil 2012, 33: 1136–1146.
36. Zhou T, Wang J, Han CX, Torao I, Guo Y. Analysis of interspike interval of dorsal horn neurons evoked by different needle manipulations at ST36. Acupunct Med 2014, 32: 43–50.
37. Zhou W, Fu LW, Tjen-A-Looi SC, Li P, Longhurst JC. Afferent mechanisms underlying stimulation modality-related modulation of acupuncture-related cardiovascular responses. J Appl Physiol 2005, 98: 872–880.
38. Wang Y, Wang Y, Liu J, Wang M. Electroacupuncture alleviates motor symptoms and up-regulates vesicular glutamatergic transporter 1 expression in the subthalamic nucleus in a unilateral 6-hydroxydopamine-lesioned hemi-parkinsonian rat model. Neurosci Bull 2018, 34: 476–484.

Neurosci. Bull. August, 2020, 36(8):919–931
https://doi.org/10.1007/s12264-020-00511-9

www.neurosci.cn
www.springer.com/12264

ORIGINAL ARTICLE

Neuronal Activity in the Cerebellum During the Sleep-Wakefulness Transition in Mice

Li-Bin Zhang[1,2] · Jie Zhang[1] · Meng-Jia Sun[1,3] · Hao Chen[1] · Jie Yan[1] · Fen-Lan Luo[1] · Zhong-Xiang Yao[1] · Ya-Min Wu[2] · Bo Hu[1]

Received: 18 September 2019 / Accepted: 9 February 2020 / Published online: 19 May 2020

Abstract Cerebellar malfunction can lead to sleep disturbance such as excessive daytime sleepiness, suggesting that the cerebellum may be involved in regulating sleep and/or wakefulness. However, understanding the features of cerebellar regulation in sleep and wakefulness states requires a detailed characterization of neuronal activity within this area. By performing multiple-unit recordings in mice, we showed that Purkinje cells (PCs) in the cerebellar cortex exhibited increased firing activity prior to the transition from sleep to wakefulness. Notably, the increased PC activity resulted from the inputs of low-frequency non-PC units in the cerebellar cortex. Moreover, the increased PC activity was accompanied by decreased activity in neurons of the deep cerebellar nuclei at the non-rapid eye-movement sleep-wakefulness transition. Our results provide *in vivo* electrophysiological evidence that the cerebellum has the potential to actively regulate the sleep-wakefulness transition.

Keywords Sleep · Wakefulness · Multiple-unit recording · Purkinje cell · Deep cerebellar nuclei

Introduction

The cerebellum is a critical component of the central nervous system that is involved in motor planning [1], motor execution [2–4], and motor learning [5–7]. However, patients suffering from cerebellar disorders have not only motor deficits, but also non-motor symptoms. For example, patients with spinocerebellar ataxias, which are characterized by degeneration of the cerebellum, often show excessive daytime sleepiness [8–10]. In addition, cerebellectomized cats show decreased wakefulness, and increased rapid eye-movement (REM) sleep [11]. Vice versa, patients suffering from primary sleep disorders often have a decreased cerebellar volume [12, 13]. Altogether, the current findings support a hypothesis that the cerebellum is involved in regulating the sleep and/or wakefulness states [14].

In support of this hypothesis, neuroanatomical studies have revealed that deep cerebellar nuclei (DCN), the final integration and output nuclei of the cerebellum, innervate several brain areas critical for maintaining or promoting wakefulness. As such, the DCN have been reported to innervate the ventral thalamus [15–17], which participates in the transition from non-REM (NREM) sleep to wakefulness [18]. In addition, the DCN have been revealed to interconnect with the hypothalamus [19–21], where several types of wakefulness-promoting and sleep-promoting neurons are located [22, 23]. Consequently, the cerebellum lies

Li-Bin Zhang and Jie Zhang have contributed equally to this work.

Electronic supplementary material The online version of this article (https://doi.org/10.1007/s12264-020-00511-9) contains supplementary material, which is available to authorized users.

✉ Ya-Min Wu
yaminwu65@hotmail.com

✉ Bo Hu
bohu@tmmu.edu.cn

[1] Department of Physiology, College of Basic Medical Sciences, Army Medical University, Chongqing 400038, China

[2] State Key Laboratory of Trauma, Burns and Combined Injury, Daping Hospital/Research Institute of Surgery, Army Medical University, Chongqing 400042, China

[3] Squadron 10, Battalion 3, College of Basic Medical Sciences, Army Medical University, Chongqing 400038, China

in a good position to communicate with arousal neurons, so as to regulate the sleep and/or wakefulness state [14, 24].

Nevertheless, the cerebellum can regulate the sleep and/or wakefulness state only if its activity changes preceding the transition between various sleep and wakefulness states. Consequently, monitoring neuronal activity in the cerebellum is the first step to uncover the specific roles and features of the cerebellum in the regulation of sleep and wakefulness. Extending early studies reported that the activity of Purkinje cells (PCs) and of DCN neurons both increase during REM sleep [25–28]. Along this line, functional imaging studies have revealed changes in cerebellar activity across various sleep stages. For instance, it has been reported that human subjects show lower cerebellar activity during NREM sleep than during wakefulness [29], and show increased activity during REM sleep [30, 31]. However, neuronal activity in the cerebellum during the transition between various sleep and wakefulness states remains largely unclear.

Consequently, in the current study, we performed multiple-unit recording in the mouse cerebellum across sleep-wakefulness cycles, in order to investigate the temporal features of cerebellar neuronal activity during this process.

Materials and Methods

Animals

All experiments were approved by the Animal Care Committee of Army Medical University. Male C57/BL6 mice (n = 10, 3–5 months old, 20 g–25 g) were individually housed in a 12-h light-dark cycle with lights on at 08:00, with free access to food and water. All experiments were conducted during the light phase of the cycle.

Surgery

The mice were implanted with a tetrode assembly attached to a microdrive, under isoflurane anesthesia (0.6%–1.0% by volume in O_2). The detailed implantation procedures have been described recently [32]. Each tetrode was composed of four tungsten wires (bare diameter, 20 μm; insulated diameter, 25 μm; California Fine Wire, Grover Beach, CA); the impedance measured before implantation ranged from 200 kΩ to 400 kΩ. One stainless-steel screw was inserted through the skull above the right hemisphere of the cerebellum to serve as ground, and another screw was inserted above the right hemisphere of the neocortex to serve as reference. These screws were secured to the skull using Metbond cement (Parkell, Shiga, Japan). Thereafter, a stainless-steel wire (bare diameter, 254 μm; insulated diameter, 330 μm; #792300, A-M Systems Inc., Sequim, WA) was implanted into the right frontal cortex (AP, + 1.7 mm; ML, + 0.5 mm; DV, + 1.0 mm). In addition, a craniotomy was made above the left cerebellum. The tetrode assembly was implanted perpendicular to the longitudinal axis with its center at the coordinates AP, − 6.3 mm; ML, − 1.7 mm, and lowered into the cerebellar cortex (depth, 1400 μm–1500 μm) with the help of a brain stereotaxic apparatus (model 68006, RWD, China). Low-viscosity silicone (Kwik-Cast™; WPI, Sarasota, FL) was then applied to cover the craniotomy. During postoperative recovery, the weight of each mouse was measured daily until it recovered to the pre-surgical level. The tips of tetrodes were moved down (∼ 70 μm/day) until the firing of putative PC was monitored.

Sleep Monitoring

Postoperative mice were individually housed in transparent plastic cages (28 × 13 × 18 cm^3) for the duration of the experiment. After ∼ 1 week of postoperative recovery and tetrode adjustment, the freely-moving mice started habituation and sleep monitoring at the beginning of the early light phase (08:00–11:00).

In Vivo Electrophysiology

As we described recently [33], in this study, we performed data acquisition with an Intan interface board (RHD2000, Intan Technologies, Los Angeles, CA). The neuronal signals were amplified, digitized at 20 kHz using a multiplexed preamplifier (C3334, Intan Technologies), and stored for off-line analysis in a 16-bit resolution format. The wide-band signal was sampled to 1250 Hz and used as the local field potential (LFP). During tetrode adjustment and recording, neuronal activity was continuously visualized using Neuroscope software (http://neurosuite.sourceforge.net) [34]. In 8 mice, initial recording was performed in the vicinity of the Purkinje cell layer (1500–2000 μm ventral to the surface) to monitor cerebellar cortical neuronal activity across sleep-wakefulness cycles. After the last PC recording in the cerebellar cortex, the tetrodes were moved down at least 280–490 μm until DCN neuronal activity was recorded. On the next day, the DCN neuronal activity across sleep-wakefulness cycles was recorded. This measure was used to minimize the possibility of recording cerebellar cortical units in the DCN, considering that a tetrode covers only ∼ 140 μm from its tip [35].

Data Analysis

Spike Sorting

The detailed procedures for unit clustering have been described [36]. Briefly, the spikes were extracted from high-pass filtered signals off-line, and their waveforms were projected onto a common basis obtained by principal component analysis of the filtered data. Single-unit spikes were isolated off-line using both semi-automatic clustering using KlustaKwik software [37] (http://klustakwik.sourceforge.net/) and manual clustering using Klusters software (http://neurosuite.sourceforge.net/) [34]. The accuracy of unit clustering was verified by confirming the existence of a 2-ms refractory period devoid of spikes in the autocorrelogram of a given single unit.

Sleep Analysis

In this study, we combined LFP oscillation in the frontal cortex and head movement of the mice (reflecting the activity of their neck muscles) to define recordings associated with distinct brain states. This method has been used to define brain states in our recent studies [32, 36] and by other research groups [38, 39]. Moreover, frequency spectrum changes in the LFP oscillation have been demonstrated to be sensitive, providing an opportunity to define state transitions with high temporal resolution (i.e., 1 s) [36, 38, 39]. Consequently, the sleep stages (NREM and REM) were determined by LFP oscillation in the frontal cortex and head movement of the mouse, according to the criteria described by the previous studies [36, 38, 39]. K-means clustering of the theta/delta ratio was automatically extracted from the power spectrogram. NREM sleep was defined as periods in the sleep epoch that met the following criteria: (1) the mouse was immobile (velocity < 0.5 cm/s for at least 10 s) and (2) slow-wave oscillations were detected. REM sleep was defined based on an elevated ratio of cortical theta (5–10 Hz) to delta (1–4 Hz) power with the requirement that a single REM bout lasted at least 10 s.

In Vivo Electrophysiological Isolation of Putative PCs

PCs were identified by their high firing activity and distinctive complex spikes in the vicinity of PC layer, according to the criteria described by ten Brinke *et al.* [40]. Putative PCs were initially identified by their intense spontaneous activity and later confirmed by the presence of both simple and complex spikes during unit clustering. The complex spikes were manually discriminated on the basis of the presence of a 1–3 ms slow component together with their stereotypical shape (i.e., board monophasic negative waves). For a putative PC, the presence of a pause (> 10 ms) in simple spike firing after a complex spike was verified.

Quantification of the Cross-Correlogram (CCG)

As described by Bartho *et al.* [41], the putative excitatory monosynaptic connection was identified by a short-latency peak in the CCG. Significant peaks (1-ms bin width) within 3 ms of the center bin were considered to be putative excitatory monosynaptic connections. A peak in a CCG was defined as significant when at least one of the bins exceeded the 99.9th percentile of the mean. The mean (control number of spikes) was calculated between -50 ms and -10 ms to control for potential low-frequency fluctuations of firing rate. Normalized CCG was obtained by dividing the observed CCG by the expected number of spikes per bin.

Statistics

Data are expressed as the mean $\pm$ S.E.M. The firing rate difference between sleep and wakefulness states was determined by paired t tests. The mean firing rate was calculated between -10 and -2 s, which served as control. The changes in neuronal activity across sleep-wakefulness transitions were then determined by paired t tests. Parametric or non-parametric tests were used as appropriate. A value of $p < 0.05$ was considered to be significant for all tests.

Histology

To visualize the tip locations of tetrodes, electrolytic lesions (30 μA for 10 s, DC current) were made at the end of all behavioral and recording experiments. The mice were anesthetized with pentobarbital (100 mg/kg intraperitoneal) and perfused with saline and 4% paraformaldehyde (PFA; prepared in 0.1 M phosphate buffer, pH 7.4). The brain was removed and post-fixed in 4% PFA for 8 h. Afterwards, the tissue was transferred to 30% sucrose for 48 h. Coronal sections (20 μm thick) were cut on a freezing microtome (CM1900, Leica, Germany) and collected in phosphate buffered saline (0.01 mol/L, pH 7.4) for later staining. After three washes (5 min each), the sections were mounted in Fluoromount medium with DAPI fluorescence (F6057, Sigma-Aldrich, St. Louis, MO). The tip placements of tetrodes were checked and the images were acquired using a fluorescence microscope (BX53, Olympus, Tokyo, Japan). In 8 mice, the recording sites in the cerebellar cortex were reconstructed on the basis of tetrode movement increments after the PC recording.

Results

Purkinje Cell Activity in the Cerebellar Cortex across the Sleep-Wakefulness Cycle

To explore cerebellar neuronal activity at the single-unit level across sleep-wakefulness cycles, we performed tetrode recordings in the cerebellar cortex. Histological results revealed valid recording sites mostly in the vicinity of the PC layer (Fig. 1). All *in vivo* tetrode recordings were performed during the light phase, and the duration of each recording was 139.5 ± 4.9 min on average (mean ± SEM, n = 10 mice).

As the sole output neurons of the cerebellar cortex, PCs integrate information in this area, and thereafter strongly control neuronal activity in the downstream DCN. Consequently, we first investigated the activity of PCs over many episodes of distinct sleep-wakefulness states. The putative PCs were initially determined *in vivo* by their spontaneous intense cellular activity. Typically, a putative PC showed an autocorrelogram with a profound central trough (Fig. 2A) and a unimodal inter-spike interval distribution with a peak at 12–30 ms (Fig. 2A). Afterwards, the putative PCs were further confirmed by the presence of both simple and complex spikes during unit clustering (Fig. 2B–D). The complex spikes were manually discriminated on the basis of the presence of a 1–3 ms slow component together with their stereotypical shape (i.e., board monophasic negative waves, Fig. 2D). For each putative PC, the presence of a pause (> 10 ms) in simple spike firing after a complex spike was verified (Fig. 2C, E). A total of 33 putative PCs were determined, showing an average firing rate of 38.7 ± 3.9 Hz.

We then calculated the average firing rates of putative PCs during each state, and compared their quantitative features across states. The brain state was determined by oscillation of the LFP in the frontal cortex and head/neck movements (Fig. 3A). The proportion of each state in our recordings was similar to that in previous reports [42, 43] (Fig. 3B). We found that the average firing rates of putative PCs were highest during wakefulness (Fig. 3A, C). Furthermore, the high PC activity was always associated with head/neck movements (Fig. 3A, upper panel). Statistical analysis revealed that the firing rates of PCs during wakefulness were significantly higher than those in NREM sleep ($t_{(32)} = -3.8725$, $P < 0.001$, paired t test, n = 33, Fig. 3C). In addition, we found a significant difference in the firing rates of PCs between REM sleep and wakefulness ($t_{(32)} = -2.7429$, $P = 0.0099$, Fig. 3C). However, there was no significant difference in the firing rates of PCs between NREM and REM sleep ($t_{(32)} = 0.8262$, $P = 0.4148$, Fig. 3C). Considering that the PCs showed several firing patterns, such as a regular pattern during NREM and a burst-like pattern during awake and REM (Fig. 3A), we further calculated the coefficient of variance (CV) of PC spikes during each state. We found that the CV of PC spikes showed changes similar to the firing rates across distinct states (awake *vs* NREM: $t_{(9)} = 3.937$, $P = 0.004$; NREM *vs* REM: $t_{(9)} = 0.094$, $P = 0.927$; awake *vs* REM: $t_{(9)} = 2.333$, $P = 0.048$, paired t test, n = 10 mice; Fig. S1A).

In addition, similar to previous *in vivo* electrophysiological studies [44, 45], we recorded complex spikes with an average rate of 1.05 ± 0.09 Hz in putative PCs (n = 33). However, there were no significant changes in complex spike rates across states (awake *vs* NREM: $t_{(32)} = 0.7363$, $P = 0.5168$; NREM *vs* REM: $t_{(32)} = -0.7117$, $P = 0.6333$; awake *vs* REM: $t_{(32)} = 0.2357$, $P = 0.8358$), indicating that climbing fiber input is unlikely to be the main signal source affecting state transitions.

Changes in PC activity have been demonstrated to be fast and temporally precise, participating in both the accurate execution and error-correction of motor behavior in the awake state [2, 4]. Therefore, we further investigated whether a fast and dynamic change of PC activity occurs during state transition. Based on the criteria listed in a

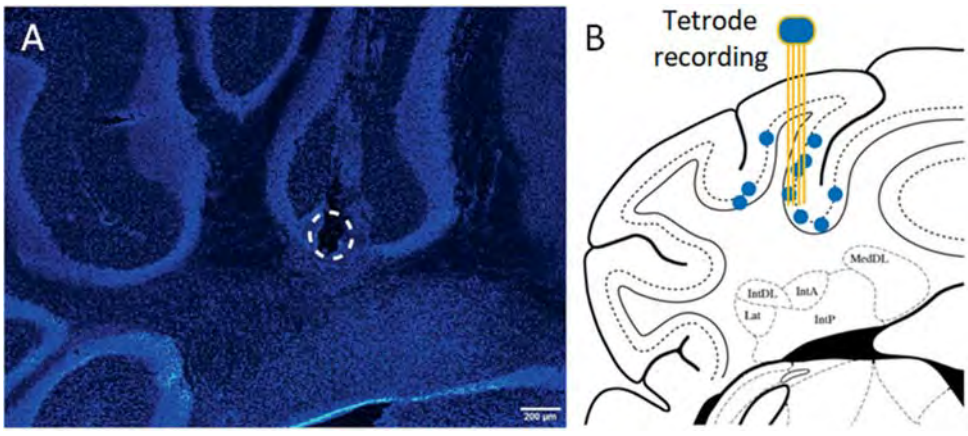

Fig. 1 Locations of recording sites in the cerebellar cortex. **A** A DAPI-stained coronal section illustrating a representative recording site in the cerebellar cortex (dashed circle) (scale bar, 200 μm). **B** Schematic of the recording sites in the cerebellar cortex (blue circles, n = 10). Note that, in 8 of the mice, the recording site was estimated by the tetrode movement distance between the initial cortical recording and final DCN recording.

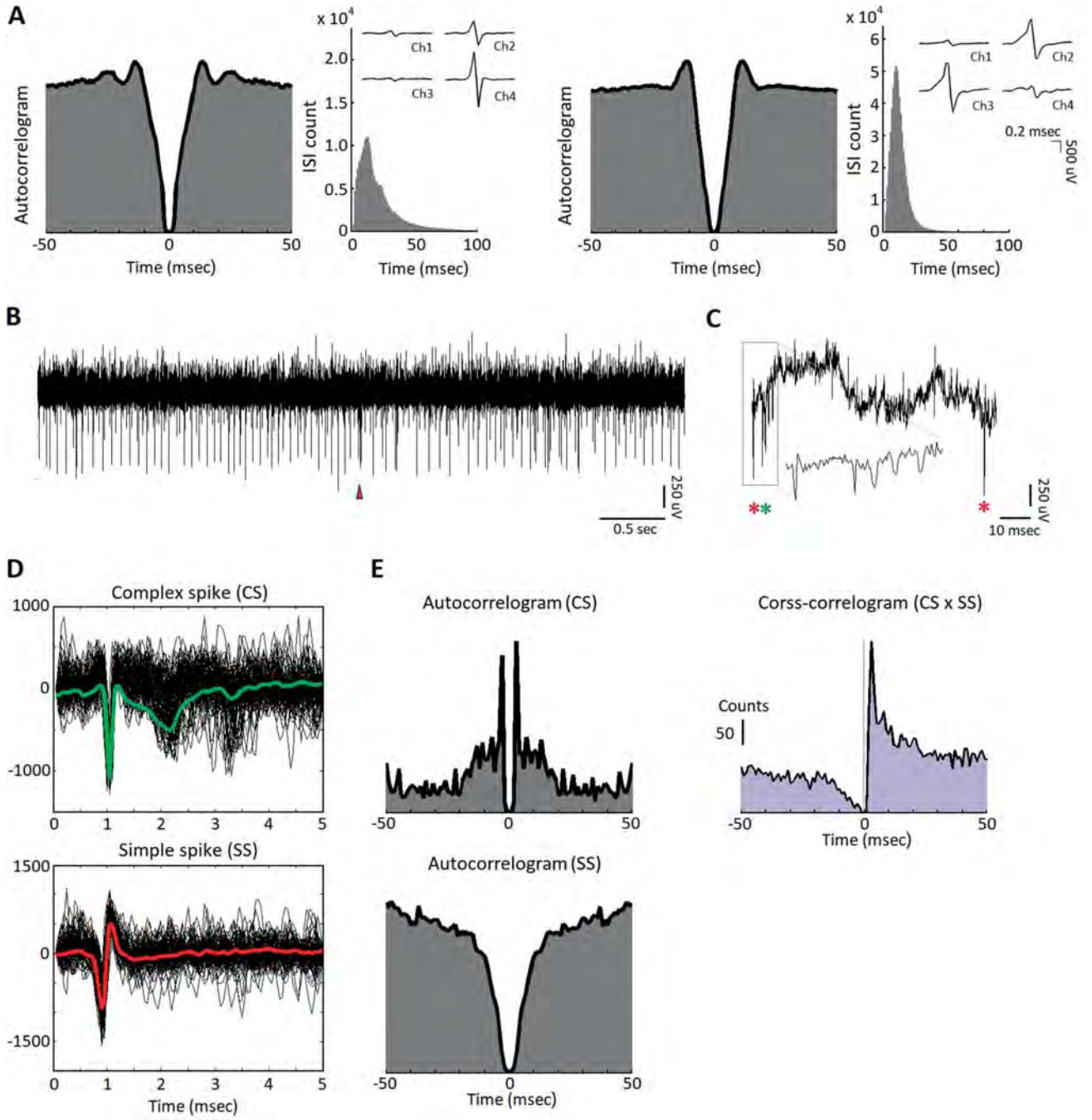

Fig. 2 Electrophysiological classification of putative Purkinje cells *in vivo*. **A** Autocorrelograms, average filtered waveforms, and inter-spike interval (ISI) distributions of two putative Purkinje cells. **B** Trace of continuous recording from the Purkinje cell layer. **C** Two simple spikes (red asterisks) and four complex spikes (green asterisk) magnified from the recording in panel **B** (red triangle). Note the pause of simple spikes after complex spikes. **D** Superimposed waveforms of 100 complex spikes (CS, upper) and simple spikes (SS, lower) in **B**. **E** Autocorrelograms of the complex spikes (CS, upper) and simple spikes (SS, lower) in **B**. The cross-correlogram between the complex spikes (CS) and simple spikes (SS) shows a decrease of simple spike firing after the occurrence of a complex spike.

recent study [23], we found that the firing activity of putative PCs increased significantly from NREM sleep to wakefulness ($t_{(32)} = -2.8529$, $P = 0.0075$, paired t test, $n = 33$, Fig. 4A, B), with 15/33 cells showing greater activity (> baseline + 1.5 SD) during wakefulness than NREM sleep (Fig. 4C). Notably, in those PCs with greater activity, the average latency between increased PC firing and wakefulness onset was 2.2 ± 0.5 s ($n = 15$). Conversely, the firing activity of putative PCs decreased when mice fell asleep ($t_{(32)} = 2.547$, $P = 0.0159$, paired t test, $n = 33$, Fig. 4D, E), with 9/33 cells showing lower activity (< baseline − 1.5 SD) during NREM sleep than

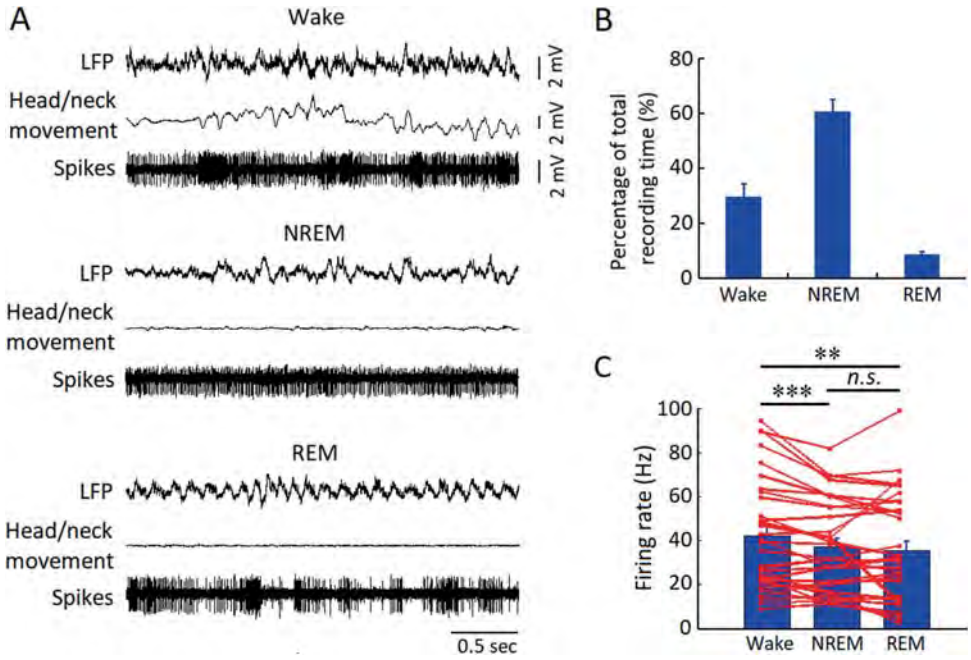

Fig. 3 Firing of putative Purkinje cells across distinct states. **A** High-pass filtered traces showing representative firing of single putative Purkinje cell across the wakefulness (upper), NREM sleep (middle), and REM sleep (lower) states. The states were determined by the local field potential (LFP) in the frontal cortex and head/neck movements. **B** Percentage of time in awake, NREM sleep, or REM sleep state during recordings, averaged from 10 mice. Data are expressed as the mean ± SEM. **C** Averaged firing rate of putative Purkinje cells (n = 33) in each state. $^{**}P < 0.01$; $^{***}P < 0.001$; *n.s.* Not significant.

wakefulness (Fig. 4F). The latency between decreased PC firing and NREM sleep onset was 3.4 ± 0.4 s (n = 9). In addition, the putative PCs tended to increase their activity at the transition from REM sleep to wakefulness ($t_{(32)} = -2.5262$, $P = 0.0167$, paired t test, n = 33, Fig. 4H, I) with a mean latency of 1.6 ± 0.4 s. We also plotted the NREM–wakefulness modulation index $(F_{NREM} - F_{wake})/(F_{NREM} + F_{wake})$, where F is the average firing rate within each state *versus* the REM–NREM modulation index $(F_{REM} - F_{NREM})/(F_{REM} + F_{NREM})$ for each PC. The NREM–wakefulness modulation index of PCs showed a unimodal distribution centered on 0.06 (Fig. S1B), which corresponded to the awake state. In contrast, the REM–NREM modulation of PCs exhibited a bimodal distribution centered on − 0.08 (Fig. S1B), with the peak corresponding to the REM–off state. These results thus suggested that the PCs are both wake–on and REM–off neurons. In contrast, there was no significant change in activity at the NREM-to-REM ($t_{(32)} = -0.1442$, $P = 0.8862$, paired t test, n = 33, Fig. S2A) or REM-to-NREM transition ($t_{(32)} = -1.5295$, $P = 0.136$, Fig. S2B). Taken together, our results provide evidence that endogenous putative PC activity is specifically correlated with and occurs prior to the state transition from sleep to wakefulness.

Non-PC Unit Activity in the Cerebellar Cortex Across the Sleep–Wakefulness Cycle

The firing activity of PCs is modulated by inputs from non-PC units such as granule cells and interneurons in the cerebellar cortex [46]. Therefore, we evaluated the firing activity of non-PC units during each state. In 10 mice, we recorded and clustered 42 non-PC units, which showed a relatively low average firing rate of 3.9 ± 0.1 Hz. The firing rates of non-PC units were significantly lower than those of the putative PCs ($Z = 7.2312$, $P < 0.001$, Wilcoxon rank sum test). In addition, no complex spikes were found in these non-PC units. Similar to the PCs, the non-PC units also exhibited brain-state-dependent activity (Fig. 5A). Notably, the lowest firing activity of non-PC units occurred during NREM sleep (NREM *vs* wakefulness: $t_{(41)} = -3.1404$, $P = 0.0031$; NREM *vs* REM: $t_{(41)} = -3.7565$, $P < 0.001$, paired t test, n = 42, Fig. 5A). In contrast, there was no significant difference in firing rates between wakefulness and REM sleep ($t_{(41)} = -1.4469$, $P = 0.1555$, Fig. 5A).

Again, we plotted the NREM–wakefulness modulation index $(F_{NREM} - F_{wake})/(F_{NREM} + F_{wake})$, where F is the average firing rate in each state *versus* the REM–NREM modulation index $(F_{REM} - F_{NREM})/(F_{REM} + F_{NREM})$. The NREM–wakefulness modulation index of non-PC units showed a unimodal distribution centered on 0.18 (Fig. 5B), which corresponded to the awake state. Moreover, the REM–NREM modulation of non-PC units also exhibited a unimodal distribution centered on 0.17 (Fig. 5B), with the peak corresponding to the REM sleep state. These results thus suggested that the non-PC units in the cerebellar cortex are both wake-on and REM-on active.

Next, we recorded the activity of non-PC units during various state transitions, and found that their activity increased significantly at the NREM sleep-to-wakefulness transition ($t_{(41)} = -2.4886$, $P = 0.0170$, paired t test,

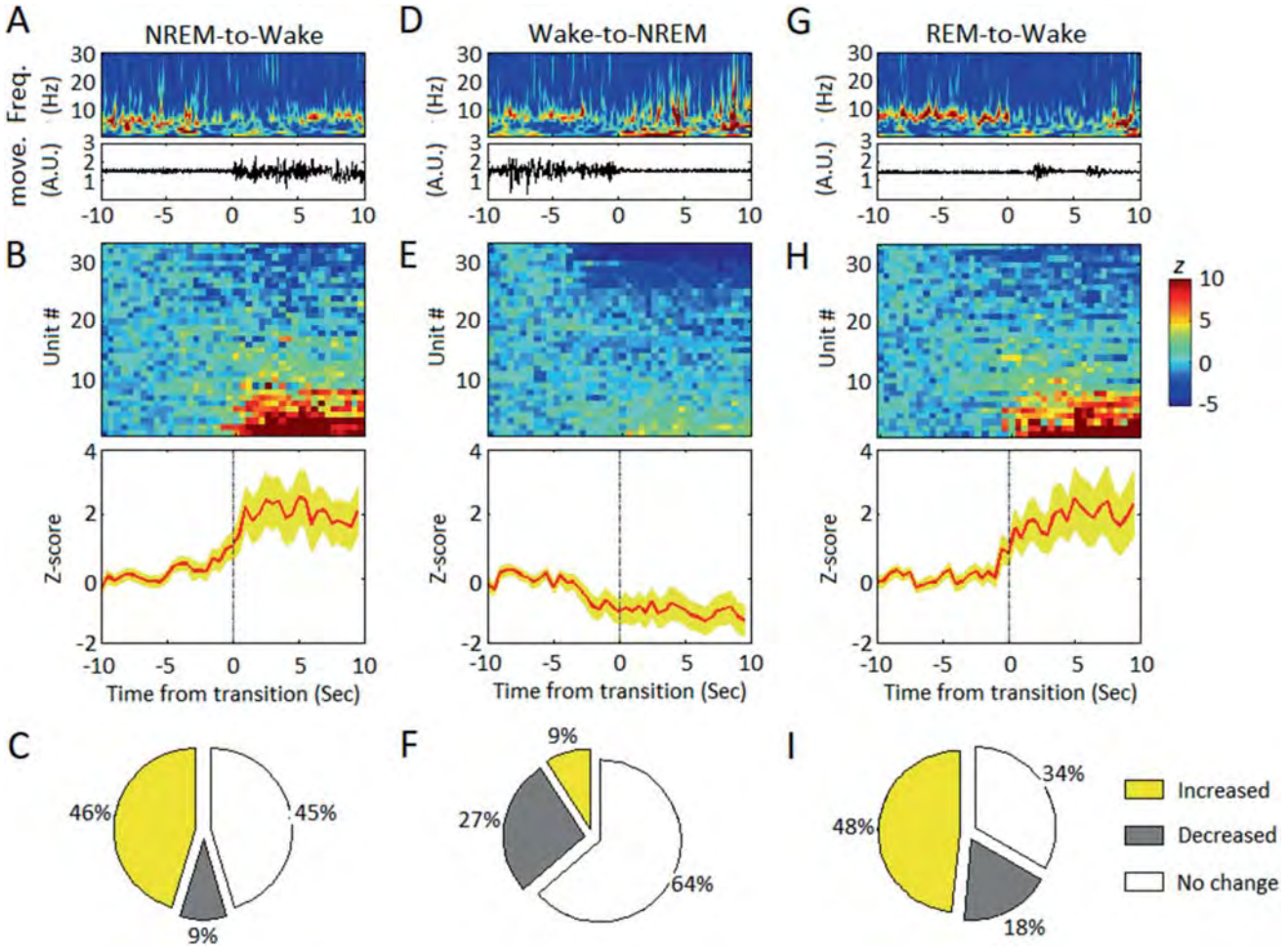

Fig. 4 Dynamics of putative Purkinje cell activity at state transitions. **A** Representative LFP power spectrum and head/neck movement traces illustrating the NREM–wakefulness transition. **B** Increased firing activity of putative Purkinje cells preceding the transition from NREM sleep to wakefulness ($n = 33$). **C** Proportions of Purkinje cells showing increased, decreased, or minimal responses to the NREM–wakefulness transition. **D** Representative LFP power spectrum and head/neck movement traces illustrating the wakefulness–NREM transition. **E** Decreased firing activity of putative Purkinje cells preceding the transition from wakefulness to NREM sleep ($n = 33$). **F** Proportions of Purkinje cells showing increased, decreased, or minimal responses to the wakefulness–NREM transition. **G** Representative LFP power spectrum and head/neck movement traces illustrating the REM–wakefulness transition. **H** Increased firing activity of putative Purkinje cells preceding the transition from REM sleep to wakefulness ($n = 33$). **I** Proportions of recorded Purkinje cells showing increased, decreased, or minimal responses to the REM–wakefulness transition. Color scale indicates the power (mV^2) of raw power spectral density in **A**, **D**, and **G**; data are expressed as the mean ± SEM; shaded areas indicate SEM in **B**, **E**, and **H**.

$n = 42$, Fig. 5C), with 24/42 cells showing greater activity during wakefulness than NREM sleep (Fig. 5D). For the non-PC units with greater activity, the mean latency between increased non-PC firing and wakefulness onset was 0.0 ± 0.6 s ($n = 24$). Conversely, the firing activity of non-PC units decreased when the mice fell asleep ($t_{(41)} = 3.9863$, $P < 0.001$, paired t test, $n = 42$, Fig. 5E), with 24/42 cells showing lower activity during NREM sleep than wakefulness (Fig. 5F). The mean latency between decreased non-PC firing and NREM sleep onset was 1.4 ± 0.9 s ($n = 24$). In contrast to the putative PCs, the non-PC units did not increase their activity at the transition from REM sleep to wakefulness ($t_{(41)} = -0.0319$, $P = 0.9747$, paired t test, $n = 42$, Fig. 5G, H). Likewise, there was no significant change in activity at the NREM-to-REM or REM-to-NREM transition (both $P > 0.05$, paired t test, $n = 42$). In sum, these results suggested that the activity of non-PC units varies with brain states, and they are especially active in the wakefulness and REM sleep states.

The PCs and non-PCs exhibited similar brain-state-dependent activities, suggesting that they interacted with each other. To test this possibility, we calculated the excitatory monosynaptic connection between non-PCs and PCs (non-PC × PC pairs) using spike cross-correlation between simultaneously-recorded non-PCs and PCs (with

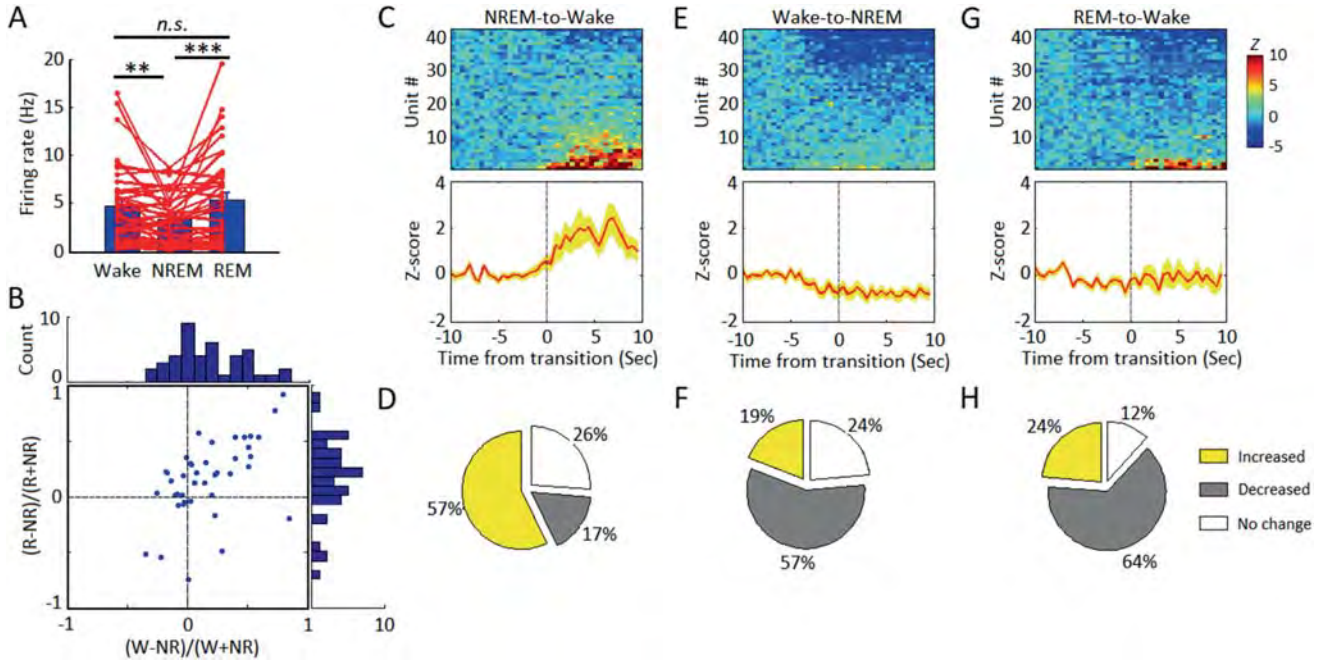

Fig. 5 Dynamics of non-PC unit activity at state transitions. **A** Averaged firing rates of non-PC units in each state ($n = 42$). Data are expressed as the mean ± SEM (**$P < 0.01$, ***$P < 0.001$, *n.s.*, Not significant). **B** REM–NREM activity difference *versus* wakefulness–NREM activity difference. Each symbol represents one neuron ($n = 42$ units from 10 mice). **C** Increased firing activity of non-PC units preceding the transition from NREM sleep to wakefulness ($n = 42$). **D** Proportions of non-PC units showing increased, decreased, or minimal responses to the NREM–wakefulness transition. **E** Decreased firing activity of non-PC units preceding the transition from wakefulness to NREM sleep ($n = 42$). **F** Proportions of non-PC units showing increased, decreased, and minimal responses to the wakefulness–NREM transition. **G** Firing activity of non-PC units at the transition from REM sleep to wakefulness ($n = 42$). **H** Proportions of non-PC units showing increased, decreased, or minimal responses to the REM-wakefulness transition. Data are expressed as the mean ± SEM (shaded areas indicate SEM) in **C**, **E**, and **G**.

non-PC spikes at $t = 0$). We detected monosynaptically-connected pairs from the neuronal pools recorded by the same tetrode (Fig. 6A). Notably, putative PCs tended to fire after the firing of a non-PC (Fig. 6A). Of 19 cross-correlograms, 7 (36.8%) had a short-latency (< 3 ms) and unimodal peak (Fig. 6B), indicating monosynaptic inputs from non-PCs to PCs. Indeed, the probability of short-latency (< 3 ms) PC firing after a non-PC spike was significantly higher than that among non-PCs ($Z = 2.113$, $P = 0.0346$, Wilcoxon rank sum test, Fig. 6C, D). These results suggested that there are significant interactions between the non-PCs and PCs across sleep-wakefulness cycles.

Neuronal Activity in the DCN Across the Sleep-Wakefulness Cycle

The DCN are the final outputs of the cerebellum, innervating several areas critical for promoting or maintaining wakefulness [15–17, 19]. Moreover, their firing is strongly controlled by inhibitory PC inputs [46, 47]. Consequently, we further investigated whether the firing of DCN units is affected by the changes in firing activity of PCs across distinct states. To this end, we moved the tetrodes from the vicinity of the PC layer into the DCN in 8 mice. The recording sites in the DCN were verified *post hoc* (Fig. 7A, B). We recorded from and clustered a total of 21 DCN units. The mean firing rate of the DCN units was 25.8 Hz ± 5.1 Hz, ranging from 2.7 to 94.9 Hz. On average, the firing rates of DCN neurons were significantly lower than those of PCs in both wakefulness and NREM sleep (awake: $Z = -2.3067$, $P = 0.0211$; NREM: $Z = -2.2002$, $P = 0.0278$, Wilcoxon rank sum test). Although there were no significant differences in the averaged firing rates among distinct states ($P > 0.05$, Fig. S3A), statistical analysis revealed decreased firing activity of DCN units at the transition from NREM sleep to wakefulness ($t_{(20)} = 2.1770$, $P = 0.0416$, paired t test, $n = 21$, Fig. 7C), with 9/21 cells showing lower activity during wakefulness than NREM sleep (Fig. 7D). In these units, the mean latency between the decreased firing and wakefulness onset was 2.0 ± 0.7 s ($n = 9$). Likewise, the firing activity of DCN units tended to decrease at the transition from REM sleep to wakefulness, although it failed to reach a significant level ($t_{(20)} = 1.8572$, $P = 0.0781$, Fig. 7E, F). Moreover, there were no significant changes in firing activity during the wakefulness–NREM ($t_{(20)} = -0.8008$, $P = 0.4326$, paired t test,

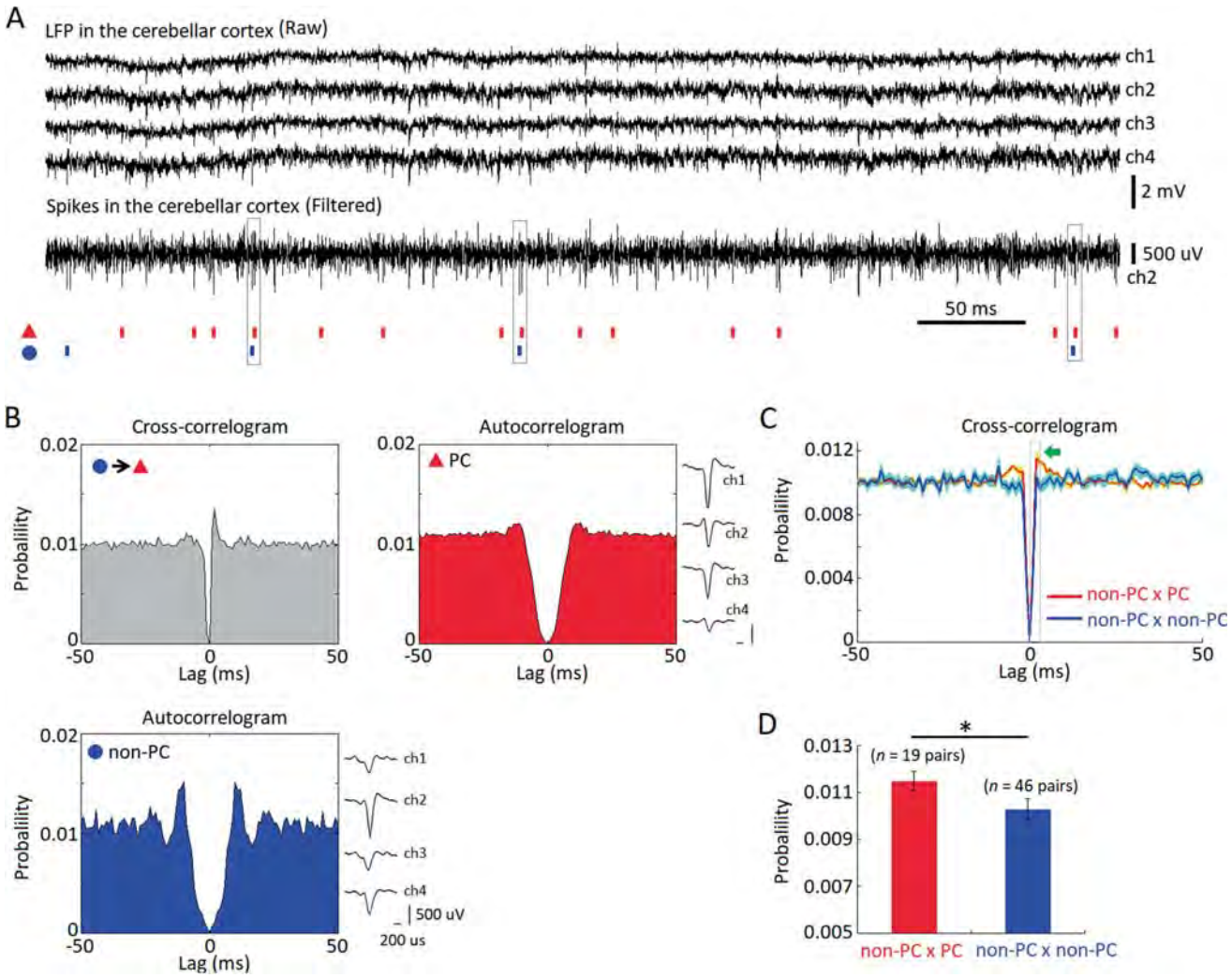

Fig. 6 Monosynaptic connections between non-PC units and PCs. **A** Raw traces showing tetrode recording (channels 1–4) in the cerebellar cortex. The high-pass filtered trace (below) shows simultaneously-recorded non-PC and PC units in channel 2. Notably, the putative PC (red) tended to fire after the firing of a non-PC unit (blue) within a 3-ms window. **B** Autocorrelograms and cross-correlogram between the non-PC unit (blue) and the PC unit (red) illustrated in **A**. **C** Normalized cross-correlograms (CCG) for non-PC × PC pairs (n = 19) and non-PC × non-PC pairs (n = 40). **D** Probability of excitatory monosynaptic connection between non-PCs and PCs was significantly greater than that between non-PC units. Data are expressed as the mean ± SEM (*$P < 0.05$).

n = 21, Fig. 7G, H), NREM–REM ($P > 0.05$, Fig. S3B, C), and REM–NREM transitions ($P > 0.05$, Fig. S3D, E). These results suggested that, in line with the change of PC firing, the downstream DCN units also exhibit significant change in firing activity, especially during the transition from NREM sleep to wakefulness.

Discussion

In order to determine the specific role of the cerebellum in the regulation of sleep and wakefulness, it is necessary to detect the activity patterns of cerebellar units during this process. To this end, we performed *in vivo* multi-unit recordings in naturally sleeping mice, and found that PCs in the cerebellar cortex exhibited significantly increased firing activity prior to the transition from sleep to wakefulness. Moreover, the increased PC activity resulted from inputs from low-frequency firing non-PC units in the cerebellar cortex. Downstream of the inhibitory PCs, neurons in the DCN manifested decreased firing during the transition from NREM sleep to wakefulness. Our results, together with information about cerebellar–hypothalamic and cerebellar–ventral thalamic circuitry, highlight the temporal features by which the cerebellum is actively involved in regulating sleep and wakefulness.

The cerebellum has long been known to be critical for motor planning [1], motor execution [2–4, 48], and motor learning [5–7]. Recently, it has also been implicated in several non-motor functions such as cognition [49], reward

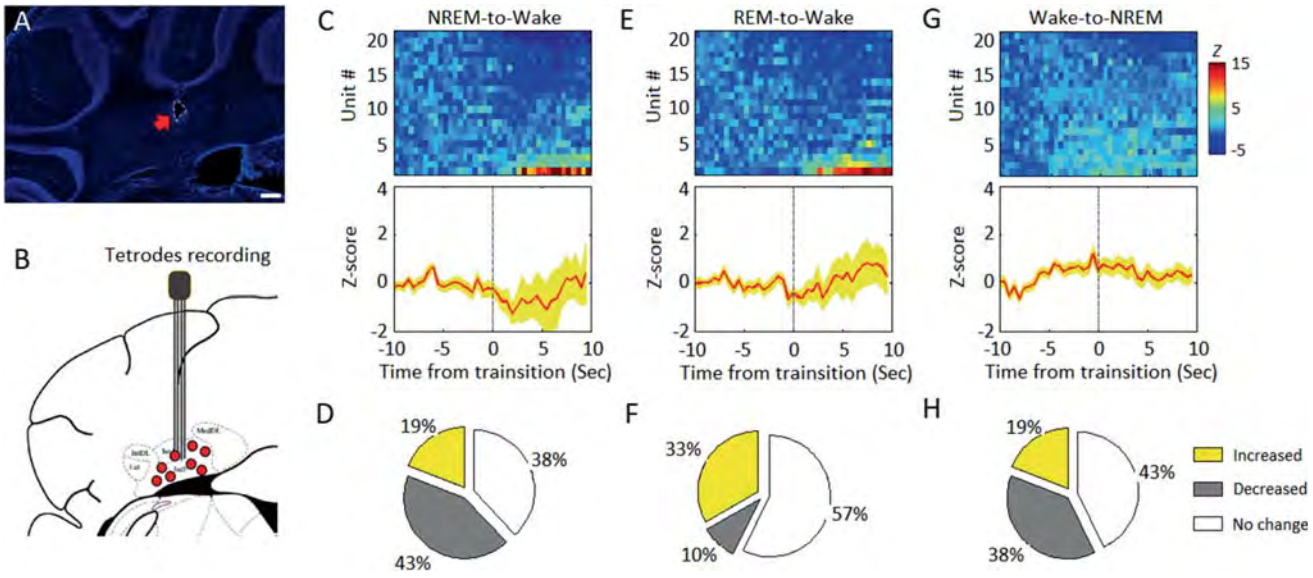

Fig. 7 Dynamics of DCN unit activity at state transitions. **A** A DAPI-stained coronal section showing a representative recording site in the DCN (arrow; scale bar, 200 μm). **B** Schematic of the recording sites in the DCN (red circles, n = 8 mice). **C** Decreased firing activity of DCN units preceding the transition from NREM sleep to wakefulness (n = 21). **D** Proportions of the DCN units showing increased, decreased, or minimal responses to the NREM–wakefulness transition. **E** Firing activity of DCN units at the transition from REM sleep to wakefulness (n = 21). **F** Proportions of DCN units showing increased, decreased, or minimal responses to the REM–wakefulness transition. **G** Firing activity of DCN units at the transition from wakefulness to NREM sleep (n = 21). **H** Proportions of DCN units showing increased, decreased, or minimal responses to the wakefulness–NREM transition. Data are expressed as the mean ± SEM (shaded areas indicate SEM in **C**, **E**, and **G**).

[50], social behavior [51], spatial learning [52, 53], and fear conditioning [54]. Aside from these non-motor functions, we showed here that neurons in the mouse cerebellum exhibited state-dependent activities across sleep-wakefulness cycles (Figs. 4, 5). In particular, the changes of cerebellar neuronal firing preceded the transitions between states. Therefore, the cerebellum might be a novel candidate for regulating sleep and/or wakefulness states *via* its interaction with arousal neurons in the ventral thalamus and hypothalamus [14]. In support of this hypothesis, sleep disturbance is common in patients suffering from cerebellar degeneration [8–10]. Likewise, increased sleep often occurs in cerebellectomized cats [11].

Previous studies combining fMRI and EEG recordings have indicated that cerebellar activity is lower during NREM than during wakefulness [29, 55]. Relative to the imaging technologies, invasive multi-unit recordings allow recordings of single unit activity at higher temporal and cellular specificity in the cerebellum [56–58]. In this study, we classified cerebellar cortical units into putative PCs and non-PCs according to their firing characteristics (Fig. 2). Notably, we found that both the putative PCs and non-PCs increased their activities prior to the transition from NREM sleep to wakefulness (Figs. 4, 5). Moreover, our results revealed that the increased PC activity resulted from the inputs of non-PCs. Along this line, both types of neurons decreased their firing activity during the transition from pre-sleep wakefulness to NREM sleep (Figs. 4, 5). Consequently, our results not only resemble the functional imaging findings in human subjects [29, 55], but also demonstrate the cellular mechanisms underlying cerebellar cortical activation during the NREM–wakefulness transition. Interestingly, significant firing changes of cerebellar cortical units did not occur during the transition between the NREM–REM or REM–NREM sleep states (Fig. S2), indicating that the cerebellar cortex might be involved in the transition between specific states. However, future experiments using Cre-dependent optogenetic or chemogenetic manipulation are needed. These experiments can reveal the control of specific neuronal activity in the cerebellar cortex [4, 59, 60], and thus determine its role in regulation of the sleep-wakefulness transition [24, 61].

Previous studies showed that the activities of PCs and DCN neurons increase during REM sleep [25–28]. In contrast, we found here that the activity of PCs decreased in REM sleep. Considering that the firing activity of PCs is strongly correlated with movement and muscle tone [2–4, 48], it is reasonable to conclude that our current results are compatible with the loss of muscle tone during REM sleep. Together with temporal dynamics of the PC activity [2–4], we speculate that PCs might be involved in the state transition by means of the change of firing activity, rather than the average firing rate. However, this speculation needs to be tested to see whether the state

transition can be induced by the rapid optogenetic manipulation of PCs.

The averaged firing rates of non-PCs recorded in the cerebellar cortex are similar to the findings reported in previous *in vivo* electrophysiological studies [57, 62]. Considering that the overwhelming majority of neurons in the cerebellar cortex are excitatory granule cells [46, 47], our results most likely reveal a change in granule cell activity during the state transition. However, we cannot exclude the possibility that distinct firing patterns occur in other non-PCs such as inhibitory Golgi cells and/or basket cells [62]. Indeed, as shown in Fig. 5C, D, the non-PCs showed both increased (57%) and decreased (17%) firing activity during the NREM-to-awake transition. This result thus leads to the interpretation that both types of non-PCs (excitatory granule cells and inhibitory Golgi cells) may be involved in the state transition.

In this study, there was a difference in the latency to the state transition between the putative PCs (2.2 $\pm$ 1.8 s) and the non-PCs (0.0 $\pm$ 2.7 s). This result seemed to contradict our proposal that there are monosynaptic inputs from the non-PCs to the PCs as shown in Fig. 6. Nevertheless, it should be noted that only 36.8% of the non-PCs had monosynaptic inputs to the PCs. Moreover, we showed that non-PCs had both increased and decreased firing activity during the NREM-to-awake transition, indicating the firing complexity of non-PCs. Previously, the cerebellar cortex has been revealed to contain a huge number of granule cells, which are inhibited by their neighboring Golgi cells [46, 47, 62]. Moreover, the activity of Golgi cells can be indirectly influenced by PCs [63]. Therefore, it is reasonable to expect that common inputs to both granule cells and Golgi cells may result in complex firing patterns in non-PCs, as evidenced by their greater variance of latency ($\pm$ 2.7 s) to the state transition.

Responding to the increased PC firing, the downstream DCN units exhibited significantly decreased firing activity during the transition from NREM sleep to wakefulness. Anatomically, as the final integration and output of the cerebellum, the DCN are strongly and reciprocally connected to several regions associated with sleep-wakefulness [15–17, 19–21]. Therefore, the change in neuronal activity enables the DCN to participate in the NREM-wakefulness transition. This notion is further supported by indirect evidence that activation of the ventral thalamus, one of the downstream areas of the DCN, induces a rapid state transition from NREM sleep to wakefulness [18]. Nevertheless, future research is needed to test whether direct activation of the DCN terminals in the ventral thalamus has a similar effect on the NREM-wakefulness transition.

It should also be noted that there was no significant change in the DCN neuronal activity during the transition from REM sleep to wakefulness (Fig. 7), implying that the cerebellum as a whole is unlikely to participate in the regulation of the REM-wakefulness transition. In support of this idea, activation of the ventral thalamus does not promote the transition from REM sleep to wakefulness [18]. As noted, however, the firing activity of PCs increases during the transition from REM sleep to wakefulness (Fig. 4), which is associated with the movements. Therefore, the question remained as to why the neuronal activity in the downstream DCN remained relatively stable. Evidence has accumulated that the DCN consists of at least three subgroups: glutamatergic, GABAergic, and glycinergic cells [64, 65]. In particular, the glutamatergic DCN neurons are inhibited by their GABAergic neighbors [65]. In this study, we expected that the increased PC activity would inhibit the downstream neurons in the DCN. Meanwhile, the inhibited GABAergic DCN cells can disinhibit the glutamatergic DCN neurons. We speculate that these two contradictory effects on the glutamatergic DCN neurons, to some extent might result in overall unchanged activity in the DCN. In addition, it has been demonstrated that the excitatory neuromodulator acetylcholine is released in the cerebellum during REM sleep [66, 67], which might antagonize the inhibitory PC effects on DCN cells during the transition from REM sleep to wakefulness.

The purpose of this study was to provide electrophysiological evidence that the cerebellum has the potential to regulate the sleep-wakefulness transition. We revealed here the temporal features of single-unit activity in the mouse cerebellum, which are essential for determining whether and how the cerebellum is actively involved in regulating the sleep-wakefulness transition. Evidence has accumulated that the cerebellum is involved in various non-motor functions by means of its connections with the cerebral cortex [1, 3, 4], hippocampus [52, 53], pontine nuclei [68], and other subcortical areas [50, 51, 54]. In this study, we focused on the cerebrocerebellum because sleep and wakefulness have been strongly associated with activity in the cerebral cortex [69, 70]. However, future experiments are needed to test whether the firing patterns of each cerebellar region show a similar spatiotemporal pattern in the various sleep stages.

Acknowledgements This work was supported by grants from the National Natural Science Foundation of China (81671315), the Natural Science Foundation of Chongqing Municipality (cstc2019jcyj-msxmX0424), the Frontier Interdisciplinary Project of the College of Basic Sciences, Army Medical University, China (2018JCQY01), and the National Training Program of Innovation and Entrepreneurship for Undergraduates, China (201990035020).

Conflict of interest The authors declare that they have no conflict of interest.

References

1. Gao Z, Davis C, Thomas AM, Economo MN, Abrego AM, Svoboda K, *et al.* A cortico-cerebellar loop for motor planning. Nature 2018, 563: 113–116.
2. Herzfeld DJ, Kojima Y, Soetedjo R, Shadmehr R. Encoding of action by the Purkinje cells of the cerebellum. Nature 2015, 526: 439–442.
3. Proville RD, Spolidoro M, Guyon N, Dugué GP, Selimi F, Isope P, *et al.* Cerebellum involvement in cortical sensorimotor circuits for the control of voluntary movements. Nat Neurosci 2014, 17:1233–1239.
4. Becker MI, Person AL. Cerebellar control of reach kinematics for endpoint precision. Neuron 2019, 103: 335–348.
5. Nguyen-Vu TD, Kimpo RR, Rinaldi JM, Kohli A, Zeng H, Deisseroth K, *et al.* Cerebellar Purkinje cell activity drives motor learning. Nat Neurosci 2013, 16: 1734–1736.
6. Yang Y, Lisberger SG. Purkinje-cell plasticity and cerebellar motor learning are graded by complex-spike duration. Nature 2014, 510: 529–532.
7. Lee KH, Mathews PJ, Reeves AMB, Choe KY, Jami SA, Serrano RE, *et al.* Circuit Mechanisms underlying motor memory formation in the cerebellum. Neuron 2015, 86: 529–540.
8. DelRosso LM, Hoque R. The cerebellum and sleep. Neurol Clin 2014, 32: 893–900.
9. Pedroso JL, Braga-Neto P, Escorcio-Bezerra ML, Abrahao A, de Albuquerque MV, Filho FM, *et al.* Non-motor and extracerebellar features in spinocerebellar ataxia type 2. Cerebellum 2017, 16: 34–39.
10. Yuan X, Ou R, Hou Y, Chen X, Cao B, Hu X, *et al.* Extra-Cerebellar signs and non-motor features in Chinese patients with spinocerebellar ataxia type 3. Front Neurol 2019, 10: 110.
11. Cunchillos JD, De Andres I. Participation of the cerebellum in the regulation of the sleep-wakefulness cycle. Results in cerebellectomized cats. Electroencephalogr Clin Neurophysiol 1982, 53: 549–558.
12. Joo EY, Noh HJ, Kim JS, Koo DL, Kim D, Hwang KJ, *et al.* Brain gray matter deficits in patients with chronic primary insomnia. Sleep 2013, 36: 1004.
13. Desseilles M, Dang-Vu T, Schabus M, Sterpenich V, Maquet P, Schwartz S. Neuroimaging insights into the pathophysiology of sleep disorders. Sleep 2008, 31: 777–794.
14. Canto CB, Onuki Y, Bruinsma B, van der Werf YD, De Zeeuw CI. The sleeping cerebellum. Trend Neurosci 2017, 40: 309–323.
15. Houck BD, Person AL. Cerebellar premotor output neurons collateralize to innervate the cerebellar cortex. J Comp Neurol 2015, 523: 2254–2271.
16. Gornati SV, Schäfer CB, Eelkman Rooda OHJ, Nigg AL, De Zeeuw CI, Hoebeek FE. Differentiating cerebellar impact on thalamic nuclei. Cell Rep 2018, 23: 2690–2704.
17. Tanaka YH, Tanaka YR, Kondo M, Terada SI, Kawaguchi Y, Matsuzaki M. Thalamocortical axonal activity in motor cortex exhibits layer-specific dynamics during motor learning. Neuron 2018, 100: 1–15.
18. Honjoh S, Sasai S, Schiereck SS, Nagai H, Tononi G, Cirelli C. Regulation of cortical activity and arousal by the matrix cells of the ventromedial thalamic nucleus. Nat Commun 2018, 9: 2100.
19. Dietrichs E, Haines DE. Interconnections between hypothalamus and cerebellum. Anat Embryol (Berl) 1989, 179: 207–220.
20. Zhu JN, Yung WH, Kwok-Chong Chow B, Chan YS, Wang JJ. The cerebellar- hypothalamic circuits: potential pathways underlying cerebellar involvement in somatic-visceral integration. Brain Res Rev 2006, 52: 93–106.
21. Çavdar S, Özgur M, Kuvvet Y, Bay HH. The Cerebello-hypothalamic and hypothalamo-cerebellar pathways via superior and middle cerebellar peduncle in the rat. Cerebellum 2018, 17: 517–524.
22. Adamantidis AR, Zhang F, Aravanis AM, Deisseroth K, de Lecea L. Neural substrates of awakening probed with optogenetic control of hypocretin neurons. Nature 2007, 450: 420–424.
23. Ren S, Wang Y, Yue F, Cheng X, Dang R, Qiao Q, *et al.* The paraventricular thalamus is a critical thalamic area for wakefulness. Science 2018, 362: 429–434.
24. Liu D, Dan Y. A motor theory of sleep-wake control: Arousal-action circuit. Annu Rev Neurosci 2019, 42: 27–46.
25. Mano N. Changes of simple and complex spike activity of cerebellar Purkinje cells with sleep and waking. Science 1970, 170: 1325–1327.
26. McCarley RW, Hobson JA. Simple spike firing patterns of cat cerebellar Purkinje cells in sleep and waking. Electroencephalogr Clin Neurophysiol 1972, 33: 471–483.
27. Hobson JA, McCarley RW. Spontaneous discharge rates of cat cerebellar Purkinje cells in sleep and waking. Electroencephalogr Clin Neurophysiol 1972, 33: 457–469.
28. Palmer C. Interpositus and fastigial unit activity during sleep and waking in the cat. Electroencephalogr Clin Neurophysiol 1979, 46: 357–370.
29. Kaufmann C, Wehrle R, Wetter TC, Holsboer F, Auer DP, Pollmächer T, *et al.* Brain activation and hypothalamic functional connectivity during human non-rapid eye movement sleep: an EEG/fMRI study. Brain 2006, 129: 655–667.
30. Hong CC, Harris JC, Pearlson GD, Kim JS, Calhoun VD, Fallon JH, *et al.* fMRI evidence for multisensory recruitment associated with rapid eye movements during sleep. Hum Brain Mapp 2009, 30: 1705–1722.
31. Miyauchi S, Misaki M, Kan S, Fukunaga T, Koike T. Human brain activity time-locked to rapid eye movements during REM sleep. Exp Brain Res 2009, 192: 657–667.
32. Zhang J, Zhang KY, Zhang LB, Zhang WW, Feng H, Yao ZX, *et al.* A method for combining multiple-units readout of optogenetic control with natural stimulation-evoked eyeblink conditioning in freely-moving mice. Sci Rep 2019, 9: 1857.
33. Qin H, Fu L, Hu B, Liao X, Lu J, He W, *et al.* A visual-cue-dependent memory circuit for place navigation. Neuron 2018, 99: 47–55.
34. Hazan L, Zugaro M, Buzsáki G. Klusters, NeuroScope, NDManager: A free software suite for neurophysiological data processing and visualization. J Neurosci Methods 2006, 155: 207–216.
35. Buzsáki G, Stark E, Berényi A, Khodagholy D, Kipke DR, Yoon E, *et al.* Tools for probing local circuits: high-density silicon probes combined with optogenetics. Neuron 2015, 86: 92–105.
36. Roux L, Hu B, Eichler R, Stark E, Buzsáki G. Sharp wave ripples during learning stabilize the hippocampal spatial map. Nat Neurosci 2017, 20: 845–853.
37. Harris KD, Henze DA, Csicsvari J, Hirase H, Buzsáki G. Accuracy of tetrode spike separation as determined by simultaneous intracellular and extracellular measurements. J Neurophysiol 2000, 84: 401–414.
38. Maingret N, Girardeau G, Todorova R, Goutierre M, Zugaro M. Hippocampo-cortical coupling mediates memory consolidation during sleep. Nat Neurosci 2016, 19: 959–964.
39. Grosmark AD, Mizuseki K, Pastalkova E, Diba K, Buzsáki G. REM sleep reorganizes hippocampal excitability. Neuron 2012, 75: 1001–1007.
40. ten Brinke MM, Boele HJ, Spanke JK, Potters JW, Kornysheva K, Wulff P, *et al.* Evolving models of Pavlovian conditioning: cerebellar cortical dynamics in awake behaving mice. Cell Rep 2015, 13: 1977–1988.
41. Bartho P, Hirase H, Monconduit L, Zugaro M, Harris KD, Buzsaki G. Characterization of neocortical principal cells and

interneurons by network interactions and extracellular features. J Neurophysiol 2004, 92: 600–608.
42. Eban-Rothschild A, Rothschild G, Giardino WJ, Jones JR, de Lecea L. VTA dopaminergic neurons regulate ethologically relevant sleep-wake behaviors. Nat Neurosci 2016, 19: 1356–1366.
43. Cho JR, Treweek JB, Robinson JE, Xiao C, Bremner LR, Greenbaum A, *et al.* Dorsal raphe dopamine neurons modulate arousal and promote wakefulness by salient stimuli. Neuron 2017, 94: 1205–1219.
44. Lang EJ. Organization of olivocerebellar activity in the absence of excitatory glutamatergic input. J Neurosci 2001, 21: 1663–1675.
45. Rasmussen A, Jirenhed DA, Wetmore DZ, Hesslow G. Changes in complex spike activity during classical conditioning. Front Neural Circuits 2014, 8: 90.
46. De Zeeuw CI, Hoebeek FE, Bosman LW, Schonewille M, Witter L, Koekkoek SK. Spatiotemporal firing patterns in the cerebellum. Nat Rev Neurosci 2011, 12: 327–344.
47. Gao Z, van Beugen BJ, De Zeeuw CI. Distributed synergistic plasticity and cerebellar learning. Nat Rev Neurosci 2012, 13: 619–635.
48. Qian A, Wang X, Liu H, Tao J, Zhou J, Ye Q, *et al.* Dopamine D4 receptor gene associated with the frontal-striatal-cerebellar loop in children with ADHD: A resting-state fMRI study. Neurosci Bull 2018, 34: 497–506.
49. Buckner RL. The cerebellum and cognitive function: 25 years of insight from anatomy and neuroimaging. Neuron 2013, 80: 807–815.
50. Wagner MJ, Kim TH, Savall J, Schnitzer MJ, Luo L. Cerebellar granule cells encode the expectation of reward. Nature 2017, 544: 96–100.
51. Carta I, Chen CH, Schott AL, Dorizan S, Khodakhah K. Cerebellar modulation of the reward circuitry and social behavior. Science 2019, 363(6424): eaav0581.
52. Rochefort C, Arabo A, André M, Poucet B, Save E, Rondi-Reig L. Cerebellum shapes hippocampal spatial code. Science 2011, 334: 385–389.
53. Burguière E, Arleo A, Hojjati Mr, Elgersma Y, De Zeeuw CI, Berthoz A, *et al.* Spatial navigation impairment in mice lacking cerebellar LTD: a motor adaptation deficit? Nat Neurosci 2005, 8: 1292–1294.
54. Lange I, Kasanova Z, Goossens L, Leibold N, De Zeeuw CI, van Amelsvoort T, *et al.* The anatomy of fear learning in the cerebellum: A systematic meta-analysis. Neurosci Biobehav Rev 2015, 59: 83–91.
55. Diedrichsen J, Verstynen T, Schlerf J, Wiestler T. Advances in functional imaging of the human cerebellum. Curr Opin Neurol 2010, 23: 382–387.
56. de Solages C, Szapiro G, Brunel N, Hakim V, Isope P, Buisseret P, *et al.* High-frequency organization and synchrony of activity in the purkinje cell layer of the cerebellum. Neuron 2008, 58: 775–788.
57. Gao H, Solages Cd, Lena C. Tetrode recordings in the cerebellar cortex. J Physiol Paris 2012, 106: 128–136.
58. Halverson HE, Khilkevich A, Mauk MD. Cerebellar processing common to delay and trace eyelid conditioning. J Neurosci 2018, 38: 7221–7236.
59. El-Shamayleh Y, Kojima Y, Soetedjo R, Horwitz GD. Selective optogenetic control of Purkinje cells in monkey cerebellum. Neuron 2017, 95: 51–62.
60. Lee KH, Mathews PJ, Reeves AM, Choe KY, Jami SA, Serrano RE, *et al.* Circuit mechanisms underlying motor memory formation in the cerebellum. Neuron 2015, 86: 529–540.
61. Lu Y, Zhu ZG, Ma QQ, Su YT, Han Y, Wang X, *et al.* A critical time-window for the selective induction of hippocampal memory consolidation by a brief episode of slow-wave sleep. Neurosci Bull 2018, 34: 1091–1099.
62. D'Angelo E, Solinas S, Mapelli J, Gandolfi D, Mapelli L, Prestori F. The cerebellar Golgi cell and spatiotemporal organization of granular layer activity. Front Neural Circuits 2013, 7: 93.
63. Hull C, Regehr WG. Identification of an inhibitory circuit that regulates cerebellar Golgi cell activity. Neuron 2012, 73: 149–158.
64. Ozcan OO, Wang X, Binda F, Dorgans K, De Zeeuw CI, Gao Z, *et al.* Differential coding strategies in glutamatergic and GABAergic neurons in the medial cerebellar nucleus. J Neurosci, 2020, 40: 159–170.
65. Uusisaari M, Knöpfel T. Functional classification of neurons in the mouse lateral cerebellar nuclei. Cerebellum, 2011, 10: 637–646.
66. Jaarsma D, Ruigrok TJ, Caffé R, Cozzari C, Levey AI, Mugnaini E, *et al.* Cholinergic innervation and receptors in the cerebellum. Prog Brain Res 1997, 114: 67–96.
67. Zhang C, Zhou P, Yuan T. The cholinergic system in the cerebellum: from structure to function. Rev Neurosci 2016, 27: 769–776.
68. Mihailoff GA, Kosinski RJ, Azizi SA, Border BG. Survey of noncortical afferent projections to the basilar pontine nuclei: a retrograde tracing study in the rat. J Comp Neurol 1989, 282: 617–643.
69. Scammell TE, Arrigoni E, Lipton JO. Neural circuitry of wakefulness and sleep. Neuron 2017, 93: 747–765.
70. Weber F, Dan Y. Circuit-based interrogation of sleep control. Nature 2016, 538: 51–59.

Neurosci. Bull. August, 2020, 36(8):932–936
https://doi.org/10.1007/s12264-020-00483-w

www.neurosci.cn
www.springer.com/12264

LETTER TO THE EDITOR

Neural Tract Degeneration Correlates with Functional Impairment in Patients with Anoxic Brain Injury: A Tract-based Spatial Statistics Study

Ji-Yun Park[1] · Sung Ho Park[2] · Jeong-Hee Yang[3] · Han Do Lee[4] · Jiho Lee[5] · Ki-Hyun Byeon[6] · Seo Young Park[7] · Dongseok Yang[6]

Received: 24 November 2019 / Accepted: 9 January 2020 / Published online: 6 April 2020

Dear Editor,

Anoxic brain injury (ABI) is a devastating event caused by cardiac arrest, chemical exposure, or trauma. Despite recent advances in medical diagnostic techniques and treatments, the survival rate after ABI is still very low. Previous studies have reported that 52.6%–64.0% of people who received cardiopulmonary resuscitation after non-traumatic cardiac arrest die, and 9.0%–18.6% remain in a permanent vegetative state within 28 days of treatment [1, 2]. Survivors suffer from a wide range of neurological sequelae, such as cognitive impairment, abnormal movement, visual dysfunction, ataxia, and behavioral changes, making it difficult for physicians to develop appropriate rehabilitative strategies [2, 3].

Variations in the clinical presentation after ABI suggest differences in the anatomical locations of the damaged brain structures, including white matter (WM) [4]. In fact, anatomical lesions in gray matter have been reported in the following proportions: cortical edema or atrophy, 44%; cerebellar lesions, 33%; basal ganglia lesions, 22%; hippocampal atrophy, 21%; and thalamic lesions, 3% [4]. The utility of WM lesions for predicting functional outcomes remains unknown.

Diffusion tensor imaging (DTI) is a non-invasive magnetic resonance imaging technique to quantitatively analyze the microstructural integrity of neural tracts in WM. The DTI metrics consist of fractional anisotropy (FA), mean diffusivity (MD), axial diffusivity (AD), and radial diffusivity (RD). Since combined FA and AD values reflect axonal injury, and a high RD value is associated with demyelination, quantitative analysis of DTI metrics has proven useful for investigating the mechanisms of brain injury [5–7]. Significant correlations have been reported between DTI metrics and the prognosis in patients with neurological disorders [5–7]. However, studies in patients with ABI have been limited by operator bias for the selective inclusion of few neural tracts without full assessment of the DTI metrics [6, 7]. Automated assessment of tract-based spatial statistics (TBSS) to examine tracts in the WM across the whole brain can overcome these limitations. In addition, the range and severity of brain lesions can be clarified by the analysis of all the DTI values based on the number of tract-specific regions of interest from TBSS [8–10].

Ji-Yun Park and Sung Ho Park have contributed equally to this work.

Electronic supplementary material The online version of this article (https://doi.org/10.1007/s12264-020-00483-w) contains supplementary material, which is available to authorized users.

✉ Dongseok Yang
fnew11@gmail.com

[1] Department of Neurology, University of Ulsan College of Medicine, Ulsan University Hospital, Ulsan 44033, Korea

[2] Department of Neurosurgery, Ulsan University Hospital, Ulsan 44033, Korea

[3] Department of Plastic Surgery, Biomedical Research Institute, Seoul National University Hospital, Seoul 03080, Korea

[4] Department of Physical Therapy, College of Ulsan, Ulsan 44022, Korea

[5] Department of Occupational and Environmental Medicine, University of Ulsan College of Medicine, Ulsan University Hospital, Ulsan 44033, Korea

[6] Physical Medicine and Rehabilitation, University of Ulsan College of Medicine, Ulsan University Hospital, Ulsan 44033, Korea

[7] Department of Clinical Epidemiology and Biostatistics, Asan Medical Center, Seoul 05505, Korea

To the best of our knowledge, this study is the first to reveal significant correlations between the severity and extent of neural tract degeneration and functional levels in patients with ABI by using TBSS. To determine whether functional impairment is correlated with the severity and range of tract changes after ABI, we measured WM changes across the brain using TBSS and the functional levels of patients using a modified Rankin Scale (mRS). The FA value was used as a marker of tract degeneration since it reflects the severity of the damage and provides more anatomical and functional information about the tracts [11]. We first compared the DTI metrics within the WM skeleton between the ABI group and healthy controls. Second, we investigated whether the degree of tract degeneration and the number of tract injuries reflected the severity of the functional impairment in patients. Last, we tested for correlations between the functional levels of patients and the values of the DTI metrics.

Twenty-one patients with ABI (11 with good outcomes [mRS scores 0–3], and 10 with poor outcomes [mRS scores 4–5]) and 22 healthy controls were enrolled (Table S1). The inclusion criteria for the patient group were as follows: (1) a clear history of ABI (cardiopulmonary arrest [$n = 9$], toxic or metabolic shock [$n = 5$], non-brain trauma [$n = 3$], anaphylactic shock [$n = 2$], and others [$n = 2$]); (2) age range 31–74 years; (3) >3 weeks and <10 weeks after ABI onset; (4) no previous history of neurological or psychiatric disorders; and (5) no combined traumatic brain injury including diffuse axonal injury or head trauma. To ensure homogeneity, healthy controls (14 males; average age 57.60 ± 14.41 years; range 30–75 years) were matched with the patient group for sex, age, onset to magnetic resonance, and educational level. There were no significant demographic differences between the patient and control groups or between the good and poor outcome groups. We extracted the values of all the DTI metrics from each tract-specific region of interest to analyze 48 tracts based on the Johns Hopkins University WM tractography atlas [8].

Between-group comparisons of voxel-wise DTI values showed significantly lower FA and higher MD and RD values in controls relative to the good and poor outcome groups, and in the good outcome group relative to the poor outcome group (family-wise error-corrected $P < 0.05$) (Fig. 1, see supplementary material for DTI data processing). These significant differences occurred extensively over the WM skeletons in the DTI maps but not the AD maps. Particularly, compared to the control group, the poor outcome group showed the strongest changes in the DTI maps; these changes affected most of the tracts in the WM skeleton. While the AD maps did not show a large overall change, certain small areas showed significant changes when the poor outcome group was compared with both the control and good outcome groups. Collectively, these findings suggested that injury to tracts is proportional to the severity of functional impairment in patients with ABI. The average values of DTI metrics for all tracts in the heathy controls/good outcome group/poor outcome group were: FA, 0.48 ± 0.03/0.45 ± 0.04/0.35 ± 0.07; MD, 0.83 ± 0.06/0.90 ± 0.08/1.00 ± 0.16; RD 0.61 ± 0.05/0.69 ± 0.08/0.83 ± 0.17; and AD 1.29 ± 0.07/1.33 ± 0.09/1.35 ± 0.16 (Fig. S1).

To calculate neural tract degeneration, we used the average FA value extracted from each tract-specific region of interest. Using this method, we measured the FA values of 27 tracts, which included 21 tracts in the right and left hemispheres and 6 single tracts. The percentage of tract degeneration was calculated as follows: [1 − (average FA value of tracts in patient)/(average FA value of tracts in controls)] × 100%.

The average degeneration of all tracts in the WM was 8.3% (range, 1.5%–23.5%) in the good outcome group and 27.7% (range, 17.8%–41.2%) in the poor outcome group (Fig. 2). In the good outcome group, the four highly-degenerated tracts were the fornix (23.5%), anterior corona radiata (15.3%), superior fronto-occipital fasciculus (15.2%), and tapetum (13.7%), while those in the poor outcome group were the fornix (41.2%), superior fronto-occipital fasciculus (37%), body of the corpus callosum (32.8%), and fornix cres (32.6%). The areas of least degeneration in the good outcome group occurred in the cingulum–hippocampus (1.5%), retrolenticular part of the internal capsule (1.9%), external capsule (2.5%), and posterior limb of the internal capsule (3.3%).

A tract was classified as injured if the median values of any of the DTI metrics were significantly different between the good outcome and the control groups, or between the poor outcome and the control groups. To determine the number of tract injuries, we calculated the median DTI values of the 48 tracts in the control and patient groups (Table S2). There were 42 injured neural tracts in the good outcome group, while all tracts in the poor outcome group were injured. Relative to the control group values, the numbers of tract injuries in the good outcome group were 34 for FA, 28 for MD, 38 for RD, and 16 for AD, while the corresponding numbers for the poor outcome group were 48 for FA, 43 for MD, 48 for RD, and only 3 for AD (Table S3).

Analysis of the relationship between neural tract integrity and functional level showed that the average FA value of all 48 tracts was significantly inversely proportional to the mRS. In contrast, the average MD and RD values were significantly positively proportional to the mRS. However, no significant correlation was found between the average AD and mRS (Fig. S2; FA: $r = -0.819$, $P < 0.001$; MD: $r = 0.760$, $P < 0.001$; RD: $r = 0.778$, $P < 0.001$; AD: $r = 0.294$, $P = 0.196$).

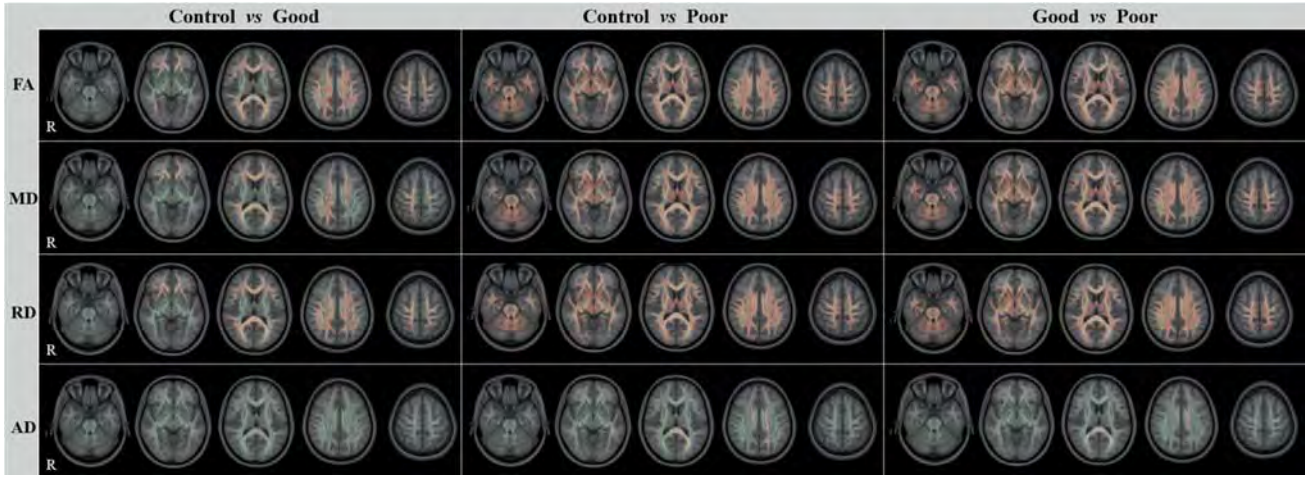

Fig. 1 TBSS of DTI maps. Results overlaid on the Montreal Neurological Institute 152-T1 template. Red, regions with significantly reduced FA and significantly elevated MD, AD, and RD (family-wise error-corrected $P < 0.05$; green, the FA skeleton). TBSS, tract-based spatial statistics; DTI, diffusion tensor imaging; FA, fractional anisotropy; MD, mean diffusivity; AD, axial diffusivity; RD, radial diffusivity.

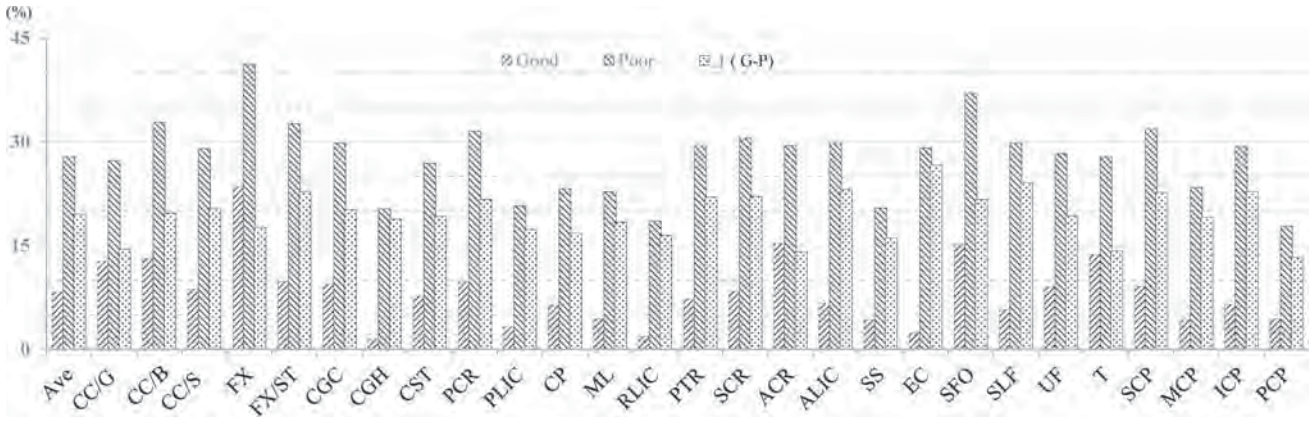

Fig. 2 Degeneration of 27 neural tracts in white matter. Bar graph showing the percentages of degenerated tracts according to the patient group. Good, good outcome group; Poor, poor outcome group; (G-P), difference between good and poor outcome groups; Ave, average; GCC, genu of corpus callosum; BCC, body of corpus callosum; SCC, splenium of corpus callosum; FX, fornix (column and body); F/ST, fornix (cres)/stria terminalis; CGC, cingulum (cingulate gyrus); CGH, cingulum (hippocampus); CST, corticospinal tract; PCR, posterior corona radiata; PLIC, posterior limb of the internal capsule; CP, cerebral peduncle; ML, medial lemniscus; RLIC, retrolenticular part of the internal capsule; PTR, posterior thalamic radiation; SCR, superior corona radiata; ACR, anterior corona radiata; ALIC, anterior limb of the internal capsule; SS, sagittal stratum; EC, external capsule; SFO, superior fronto-occipital fasciculus; SLF, superior longitudinal fasciculus; UF, uncinate fasciculus; T, tapetum; SCP, superior cerebellar peduncle; MCP, middle cerebellar peduncle; PCP, posterior cerebellar peduncle; ICP, inferior cerebellar peduncle.

For the first time, we studied the degeneration of 27 neural tracts and the degree of functional impairment after ABI. The vulnerable areas and the severity of injuries to the tracts were demonstrated by quantitative analysis of all the DTI metrics and DTI maps simultaneously. This unique tool of tract degeneration analysis identified the vulnerable and resistant tracts in the WM after ABI. Most FA, RD, and MD values were strongly correlated with the functional levels of ABI patients. However, no such correlation was found between the AD values and functional levels.

We found varying degrees of neural tract degeneration, ranging from 1.5% to 21.5% in the good outcome group and from 18.5% to 41.2% in the poor outcome group. These ranges are consistent with those reported in previous studies: they reported that 6 pairs of tracts and the fornix in patients with chronic ABI show a range of 1.0% to 20.0% degeneration in an intact alertness group and a range of 5.9% to 29.4% in an impaired alertness group [7]; in patients with stroke, 15% degeneration occurs in the corticospinal tract-related pathway at 2 months to 6 months [12]; and in the fornix, a range of 23% to 42% degeneration occurs within 2 months after temporal lobe surgery [13]. These results are consistent with previous results, which

reported that the fornix and corpus callosum are among the most vulnerable tracts [2–4].

Interestingly, we found that the superior fronto-occipital fasciculus and anterior corona radiata were vulnerable structures after ABI; to our knowledge, this has never been reported. Notably, in the good outcome group, the sensory tracts were relatively intact (medial lemniscus, 4.4%), which contradicts a previous study which found degeneration in many areas except for the corticospinal tract in patients with good outcomes after ABI [7]. These findings overcome the limitations of the previous studies on ABI in adults, where the focus was on the limbic system or the gray matter [3, 4].

Patients in the good outcome group who could walk independently and perform activities of daily living by themselves may be tolerable to neural tract injuries. This enables compensatory activity to maintain functions and to perform important roles in memory, execution, and emotion, despite the fornix and corpus callosum being among the most degenerated tracts. The least affected tracts may also contribute to cognition, emotion, and social desirability [9, 10].

Quantitative analysis of the DTI metrics provides insight into the mechanisms of ABI based on the following observations. First, we found a high proportion of injured tracts in the good outcome group (42/48, 87.5%), although anoxic injuries led to tract degeneration in only 8.3% of the WM. Second, a poor recovery after ABI correlated with more severe and extensive tract injury in both the good and poor groups. These findings of extensive WM injury are supported by previous studies, which reported that persistent neurological sequelae develop in 30%–60% of ABI patients [2, 3]. In clinical practice, injury to almost all tracts, resulting in severe damage including Wallerian degeneration, has been identified in patients. Our findings support the conclusion that the prognosis of patients with ABI has not improved as much in recent years as those with non-ABI, such as traumatic brain injury [3]. In humans, complete Wallerian degeneration is known to occur within two months after ABI [14]. At two weeks, the reduced AD value likely reflects disintegration of the axonal skeleton. The decrease in AD continued for four weeks and stopped at five weeks, whereas demyelination continued until the end of Wallerian degeneration, contributing to the elevated MD value. The markedly elevated RD value indicated myelin sheath degeneration from two weeks to one month after injury. A few studies have reported serial changes in DTI over 4 months following stroke and surgery, including AD and RD values in the corpus callosum, fornix, and tracts related to the motor pathway [13–15]. These studies showed that the FA value was distinctively reduced at 1 week after injury and persisted for 4 months. In parallel, the RD value markedly increased over the same time period, while the AD value declined during the first 4 weeks and then returned to normal or was slightly elevated from 1 month to 4 months. Thus, the elevated RD value during the 4-week to 4-month period may lead to elevation of the MD value, which coincides with our results. This suggests that the AD value does not correlate with the mRS, as in our results. Studies of the temporal changes in DTI metrics following tract injury are summarized in Table S4.

Collectively, our findings from the quantitative analysis of DTI metrics and maps suggested that a change in the MD value was due to the RD value, but not the AD value, during the late subacute stage (5-week onset). Therefore, demyelination probably occurred at a much higher rate and over a more extensive area than axonal injury in both the good and poor outcome groups. These findings may provide insight into the mechanisms underlying microstructural changes over time and contribute to pharmaco-therapeutic interventions after ABI.

Predicting the functional level is important for the rehabilitation team to manage patients who may regain consciousness in the late subacute phase after ABI. We found that the DTI values 5 weeks after ABI correlated significantly with the functional level at 6 months. Our results are consistent with previous reports which showed that the average FA value in 20 neural tract regions predicts the 1-year functional outcome [11]. Overall, our results suggest that a correlation between tract integrity and gross functional level could inform prompt therapeutic strategies. However, our findings should be interpreted with caution because of the limited sample size in each group and analysis restricted to the WM. In addition, we did not investigate serial changes in DTI metrics at the end-point for tract degeneration and showed only the trend view of DTI maps because of the atypical process of TBSS analysis.

In conclusion, our findings reveal the relationship between structural changes in neural tracts and the functional impairments in patients with ABI. Quantitative analysis of all the DTI metrics and DTI maps, including axial and radial diffusivity, may aid neuroscientists in analyzing the role of the changes in axons and myelin after ABI.

Acknowledgements This work was supported by the Basic Science Research Program of the National Research Foundation of Korea funded by the Ministry of Education (2013R1A1A4A01013178).

Conflict of interest The authors declare that there is no conflict of interest.

References

1. Pfeifer R, Borner A, Krack A, Sigusch HH, Surber R, Figulla HR. Outcome after cardiac arrest: predictive values and limitations of the neuroproteins neuron-specific enolase and protein S-100 and the Glasgow Coma Scale. Resuscitation 2005, 65: 49–55.
2. Lu-Emerson C, Khot S. Neurological sequelae of hypoxic-ischemic brain injury. Neuro Rehabilitation 2010, 26: 35–45.
3. Anderson CA, Arciniegas DB. Cognitive sequelae of hypoxic-ischemic brain injury: a review. NeuroRehabilitation 2010, 26: 47–63.
4. Hopkins RO, Bigler ED. Neuroimaging of anoxic injury: implications for neurorehabilitation. NeuroRehabilitation 2012, 31: 319–329.
5. Moulton E, Amor-Sahli M, Perlbarg V, Pires C, Crozier S, Galanaud D*, et al.* Axial diffusivity of the corona radiata at 24 hours post-stroke: A new biomarker for motor and global outcome. PLoS One 2015, 10: e0142910.
6. van der Eerden AW, Khalilzadeh O, Perlbarg V, Dinkel J, Sanchez P, Vos PE*, et al.* White matter changes in comatose survivors of anoxic ischemic encephalopathy and traumatic brain injury: comparative diffusion-tensor imaging study. Radiology 2014, 270: 506–516.
7. Lee AY, Shin DG, Park JS, Hong GR, Chang PH, Seo JP*, et al.* Neural tracts injuries in patients with hypoxic ischemic brain injury: diffusion tensor imaging study. Neurosci Lett 2012, 528: 16–21.
8. Raikes AC, Bajaj S, Dailey NS, Smith RS, Alkozei A, Satterfield BC*, et al.* Diffusion Tensor Imaging (DTI) correlates of self-reported sleep quality and depression following mild traumatic brain injury. Front Neurol 2018, 9: 468.
9. Huang H, Gundapuneedi T, Rao U. White matter disruptions in adolescents exposed to childhood maltreatment and vulnerability to psychopathology. Neuropsychopharmacology 2012, 37: 2693–2701.
10. Xiao J, He Y, McWhinnie CM, Yao S. Altered white matter integrity in individuals with cognitive vulnerability to depression: a tract-based spatial statistics study. Sci Rep 2015, 5: 9738.
11. Luyt CE, Galanaud D, Perlbarg V, Vanhaudenhuyse A, Stevens RD, Gupta R*, et al.* Diffusion tensor imaging to predict long-term outcome after cardiac arrest: a bicentric pilot study. Anesthesiology 2012, 117: 1311–1321.
12. Werring DJ, Toosy AT, Clark CA, Parker GJ, Barker GJ, Miller DH*, et al.* Diffusion tensor imaging can detect and quantify corticospinal tract degeneration after stroke. J Neurol Neurosurg Psychiatry 2000, 69: 269–272.
13. Liu M, Gross DW, Wheatley BM, Concha L, Beaulieu C. The acute phase of Wallerian degeneration: longitudinal diffusion tensor imaging of the fornix following temporal lobe surgery. Neuroimage 2013, 74: 128–139.
14. Yu C, Zhu C, Zhang Y, Chen H, Qin W, Wang M*, et al.* A longitudinal diffusion tensor imaging study on Wallerian degeneration of corticospinal tract after motor pathway stroke. Neuroimage 2009, 47: 451–458.
15. Concha L, Gross DW, Wheatley BM, Beaulieu C. Diffusion tensor imaging of time-dependent axonal and myelin degradation after corpus callosotomy in epilepsy patients. Neuroimage 2006, 32: 1090–1099.

Neurosci. Bull. August, 2020, 36(8):937–941
https://doi.org/10.1007/s12264-020-00507-5

www.neurosci.cn
www.springer.com/12264

LETTER TO THE EDITOR

Probing for Conditioned Hallucinations Through Neural Activation in a Ketamine Mouse Model of Schizophrenia

Jenny L. Wu[1] · Rebecca P. Haberman[1] · Michela Gallagher[1] · Ming Teng Koh[1]

Received: 24 November 2019 / Accepted: 31 January 2020 / Published online: 4 May 2020

Dear Editor,

When two stimuli such as a tone and a visual stimulus are repeatedly presented together, individuals diagnosed with hallucinations tend to report hearing the tone subsequently in response to the visual stimulus alone [1]. Such conditioned hallucinations involved evoked sensory representations as evidenced by increased neural activation in tone-responsive brain regions during the conditioned hallucinations. These and other observations underscore the importance of prior associative experiences in driving hallucinatory perception, and reflect new efforts to conceptualize and understand psychosis from a cognitive perspective.

Based on the cognitive perspective described above, we and others have shown that mice used to model schizophrenia were more susceptible to psychosis-like behavior than normal animals as instantiated by a greater tendency to form associations between stimuli or events that were mediated by prior experience [2–4]. For example, using a well-established ketamine mouse model that is known to recapitulate many of the symptoms seen in schizophrenia [5, 6], we used a representation-mediated learning paradigm to show that, when an odor and a taste are repeatedly paired, ketamine-exposed mice have an increased tendency to use the odor to evoke a putative inner representation of the taste that could enter into an association with illness [3]. Our data in that study also showed that this increased tendency can be blocked by the anti-psychotic dopamine antagonist risperidone, suggesting that the hallucinatory-like perception is likely due to dopamine hyper-function.

In the present study, also using the ketamine model of schizophrenia in which mice were exposed sub-chronically to ketamine during adolescence and tested ketamine-free in young adulthood, we investigated whether an odor activates a representation of a taste based on prior association by examining neural activation in the primary taste-responsive cortical region after odor exposure. Neural activation of the taste-responsive region in this context would provide evidence for an induction of a taste percept at the neural level in the absence of the taste itself, phenomenologically consistent with hallucinations in which a stimulus is perceived without direct external sensory input from the stimulus. To measure neural activation, we used the induction of c-fos, an immediate-early gene induced by neural activity, as a marker to detect the activation of a taste percept in the insular (primary taste) cortex of adult mice previously exposed to either ketamine or vehicle during adolescence. Importantly, prior research has shown that activation of the taste area in the insular cortex resembles the natural neural representation of taste stimuli [7], and stimulation of the taste cortex in the absence of an actual taste can initiate taste percepts to guide behavior [8].

Starting at 35 days of age, mice were exposed to saline or ketamine (16 mg/kg) [3] daily for 2 weeks and then left undisturbed for a week for drug washout before the commencement of odor–taste exposure training. The mice received odor–taste compound exposures on days 1–3 of training, and odor exposure alone (with water to consume) aimed at activating a taste representation on day 4 prior to perfusion (see Supplementary Materials). No differences in

Electronic supplementary material The online version of this article (https://doi.org/10.1007/s12264-020-00507-5) contains supplementary material, which is available to authorized users.

✉ Ming Teng Koh
mtkoh@jhu.edu

[1] Department of Psychological and Brain Sciences, Johns Hopkins University, Baltimore, MD 21218, USA

the mean fluid intake of mice between the vehicle (n = 8) and ketamine (n = 9) groups occurred during training or on day 4 (Fig. 1A). The mean intensity of c-fos mRNA expression in the insular cortex of mice in the ketamine group was significantly stronger than that in the vehicle group [$t(15)$ = 2.2, P = 0.044; Fig. 1B; see Fig. S1 for representative photomicrographs of c-fos mRNA expression in the insular cortex]. Additional analysis of the striatum, which served as a control region, showed no differences between groups (mean c-fos intensity in vehicle, 0.158; with ketamine, 0.150; $t < 1$, Fig. S2), showing that the increased c-fos expression in the ketamine group did not occur brain-wide. These data, taken together, suggest that a history of ketamine exposure during adolescence increases the tendency for neural activation of an absent stimulus in a brain region known to be responsive to the taste stimulus.

Increased dopamine activation is thought to drive conditioned hallucinations. The excess dopamine activity likely originates in the ventral tegmental area (VTA), while

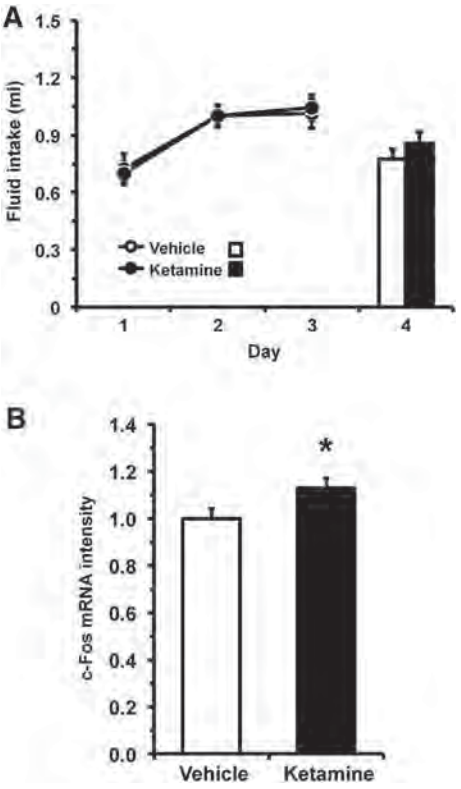

Fig. 1 Fluid intake during training and c-fos expression. **A** Vehicle- and ketamine-exposed mice drank the same amount of sucrose solution on days 1–3 of training in compound exposure with an almond odor. The mice were exposed to the odor with water to drink on day 4 prior to perfusion. **B** Ketamine-exposed mice induced significantly stronger c-fos expression in the insular cortex than in vehicle control mice in response to an odor previously paired with a taste. The expression levels were normalized to the mean of the control group.

neural activity in the hippocampus plays a key role in controlling dopamine neuron firing in the VTA [9]. Increased hippocampal activity has been noted in patients at risk for schizophrenia during the emergence of psychosis, a condition recapitulated in mice exposed to ketamine during development and in other models of schizophrenia [3, 10–12]. Hippocampal hyperactivity accompanied by increased dopamine in the VTA could therefore comprise a network of circuits that is altered in psychosis to generate a greater cognitive bias toward prior perceptual knowledge over sensory evidence. Here, in a second experiment to elucidate the role of the hippocampus in conditioned hallucinations, we lesioned the dorsal hippocampus of ketamine-exposed mice to assess its effect on the activation of a taste percept at the neural level in the absence of a taste using an odor–taste associative task.

About a week prior to the odor–taste experiment, ketamine-exposed mice with sham (n = 8) or hippocampal lesions (n = 8) were injected with a small dose of amphetamine (1 mg/kg) or vehicle saline (using a within-subject design with counterbalancing for order of exposure), a commonly used behavioral assay to validate dopaminergic perturbation that is central to psychosis. The locomotor activity of sham and lesioned mice during 20 min of baseline (prior to injection) and subsequently after saline or amphetamine administration showed that mice with hippocampal lesions were considerably more active overall than sham controls (Fig. 2), consistent with extensive reports of increased locomotor activity in animals with hippocampal lesions. We first analyzed the effect of the amphetamine challenge in the sham and lesioned groups separately, and then compared the effect size (percentage change in activity) between the groups. In the sham group (Fig. 2A), repeated measures ANOVA during baseline (first 20 min) indicated no interaction or main effect of treatment (saline *versus* amphetamine); a significant main effect of time interval reflected decreased activity during habituation to the arena [$F(1, 7)$ = 51.14, P = 0.001]. After injection, activity in the sham mice was significantly higher in response to amphetamine than saline [$F(1, 7)$ = 9.91, P = 0.016]. No main effect of time or interaction between drug × time was found. In the lesioned group, the same analysis at baseline showed no interaction, main effect of treatment, or main effect of time interval (Fig. 2B). When challenged with amphetamine, the locomotor activity of lesioned mice was dramatically elevated compared to saline injection [$F(1, 7)$ = 13.97, P = 0.001]. No main effect of time or interaction between drug × time was found. Additional analysis showed that, while the locomotor activity of sham-lesioned mice increased in response to amphetamine by an average of 46.5% (compared to saline), the hippocampus-lesioned mice had a markedly larger increase of 124.1% [$t(14)$ = 2.58, P = 0.022]. Taken together, these data

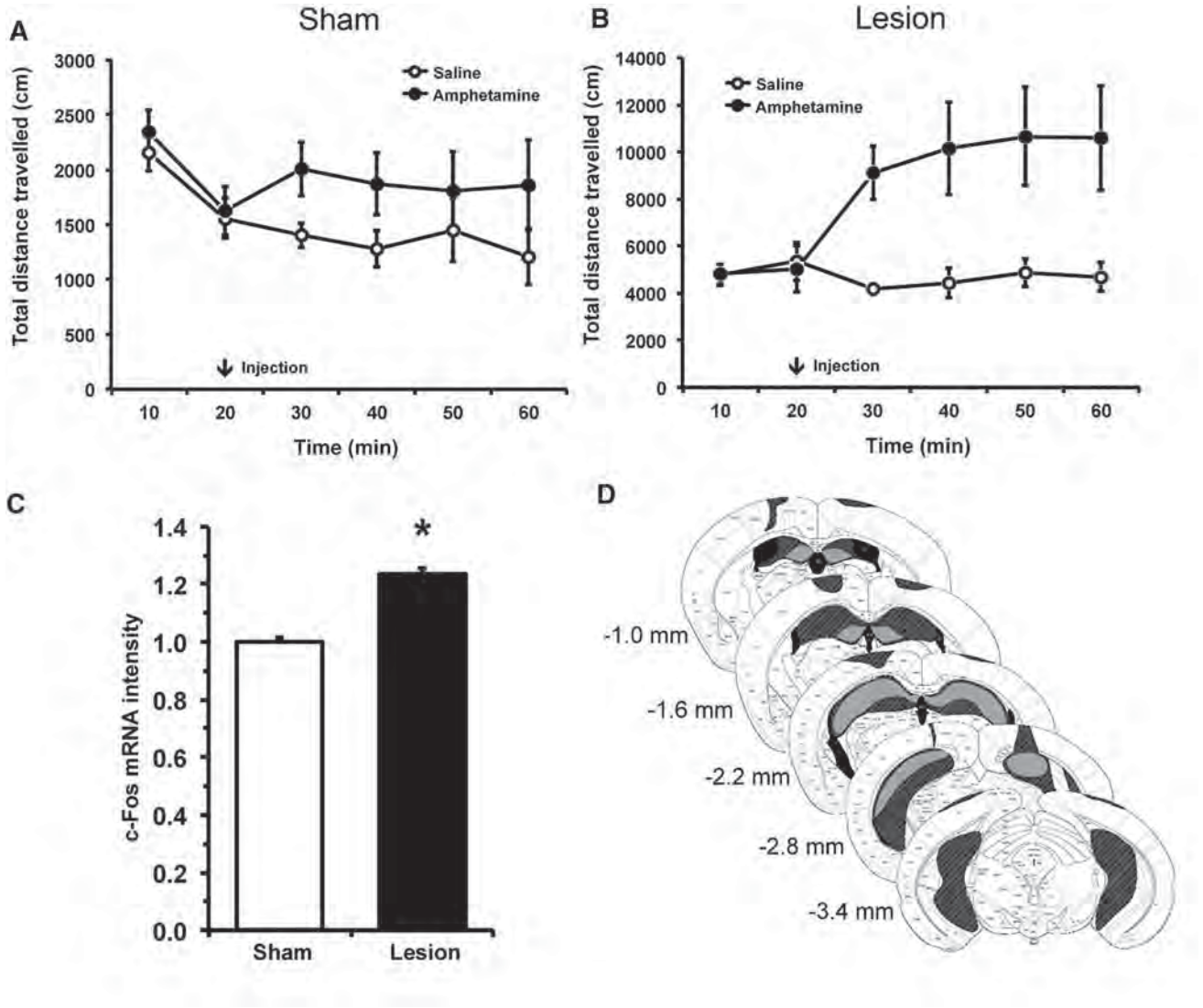

Fig. 2 Hippocampal lesions in ketamine-exposed mice. **A, B** Compared to sham control mice (**A**), ketamine-exposed mice with hippocampal lesions (**B**) showed a markedly larger increase in locomotor activity to amphetamine. **C** Ketamine-exposed mice with hippocampal lesions showed a higher overall expression of c-fos mRNA in the insular cortex than ketamine-exposed mice with sham lesions. **D** Schematics of the largest (hatched dark gray) and smallest (light gray) extent of the hippocampal lesions (coordinates relative to bregma).

showed that ketamine-exposed mice with hippocampal lesions were hyper-responsive to amphetamine, suggesting that damage to the hippocampal formation potentially increases the predisposition to psychosis-like symptoms in this behavioral assay.

The mice with hippocampal and sham lesions were subsequently water-deprived and trained to drink on a limited-access schedule. Training on the odor–taste task commenced thereafter as described above for the first experiment. The mean intensity of c-fos mRNA expression in the insular cortex of the two groups showed that the mice with hippocampal lesions had a stronger neural activation in response to an odor previously paired with a taste than those with sham lesions [$t(14) = 2.32$, $P = 0.036$; Fig. 2C and S3], suggesting that hippocampal lesions in ketamine-exposed mice enhance the associative activation of a taste representation in a primary taste-responsive brain region in the absence of an actual taste. The extent of the hippocampal lesions is illustrated in Fig. 2D.

Using a well-established animal model that recapitulates psychosis-like symptoms, we showed that, in mice exposed to ketamine during adolescence, stronger neural activation was induced in the taste-responsive region of the insular cortex in response to an odor previously associated with a taste than in control mice. The stronger neural activation seen here is consistent with the behavioral findings that ketamine-exposed mice have an increased tendency to evoke an internal representation of a taste that can enter

into an association with illness during conditioning in response to an odor that had gone through odor–taste pairing [3]. Our data are also in line with findings in other animal models of schizophrenia showing an increased tendency in this type of representation-mediated learning [2, 4]. In particular, Fry *et al.* [2] recently showed that transgenic mice with dominant-negative expression of Disrupted-In-Schizophrenia-1 exhibit stronger perceptual processing of an absent taste to an auditory cue previously paired with the taste, and display greater c-fos expression in the insular cortex in response to that cue. In addition, treatment with haloperidol [2] or risperidone [3] effectively reduces the increased tendency for representation-mediated learning in mice used to model schizophrenia, suggesting that dopaminergic hyper-function likely contributes to the heightened tendency.

Our data for hippocampal lesions in ketamine-exposed mice showed increased behavioral responsiveness to amphetamine above the level of ketamine-exposed animals with sham lesions, indicating significant elevation of dopaminergic function from the lesions beyond the effect of ketamine exposure, and foreshadowing a potential for stronger conditioned hallucinations. Indeed, when the same mice were trained and tested in the odor–taste associative task, those with hippocampal lesions had stronger c-fos activation in response to the odor in the insular cortex than sham control mice. Taken together, these findings indicate that ketamine-exposed mice evoke a stronger hallucination-like percept at the neural level, and hippocampal damage in such animals further heightens these effects.

The activation of a taste percept at the neural level in the absence of an actual taste is similar in principle to a hallucination in which a stimulus is experienced in its absence. Whether hallucinations are triggered by associative stimuli or events is supported by evidence emphasizing the importance of prior associative experiences in eliciting hallucinations [1]. The conceptualization of hallucinations in such a cognitive framework allows for new ways to study and understand the phenomenon of hallucination and its neurobiological underpinnings, including in the laboratory setting with human and animal subjects using Pavlovian conditioning to establish prior associations [1–4]. While human test participants can verbally report the perception of a (hallucinatory) stimulus, behavioral studies with animals require indirect inference of the perception of an absent stimulus through downstream changes in behavior such as with representation-mediated taste aversion learning. In one version of that learning paradigm for example, odor activates a taste representation in the presence of illness to subsequently induce a conditioned taste aversion which serves as the primary measure to infer the occurrence of taste representation as a surrogate for a hallucination-like response. Our study offers another way to probe for hallucination-like perception through neural activation of the absent stimulus in animals (see also the recent study by Fry *et al.* [2]). Converging evidence of enhanced hallucination-like perception from both methods, such as that with the ketamine animal model, would strengthen our confidence in the findings.

Individuals with schizophrenia and ketamine-exposed mice show increased metabolic activity in the hippocampus, and hippocampal activity is known to exert considerable control over dopaminergic activity in the mesolimbic system. For example, intracranial administration of a GABA agonist into the hippocampus has been shown to reduce excess dopamine activity in the VTA and psychosis-like symptoms in an animal model of schizophrenia [9]. Lesions of the hippocampus as in the present study could similarly have the same effect although increased behavioral impairment including psychosis has been noted in schizophrenic patients with hippocampal structural deficits [13]. Our data with ketamine-exposed mice in fact showed that hippocampal lesions increased dopaminergic function coupled with enhanced neural activation in gustatory cortex in the absence of a taste stimulus. One possible explanation is that functional compensation for hippocampal lesions results in upregulation of dopamine release in regions such as the nucleus accumbens, although the exact mechanism of action by which that would occur is not fully delineated. It is worth noting that the dorsal and ventral hippocampus may exert different effects on downstream dopaminergic activity. While inhibition of neural activity in the ventral hippocampus reduces dopaminergic responsiveness [9, 14], the disruption of dorsal hippocampal activity *via* lesions such as in our study appears to increase dopaminergic responses that likely contribute to the stronger activation of a hallucination-like taste percept.

The most common hallucinations experienced by humans are auditory and visual [15, 16]. The use of taste to induce a conditioned taste hallucination in rodents partly takes advantage of the species' highly sensitive taste/gustatory system, as well as being influenced by the precedents set by pioneering studies on representation-mediated taste/food aversion learning [17]. Future studies of conditioned hallucinations in animals are needed to investigate other sensory modalities to assess the generality of these effects. For example, a recent study using a newly-developed single-neuron-resolution optogenetic technique to control neuronal activity patterns in the visual cortex of mice successfully imaged neural ensembles associated with the perception of visual stimuli, and then optogenetically evoked hallucinatory visual percepts of those stimuli using the recorded neural ensembles [18]. Whether prior associative experiences between a visual stimulus and an auditory cue would subsequently render the auditory cue,

either from hearing or *via* optogenetic stimulation of selected neurons in the auditory cortex, with the ability to evoke the same visual percepts, is intriguing. Similarly, investigating whether an extended chain of prior associations or associations established under high stress supports or intensifies conditioned hallucinations in animals used to model psychosis would also be useful to expand the boundaries of our understanding.

Insofar as taste hallucinations in rodents serve as a useful proxy to investigate the experience of hallucination in humans, our findings show that prior associative experience with odor and taste readily endow an odor with the ability to more strongly trigger taste-processing at the neural level in ketamine-exposed mice than in controls, and that hippocampal lesions in the ketamine-treated animals amplify dopamine hyper-responsiveness and further heighten the perceptual processing of an absent stimulus akin to a hallucination.

Acknowledgements We thank Daniel Romero and Paige Ahrens for their excellent technical assistance. This work was supported by the Silvo O. Conte Center (P50MH094268). JLW is supported by an Albstein Research Scholarship at Johns Hopkins University.

Conflict of interest The authors claim that there are no conflicts of interest.

References

1. Powers AR, Mathys C, Corlett PR. Pavlovian conditioning–induced hallucinations result from overweighting of perceptual priors. Science 2017, 357: 596–600.
2. Fry BR, Russell N, Gifford R, Robles CF, Manning CE, Sawa A, *et al.* Assessing reality testing in mice through dopamine-dependent associatively evoked processing of absent gustatory stimuli. Schizophr Bull 2020, 46, 54–67.
3. Koh MT, Ahrens PS, Gallagher M. A greater tendency for representation mediated learning in a ketamine mouse model of schizophrenia. Behav Neurosci 2018, 132: 106–113.
4. McDannald MA, Whitt JP, Calhoon GG, Piantadosi PT, Karlsson RM, O'Donnell P, *et al.* Impaired reality testing in an animal model of schizophrenia. Biol Psychiatry 2011, 70: 1122–1126.
5. Neill JC, Barnes S, Cook S, Grayson B, Idris NF, McLean SL, *et al.* Animal models of cognitive dysfunction and negative symptoms of schizophrenia: focus on NMDA receptor antagonism. Pharmacol Ther 2010, 128: 419–432.
6. Frohlich J, Van Horn JD. Reviewing the ketamine model for schizophrenia. J Psychopharmacol 2014, 28, 287–302.
7. Saddoris MP, Holland PC, Gallagher M. Associatively learned representations of taste outcomes activate taste-encoding neural ensembles in gustatory cortex. J Neurosci 2009, 29: 15386–15396.
8. Peng Y, Gillis-Smith S, Jin H, Tränkner D, Ryba NJ, Zuker CS. Sweet and bitter taste in the brain of awake behaving animals. Nature 2015, 527: 512–515.
9. Gill KM, Lodge DJ, Cook JM, Aras S, Grace AA. A novel α5GABA(A)R-positive allosteric modulator reverses hyperactivation of the dopamine system in the MAM model of schizophrenia. Neuropsychopharmacology 2011, 36: 1903–1911.
10. Lodge DJ, Grace AA. Aberrant hippocampal activity underlies the dopamine dysregulation in an animal model of schizophrenia. J Neurosci 2007, 27: 11424–11430.
11. Tregellas JR, Smucny J, Harris JG, Olincy A, Maharajh K, Kronberg E, *et al.* Intrinsic hippocampal activity as a biomarker for cognition and symptoms in schizophrenia. Am J Psychiatry 2014, 171: 549–556.
12. Schobel SA, Chaudhury NH, Khan UA, Paniagua B, Styner MA, Asllani I, *et al.* Imaging patients with psychosis and a mouse model establishes a spreading pattern of hippocampal dysfunction and implicates glutamate as a driver. Neuron 2013, 78: 81–93.
13. Zierhut KC, Graßmann R, Kaufmann J, Steiner J, Bogerts B, Schiltz K. Hippocampal CA1 deformity is related to symptom severity and antipsychotic dosage in schizophrenia. Brain 2013, 136: 804–814.
14. Donegan JJ, Boley AM, Yamaguchi J, Toney GM, Lodge DJ. Modulation of extrasynaptic $GABA_A$ alpha 5 receptors in the ventral hippocampus normalizes physiological and behavioral deficits in a circuit specific manner. Nature Comm 2019, 10: 1–12.
15. Bauer SM, Schanda H, Karakula H, Olajossy-Hilkesberger L, Rudaleviciene P, Okribelashvili N, *et al.* Culture and the prevalence of hallucinations in schizophrenia. Compr Psychiatry 2011, 52: 319–325.
16. Li B, Cui LB, Xi YB, Friston KJ, Guo F, Wang HN, *et al.* Abnormal effective connectivity in the brain is involved in auditory verbal hallucinations in schizophrenia. Neurosci Bull 2017, 33: 281–291.
17. Holland PC. Acquisition of representation-mediated conditioned food aversions. Learn Motiv 1981, 12: 1–18.
18. Marshel JH, Kim YS, Machado TA, Quirin S, Benson B, Kadmon J, *et al.* Cortical layer-specific critical dynamics triggering perception. Science 2019, 365. pii: eaaw5202.

Neurosci. Bull. August, 2020, 36(8):942–946
https://doi.org/10.1007/s12264-020-00503-9

www.neurosci.cn
www.springer.com/12264

LETTER TO THE EDITOR

CSF Brain-Reactive Autoantibodies are Elevated in Patients with Viral Encephalitis

Zhong-Yuan Yu[1] · Jian-Hong Wang[2] · Wei-Wei Li[1,3] · Ye-Ran Wang[1] · Noralyn B. Mañucat-Tan[4] · Jun Wang[1] · Ju Wang[5] · Gao-Yu Cui[5] · Jie-Xiang Pan[5] · Shui-Xian Zhang[5] · Zu-Juan Liu[6] · Liang Tan[5] · Yu-Hui Liu[1]

Received: 11 September 2019 / Accepted: 10 December 2019 / Published online: 30 April 2020

Dear Editor,

Brain-reactive autoantibodies are thought to play an important role in mediating disorders of the central nervous system (CNS). These antibodies direct the processes underlying several diseases, such as multiple sclerosis (MS), neuromyelitis optica (NMO), and neuropsychiatric systemic lupus erythematosus [1–3]. In infectious diseases of the CNS, the pathogen itself is regarded to play a major role in the pathogenesis [4]. In recent years, post-viral autoimmune reactions have been identified to be critical factors that influence the pathogenesis [5, 6]. The best understood example is anti-NMDAR (*N*-methyl-D-aspartate receptor) encephalitis [7], which is commonly caused by viral infections, especially by herpes simplex virus (HSV) infection.

The outcome of a viral insult to the CNS is determined by the neurovirulence of the infecting virus [8]. While patients with virus infection may recover from the neurological dysfunction after virus clearance, some may suffer from post-viral autoimmune encephalitis, which is reported to occur a few weeks or months after the infection [9]. In many cases, brain-reactive autoantibodies have been detected in parallel with the disease onset, suggesting that autoimmunity is an early event in viral encephalitis (VE) [10]. Indeed, the major role of the virus itself in the pathogenesis of the disease in the acute phase of infection is evident. However, it is not yet clear whether the virus-associated autoimmune reactions have pathological effects in the early stage of the disease, rather than only in the post-viral stages.

In the present study, we aimed to investigate the levels of brain-reactive autoantibodies in the cerebral spinal fluid (CSF) and their correlation with disease severity. We also tested whether these antibodies have pathogenic effects on neurons *in vitro*. The types of brain-reactive autoantibodies generated after viral infections are related to the type of virus. Furthermore, one specific virus may trigger different types of autoantibodies [11–13]. Therefore, we regard the brain-reactive antibodies as an integral pool in which to investigate their levels and functions.

Here, we recruited 48 VE patients and 40 normal controls (NCs). There were no significant differences in age, gender, and CSF glucose levels between the NC and VE participants ($P > 0.05$). The CSF white blood cell

Zhong-Yuan Yu and Jian-Hong Wang contributed equally to this work.

Electronic supplementary material The online version of this article (https://doi.org/10.1007/s12264-020-00503-9) contains supplementary material, which is available to authorized users.

✉ Liang Tan
tracy200712@hotmail.com

✉ Yu-Hui Liu
liuyuhui07-8909@163.com

1 Department of Neurology and Clinical Center for Neuroscience, Daping Hospital, Third Military Medical University (Army Medical University), Chongqing 400042, China

2 Department of Neurology, Sichuan Academy of Medical Sciences and Sichuan Provincial People's Hospital, Chengdu 610072, China

3 Chengdu Military General Hospital, Chengdu 610083, China

4 School of Pharmacy and Medical Sciences, University of South Australia, Adelaide, Australia

5 Department of Neurosurgery, Southwest Hospital, Third Military Medical University (Army Medical University), Chongqing 400038, China

6 Third Military Medical University (Army Medical University), Chongqing 400038, China

(WBC, $P < 0.0001$) and CSF protein levels ($P < 0.0001$) significantly differed between the two groups. Moreover, the major CSF viruses identified were Epstein-Barr virus and HSV (Table S1).

To confirm that brain-reactive autoantibodies exist in human CSF, we first conducted immunofluorescence staining. Human brain sections were co-stained with human CSF and anti-NeuN antibodies. All sections contained double-positive cells (CSF and anti-NeuN antibody) in both the NC and VE groups, indicating that brain-reactive autoantibodies are ubiquitous in human CSF. Notably, immunofluorescence staining showed that most of the CSF brain-reactive autoantibodies preferentially bound to neuronal membranes (Fig. 1A, B). Moreover, the number of double-positive cells, indicating the relative level of brain-reactive autoantibodies, was significantly higher in VE patients than in NCs (Fig. 1D). These results indicated that brain-reactive autoantibodies are increased in the CSF of VE patients. MRI abnormalities indicated parenchymal damage or meningopathy, so we further conducted subgroup analysis to investigate the CSF levels of brain-reactive autoantibodies in patients with and without MRI abnormalities. We found that the relative CSF autoantibody levels were significantly higher in patients with MRI abnormalities than those without them (Fig. 1C, E).

We used ELISA assays to explore the changes of inflammatory factors in VE patients, and found that the levels of CSF tumor necrosis factor alpha (TNF-α) and interleukin (IL)-6 were significantly higher in VE patients than in NCs (both $P < 0.001$). However, we found no significant difference in CSF IL-1β levels between NCs and VE patients (Fig. S1). Analysis by Spearman correlations between indicators of disease severity and the relative levels of brain-reactive autoantibodies as indicated by immunofluorescence staining showed that none of the inflammatory factors was correlated with the relative level of autoantibodies (Fig. S2A–C). However, we found that the CSF WBC and protein levels were positively correlated with the relative level of CSF brain-reactive autoantibodies in VE patients (Fig. S2D, E), indicating that these autoantibodies might participate in the pathogenesis of the disease and might be potential biomarkers of disease severity. No significant correlation was found between the CSF levels of brain-reactive autoantibodies and glucose (Fig. S2F).

To investigate the functions of brain-reactive autoantibodies in the CSF, we isolated them from the CSF of NCs and patients with VE. After co-culture of the autoantibodies and SH-SY5Y cells for 24 h, phase-contrast microscopy showed that autoantibody stimulation decreased the number of adhering cells and shortened the neurites (Fig. 2A–C). Moreover, brain-reactive autoantibodies from the VE group were more toxic to SH-SY5Y cells than those from the NC group, as reflected by shorter neurite length (Fig. 2B, C). To confirm this, we performed CCK8 analysis and found that brain-reactive autoantibodies decreased the viability of SH-SY5Y cells (Fig. 2J). In addition, brain-reactive autoantibodies from the VE group were more toxic to SH-SY5Y cells, as reflected by lower cell viability than those from the NC group (Fig. 2J). We also analyzed the apoptosis of SH-SY5Y cells with TUNEL staining and demonstrated that treatment with brain-reactive autoantibodies from both the VE and NC groups increased the ratio of TUNEL-positive SH-SY5Y cells compared to controls (Fig. 2D–F). The ratio of TUNEL-positive cells in the VE group approximately doubled that in the NC group (Fig. 2K). We then assessed neurite outgrowth in primary neuronal cultures from C57 mice. Tuj1 staining indicated that primary neurons cultured with brain-reactive autoantibodies from the VE group had shorter neurites than those cultured with the autoantibodies from the NC group or vehicle controls (Fig. 2G–I, L).

The elevation of brain-reactive antibodies in the CSF of VE patients may be explained by several possible mechanisms (reviewed in [14]). First, the release of neuronal antigens after neuronal degeneration. Specific antigens are transported to local lymph nodes and presented to specific B cells, which then mature into plasma cells. Co-stimulatory signals might stem from necrotic tissue or the virus directly, including pathogen-associated molecular patterns. Alternatively, the inflammatory milieu subsequent to viral infection might lead to unspecific stimulation of brain plasma cells. This could explain why the autoantibodies are not restricted to target NMDARs, but also to dopamine D2 receptors [15], α-amino-3-hydroxy-5-methyl-4-isoxazolepropionic acid receptors, and gamma aminobutyric acid receptors [9]. Such polyspecific B-cell activation is seen in other types of CNS autoimmune disorder, such as MS. Furthermore, autoimmunity may result from molecular mimicry, where epitopes on the viral surface that are similar to neuronal antigens may trigger specific autoantibodies that cross-react with neurons [16]. In the present study, the VE patients were infected by various viruses, which could have generated different autoantibodies. Therefore, we regard the brain-reactive autoantibodies as an integral pool in which to investigate their levels and functions.

Brain-reactive autoantibodies have been suggested to participate in different pathological processes [17, 18]. Previously, the recognition of autoantibodies in CNS diseases has mainly been for the autoimmune diseases, such as MS and NMO. It has been suggested that brain-reactive autoantibodies can also be triggered by viruses [19]. However, post-viral autoimmune reactions are thought to occur in the late stage of the disease or after

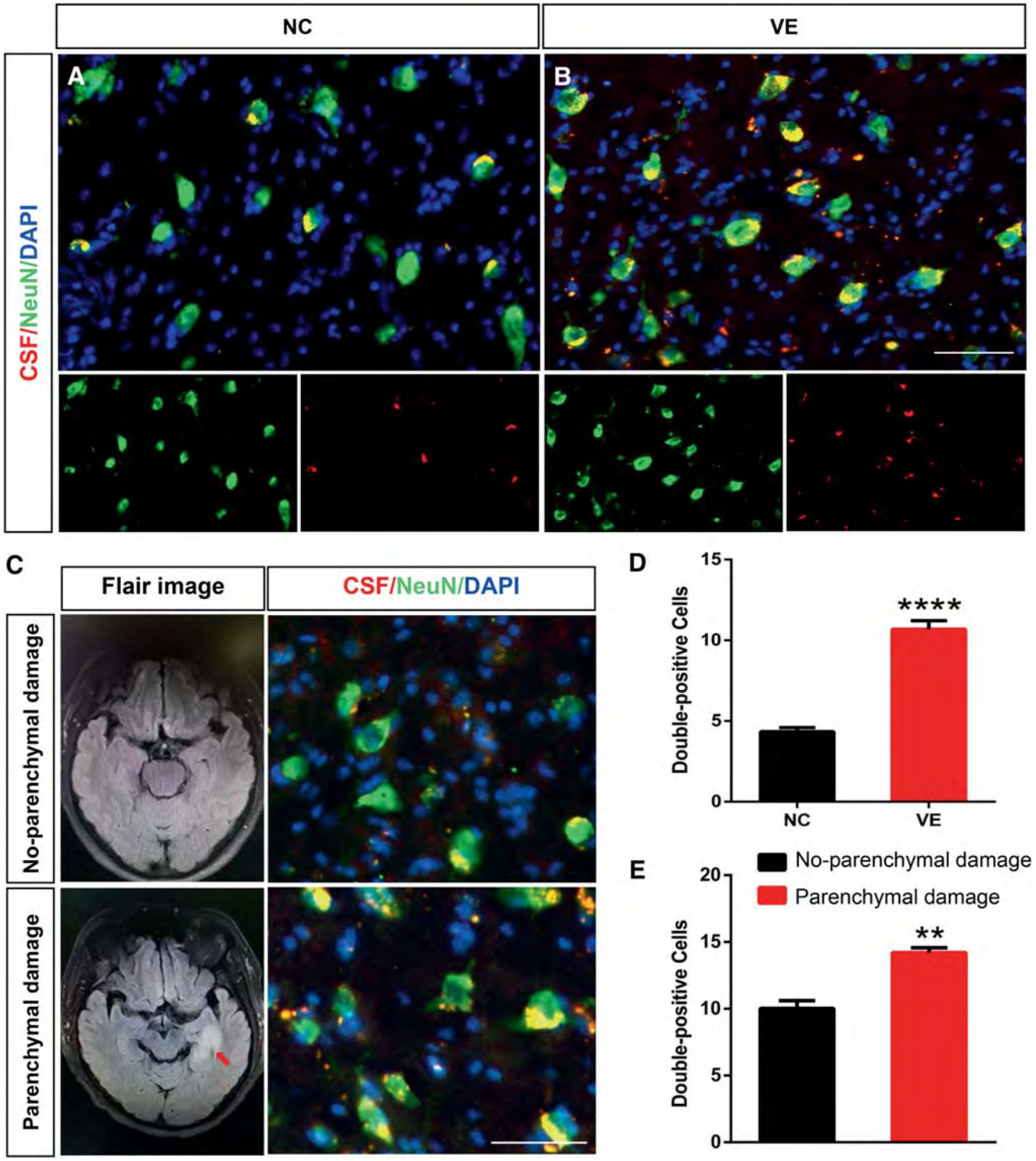

Fig. 1 CSF levels of brain-reactive autoantibodies in VE patients as indicated by immunofluorescence staining. **A**, **B** Representative immunofluorescence staining images of CSF (red) and anti-NeuN antibodies (green), and DAPI (blue) in human brain. **C** Representative MRI and immunofluorescence staining images from VE patients with or without parenchymal damage. **D**, **E** Quantification of double-positive cells in human brain. Data are expressed as the mean ± SEM (n = 40 for NC group, n = 48 for VE group; n = 40 for no-parenchymal damage group, n = 5 for parenchymal damage group). Scale bar = 50 μm.

clearance of the viruses [9]. In the early stage of VE, the neurological dysfunction may be directly related to the neurovirulence of the infecting virus. Currently, few studies have focused on the role of autoantibodies in the pathogenesis of VE at the early stage. In the present study, we found that brain-reactive autoantibodies are elevated in

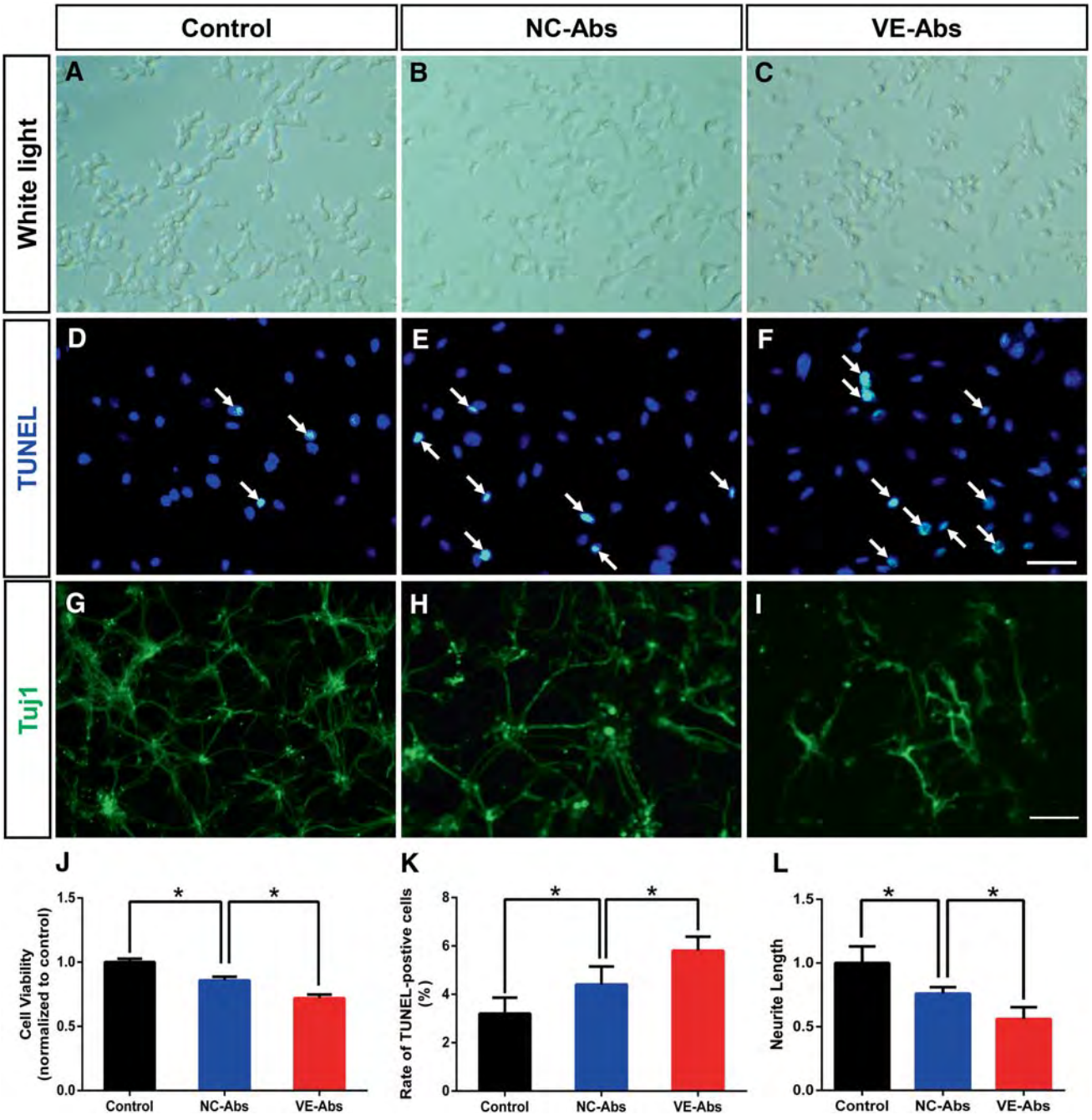

Fig. 2 Effects of human CSF brain-reactive autoantibodies on the viability of SH-SY5Y cells and neurite outgrowth of primary neurons. **A–C** Representative light-microscopic images of SH-SY5Y cells exposed to CSF brain-reactive autoantibodies. **D–F** Representative images of TUNEL-stained SH-SY5Y cells (arrows) exposed to CSF brain-reactive autoantibodies. **G–H** Representative Tuj1-staining of primary neurons exposed to CSF brain-reactive autoantibodies. **J–L** Quantification of viability of SH-SY5Y cells (**J**), TUNEL-positive SH-SY5Y cells (**K**), and neurite length of primary neurons (**L**). Data are expressed as the mean ± SEM (n = 5/group). Scale bar = 50 μm.

the CSF of VE patients. The pathological importance of such an elevation is not yet clear. Brain-reactive autoantibodies, which may cross-bind with neurons, are generally regarded to be neurotoxic in many diseases [20, 21]. We found that brain-reactive autoantibodies were correlated with diverse disease-related factors (CSF protein and CSF WBC), indicating that this pool of autoantibodies may participate in the pathogenesis of the disease.

We further co-cultured SH-SY5Y cells with isolated autoantibodies, and found that they were toxic *in vitro*, as reflected by decreased cell viability and shortened neurites, indicating that pathogenic autoantibodies exist among

those isolated from the CSF of VE patients. Furthermore, the viability of SH-SY5Y cells was lower and the average neurite length was shorter after exposure to autoantibodies from VE patients than to those from NCs. Moreover, the autoantibodies decreased the neurite growth of primary neurons. This finding raised the possibility that the proportion of pathogenic autoantibodies is higher in the CSF of VE patients. However, we did not isolate specific autoantibodies, so further studies are needed focusing on the role of specific autoantibodies in the pathogenesis of VE at the early stage.

In summary, we found that human CSF contains pathogenic brain-reactive autoantibodies, which are increased in VE patients at the early stage. We propose that brain-reactive autoantibodies participate in the pathogenesis of VE at the early stage. Studies with a larger sample size are needed to verify the findings of the present study.

Acknowledgements We thank all the participants for their support. This work was supported by the National Natural Science Foundation of China (81600936 and 81701046) and the Natural Science Foundation of Chongqing Municipality, China (cstc2018jcyJAX0511).

Conflict of interest The authors declare that they have no competing interests.

References

1. Shimizu F, Nishihara H, Kanda T. Blood-brain barrier dysfunction in immuno-mediated neurological diseases. Immunol Med 2018, 41: 120–128.
2. Guo MF, Ji N, Ma CG. Immunologic pathogenesis of multiple sclerosis. Neurosci Bull 2008, 24: 381–386.
3. Liu HY, Chen CY, Hsueh YP. Innate immune responses regulate morphogenesis and degeneration: roles of Toll-like receptors and Sarm1 in neurons. Neurosci Bull 2014, 30: 645–654.
4. Chiu IM. Infection, pain, and itch. Neurosci Bull 2018, 34: 109–119.
5. Jones BE, Tovar KR, Goehring A, Jalali-Yazdi F, Okada NJ, Gouaux E, *et al.* Autoimmune receptor encephalitis in mice induced by active immunization with conformationally stabilized holoreceptors. Sci Transl Med 2019, 11.
6. Alexopoulos H, Dalakas MC. The immunobiology of autoimmune encephalitides. J Autoimmun 2019, 104: 102339.
7. Dalmau J, Armangue T, Planaguma J, Radosevic M, Mannara F, Leypoldt F, *et al.* An update on anti-NMDA receptor encephalitis for neurologists and psychiatrists: mechanisms and models. Lancet Neurol 2019, 18: 1045–1057.
8. Kennedy PG. Viral encephalitis. J Neurol 2005, 252: 268–272.
9. Armangue T, Moris G, Cantarin-Extremera V, Conde CE, Rostasy K, Erro ME, *et al.* Autoimmune post-herpes simplex encephalitis of adults and teenagers. Neurology 2015, 85: 1736–1743.
10. Pruss H, Finke C, Holtje M, Hofmann J, Klingbeil C, Probst C, *et al. N*-methyl-D-aspartate receptor antibodies in herpes simplex encephalitis. Ann Neurol 2012, 72: 902–911.
11. Schabitz WR, Rogalewski A, Hagemeister C, Bien CG. VZV brainstem encephalitis triggers NMDA receptor immunoreaction. Neurology 2014, 83: 2309–2311.
12. Xu CL, Liu L, Zhao WQ, Li JM, Wang RJ, Wang SH, *et al.* Anti-*N*-methyl-D-aspartate receptor encephalitis with serum anti-thyroid antibodies and IgM antibodies against Epstein-Barr virus viral capsid antigen: a case report and one year follow-up. BMC Neurol 2011, 11: 149.
13. Linnoila JJ, Binnicker MJ, Majed M, Klein CJ, McKeon A. CSF herpes virus and autoantibody profiles in the evaluation of encephalitis. Neurol Neuroimmunol Neuroinflamm 2016, 3: e245.
14. Pruss H. Postviral autoimmune encephalitis: manifestations in children and adults. Curr Opin Neurol 2017, 30: 327–333.
15. Mohammad SS, Sinclair K, Pillai S, Merheb V, Aumann TD, Gill D, *et al.* Herpes simplex encephalitis relapse with chorea is associated with autoantibodies to *N*-methyl-D-aspartate receptor or dopamine-2 receptor. Mov Disord 2014, 29: 117–122.
16. Lucchese G, Stahl B. Peptide sharing between viruses and DLX proteins: A potential cross-reactivity pathway to neuropsychiatric disorders. Front Neurosci 2018, 12: 150.
17. Schwartz N, Stock AD, Putterman C. Neuropsychiatric lupus: new mechanistic insights and future treatment directions. Nat Rev Rheumatol 2019, 15: 137–152.
18. Jones KL, Van de Water J. Maternal autoantibody related autism: mechanisms and pathways. Mol Psychiatry 2019, 24: 252–265.
19. Diamond B, Honig G, Mader S, Brimberg L, Volpe BT. Brain-reactive antibodies and disease. Annu Rev Immunol 2013, 31: 345–385.
20. Jurek B, Chayka M, Kreye J, Lang K, Kraus L, Fidzinski P, *et al.* Human gestational N-methyl-D-aspartate receptor autoantibodies impair neonatal murine brain function. Ann Neurol 2019, 86: 656–670.
21. Shimizu F, Takeshita Y, Sano Y, Hamamoto Y, Shiraishi H, Sato T, *et al.* GRP78 antibodies damage the blood-brain barrier and relate to cerebellar degeneration in Lambert-Eaton myasthenic syndrome. Brain 2019, 142: 2253–2264.

Neurosci. Bull. August, 2020, 36(8):947–950
https://doi.org/10.1007/s12264-020-00508-4

www.neurosci.cn
www.springer.com/12264

LETTER TO THE EDITOR

Ghrelin Reduces A-Type Potassium Currents in Dopaminergic Nigral Neurons *via* the PLC/PKCδ Pathway

Bao Xue[1,2] · Chen Li[1,2] · Xiaoli Chang[1,2,3] · Hong Jiang[1,2] · Limin Shi[1,2] · Junxia Xie[1,2]

Received: 7 October 2019 / Accepted: 29 February 2020 / Published online: 9 May 2020

Dear Editor,

Ghrelin, an endogenous ligand of growth hormone secretagogue receptor 1a (GHS-R1a), is a 28-amino-acid peptide that regulates growth hormone secretion, metabolism, food intake, mood, cognition, memory, and neuroprotection [1–3]. Recent studies have suggested that these functions of ghrelin are achieved by its modulation of the electrophysiological properties of neurons. Andrews *et al.* showed that the excitatory effects of ghrelin on dopaminergic neurons in the substantia nigra pars compacta (SNc) are associated with neuroprotection and motor modulation [4, 5]. Electrophysiologically, dopaminergic neurons are excitable cells with low-frequency pacemaker activity *in vitro* and tonic irregular single-spike or phasic bursting activity *in vivo* [5, 6]. In addition, changes in neuronal activity affect dopamine release at the axon terminals, which in turn modulates basic motor activity [7]. The ion channel mechanisms underlying the electrical activity of these cells are of particular interest and importance because of their relevance to voluntary movement and their involvement in neurological disorders such as Parkinson's disease (PD).

Our previous results have shown that ghrelin excites dopaminergic neurons in the SNc by inhibiting the Kv7/KCNQ/M channel [5]. We suspect that other K^+ channels are also involved. Transient A-type K^+ channels (I_A) are strongly expressed in dopaminergic SNc neurons and play a key role in pacemaker control [9]. Pharmacological inhibition of I_A by its blocker 4-aminopyridine (4-AP) or AmmTX3 depolarizes the membrane potential, enhances the neuronal excitability, reduces motor deficits, and improves short-term social recognition and spatial memory in animal models of PD. These findings indicate a potential therapeutic action of I_A in PD [10]. In ventricular myocytes, ghrelin activates the phospholipase C/protein kinase C (PLC/PKC) signaling cascade and inhibits I_A [11]. Preferential inhibition of I_A *via* the PKA, PKC, and mitogen-activated protein kinase signaling pathways has also been reported in hippocampal pyramidal neurons [12]. However, the effects of ghrelin on I_A in dopaminergic SNc neurons remain unclear.

To elucidate how ghrelin regulates I_A, we made whole-cell patch-clamp recordings in brain slices of the SNc from C57BL/6 mice at postnatal days 15–20. First, we found that ghrelin (100 nmol/L) increased the spontaneous firing rates of dopaminergic neurons, and this was blocked by 4-AP (1 mmol/L) (Fig. S1). These results indicated that the excitatory effect of ghrelin is mediated through I_A. Then, we recorded I_A following a standard two-step voltage protocol [13]. After a stable recording was achieved, we applied ghrelin and recorded a significant reduction in the I_A amplitude (Fig. 1A). This inhibitory effect occurred immediately, reaching the maximal reduction within

Electronic supplementary material The online version of this article (https://doi.org/10.1007/s12264-020-00508-4) contains supplementary material, which is available to authorized users.

✉ Limin Shi
slm0532@163.com

✉ Junxia Xie
jxiaxie@public.qd.sd.cn

[1] Department of Physiology, Shandong Provincial Key Laboratory of Pathogenesis and Prevention of Neurological Disorders, School of Basic Medicine, Qingdao University, Qingdao 266071, China

[2] Institute of Brain Science and Disease, Qingdao University, Qingdao 266071, China

[3] Institute of Acupuncture, Shandong University of Traditional Chinese Medicine, Jinan 250355, China

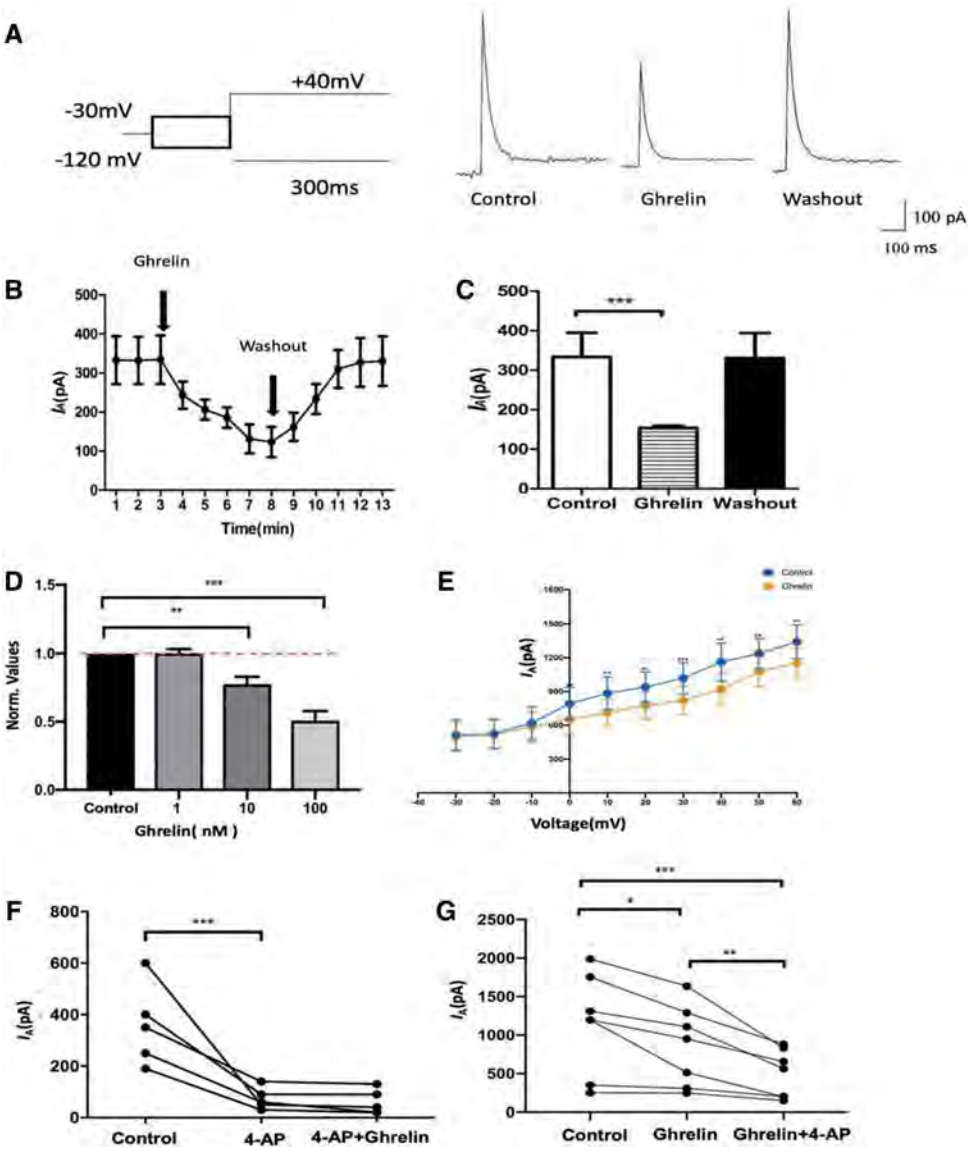

Fig. 1 Ghrelin suppresses A-type K^+ currents. **A** Left, I_A was obtained by subtracting the currents induced by the two-voltage protocols; right, examples showing that ghrelin reversibly reduces I_A. **B** Time course of the effect of ghrelin (100 nmol/L) on dopaminergic neurons. **C** Statistical analysis of I_A amplitude as the mean peak current (mean ± SEM, $n = 5$). **D** Dose-dependent effects of ghrelin on I_A ($n = 5$–7, $^{**}P < 0.01$, $^{***}P < 0.001$). **E** Current–voltage relationships of the peak I_A with/without ghrelin recorded at holding potentials from − 30 to + 60 mV ($n = 7$, $^{**}P < 0.01$, $^{***}P < 0.001$). **F** Statistical analysis showing the changes of I_A in all dopaminergic neurons in the presence of 4-AP and 4-AP + Ghrelin ($n = 5$, $^{***}P < 0.001$, 4-AP *vs* control). **G** Statistical analysis showing the changes of I_A in all dopaminergic neurons in the presence of Ghrelin and 4-AP + Ghrelin ($n = 7$, $^{*}P < 0.05$, Ghrelin *vs* control; $^{**}P < 0.01$, Ghrelin *vs* 4-AP + Ghrelin; $^{***}P < 0.001$, Ghrelin + 4-AP *vs* Control).

5 min, and the amplitude of I_A fully recovered 4 min after the removal of ghrelin (Fig. 1B). Further statistical analysis showed that the mean amplitude of I_A was 333.68 ± 143.76 pA in recorded dopaminergic neurons, and decreased to 153.43 ± 167.87 pA after ghrelin application (Fig. 1C). We also tested the effects of ghrelin at two other doses. At 10 nmol/L, ghrelin inhibited I_A by 20% (Fig. 1D), while 1 nmol/L had no effect. Considering the dose-dependent effect, 100 nmol/L was chosen for subsequent experiments. Fig. 1E shows the effects of ghrelin with depolarizing pulses ranging from − 30 to + 60 mV. The average *I–V* curves demonstrated that ghrelin significantly inhibited I_A with increasing voltage. Ghrelin shifted the V_{50} of I_A from 18.70 mV to 32.63 mV (Fig. S2), which indicated that ghrelin changes the activation characteristics of I_A, causing its activation curve to move to the right.

We further investigated whether the effect of ghrelin was indeed mediated through the inhibition of I_A. The application of 4-AP (1 mmol/L) significantly reduced the amplitude of I_A from 363.67 ± 154 pA to 77 ± 41 pA (Fig. 1F). In the presence of 4-AP, further use of ghrelin had little effect on I_A. Moreover, as ghrelin inhibited only half of the total I_A, we also investigated whether 4-AP could further affect I_A. The results showed that ghrelin significantly reduced the amplitude of I_A from 1150.95 ± 178 pA to 865.59 ± 127 pA, and addition of 4-AP further inhibited I_A to 499.51 ± 84 pA (Fig. 1G).

We next studied the mechanisms and signaling pathways involved in the inhibitory effect of ghrelin on I_A. Bath application of the GHS-R1a antagonist D-[Lys3]-GHRP-6 alone had no effect on I_A, but completely abolished the ghrelin-induced inhibition of I_A (Fig. 2A, B). However,

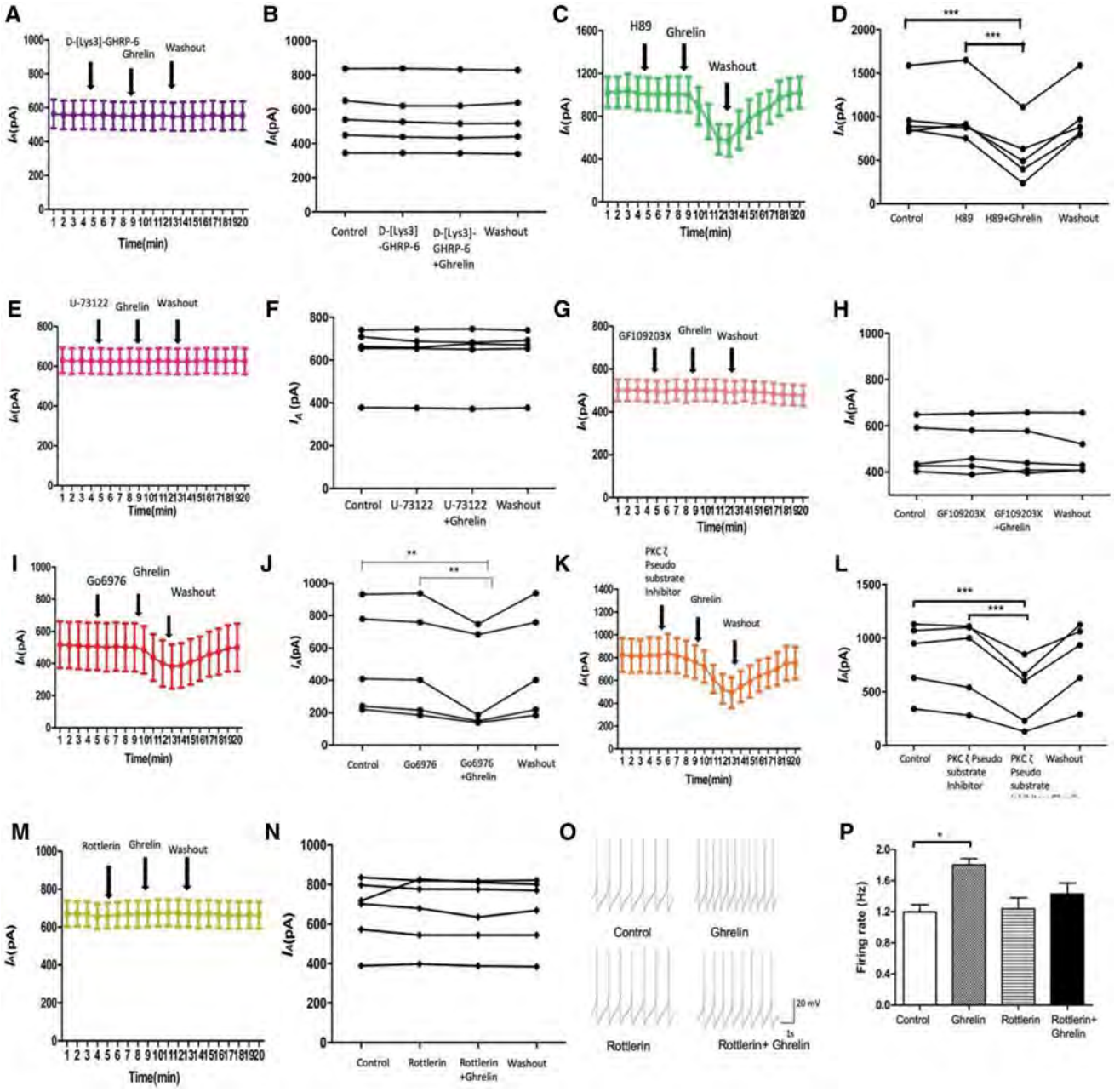

Fig. 2 Involvement of the GHS-R1a/cAMP/PKA or GHS-R1a/PLC/PKC pathway in the I_A response to ghrelin. **A** Time course of the effects of D-[Lys3]-GHRP-6 and ghrelin on dopaminergic neurons. **B** Statistical analysis showing that ghrelin fails to inhibit I_A in the presence of D-[Lys3]-GHRP-6 (n = 5). **C–N** Summary of effects of inhibitors on ghrelin signaling transduction pathways: **C**, **D** Ghrelin inhibits I_A in the presence of the PKA inhibitor H89 (n = 5, $^{***}P < 0.001$); **E–H** the PLC inhibitor U-73122 (**E, F**; n = 5) and the PKC inhibitor GF109203X (**G**, **H**; n = 5) abolish the inhibitory effect of ghrelin on I_A; **I–N** ghrelin still inhibits I_A when co-applied with the cPKC inhibitor Go6976 (**I**, **J**; n = 5, $^{**}P < 0.01$) or a PKCζ inhibitor (PKCζ Pseudo Substrate Inhibitor) (**K, L**; n = 5, $^{***}P < 0.001$), but has no effect on I_A in the presence of the PKCδ inhibitor Rottlerin (**M, N**, n = 6). **O, P** Rottlerin abolishes the excitatory effect of ghrelin on dopaminergic neurons. Application of ghrelin alone increases the firing rate, but fails to further increase the firing rate in the presence of Rottlerin (n = 5, $^{*}P < 0.05$).

ghrelin still inhibited I_A in the presence of the PKA inhibitor H89 (1 μmol/L) (Fig. 2C, D), suggesting that the PKA pathway is unlikely to be involved in the action of ghrelin. Then, we examined the effects of the PLC/PKC signaling pathway. As a control, application of either the PLC inhibitor U-73122 (10 μmol/L) (Fig. 2E, F) or the PKC inhibitor GF109203X (5 μmol/L) (Fig. 2G, H) alone had no effect on I_A. In contrast, either U-73122 or GF109203X abolished the ghrelin-induced effect on I_A. These results demonstrated that the GHS-R1a-PLC-PKC

pathway is involved in the effects of ghrelin-induced inhibition of I_A on dopaminergic neurons in the SNc.

PKC is a large protein family. According to their molecular structure, the PKC family members are divided into classical PKCs (cPKCs, including PKCα, PKCβI, PKCβII, and PKCγ), novel PKCs (nPKCs, including PKCδ, PKCε, PKCη, PKCθ, and PKCμ), and atypical PKCs (aPKCs, including PKCλ, PKCζ, and PKCι). We found that 300 nmol/L Go6976 (selective inhibitor of cPKCs) did not abolish the effect of ghrelin on I_A (Fig. 2I, J). Also, 1 μmol/L PKCζ Pseudo Substrate Inhibitor, a selective PKCζ inhibitor, did not affect the I_A response to ghrelin (Fig. 2K, L). As PKCδ is highly expressed in dopaminergic nigral neurons, we further used the PKCδ inhibitor Rottlerin (10 μmol/L) to assess the changes of I_A. Bath application of Rottlerin alone had no effect on I_A. In contrast, when added together with ghrelin, Rottlerin completely abolished the ghrelin-induced inhibition of I_A (Fig. 2M, N). Consistent with this, Rottlerin abolished the enhancement of spiking activity by ghrelin (Fig. 2O, P). These results indicate that the effects of ghrelin are mediated by activation of the PKCδ isoform.

Our previous data have shown that ghrelin enhances dopaminergic neuronal excitability by inhibiting Kv7/KCNQ/M channels [5]. This suggested that voltage-gated K^+ channels are key players underlying the excitatory effects of ghrelin. Indeed, we found that the inhibition of I_A by ghrelin is rapid and reversible. As regards signal transduction mechanisms, although the activation of PKA has been reported to lead to the phosphorylation of I_A mediated by Kv4.2 in pyramidal neurons of the hippocampal CA1 region [14], our investigations further demonstrated that ghrelin induced inhibition of I_A in dopaminergic SNc neurons *via* the GHS-R1a/PLC/PKCδ but not the PKA pathway. Furthermore, the specific blocker of I_A, 4-AP, blocked the excitatory effects of ghrelin. Inhibition of I_A may contribute to the ghrelin-induced excitation of dopaminergic neurons. In fact, both Kv7/KCNQ channels and A-type K^+ channels can be phosphorylated by the activation of PKC [15]. Therefore, we propose that both channels may be the underlying targets of ghrelin in dopaminergic nigral neurons. Also, as accumulating evidence has associated K^+ channels with various diseases [8], voltage-gated K^+ channels may be a promising new target for PD treatment.

Acknowledgements This work was supported by the National Natural Science Foundation of China (31671054, 31771124 and 81430024), the Postdoctoral Science Foundation of China (2017M610412 and 2018T110666), the Bureau of Science and Technology of Qingdao Municipality, China (17-1-1-44-jch), and the Taishan Scholars Construction Project of Shandong Province, China.

Conflict of interest The authors declare that they have no conflict of interest.

References

1. Kojima M, Hosoda H, Date Y, Nakazato M, Matsuo H, Kangawa K. Ghrelin is a growth-hormone-releasing acylated peptide from stomach. Nature 1999, 402: 656–660.
2. Mandal A, Prabhavalkar KS, Bhatt LK. Gastrointestinal hormones in regulation of memory. Peptides 2018, 102: 16–25.
3. Jiao Q, Du X, Li Y, Gong B, Shi L, Tang T, *et al.* The neurological effects of ghrelin in brain diseases: beyond metabolic functions. Neurosci Biobehav Rev 2017, 73: 98–111.
4. Andrews ZB, Erion D, Beiler R, Liu ZW, Abizaid A, Zigman J, *et al.* Ghrelin promotes and protects nigrostriatal dopamine function *via* a UCP2-dependent mitochondrial mechanism. J Neurosci 2009, 29: 14057–14065.
5. Shi L, Bian X, Qu Z, Ma Z, Zhou Y, Wang K, *et al.* Peptide hormone ghrelin enhances neuronal excitability by inhibition of Kv7/KCNQ channels. Nat Commun 2013, 4: 1435.
6. Liu C, Xue Y, Liu MF, Wang Y, Liu ZR, Diao HL, *et al.* Orexins increase the firing activity of nigral dopaminergic neurons and participate in motor control in rats. J Neurochem 2018, 147: 380–394.
7. Dragicevic E, Schiemann J, Liss B. Dopamine midbrain neurons in health and Parkinson's disease: emerging roles of voltage-gated calcium channels and ATP-sensitive potassium channels. Neuroscience 2015, 284: 798–814.
8. Chen X, Xue B, Wang J, Liu H, Shi L, Xie J. Potassium channels: a potential therapeutic target for Parkinson's disease. Neurosci Bull 2018, 34: 341–348.
9. Liss B, Franz O, Sewing S, Bruns R, Neuhoff H, Roeper J. Tuning pacemaker frequency of individual dopaminergic neurons by Kv4.3L and KChip3.1 transcription. EMBO J 2001, 20: 5715–5724.
10. Haghdoost-Yazdi H, Piri H, Najafipour R, Faraji A, Fraidouni N, Dargahi T, *et al.* Blockade of fast A-type and TEA-sensitive potassium channels provide an antiparkinsonian effect in a 6-OHDA animal model. Neurosciences (Riyadh) 2017, 22: 44–50.
11. Sun Q, Zang WJ, Chen C. Growth hormone secretagogues reduce transient outward K^+ current *via* phospholipase C/protein kinase C signaling pathway in rat ventricular myocytes. Endocrinology 2010, 151: 1228–1235.
12. Hoffman DA, Johnston D. Downregulation of transient K^+ channels in dendrites of hippocampal CA1 pyramidal neurons by activation of PKA and PKC. J Neurosci 1998, 18: 3521–3528.
13. Yang F, Feng L, Zheng F, Johnson SW, Du J, Shen L, *et al.* GDNF acutely modulates excitability and A-type K(+) channels in midbrain dopaminergic neurons. Nat Neurosci 2001, 4: 1071–1078.
14. Yuan LL, Adams JP, Swank M, Sweatt JD, Johnston D. Protein kinase modulation of dendritic K^+ channels in hippocampus involves a mitogen-activated protein kinase pathway. J Neurosci 2002, 22: 4860–4868.
15. Delmas P, Brown DA. Pathways modulating neural KCNQ/M (Kv7) potassium channels. Nat Rev Neurosci 2005, 6: 850–862.

Neurosci. Bull. August, 2020, 36(8):951–954
https://doi.org/10.1007/s12264-020-00516-4

www.neurosci.cn
www.springer.com/12264

RESEARCH HIGHLIGHT

TASK-3: New Target for Pain-Relief

Wen-Jing Ren[1,2] · Henning Ulrich[3] · Alexey Semyanov[4] · Peter Illes[1,5] · Yong Tang[1,2]

Received: 14 February 2020 / Accepted: 24 April 2020 / Published online: 26 May 2020

Morphine and other opioids are among the most effective analgesics for treating pain. However, drug dependence and other deleterious side effects of opioids have limited their clinical applicability. Recent studies suggest that the use of opioids for pain control may even exacerbate disease outcomes in some pain-producing conditions, such as acute pancreatitis [1]. Thus, there is a clinically unmet demand for the discovery of new therapeutic targets for developing a new generation of analgesics potentially devoid of opioid-like adverse side effects. In most cases, the initial proof-of-concept identification of a protein as a potential druggable target is dependent on the use of genetically modified rodent models, such as gene-knockout mice. However, knocking out the targeted gene may produce undesirable modifications of other functionally coupled genes. These off-target side effects discredit target validation work using genetic methods. For instance, Nav1.7-knockout mice or humans with a Nav1.7 loss-of-function mutation exhibited remarkably low sensitivity to pain [2–5], which led to substantial efforts by academics and the pharmaceutical industry in a search for Nav1.7-specific antagonists [2–5]. However, it turned out that potent and selective Nav1.7 antagonists have weak analgesic activity [6]. Later studies found that disrupted opioid-related signaling contributes to the low pain sensitivity in humans and mice lacking Nav1.7 [7]. Due to the intrinsic problem of the genetic methods, selective chemical probes provide a complementary means of target discovery and validation, particularly in pain.

TASK-3 channels, members of the two-pore domain K^+ (K2P) channel family, are highly expressed in neurons in several tissues of the peripheral and central nervous systems including dorsal root ganglia (DRG), spinal cord, brain [8] and other tissues such as the carotid body glomus [9]. They have also been detected in astrocytes in culture [10, 11]. However, the *in situ* evidence for their presence in glia has been lacking. TASK-3 channels produce a background K^+ conductance, which is involved in the regulation of membrane excitability and K^+ homeostasis [12]. In the central nervous system, TASK-3 channels regulate membrane excitability in cholinergic neurons in the habenula and granule neurons in the cerebellum [8, 13], and are involved in a variety of neurological disorders including sleep disorder [13], ischemia [14], and depression [15]. In the peripheral system, TASK-3 channels are expressed in mouse carotid body type-1 cells, and may play a role in chemoreception [9]. Most of the previous studies were performed largely using TASK-3-knockout mice [9, 14–16] and the TASK-3 inhibitor PK-THPP [17], which also inhibits TASK-1, a TASK-3 homologue. The only reported (relatively) selective TASK-3 activator is terbinafine [18], which is an antifungal drug with significant peripheral and central side effects including diarrhea, liver

✉ Peter Illes
peter.illes@medizin.uni-leipzig.de

✉ Yong Tang
tangyong@cdutcm.edu.cn

[1] International Collaborative Centre on Big Science Plan for Purine Signaling, Chengdu University of Traditional Chinese Medicine, Chengdu 610075, China

[2] Acupuncture and Chronobiology Key Laboratory of Sichuan Province, Chengdu 610075, China

[3] Department of Biochemistry, Institute of Chemistry, University of São Paulo, São Paulo 05508, Brazil

[4] Shemyakin-Ovchinnikov Institute of Bioorganic Chemistry, Russian Academy of Sciences, Moscow, Russia 117997

[5] Rudolf-Boehm-Institut für Pharmakologie und Toxikologie, Universitaet Leipzig, 04109 Leipzig, Sachsen, Germany

inflammation, and dizziness. Using terbinafine, a recent study suggested that TASK-3 channels in the spinal cord are involved in chronic pain [19]. A previous study reported that TASK-3-knockout mice display enhanced sensitivity to cold in the acetone test [16], suggesting a possible peripheral mechanism for TASK-3 in nociception and chronic pain. However, the beneficial effects of activating peripheral TASK-3 under pathological pain states remain largely unknown. The research team [20] employed a structure-based rational drug design approach to discover selective activators of TASK-3. To this end, structural modeling and visual screening followed by *in vitro* screening using electrophysiology led to the identification of an allosteric agonist of TASK-3 named CHET3. CHET3 is highly selective compared with activities at other K2P channels and other typical K^+ channels as well as typical pain-related G protein-coupled receptors. By combining biological computations and mutagenesis, a binding model of CHET3 in TASK-3 was proposed and the mechanisms underlying the activation of TASK-3 by CHET3 using molecular dynamics simulation were elucidated.

With CHET3, the authors, for the first time, systematically evaluated the analgesic functions of the activation of TASK-3 (Fig. 1). First of all, they showed that, *via* intraperitoneal injection, CHET3 displays anti-nociceptive effects in the tail-immersion and paw-pressure tests. In several rodent models of acute and chronic pain, CHET3 showed an ability to attenuate cold hyperalgesia, heat hyperalgesia, and mechanical allodynia, indicating that it is a lead compound for treating pain. Notably, CHET3 showed better anti-cold hyperalgesia than Pregabalin in a mouse model of neuropathic pain, a first-line clinically-used drug for neuropathic pain. To demonstrate that CHET3 targets TASK-3 for analgesia, the authors adopted both chemical and genetic approaches. Using chemistry, they synthesized two derivatives of CHET3: a positive control that was also a potent CHET3 activator, and a negative control that was inactive. Then, they nicely showed that the positive control was active and the negative control was inactive in pain models. Last, CHET3 was completely inactive in TASK-3-knockout mice in all of the animal pain tests used. Notably, the TASK-3-knockout mice exhibited enhanced sensitivity to thermal and mechanical stimuli in chronic pain, which strongly suggests that TASK-3 is an intrinsic regulator of pain sensation. After clarifying the analgesic roles of TASK-3, a mechanistic study was designed. The pharmacokinetics of CHET3 defined a peripheral role and excluded its central action. With a focus on DRG cells, they mapped out the cellular location of TASK-3 in DRG using the RNAscope technique, a recently-developed *in situ* mRNA detection method. TASK-3-positive cells are small nociceptive neurons abundantly expressing TRPV1, TRPM8, or tyrosine hydroxylase, which are markers of thermal- and mechanical-sensitive neurons. As expected, CHET3 was able to reduce the excitability of nociceptive neurons by increasing the K^+ conductance as shown by electrophysiology and Ca^{2+} imaging.

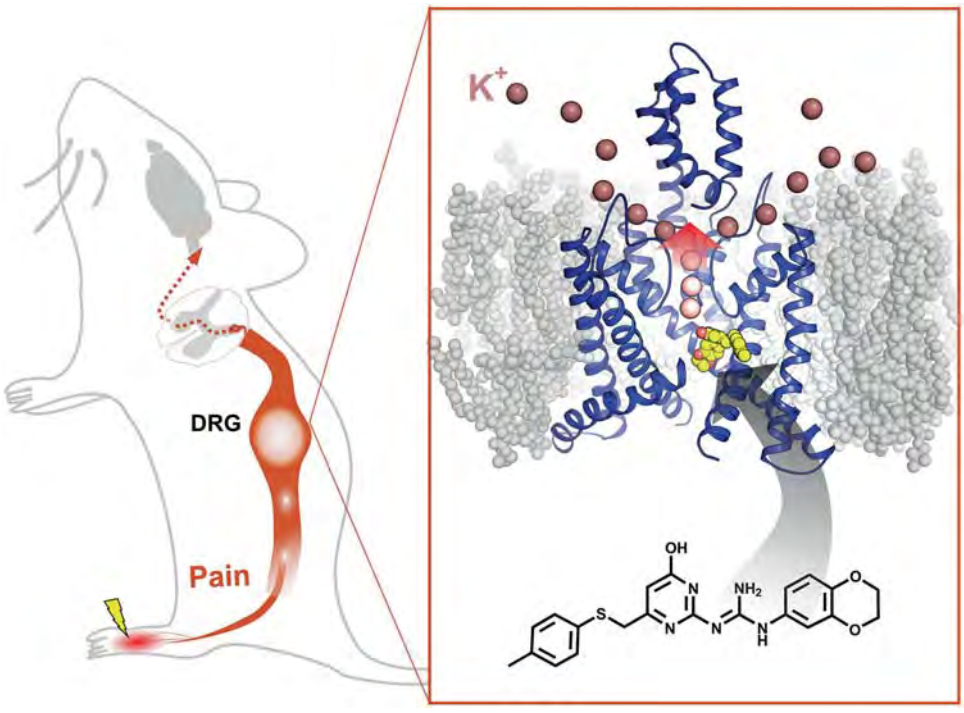

Fig. 1 Cartoon showing that the selective activation of TASK-3 in dorsal root ganglion (DRG) neurons produces the extrusion of K^+, which reduces the excitability of nociceptive neurons, and consequently inhibits the transduction of pain signaling from the DRG to the central nervous system. Right panel shows the docking of the allosteric agonist CHET3 to a TASK-3 homology model.

TASK-3 was found to be expressed in mouse carotid body type-1 cells, and studies using mice with global knockout of TASK suggest that TASK-3 plays a role in chemoreception [9]. However, the precise role of TASK channels (TASK-1, TASK-3 and/or TASK3/1) in peripheral chemoreception (carotid body) is still a matter of debate. Thus, the use of the peripherally-acting selective activator of TASK-3 allowed the authors to verify the role of TASK-3 and TASK-3/1 in peripheral chemoreception that mainly involves the carotid body. The data suggest that CHET3 has no effect on respiratory and cardiovascular function in mice. To definitively exclude a role of TASK channels in peripheral chemoreception through the carotid body, further studies using both tissue-specific knockout mice and more compounds such as the TASK inhibitor PK-THPP are needed. Overall, using computation, pharmacology, electrophysiology, chemistry, and analysis of behavioral tests, this multidisciplinary work uncovered and characterized a 'first-of-the-kind' selective activator for a K2P channel, and revealed a new biological function of its target. This study provides mechanistic insights into K2P activation and biological function and highlights the translational potential of CHET3 as a lead compound targeting TASK-3 in pain medicine. More importantly, this study opens up exciting new avenues for further exploring TASK-related physiology and pathophysiology.

Many questions are still waiting for answers and research directions arise from this discovery of TASK-3 as a novel pain target. First, based on the RNAscope data reported in this study, TASK-3 was not abundantly expressed in DRG; instead, it was sparsely expressed in TRPV1- or TRPM8-positive cells, which was confirmed by the functional study using electrophysiology. Indeed, only $<$20% of DRG neurons responded to CHET3. It is thus intriguing that the selective activation of TASK-3-containing channels has a remarkable effect in analgesia. Further studies analyzing the transcriptomic and projection profiles of TASK-3-positive sensory neurons would provide more insights into the regulatory role of TASK-3 in pain signaling. Second, does TASK-3 play a role in the regulation of neural plasticity in the central sensitization of chronic pain? Third, it is noteworthy that the authors found that TASK-3 was expressed strongly in the trigeminal ganglia, suggesting that TASK-3 may play potential roles in migraine and trigeminal neuralgia. This would be an interesting way to continue research in the TASK field. Last, the most important issue is that *in situ* evidence for TASK-3 expression in human sensory neurons is lacking. Without this in hand, it is difficult to evaluate the clinical application of TASK-3 activators in treating pain at the bedside. Further studies involving human tissues are keenly awaited for the translational aspects in this field and more effort should be devoted to the development of the next generation of TASK-selective compounds. Beyond pain, centrally-acting TASK-3 activators may be useful in the treatment of sleep disorders. And the question also arises whether TASK-3 is involved in itch. The co-localization of TASK-3 with TRPV1 and TRPM8 suggests that this may be a research direction worth pursuing.

Acknowledgements The authors' research is supported by the National Key R&D Program of China (2019YFC1709101), The Project First-Class Disciplines Development of Chengdu University of TCM (CZYHW1901), São Paulo Research Foundation (FAPESP 2018/07366-4), the National Natural Science Foundation of China (81904312 and 81774437), and the Sichuan Science and Technology Program, China (2019YFH0108, 2018HH0123, and 2018SZ0257).

Conflict of interest The authors declare that they have no conflict of interest.

References

1. Barlass U, Dutta R, Cheema H, George J, Sareen A, Dixit A, *et al.* Morphine worsens the severity and prevents pancreatic regeneration in mouse models of acute pancreatitis. Gut 2018, 67: 600–602.
2. Bang S, Yoo J, Gong X, Liu D, Han Q, Luo X, *et al.* Differential inhibition of Nav1.7 and neuropathic pain by hybridoma-produced and recombinant monoclonal antibodies that target Nav1.7: Differential activities of Nav1.7-targeting monoclonal antibodies. Neurosci Bull 2018, 34: 22–41.
3. Minett MS, Nassar MA, Clark AK, Passmore G, Dickenson AH, Wang F, *et al.* Distinct Nav1.7-dependent pain sensations require different sets of sensory and sympathetic neurons. Nat Commun 2012, 3: 791.
4. Cox JJ, Reimann F, Nicholas AK, Thornton G, Roberts E, Springell K, *et al.* An SCN9A channelopathy causes congenital inability to experience pain. Nature 2006, 444: 894–898.
5. Goldberg YP, MacFarlane J, MacDonald ML, Thompson J, Dube MP, Mattice M, *et al.* Loss-of-function mutations in the Nav1.7 gene underlie congenital indifference to pain in multiple human populations. Clin Genet 2007, 71: 311–319.
6. Emery EC, Luiz AP, Wood JN. Nav1.7 and other voltage-gated sodium channels as drug targets for pain relief. Expert Opin Ther Targets 2016, 20: 975–983.
7. Minett MS, Pereira V, Sikandar S, Matsuyama A, Lolignier S, Kanellopoulos AH, *et al.* Endogenous opioids contribute to insensitivity to pain in humans and mice lacking sodium channel Nav1.7. Nat Commun 2015, 6: 8967.
8. Talley EM, Solorzano G, Lei Q, Kim D, Bayliss DA. CNS distribution of members of the two-pore-domain (KCNK) potassium channel family. J Neurosci 2001, 21: 7491–7505.
9. Turner PJ, Buckler KJ. Oxygen and mitochondrial inhibitors modulate both monomeric and heteromeric TASK-1 and TASK-3 channels in mouse carotid body type-1 cells. J Physiol 2013, 591: 5977–5998.
10. Rusznak Z, Pocsai K, Kovacs I, Por A, Pal B, Biro T, *et al.* Differential distribution of TASK-1, TASK-2 and TASK-3 immunoreactivities in the rat and human cerebellum. Cell Mol Life Sci 2004, 61: 1532–1542.
11. Gnatenco C, Han J, Snyder AK, Kim D. Functional expression of TREK-2 K^+ channel in cultured rat brain astrocytes. Brain Res 2002, 931: 56–67.

12. Bayliss DA, Barrett PQ. Emerging roles for two-pore-domain potassium channels and their potential therapeutic impact. Trends Pharmacol Sci 2008, 29: 566–575.
13. Ge F, Mu P, Guo R, Cai L, Liu Z, Dong Y, *et al.* Chronic sleep fragmentation enhances habenula cholinergic neural activity. Mol Psychiatry 2019. doi: https://doi.org/10.1038/s41380-019-0419-z.
14. Yao C, Li Y, Shu S, Yao S, Lynch C, Bayliss DA, *et al.* TASK channels contribute to neuroprotective action of inhalational anesthetics. Sci Rep 2017, 7: 44203.
15. Gotter AL, Santarelli VP, Doran SM, Tannenbaum PL, Kraus RL, Rosahl TW, *et al.* TASK-3 as a potential antidepressant target. Brain Res 2011, 1416: 69–79.
16. Morenilla-Palao C, Luis E, Fernandez-Pena C, Quintero E, Weaver JL, Bayliss DA, *et al.* Ion channel profile of TRPM8 cold receptors reveals a role of TASK-3 potassium channels in thermosensation. Cell Rep 2014, 8: 1571–1582.
17. Cotten JF. TASK-1 (KCNK3) and TASK-3 (KCNK9) tandem pore potassium channel antagonists stimulate breathing in isoflurane-anesthetized rats. Anesth Analg 2013, 116: 810–816.
18. Wright PD, Veale EL, McCoull D, Tickle DC, Large JM, Ococks E, *et al.* Terbinafine is a novel and selective activator of the two-pore domain potassium channel TASK3. Biochem Biophys Res Commun 2017, 493: 444–450.
19. Garcia G, Noriega-Navarro R, Martinez-Rojas VA, Gutierrez-Lara EJ, Oviedo N, Murbartian J. Spinal TASK-1 and TASK-3 modulate inflammatory and neuropathic pain. Eur J Pharmacol 2019, 862: 172631.
20. Liao P, Qiu Y, Mo Y, Fu J, Song Z, Huang L, *et al.* Selective activation of TWIK-related acid-sensitive K^+ 3 subunit-containing channels is analgesic in rodent models. Sci Transl Med 2019, 11. pii: eaaw8434.

Neurosci. Bull. August, 2020, 36(8):955–957
https://doi.org/10.1007/s12264-020-00504-8

www.neurosci.cn
www.springer.com/12264

RESEARCH HIGHLIGHT

A Lower-Brainstem Structure Coordinates Acquisition of Negative Experience

Lei Li[1,2]

Received: 20 December 2019 / Accepted: 15 January 2020 / Published online: 25 April 2020

To survive, animals must process aversive or stressful events quickly, and evaluate and store the related information. Accumulating neural circuity studies have identified key brain nuclei, such as the amygdala, lateral habenula (LHb), periaqueductal grey (PAG), ventromedial hypothalamic nucleus, hippocampus, among others, in the processing of negative experiences [1, 2]. Yet more work is needed to determine how these brain structures coordinate with each other in coping with such experiences.

A recent study published in *Science* entitled "Median raphe controls acquisition of negative experience in the mouse" from Dr. Nyiri's group at the Hungarian Academy of Sciences sheds new light on this complex and important question [3]. Using cell-type-specific neuronal tracing, block-face scanning immunoelectron microscopy, *in vivo* and *in vitro* electrophysiology, and optogenetic and chemogenetic manipulations together with behavioral tasks, they revealed that the median raphe region (MRR, also named median raphe nucleus, MnR), especially the vesicular glutamate transporter 2 (vGluT2)-positive neurons in the MRR may serve as a key hub for the coordination of negative experience processing.

While the serotoninergic neurons in the MRR have been investigated, Szőnyi *et al.* studied a previously neglected neuron type – vGluT2-neurons. These constitute at least 20% of all MRR neurons, and are distributed both in the median and the paramedian parts of the region. Using multichannel recording and optogenetic tagging, they showed that MRR vGluT2-neurons respond selectively to an aversive stimulus (air puffs) and to a much lesser extent to mildly aversive light-emitting diode flashes, while they do not respond to the rewarding stimulus of water drops.

Three groups of functional experiments were carried out to decipher the roles of MRR vGluT2-neurons in negative experience. First, acute *in vivo* optogenetic somatic activation of these neurons caused significant real-time place aversion and conditioned place aversion, and a decrease in nose-pokes for food pallet rewards in hungry mice after pairing. Second, *in vivo* chemogenetic activation of the soma of the neurons led to highly aggressive behavior in a social interaction test and the resident-intruder test. Moreover, chronic chemogenetic activation of somata for 3 weeks induced anhedonia in the sucrose preference test. Third, the optogenetic activation of the MRR vGluT2-neurons triggered movement of the mice as well as hippocampal theta oscillations. In a loss-of-function study using a delay-cued fear conditioning paradigm, optogenetic inhibition of these neurons during the presentation of adverse stimuli decreased contextual freezing behavior and generalized conditioned fear, showing their essential role in storing the memory of a negative experience.

Szőnyi *et al.* reached the conclusion that "MRR controls acquisition of negative experience in the mouse" based not only on the above functional data but also their solid and detailed tracing of the inputs and outputs of MRR vGluT2-neurons. It is worth pointing out that the use of block-face scanning immunoelectron microscopy to demonstrate the details of the synapses formed by MRR vGluT2-neurons with their downstream targets is a highlight. As shown in Figure 1 (green lines), MRR vGluT2-neurons receive

✉ Lei Li
saralilei@siat.ac.cn

[1] Guangdong Provincial Key Laboratory of Brain Connectome and Behavior, CAS Key Laboratory of Brain Connectome and Manipulation, the Brain Cognition and Brain Disease Institute, Shenzhen Institutes of Advanced Technology, Chinese Academy of Sciences, Shenzhen 518000, China

[2] Shenzhen-Hong Kong Institute of Brain Science-Shenzhen Fundamental Research Institutions, Shenzhen 518055, China

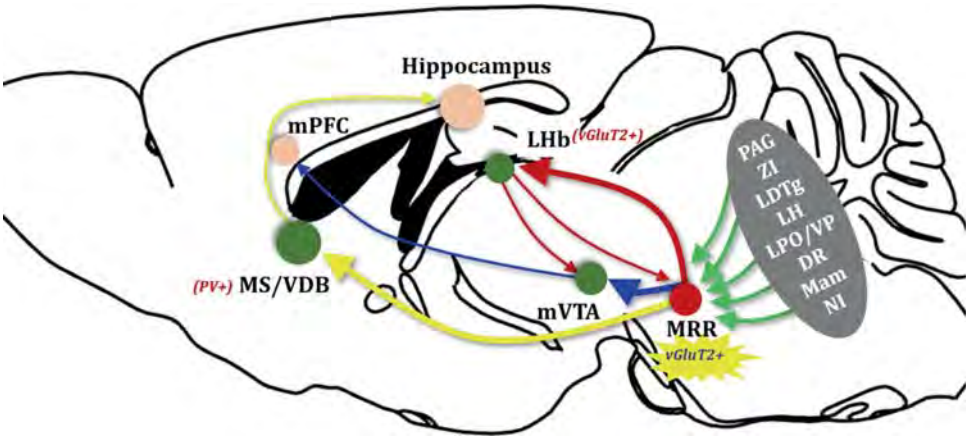

Fig. 1 The median raphe region (MRR) is a lower-brainstem structure that coordinates the acquisition of negative experience. MRR vGluT2-neurons receive extensive inputs from negative experience-related regions and coordinate negative experience processing *via* three key pathways: MRR–LHb, MRR–mVTA, and MRR–MS/VDB (*MRR* median raphe region, *vGluT2* vesicular glutamate transporter 2, *LHb* lateral habenula, *mVTA* medial ventral tegmental nucleus, *MS/VDB* medial septum and vertical limb of the diagonal band of Broca, *PV* parvalbumin, *mPFC* medial prefrontal cortex, *PAG* periaqueductal gray, *ZI* zona incerta, *LDTg* laterodorsal tegmental nucleus, *LH* lateral hypothalamus, *LPO/VP* lateral preoptic area and ventral pallidum, *DR* dorsal raphe, *Mam* mammillary complex, *NI* nucleus incertus).

extensive inputs from aversion-, defense- and memory-related areas including the PAG, zona incerta, laterodorsal tegmental nucleus, lateral hypothalamus, lateral preoptic area and ventral pallidum, dorsal raphe, mammillary complex, and nucleus incertus. In the downstream tracing of MRR vGluT2-neurons, three structures were intensively studied: the LHb, medial ventral tegmental nucleus (mVTA), and medial septum/vertical limb of the diagonal band of Broca (MS/VDB). First, using double-injection of tracers, they found that MRR vGluT2-neurons establish glia-enwrapped synapses on LHb vGluT2-neurons, which then project to the mVTA. The vGluT2-positive MRR neurons and the vGluT2-positive LHb neurons projecting to the MRR also form direct reciprocal connections (Fig. 1, red lines). Second, MRR vGluT2-neurons directly innervate neurons in the mVTA that project to the medial prefrontal cortex (Fig. 1, blue lines). Third, MRR vGluT2-neurons also directly innervate parvalbumin-positive neurons in the MS/VDB that project to the hippocampus (Fig. 1, yellow lines). These anatomical tracing data provide structural rationales for the functional experiments and elaborate on the role of the MRR as a key hub for the acquisition of negative experience.

Exploring the question of negative experience coordination is no doubt very challenging considering the scope of "negative experience" and its complex processes [1, 4–8]. Negative experience in this study alone incorporates behavioral concepts that include active avoidance, conditioned fear, aggression, and depression. The related coordination includes at least the recognition of aversive/alerting signals, the production of quick and adequate behavioral responses, and the possible learning procedures [9, 10]. It is exciting to see in this article the identification of a new group of functional neurons in the MRR and their roles in the acquisition of negative experience along with detailed anatomical support.

In the field of the neural circuity underlying negative experience processing, the idea that one structure in the brainstem can coordinate the activities of several upstream convergent inputs and several downstream outputs simultaneously is intriguing. The detailed mechanism of the coordination, especially at different time scales (acute aversion and long-term hippocampal memory encoding), would help in the understanding of neuronal information processing in general and even in neurocomputation.

Psychiatric disorders present a unique and enormous challenge. Disorders such as depression and post-traumatic stress disorder are proposed to result from neural circuit disruption. Accumulating evidence has shown the involvement of the MRR in anxiety and other psycho-behavioral states [1]. The detailed anatomical structure of the inputs/outputs of MRR vGluT2-neurons and their physiological functions provide a rational basis for future studies: to investigate the connection between malfunction in this key hub and negative experience-related mood disorders, which might suggest new therapies.

Acknowledgements: This research highlight article was supported by the National Natural Science Foundation of China (31971072 and 81671444), Guangdong International Cooperation Grant (2019A050510032), Shenzhen Science and Technology Innovation Committee Fund (JCYJ20180508152336419), and Guangdong Provincial Key Laboratory of Brain Connectome and Behavior (2017B030301017).

Conflict of interest The author declares no competing interest.

References

1. Gross CT, Canteras NS. The many paths to fear. Nat Rev Neurosci 2012, 13: 651–658.
2. Wang L, Chen IZ, Lin D. Collateral pathways from the ventromedial hypothalamus mediate defensive behaviors. Neuron 2015, 85: 1344–1358.
3. Szőnyi A, Zichó K, Barth AM, Gönczi RT, Schlingloff D, Török B*, et al.* Median raphe controls acquisition of negative experience in the mouse. Science 2019, 366: eaay8746.
4. Cao X, Li LP, Wang Q, Wu Q, Hu HH, Zhang M*, et al.* Astrocyte-derived ATP modulates depressive-like behaviors. Nat Med 2013, 19: 773–777.
5. Cui Y, Yang Y, Ni Z, Dong Y, Cai G, Foncelle A*, et al.* Astroglial Kir4.1 in the lateral habenula drives neuronal bursts in depression. Nature 2018, 554: 323–327.
6. Li L, Feng X, Zhou Z, Zhang H, Shi Q, Lei Z*, et al.* Stress accelerates defensive responses to looming in mice and involves a locus coeruleus-superior colliculus projection. Curr Biol 2018, 28: 859–871 e855.
7. Li Y, Zeng J, Zhang J, Yue C, Zhong W, Liu Z*, et al.* Hypothalamic circuits for predation and evasion. Neuron 2018, 97: 911–924 e915.
8. Yang H, Yang J, Xi W, Hao S, Luo B, He X*, et al.* Laterodorsal tegmentum interneuron subtypes oppositely regulate olfactory cue-induced innate fear. Nat Neurosci 2016, 19: 283–289.
9. Luo H, Liu Z, Liu B, Li H, Yang Y, Xu ZD. Virus-mediated overexpression of ETS-1 in the ventral hippocampus counteracts depression-like behaviors in rats. Neurosci Bull 2019, 35: 1035–1044.
10. Tang N, Ding YF, Zhang W, Hu J, Xu XH. Stay active to cope with fear: a cortico-intrathalamic pathway for conditioned flight behavior. Neurosci Bull 2019, 35: 1116–1119.

Neuroscience Bulletin

Neuroscience Bulletin

Copyright Information

For Authors

As soon as an article is accepted for publication, authors will be requested to assign copyright of the article (or to grant exclusive publication and dissemination rights) to the publisher (respective the owner if other than Springer Nature). This will ensure the widest possible protection and dissemination of information under copyright laws.

More information about copyright regulations for this journal is available at www.springer.com/12264

For Readers

While the advice and information in this journal is believed to be true and accurate at the date of its publication, neither the authors, the editors, nor the publisher can accept any legal responsibility for any errors or omissions that may have been made. The publisher makes no warranty, express or implied, with respect to the material contained herein.

All articles published in this journal are protected by copyright, which covers the exclusive rights to reproduce and distribute the article (e.g., as offprints), as well as all translation rights. No material published in this journal may be reproduced photographically or stored on microfilm, in electronic data bases, on video disks, etc., without first obtaining written permission from the publisher (respective the copyright owner if other than Springer Nature). The use of general descriptive names, trade names, trademarks, etc., in this publication, even if not specifically identified, does not imply that these names are not protected by the relevant laws and regulations.

Springer Nature has partnered with Copyright Clearance Center's RightsLink service to offer a variety of options for reusing Springer Nature content. For permission to reuse our content please locate the material that you wish to use on link.springer.com or on springerimages.com and click on the permissions link or go to copyright.com and enter the title of the publication that you wish to use. For assistance in placing a permission request, Copyright Clearance Center can be contacted directly via phone: +1-855-239-3415, fax: +1-978-646-8600, or e-mail: info@copyright.com

Journal Website

www.springer.com/12264
Electronic edition: link.springer.com/journal/12264

Subscription Information

Volume 36 (12 issues) will be published in 2020.

ISSN: 1673-7067 print
ISSN: 1995-8218 electronic

For information on subscription rates please contact Springer Nature Customer Service Center: customerservice@springernature.com

The Americas (North, South, Central America and the Caribbean)
Springer Nature Journal Fulfillment,
Harborside Plaza II,
200 Hudson Street, Jersey City, NJ 07302, USA
Tel. 800-SPRINGER (777-4643); 212-460-1500 (outside North America)

Outside the Americas
Springer Nature Customer Service Center GmbH, Tiergartenstr. 15, 69121 Heidelberg, Germany
Tel.: +49-6221-345-4303

Advertisements

E-mail contact: advertising@springer.com or anzeigen@springer.com (Germany)

Disclaimer

Springer Nature publishes advertisements in this journal in reliance upon the responsibility of the advertiser to comply with all legal requirements relating to the marketing and sale of products or services advertised. Springer Nature and the editors are not responsible for claims made in the advertisements published in the journal. The appearance of advertisements in Springer Nature publications does not constitute endorsement, implied or intended, of the product advertised or the claims made for it by the advertiser.

Office of Publication

Springer Nature Singapore Pte Ltd.
152 Beach Road, #21-01/04
Gateway East, Singapore 189721, Singapore

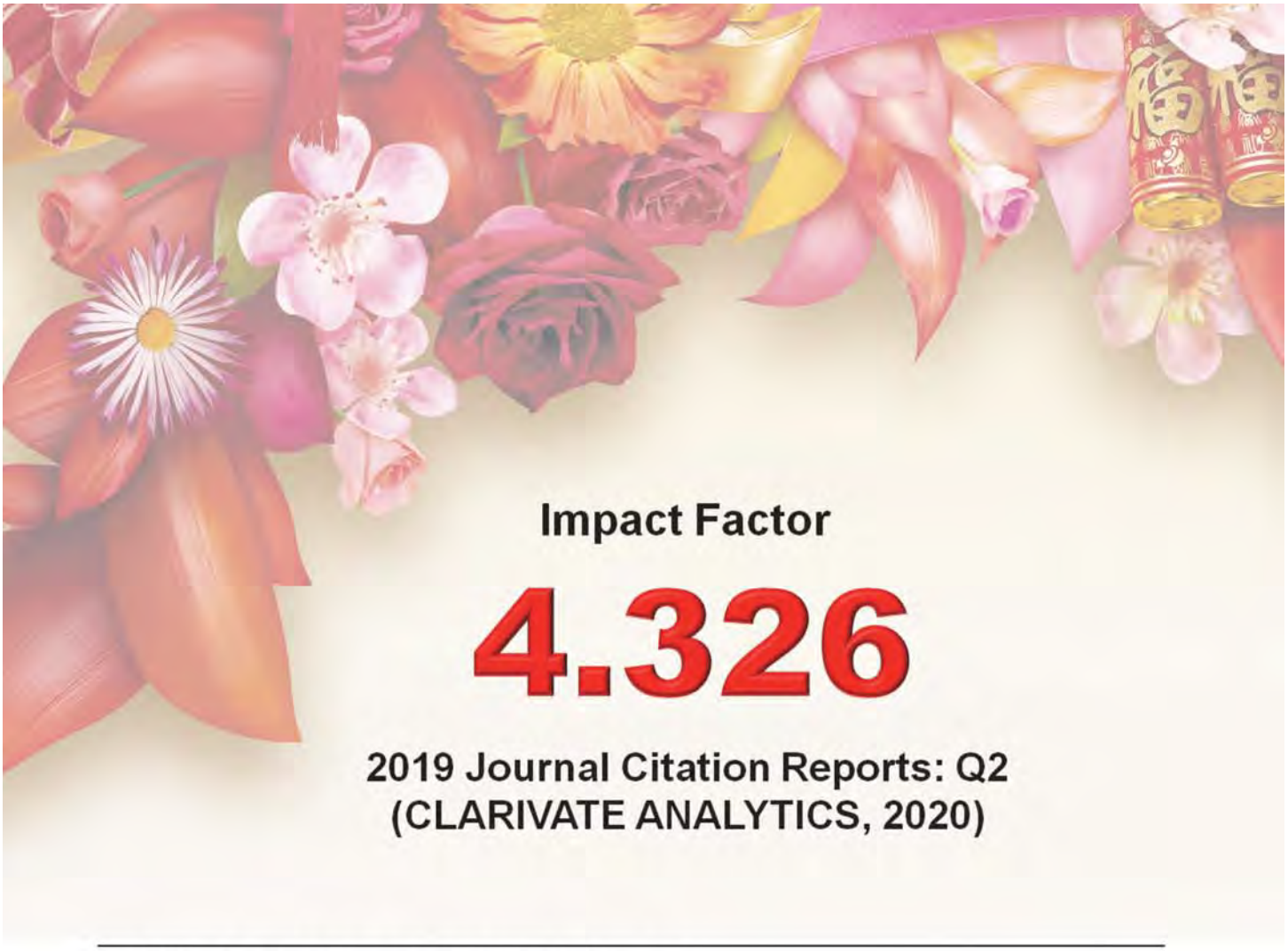

NEUROSCIENCE BULLETIN 神经科学通报 (Monthly)

Vol. 36 No. 8 August 15, 2020

Sponsored by: Shanghai Institutes for Biological Sciences, Chinese Academy of Sciences
Chinese Neuroscience Society
Second Military Medical University

Editors-in-Chief: Shumin Duan, Ru-Rong Ji

Edited by: Editorial Board of *Neuroscience Bulletin*
319 Yueyang Road, Building 31 B, Room 405, Shanghai 200031, China
Phone: +86-21-54922863; Fax: +86-21-54922833
E-mail:nsb@sibs.ac.cn; http://www.neurosci.cn

Editors: Bin Wei, Zhi-Rui Liu

Published by: Shanghai Institutes for Biological Sciences, Chinese Academy of Sciences (320 Yueyang Road, Shanghai)

Printed by: Shanghai Shengtong Times Printing Co., Ltd (A6, No. 2888, Caolang Highway, Jinshan District, Shanghai)

Overseas Distributed by: Springer Nature

Home Distributed by: Local Post Offices

ISSN 1673-7067
CN 31-1975/R

Post Office Code Number: 4-608
Permit of Ad. Number: 3100420130051
Price: ¥ 100.00

ISSN 1673-7067

OLYMPUS

转盘共聚焦超分辨显微镜

SpinSR10

IXplore

兼顾分辨率和速度的
转盘共聚焦活细胞超分辨系统 SpinSR10

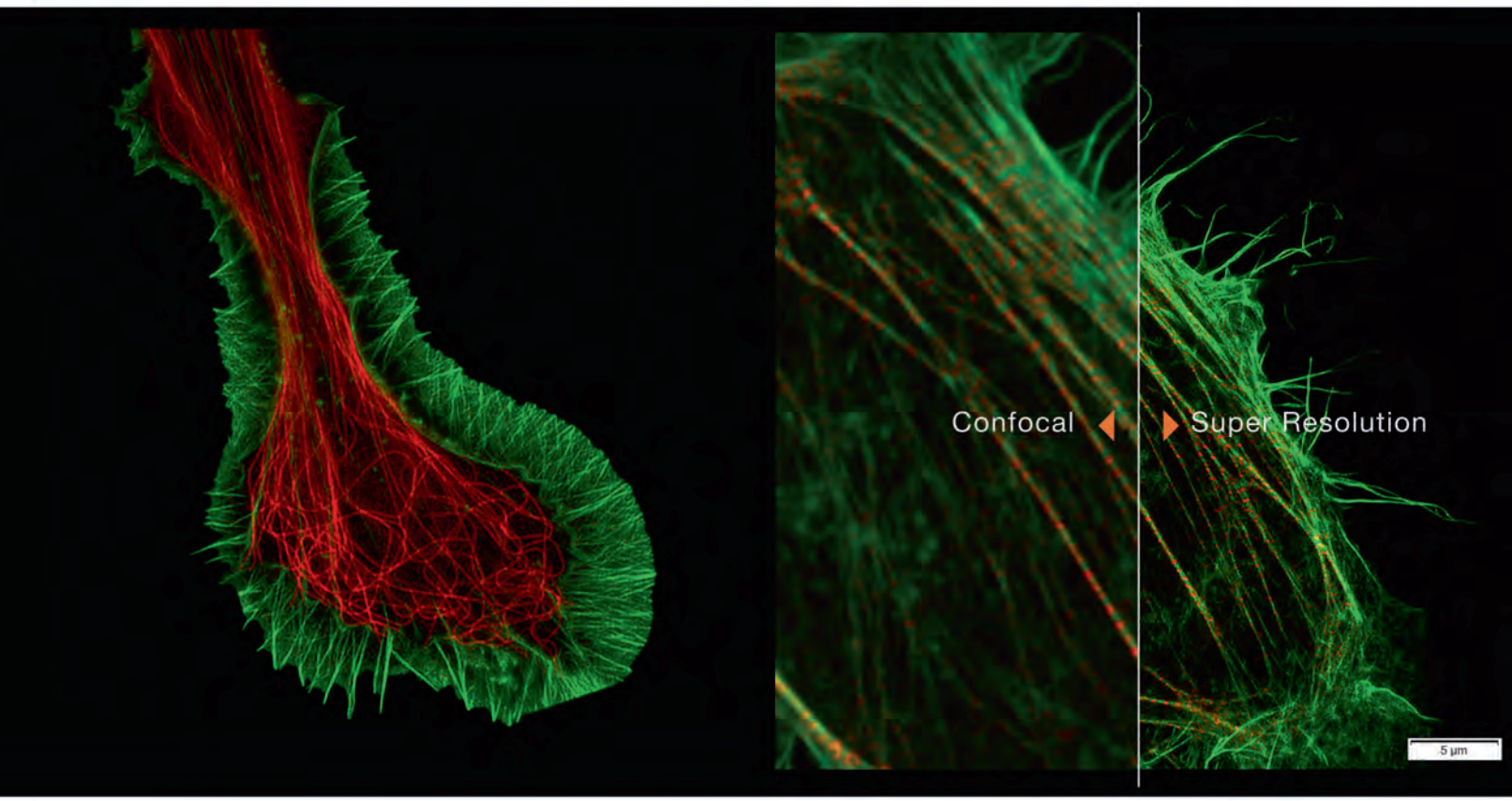

- 分辨率高达110 nm的实时超分辨率成像
- 专有反卷积算法进一步提升图像质量
- 宽视野成像，速度高达 200fps
- 特色硅油物镜可以实现活细胞深层成像
- 宽场、共聚焦、超分辨率模式自由切换
- 功能强大的智能cellSens软件平台

奥林巴斯（北京）销售服务有限公司

北京朝阳区酒仙桥路10号恒通商务园B12C座2F （北京） 010-59756006
上海市徐汇区淮海中路1010号嘉华中心11楼 （上海） 021-51582084
广州市环市东路403号广州电子大厦16楼 （广州） 020-61227171
陕西省西安市新城区尚德路85号太平洋保险大厦8F （西安） 029-87206108
湖北省武汉市江岸区中山大道1628号武汉天地企业中心5号7楼701单元 （武汉） 027-82718838
四川省成都市人民南路四段三号来福士广场T1-11楼 （成都） 028-86703700
辽宁省沈阳市沈河区友好街10号新地中心1号楼3501室 （沈阳） 024-23342084

http://www.olympus-lifescience.com.cn/zh/